FRIEDRICH-SCHILLER-
UNIVERSITÄT
JENA

Physical approaches for the performance optimization and investigation of organic batteries

Dissertation
(kumulativ)
zur Erlangung des akademischen Grades
doctor rerum naturalium (Dr. rer. nat.)

vorgelegt dem Rat der Chemisch-Geowissenschaftlichen Fakultät
der Friedrich-Schiller-Universität Jena

von Christian Stolze, M. Sc.
geboren am 26.12.1987 in Magdeburg

Gutachter:

1. Prof. Dr. Ulrich S. Schubert Friedrich-Schiller-Universität Jena
2. Prof. Dr. Andrea Balducci Friedrich-Schiller-Universität Jena

Tag der öffentlichen Verteidigung: 19. Juni 2020

Table of contents

Documentation of Authorship

This section contains a list of individual authors' contributions to the publications reprinted in this thesis.

P1: *Directional Solidification with Constant Ice Front Velocity in the Ice-Templating Process*
C. Stolze,[1] T. Janoschka,[2] U. S. Schubert,[3] F. A. Müller,[4] S. Flauder,[5] *Adv. Eng. Mater.* **2016**, *18*, 111–119.

Author	1	2	3	4	5
Conceptual contribution	■				■
Experimental investigations	■				■
Computational & analytical investigations	■				
Preparation of the manuscript	■				
Correction of the manuscript		■	■	■	■
Supervision of C. Stolze			■		
Proposal for crediting publication equivalents	1.0				

P2: *Investigation of Ice-templated Porous Electrodes for Application in Organic Batteries**
C. Stolze,[1] T. Janoschka,[2] S. Flauder,[3] F. A. Müller,[4] M. D. Hager,[5] U. S. Schubert,[6] *ACS Appl. Mater. Interfaces* **2016**, *8*, 23614–23623.

Author	1	2	3	4	5	6
Conceptual contribution	■	■				
Synthesis of polymers		■				
Electrochemical investigations	■					
Electrode preparation and investigations	■	■	■			
Battery performance investigations	■					
Preparation of the manuscript	■	■				
Correction of the manuscript			■	■	■	■
Supervision of C. Stolze					■	■
Proposal for crediting publication equivalents	1.0					

** This publication was also used as part of the cumulative PhD thesis of Dr. T. Janoschka.*

P3: *A Tubular Polymer Redox Flow Battery with a Ceramic Membrane*
C. Stolze,[1] C. Schmerbauch,[2] C. Friebe,[3] U. S. Schubert,[4] *Energy Technol.* **2017**, *5*, 225–227.

Author	1	2	3	4
Conceptual contribution	■	■		
Cell design	■	■		
Electrochemical characterization		■		
Battery performance investigations		■		
Preparation of the manuscript	■			
Correction of the manuscript		■	■	■
Supervision of C. Stolze				■
Proposal for crediting publication equivalents	0.5			

P4: *Microtubular Flow Cell Design Utilizing Commercial Hollow Fiber Dialysis Membranes for Size-Exclusion Based Flow Batteries*
C. Stolze,[1] T. Janoschka,[2] J. Winsberg,[3] M. Strumpf,[4] M. D. Hager,[5] U. S. Schubert,[6] *Energy Technol.* **2018**, *6*, 2296–2310.

Author	1	2	3	4	5	6
Conceptual contribution	■	■			■	■
Synthesis of polymers		■	■	■		
Theoretical investigations	■					
Experimental investigations	■					
Preparation of the manuscript	■					
Correction of the manuscript		■	■		■	■
Supervision of C. Stolze					■	■
Proposal for crediting publication equivalents	1.0					

P5: *State-of-charge Monitoring for Redox Flow Batteries: A Symmetric Open-circuit Cell Approach*

C. Stolze,[1] M. D. Hager,[2] U. S. Schubert,[3] *J. Power Sources* **2019**, *423*, 60–67.

Author	1	2	3
Conceptual contribution	■		
Electrochemical characterization	■		
Online state-of-charge monitoring experiments	■		
Preparation of the manuscript	■		
Correction of the manuscript		■	■
Supervision of C. Stolze		■	■
Proposal for crediting publication equivalents	1.0		

P6: *An Amperometric, Temperature-independent, and Calibration-free Method for the Real-time State-of-charge Monitoring of Redox Flow Battery Electrolytes*

C. Stolze,[1] J. P. Meurer,[2] M. D. Hager,[3] U. S. Schubert,[4] *Chem. Mater.* **2019**, *31*, 5363–5369.

Author	1	2	3	4
Conceptual contribution	■			
Electrochemical characterization	■	■		
Temperature investigations	■	■		
Online state-of-charge monitoring experiments	■			
Preparation of the manuscript	■			
Correction of the manuscript		■	■	■
Supervision of C. Stolze			■	■
Proposal for crediting publication equivalents	1.0			

Erklärung zu den Eigenanteilen des Promovenden/der Promovendin sowie der weiteren Doktoranden/Doktorandinnen als Koautoren an den Publikationen und Zweitpublikationsrechten bei einer kumulativen Dissertation

Für alle in dieser kumulativen Dissertation verwendeten Manuskripte liegen die notwendigen Genehmigungen der Verlage („Reprint permissions“) für die Zweitpublikation vor.

Die Co-Autorinnen/-Autoren der in dieser kumulativen Dissertation verwendeten Manuskripte sind sowohl über die Nutzung, als auch über die oben angegebenen Eigenanteile der weiteren Doktorandinnen/Doktoranden als Co-Autorinnen/Autoren an den Publikationen und Zweitpublikationsrechten bei einer kumulativen Dissertation informiert und stimmen dem zu.

Die Anteile des Promovenden sowie der weiteren Doktorandinnen/Doktoranden als Co-Autorinnen/Co-Autoren an den Publikationen und Zweitpublikationsrechten bei einer kumulativen Dissertation sind in der Anlage aufgeführt.

Christian Stolze		Jena	
Name des Promovenden	Datum	Ort	Unterschrift

Ich bin mit der Abfassung der Dissertation als publikationsbasierte Dissertation, d.h. kumulativ, einverstanden und bestätige die vorstehenden Angaben.

Prof. Dr. Ulrich S. Schubert		Jena	
Name Betreuer	Datum	Ort	Unterschrift

Dr. Martin D. Hager		Jena	
Name Betreuer	Datum	Ort	Unterschrift

1 Introduction

The past decades are marked by an ever increasing scientific understanding and societal awareness of the impact humanity has on the natural ecosystem. Among the increasing number of ecological problems,[1] climate change seems to be the issue with the most severe consequences for humanity and the ecosystem as a whole. While the observed increase of the global mean temperature is the most prominent indicator for this climatic change, its cause is attributed mainly to the continuous accumulation of the greenhouse gas CO_2 in the atmosphere. The observed temporal correlation between the global mean temperature increase by approximately +0.95 °C (mean temperature anomaly above 20th century average, 2019) and the increase of the global average CO_2 concentration in earth's atmosphere from approximately 280 ppm (1750) to 409 ppm (2019) since the beginning of the industrialization, led to the scientific conclusion that this global temperature change is a human-caused process.[2-4] It is attributed mainly to the massive burning of fossil fuels such as coal, oil, and gas which power our industrialized societies.[2] Due to that, an international agreement aiming for the total reduction of human-made CO_2 emissions and the limitation of the global average temperature increase to "well below 2 °C above pre-industrial levels" was set up.[5] To achieve this reduction, a consequent reorganization of our fossil resource based society to one based on renewable material and energy resources is inevitable. Although electricity today only has a 20% share in the global energy consumption, the transformation of the electricity grid to the use of renewable energy resources is in the center of all efforts. This can be attributed to fact that electricity generated from renewable energies in combination with ongoing electrification of our society has a vast potential for massive reduction of CO_2 emissions. With respect to this, the IRENA predicts that by 2050 up to 42% of the overall global energy demand could be covered by renewable electricity due to wide-spread installation of renewable energy as well as the electrification of vehicles, electrification of the heat sector, and the application of power-to-hydrogen technologies.[6]

However, the reorganization of the electricity grid is complicated by the volatility of the most important renewable energy resources, *i.e.*, wind and solar power, which places massive strains on the grid stability.[7] In order to provide a stable and reliable electricity supply, this intermittent electricity generation needs to be decoupled from the unpredictable consumption. To do so, energy has to be stored in times of high generation and low demand for times at which the generation is low and the consumption is high. In this context, stationary batteries are regarded as an important part of the solution to the aforementioned challenges.[6-9] At the same time, the demand for electric vehicles, mobile computers, mobile phones, and smart devices for the internet of things further increases and, consequently, is calling for mobile, quickly rechargeable, cost-efficient, and durable batteries. While lead-acid batteries and nickel-cadmium batteries have covered the battery demand in the past century, their market share and growth rate is continuously declining. Instead, lithium-ion batteries containing cobalt oxide are currently the primary approach to cover the increasing demand in both mobile and stationary applications.[10] However, the limited amount of extractable lithium and cobalt on earth,[11] the socioeconomically and ethically critical conditions under which cobalt is extracted,[12, 13] the limited safety due to flammable materials,[14] and the intrinsic environmental concerns[15] stress the requirement for alternative storage materials.

On the other hand, organic chemical compounds have been investigated for various applications in electronics such as displays, printable circuits, and solar cells in the past decades.[16, 17] However, despite the early attempts to build battery electrodes from redox-active organics which followed the discovery of the electrical conductivity of doped conjugated polymers in the 1980s, no significant applications arose at that time.[18-21] This circumstance can be attributed to the materials' low energy densities as well as their unfavorable sloping potential profile,[22, 23] and the advent of the highly successful lithium-ion battery around the same time.[24, 25] In the early 2000s, however, Nakahara *et al.* and Nishide *et al.* reported a re-chargeable organic battery utilizing a nitroxide radical containing polymer as cathode material and lithium metal as anode material.[26, 27]

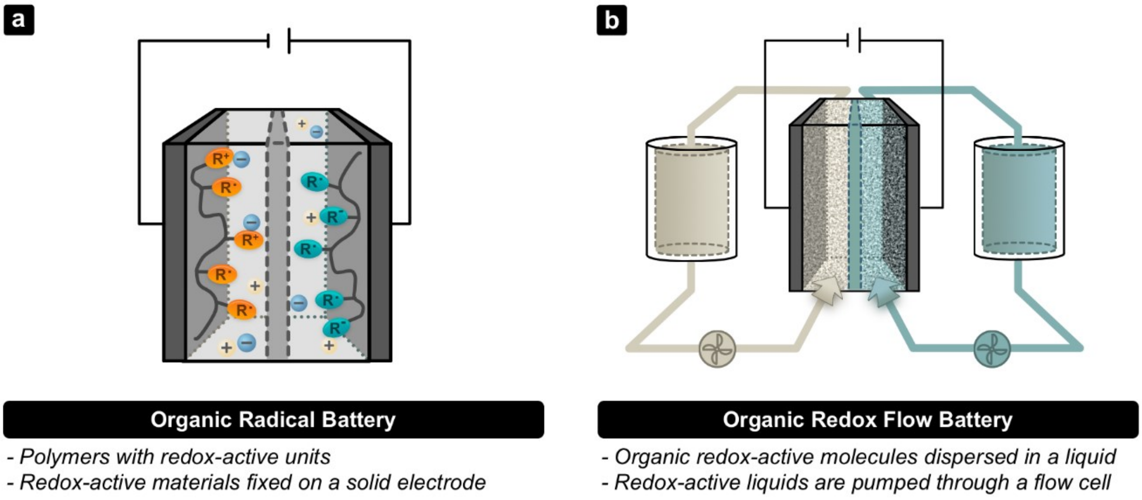

Figure 1.1. Schematic illustration of (a) an organic radical battery and (b) an (organic) redox flow battery.

Due to the utilization of moieties containing stable radicals, these batteries were termed organic radical batteries (ORBs). The principle setup of ORBs resembles the setup of conventional batteries, except for the fact that insoluble redox-active polymers are utilized as storage materials (**Figure 1.1a**). Their exceptionally high power density, chemical tunability, potentially low cost, and reliance on non-abundant resources promoted this new battery type as one of the most promising storage technologies. A tremendous amount of research effort was, thus, put into the development of new organic redox-active molecules in the past two decades,[22, 28, 29] resulting in a myriad of investigated compounds. Although some severe obstacles like long-term stability issues and a lack of suitable anodic compounds still prevail, organic batteries are continuously evolving. In particular, the successful extension of the chemical principles of ORBs to the redox flow battery (RFB) concept represented a milestone for stationary electricity storage.[30, 31] While conventional batteries and ORBs rely on solid electrodes, which are electrically isolated by a separator and are connected by an electrochemically inert ion conducting electrolyte (**Figure 1.1a**), RFBs utilize redox-active liquids. That is, the redox-active compounds of the anode and cathode are dissolved or suspended in water or an organic solvent and are pumped through electrically conductive porous electrodes, at which the electrochemical reaction can take place (**Figure 1.1b**). Instead of a separator, an ion-conducting membrane is applied, which enables the passage of supporting electrolyte ions and prevents cross-over of the redox-active species between the different half-cells.[32-34] Due to this separation of storage material and solid electrode, the capacity and power of a RFB are scalable independently from each other. This represents an ideal system property for stationary energy storage, which is also unique among battery technologies. While RFBs historically utilized inorganic materials like zinc, bromine, and vanadium, more recent approaches focus on organic redox-active small molecules and polymers.[35, 36] Recent research efforts on both anodic and cathodic organic compounds resulted in redox-active molecules that equal or surpass the energy density of their inorganic counterparts,[37-39] including the commercially most relevant vanadium-based redox chemistry which yields an energy density of approximately 25 Wh L^{-1}.[33]

Although the research on organic batteries in general is a highly interdisciplinary field, the majority of scientific work is focused on chemical synthesis and the development of novel redox-active materials. Furthermore, these are investigated mainly in standard cells with standard methods known from lithium-ion battery research. The unique properties and tunability of organic compounds, however, clearly enable novel approaches for electrode processing as well as battery designs and demands novel characterization techniques to understand the physicochemical properties of redox-active organic compounds. For example, it has been demonstrated that the flexibility of polymeric films and the synthetic adjustability of organic compounds enables the utilization of modern and cost-efficient printing techniques like inkjet printing.[40] With regard to characterization techniques and organic redox flow batteries, *e.g.*, it was recently reported that non-conventional cycling methods can provide detailed information about the stability of a single redox-active organic compound under realistic operation conditions.[41] The results of this particular study suggest that cycle stability, which is conventionally utilized to characterize the stability of electrode materials, is an insufficient figure of merit for organic batteries.

Their clearly is an unsatisfied requirement for such methodological investigations as well as for the exploitation of non-conventional processing and design approaches. Nevertheless, both can significantly help to understand the electrochemical processes in organic electrodes, to assess degradation mechanisms, to optimize their performance, to speed up the research processes, and to make use of their full potential as novel energy storage materials. The PhD thesis at hand, therefore, aims at contributing a physical perspective to the performance optimization and investigation of organic radical as well as redox flow batteries, which is beyond the synthesis and optimization of new redox active organic compounds.

In this context, **Chapter 2** describes work performed on the ice-templating of porous electrodes for ORBs as a novel electrode processing technique for this battery type. Theoretical insights into the fundamental processes of the directional solidification of aqueous suspensions are explored at first. This process is the basis for ice-templating techniques, which have been previously applied for the preparation of, *e.g.*, porous ceramic structures. Due to the positive effects on rate capability reported for meso- and microporous electrode structures,[42-52] the ice-templating process is applied to organic battery electrode materials. The resulting porous electrodes are investigated with regard to their electrochemical performance with a main focus on their rate capability.

While high rate capabilities and power densities, respectively, are demanded for mobile devices in order to provide swift rechargeability in a compact and light-weight device, the same parameter is of equal importance for stationary batteries for different reasons. Redox flow batteries, for example, have to cover a broad range of power densities to effectively provide or store electrical energy over time-scales ranging from seconds to hours. Furthermore, a high power density correlates to a lower material consumption and, hence, lower overall material costs for a system with a defined power demand. With regard to that, **Chapter 3** presents investigations on non-conventional cell geometries for RFBs. While the majority of flow battery research projects is currently focused on the development of new electrochemically active compounds and the improvement of existing filter-press designs, studies on alternative cell designs or operation concepts is sparse. In fact, the conventional filter-press design used in flow batteries today dates back to its invention in the 1950s and has not changed fundamentally since.[32, 34] On the other hand, redox flow batteries in general still struggle with high system costs, comparably low system efficiencies, and limited rate capabilities. Cell design concepts based on alternative geometries might provide means to reduce material consumption, enable the application of novel cell materials, simplify production processes, and to improve power densities. Each would contribute to a significant decrease in system costs. In particular, tubular and microtubular cell designs could benefit from lower sealing areas and increased power densities due to higher membrane area to volume ratios. A goal of this thesis, therefore, was to investigate the performance properties of such tubular flow cells.

Measures for performance optimization, however, go beyond the direct improvement of material and cell properties. A control of operational parameters is equally important and enables to optimize the battery performance for a chosen battery configuration. With regard to this and due to the severe importance of the state-of-charge (SOC) for a performance-optimized and safe operation of any battery, **Chapter 4** features the investigation of two online SOC monitoring methods for redox flow battery electrolytes. The first approach represents a modification to the existing open-circuit cell method, which estimates the SOC of a single RFB electrolyte from its equilibrium potential measured *versus* a reference electrode. While usually standard reference electrodes like, *e.g.*, Ag/AgCl electrodes are used, it is demonstrated that the flow battery electrolyte itself can provide a stable reference potential if used within the reference half-cell of a symmetric open-circuit cell. This approach improves the open-circuit cell method by, *e.g.*, reducing the need for frequent re-calibration and the ability for an *in-situ* production of the reference electrolyte. Despite that, however, it still shares the usual issues connected with all state-of-the-art SOC monitoring methods. The latter include temperature dependency, the general need for calibration, and unknown systematic SOC estimation errors originating from the calibration procedure. The second approach presented within this PhD thesis relies on an amperometric measurement of mass-transfer limited currents. Equations are derived which enable the calibration-free online monitoring of the state-of-charge of theoretically arbitrary redox flow battery electrolytes. The proposed mathematical framework and the experimental findings suggest that this method is independent from temperature, concentration, and any other system parameter.

2 Directional solidification and ice-templating for organic batteries

Parts of this chapter have been published in: **P1)** C. Stolze, T. Janoschka, U. S. Schubert, F. A. Müller, S. Flauder, *Adv. Eng. Mater.* **2016**, *18*, 111–119. **P2)** C. Stolze, T. Janoschka, S. Flauder, F. A. Müller, M. D. Hager, U. S. Schubert, *ACS Appl. Mater. Interfaces* **2016**, *8*, 23614–23623.

Ice-templating (or freeze-casting) is a comparably simple method to prepare porous materials with defined pore properties and macroscopically aligned pore direction. It has numerous potential applications for the production of porous materials as, *e.g.*, for biomedical applications, membranes, electrode materials, and filters.[53-56] The basic process can be described as follows: An aqueous suspension or solution is usually cooled from the bottom using a cooling plate of defined temperature to create a vertical temperature gradient. At sufficiently high solidification velocities, lamellar ice crystals start to grow in the direction of this temperature gradient. At the phase boundaries, particles and molecules are rejected from the ice phase and, subsequently, gather between the lamellae forming a separate solid phase. After this freezing process, the ice phase is removed by lyophilization leaving behind a porous body consisting of the materials that were formerly suspended/dissolved within the initial sample liquid (**Figure 2.1a**). During the solidification process, the tips of the lamellae form a common phase boundary that is usually referred to as the ice front (**Figure 2.1b**).

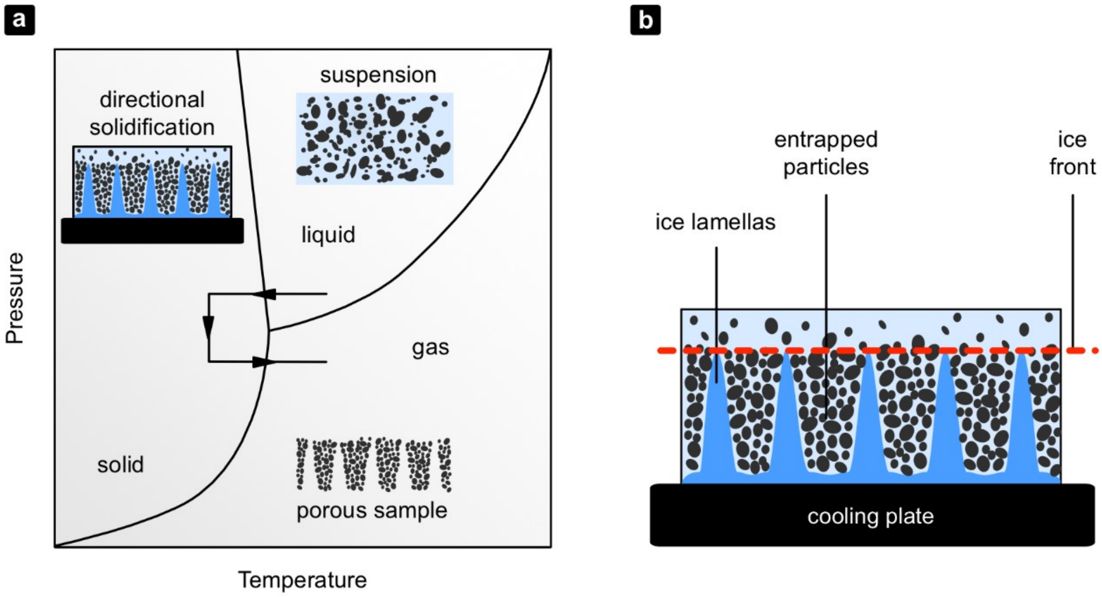

Figure 2.1. Schematic illustration of: (a) the ice templating process starting with a suspension which is directionally solidified and subsequently lyophilized (redrawn with permission; Copyright 2008, John Wiley & Sons, Inc);[53, 57] (b) the envelope of the lamella tip positions approximately is a horizontal line which represents the macroscopic phase boundary, *i.e.*, the ice front.

The method offers several options to control the structural properties of the resulting porous samples. In particular, the composition of the sample liquid and the thermodynamic conditions applied to drive the solidification have been proven to strongly influence the pore sizes and shapes.[53, 58-60] For suspensions, it was demonstrated that the pore dimensions of an ice-templated sample are directly related to the velocity at which the phase boundary between liquid water and ice (*i.e.,* the so-called ice front) moves forward during the directional solidification.[56, 61-64] It is, thus, highly desirable to understand the directional solidification process in depth in order to find ways to control the ice front velocity.

2.1 Directional solidification with constant ice-front velocity

First theoretical investigations on the directional solidification of water have been carried out long before applications like ice-templating arose. J. Stefan theoretically investigated the formation of ice in the polar oceans in his work from 1889.[65] He described the process mathematically by applying the heat equation to a domain of water, which is cooled from only one side (by the atmosphere). Since he was the first to mathematically treat a boundary value problem with a moving system boundary, the whole class of such mathematical problems is often referred to as Stefan problems. Within the context of cryobiology, Rubinsky *et al.* developed numerical procedures to calculate the ice front evolution for Stefan problems with different cooling functions applied to one boundary.[66-68] However, neither the theoretical results of J. Stefan nor those of Rubinsky were recognized or utilized in early ice-templating approaches. These early methods relied on the single-sided cooling of a suspension with a constant cooling temperature.[59] With this approach the ice front velocity decreases proportionally with $t^{-0.5}$, where t is the time. This had been theoretically predicted by J. Stefan and was experimentally verified by direct measurements of the ice front position during ice-templating approaches later.[62, 65, 69] Consequently, pore diameters of the ice-templated samples varied over 500% between the bottom and the top of the sample. To mitigate this problem, Waschkies *et al.* used an analytical cooling function representing the quasi-stationary solution to an inverse Stefan problem with constant ice front velocity.[62] The specific constant cooling rate required for a desired constant ice front velocity can be estimated by this cooling function from the thermal properties of the slurry and the solid phases. As a result, an approximately constant ice front velocity was directly measured for alumina-based slurries. Consequently, these authors achieved significantly lower variances for the average pore sizes in a single sample of only 20 to 60% over a sample height of 35 mm. Flauder *et al.* proposed the utilization of an exponential cooling function to achieve constant ice front velocities within a single-sided ice-templating setup with thermally isolated sample mold.[70, 71] It was empirically demonstrated that constant mean pore diameters can be obtained for water-based β-tricalcium phosphate (β-TCP) suspensions over sample heights of at least 20 mm. Although these studies represented the first application of the exponential cooling function to the ice-templating process, the function itself was historically found by J. Stefan as an educated guess in his aforementioned publication.[65]

Some theoretical investigations on this analytical exponential cooling function have been carried out by the author of this PhD thesis in a previous master thesis.[57] For example, it was demonstrated that the quasi-stationary case utilized by Waschkies *et al.* represents a linear approximation of this exponential cooling function. It can, therefore, be regarded as a more general approach to the directional solidification with constant ice front velocity. Consequently, a first goal of this PhD thesis was to verify the theoretical results of the master thesis experimentally and to extend the theoretical analysis by numerical simulations.

For the general Stefan problem that describes the directional solidification of a liquid, two phases have to be considered – a liquid and a solid phase – on which the heat equation,

$$\frac{\partial T(\vec{r},t)}{\partial t} = \triangle\left(k\,T(\vec{r},t)\right), \tag{1}$$

has to be solved under suitable initial and boundary conditions. In equation (1), $T(\vec{r},t)$ is the temperature distribution and $k = \lambda\,(\rho c)^{-1}$ is the thermal diffusivity obtained from the thermal conductivity, λ, the density, ρ, and the specific heat capacity, c, of the specific phase. The boundary between the phases is defined as the ice front and its position changes throughout the solidification process. The general Stefan problem of directional solidification is too complex to obtain a general analytical solution. However, under the following assumption a significant simplification of the mathematical treatment is possible:

(1) The initial liquid is homogeneous and cooled from only one boundary (at the cooling plate), so that a one-dimensional treatment is valid.
(2) The system is thermally insulated from its environment at all boundaries except for the boundary, which is in contact with the cooling plate.

(3) The complete liquid has an initial temperature, which equals its freezing temperature and, consequently, the heat conduction within the liquid phase is negligible.

(4) The initial position of the ice front is $s(t=0)=0$, *i.e.*, there is no solid phase present at the beginning of the process.

(5) The ice front velocity, $\dot{s}(t)=v_f$, is constant throughout the whole solidification process.

(6) The heat released at the ice front during the phase transition is completely conducted through the solid phase.

Hence, the Stefan problem describing the directional solidification with constant ice front velocity for a homogenous liquid with the freezing temperature T_0 and of height L can be formulated as follows:

$$\frac{\partial T_s(z,t)}{\partial t}=k_s\frac{\partial^2 T_s(z,t)}{\partial z^2}, \qquad \forall\, z\le s(t)\le L, \tag{2a}$$

$$T_s(0,t)=f(t), \tag{2b}$$

$$\left.\frac{\partial T_s(z,t)}{\partial z}\right|_{z=L}=0, \tag{2c}$$

$$T_s(s(t),t)=T_0, \tag{2d}$$

$$\lambda_s\left.\frac{\partial T_s(z,t)}{\partial z}\right|_{z=s(t)}=h_f\rho_s\frac{ds(t)}{dt}=h_f\rho_s v_f, \tag{2e}$$

$$s(0)=0. \tag{2f}$$

The index s denotes the parameters and variables in the solid phase, $s(t)$ the position of the ice front at time t, $f(t)$ the time-dependent temperature of the cooling plate, and L denotes the height of the complete sample. Furthermore, T_0 represents the liquidus temperature of the liquid, λ_s the thermal conductivity of the solid phase, ρ_s the density of the solid phase, and h_f the specific latent heat of solidification.

The pair of functions, $(T_s(z,t);\ f(t))$, is referred to as the solution of this moving boundary value problem. They answer the question, what temperature $f(t)$ has to be applied to the one boundary of the sample in order to realize a directional solidification with constant ice front velocity. Since in this case $f(t)$ is the unknown function and not $s(t)$, a so-called inverse Stefan problem is treated here. While no analytical derivation of the solution to this problem could be given by J. Stefan,[65] it was demonstrated as part of this PhD thesis that a derivation is possible using a power series expansion (Taylor series),

$$T(z,t) = \sum_{m=0}^{\infty} \sum_{n=0}^{\infty} a_{m,n} z^m t^n \tag{3}$$

The further steps to calculate the coefficients a_{mn} and, hence, to obtain the solution to the Stefan problem is rather extensive, but straightforward. The final solution is an exponential function which represents the temperature distribution in the complete solid phase at any time during the solidification process,

$$T_s(z,t) = T_0 + \frac{h_f}{c_s}\left[1 - \exp\left(\frac{v_f^2}{k_s}t - \frac{v_f}{k_s}z\right)\right]. \tag{4}$$

According to equation (2b), the cooling function, $f(t)$, is readily obtained:

$$f(t) = T_0 + \frac{h_f}{c_s}\left[1 - \exp\left(\frac{v_f^2}{k_s}t\right)\right]. \tag{5}$$

Equations (4) and (5) represent the unique solution to the inverse Stefan problem with constant ice front velocity. It should be noted that Alifanov was able to proof that a solution to any inverse Stefan problem is unique, if it exists.[72] Consequently, the derived cooling function is the only cooling function available to achieve a directional solidification with constant ice front velocity under the aforementioned conditions.

While the analytical treatment presented so far involved a number of rather idealizing assumptions, an additional numerical analysis was performed with the following more complex inverse Stefan problem:

$$\begin{aligned} \frac{\partial T_s(z,t)}{\partial t} &= k_s \frac{\partial^2 T_s(z,t)}{\partial z^2} \qquad \forall\, z \le s(t) \le L \\ \frac{\partial T_l(z,t)}{\partial t} &= k_l \frac{\partial^2 T_l(z,t)}{\partial z^2} \qquad \forall\, z \ge s(t) \end{aligned} \tag{6a}$$

$$T_s(0,t) = f(t), \tag{6b}$$

$$T_s(s(t),t) = T_l(s(t),t) = \vartheta_0\big(T_s(s(t),t)\big), \tag{6c}$$

$$\left.\frac{\partial T_l(z,t)}{\partial z}\right|_{z=L} = \alpha\left(T_l(L,t) - T_e\right) \tag{6d}$$

$$\lambda_s \left.\frac{\partial T_s(z,t)}{\partial z}\right|_{z=s(t)} - \lambda_l \left.\frac{\partial T_l(z,t)}{\partial z}\right|_{z=s(t)} = h_f \rho_s \frac{ds(t)}{dt}, \tag{6e}$$

$$T_l(z,0) = T_p, \quad s(0) \le z \le L, \tag{6f}$$

$$s(0) = 0. \tag{6g}$$

In addition to the previously defined variables and constants, T_p is the initial temperature of the liquid, T_e is the constant temperature of the environment, and α is the heat transfer coefficient between the sample liquid and the surrounding air. The value of α is approximated as $\alpha = 10$ W m^{-2} K^{-1} for a water/air interface with a temperature difference of 1 to 10 K in still air.[73] While in ideal systems the freezing temperature of a liquid is a constant, real systems might exhibit supercooling effects. Such effects might appear, if the local temperature required to drive sufficient ice crystal nucleation is below the liquids standard freezing temperature. As a consequence, $\vartheta_0(T_s(s(t),t))$ was introduced and represents the freezing temperature as a function of the current ice front temperature. Initially, the liquid near the cooling finger might be supercooled until the formation of thermodynamically stable ice crystal nuclei is enabled. At that point, a rapid growth of these nuclei and, thus, a macroscopically observable phase transition is initiated. Subsequently, the temperature at the ice front increases quickly due to the released heat of solidification until it reaches the liquids standard freezing temperature, T_0, which is sufficient to drive the further solidification. Apart from that, equations (6a) to (6g) take into account the heat conduction within the liquid phase and heat exchange with the surrounding environment. This mathematical formulation neglects the assumptions (2), (3), and (6) stated above and, therefore, describes a physically less idealized situation than treated analytically before.

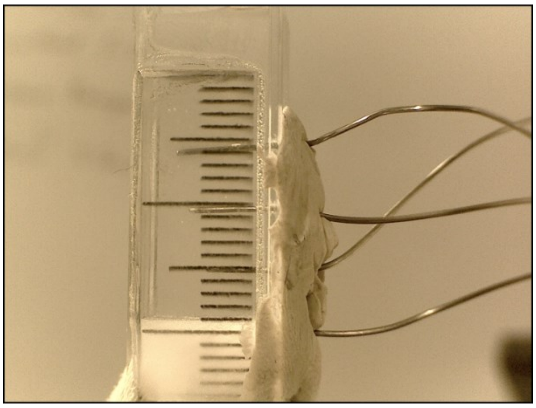

Figure 2.2. Photography of a directional solidification experiment. The sample mold with an attached millimeter scale and four temperature sensors (wires) contains partly frozen water with a defined ice front. The millimeter scale enables the time-resolved observation of the ice front movement, while the four temperature sensors reach into the sample liquid to monitor the temperature within the sample.

The directional solidification of pure water samples and a β-TCP suspension was empirically investigated in a cooling room ($T_e = 5$ °C) under experimental conditions reflecting the boundary value problem stated by equations (6a) to (6g). The analytically derived cooling function, equation (5), was applied to the bottom of the sample liquid with preset ice front velocities, v_f, of 10, 25, and 50 µm s^{-1}. The movement of the ice front over time was measured using an USB digital microscope and the spatial temperature evolution within the sample was monitored using four temperature probes inserted into the liquid at vertical distances of approximately 5 mm (**Figure 2.2**).

Figure 2.3 shows the temperature evolution in a pure water sample measured at five different positions as well as the observed ice front movement over time. The experimental results are directly compared with the theoretically expected values. For the preset velocities of 10 and 25 µm s^{-1}, the theoretical cooling function could be experimentally realized to a high degree of accuracy. However, it was technically difficult to achieve the same accuracy for the 50 µm s^{-1} particularly in the lower temperature range. The rather high deviation can be attributed to the high cooling rates of approximately 0.5 K s^{-1} required to drive a solidification at this high ice front velocity, which could not be realized reliably for the complete process with the utilized cooling procedure. As can be judged from **Figure 2.3 (d to f)**, the overall ice front movement was in good agreement with the theoretical expectation. For the sample with an approximate ice front velocity of 50 µm s^{-1}, the ice front movement was investigated only for the time range of 350 s where an acceptable agreement between theoretical and experimentally applied cooling function was evident. However, a significant deviation from the constant

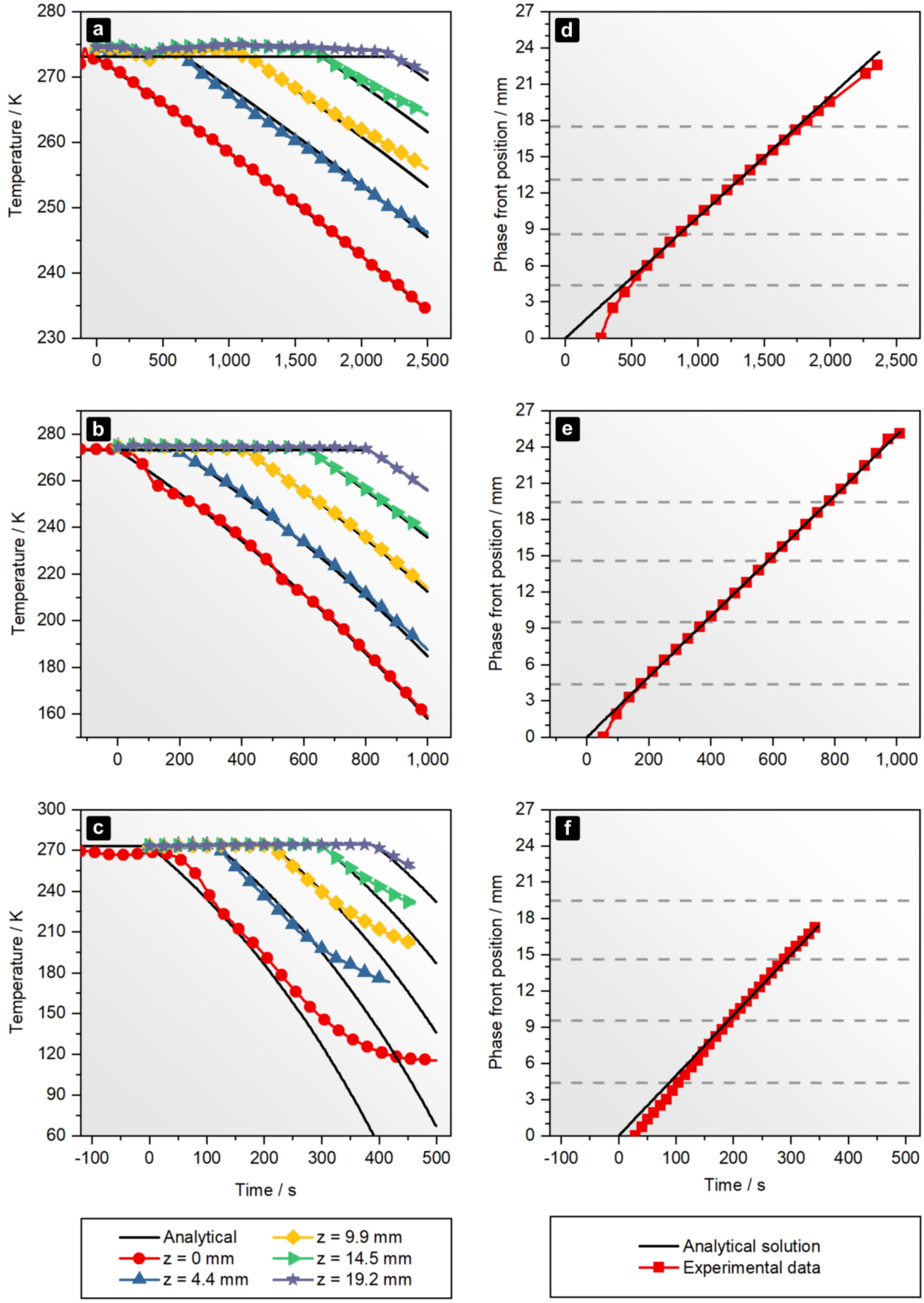

Figure 2.3. Temperature evolution at different positions (z-values) within the sample and at the cooling finger (z = 0 mm) for v_f = 10 µm s^{-1} (a), 25 µm s^{-1} (b) and 50 µm s^{-1} (c), as well as the ice front movement for the same velocities (d to f). Black lines represent the theoretically expected values. The dotted lines in the graphs on the right-hand side mark the positions of the temperature probes.

ice front velocity was observed at the beginning of the process in all cases. A delay of 50 to 250 s between the start of the cooling process and the formation of an ice front indicated the presence of a supercooling effect. This effect and other experimental deviations from the idealized assumptions made during the derivation of the analytical cooling function were investigated with numerical simulations. It was anticipated that the observed deviations are mainly caused by a combination of the following experimental circumstances:

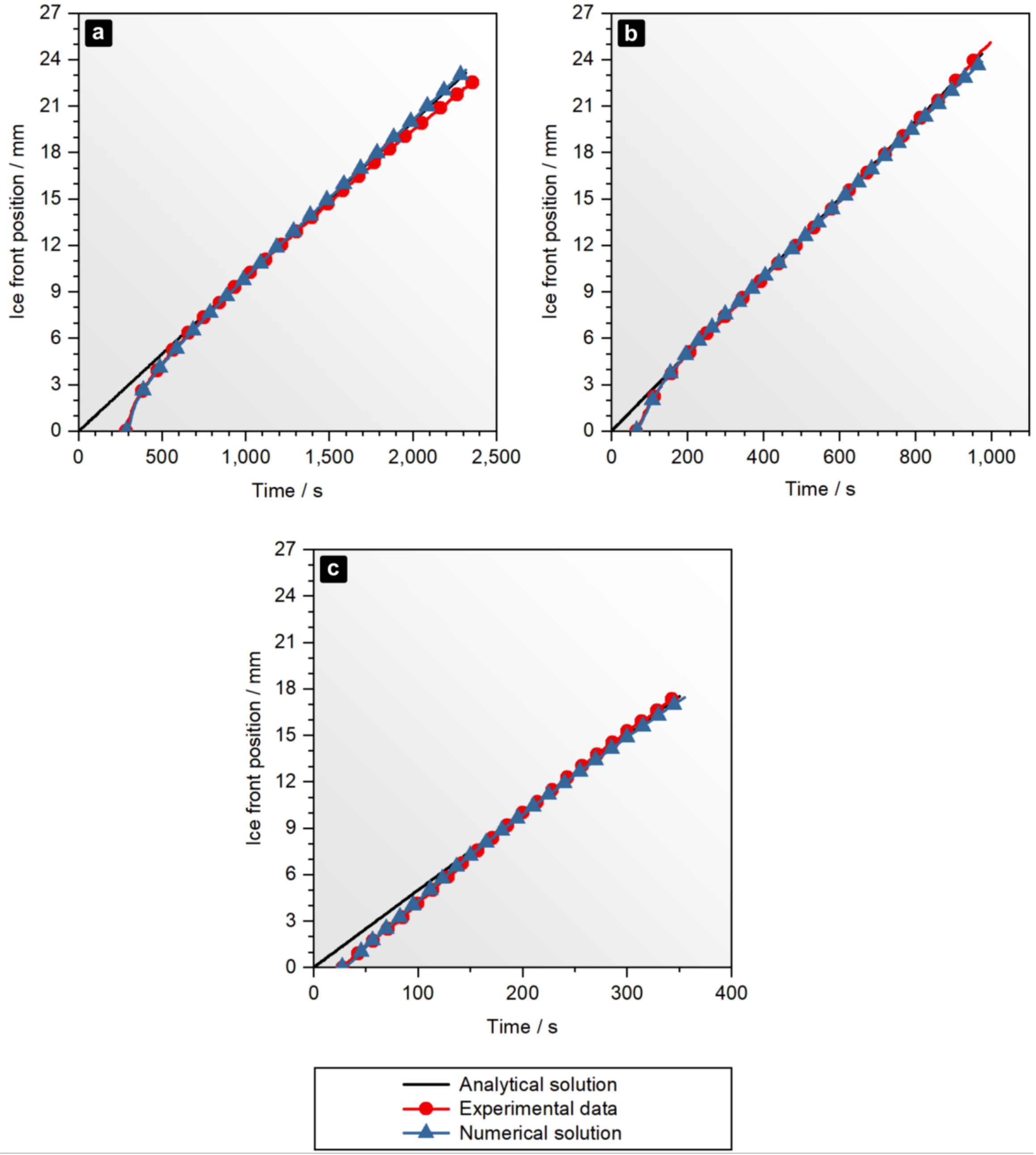

Figure 2.4. Comparison of the analytically and numerically calculated ice front movement with the experimentally measured positions for ice front velocities of (a) 10 µm s^{-1}, (b) 25 µm s^{-1}, and (c) 50 µm s^{-1}.

(i) A missing thermal insulation from the environment, (ii) the liquid was initially not at its freezing temperature, and (iii) supercooling effects occurred at the beginning of the process. Using the aforementioned inverse Stefan problem, equations (6a) to (6g), the effect of conditions (i) to (iii) on the theoretical ice front evolution were studied. The problem was solved numerically using the experimentally realized cooling functions $f(t)$ for each velocity as model input. **Figure 2.4** illustrates the numerically predicted ice front movement in comparison with the experimental data and the analytical solution for each of the three ice front velocities. The obtained numerical results exhibited an excellent agreement with the experiment in all cases. In particular, the accelerated ice front movement at the beginning of the solidification process could be successfully predicted by modelling a supercooling of up to 7 K below the liquid's freezing temperature. Physically, the supercooling most-likely occurs because no thermodynamically stable ice crystal nucleation takes place until a specific temperature is reached. At this temperature, growing crystallization nuclei are generated leading to a fast solidification of the supercooled liquid layer. This hypothesis is supported by the common observation of smaller structure sizes in the initial layer of ice-templated samples.[61, 69, 74, 75] In particular, Lasalle *et al.* already performed experimental investigations on supercooling effects in the context of ice-templating and suggested it to be the main cause for the structure formation within the initial layer. However, these authors reported supercooling of up to 22 K in distilled water,[74] whereas our model exhibited an excellent correspondence to the experimentally measured ice front movement, if supercooling temperatures of up to 7 K below the freezing point were assumed. Parameter variations in the simulations indicate that for the 10 μm s^{-1} samples the tendency of the decreasing ice front velocity at the end of the process might originate from heat transfer from the environment, which is underestimated by the presented model. It has to be taken into account that heat exchange with the environment naturally occurs across all system boundaries of the sample vessel. However, in the presented one-dimensional model only the upper liquid-air-interface could be considered. While this heat-transfer can be suppressed by an appropriate thermal insulation of the sample vessel,[70, 71] the supercooling effects are difficult to prevent. Nevertheless, the results reported by Lasalle *et al.* suggest that the supercooling can be influenced by the addition of dispersants to the sample liquid.[74] Regarding suspension-based sample liquids, the modification of particle sizes can have an impact on the degree of supercooling as well.[75]

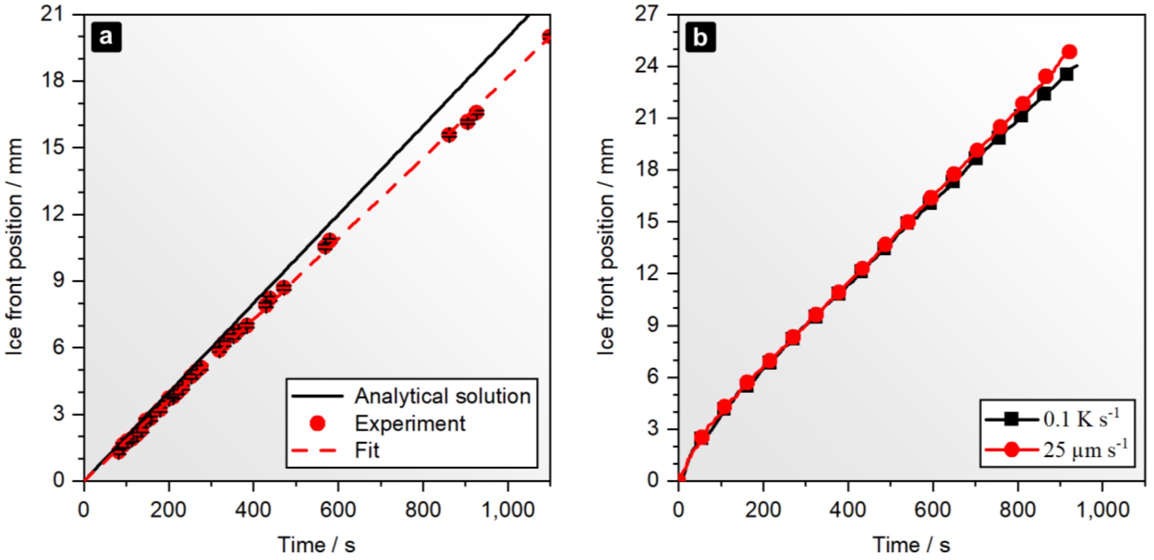

Figure 2.5. (a) Ice front evolution of a β-TCP suspension subjected to a directional solidification with a theoretical ice front velocity of $v_f = 20$ µm s^{-1}. The experiment is compared to the analytical solution and a linear regression was performed, revealing a slope of 18.2 ± 0.1 µm s^{-1}; (b) Comparison of the ice front evolution over time between one water sample frozen using a linear cooling function (0.1 K s^{-1}) and the other frozen using the exponential cooling function ($v_f = 25$ µm s^{-1}).

It was recently shown that the application of the discussed exponential cooling function in ice-templating processes with β-TCP suspensions produces homogeneous pore structures over the complete height of the obtained porous samples.[71] While this represents an indirect proof for an ice front movement with constant velocity, the ice front velocity during such a process was not measured directly so far. As a consequence, the described experimental procedure was applied to a β-TCP suspension and an ice front velocity of 20 µm s^{-1} was desired. In order to calculate the suitable exponential cooling function, the required material parameters have been calculated from the parameters known for pure tricalcium phosphate and pure ice at 273 K.[70, 71] The measured ice front movement is displayed in **Figure 2.5a**. A linear regression was performed on the experimental data, which revealed a constant ice front velocity of 18.2 ± 0.1 µm s^{-1}. If one neglects the data points recorded at the end of the solidification process, for which a slight deviation from the linear behavior is evident most-likely due to the heat exchange with the environment, an ice front velocity of 18.9 ± 0.1 µm s^{-1} is obtained. Both values deviate by not more than 9% from the theoretically predicted velocity of 20 µm s^{-1}. This small amount of deviation can be attributed to unknown errors in the chosen material constants, the previously discussed non-idealities of the experimental setup, and the fact that the model does not take into account any interactions between the suspended particles or with the ice front during the phase formation. While the results are encouraging, the discussed physics also defines clear limits for the applicability of this process in the context of ice templating. As has been derived during the aforementioned master thesis,[57] the maximum sample height, L_{max}, that can be realized with a constant ice front velocity can be estimated from the lower temperature limit of the setup, f_{min}, and the thermal properties of the sample:

$$L_{max} = \frac{k_s}{v_f} \ln\left(1 - \frac{c_s}{h_f}[f_{min} - \mathrm{T}_0]\right). \tag{7}$$

The temperature of the experimental setup used in the presented experiments was limited by the temperature of the liquid nitrogen reservoir used for cooling and, thus, has a minimum value of $f_{min} = 77$ K. Consequently, the maximum sample height of a β-TCP suspension for a constant ice front velocity of $v_f = 20$ µm s^{-1} is 45.6 mm. The maximum height for a pure water sample is 94.1 mm at $v_f = 10$ µm s^{-1} and 18.8 mm at $v_f = 50$ µm s^{-1}. As has been indicated by experimental observations for the 50 µm s^{-1} sample in this study, the upper limit for the ice front velocity is, however, also related to the maximum cooling rate that can be provided by the experimental setup.

In a last experiment, it was demonstrated that the quasi-stationary cooling function reported by Waschkies *et al.*[62] provides only limited control over the ice front velocity. **Figure 2.5b** illustrates the experimentally measured ice front movement in two water samples. The first was solidified using the exponential cooling function with $v_f = 25$ µm s^{-1}, whereas the second represents the data for a sample to which a linear cooling rate of 0.1 K s^{-1} was applied. The latter corresponds to an ice front velocity of $v_f \approx 27$ µm s^{-1} according to the quasi-stationary cooling function. The resulting ice front positions monitored over time increasingly deviate from each other after the initial phase of supercooling. The ice front velocity of the sample frozen with the quasi-stationary function continuously decreases and falls below the velocity of the first sample. That is because the quasi-stationary solution neglects the increasing cooling rates required to keep up the constant heat flux at the ice front through the continuously growing solid phase. This corresponds to the fact that the quasi-stationary solution is obtained from the exponential cooling function as a linear approximation under the assumption of high phase transitions numbers.[57, 76] However, the experiment also reveals that the quasi-stationary solution is a good approximation for applications where only small sample heights are required and slight deviations from the constant velocity are acceptable.

2.2 Investigation of ice-templated porous electrodes for application in organic batteries

Porous electrodes with pores in the nano- to macroscopic range have already proven to be beneficial for organic batteries.[42-52] In particular, porosity can have a significantly positive influence on the electrochemical rate performance, which can be attributed mainly to the large surface area of the electrolyte-electrode interface. This enables a large interaction surface and, thus, short distances for the required counter ion movement as well as high exchange currents. However, the reported methods to fabricate porous electrodes applied so far lead to random and undefined pore structures. As detailed before, ice-templating is a method that offers a considerable control over the pore structure of porous samples. At the beginning of this PhD thesis, only a few studies have dealt with utilizing this technique for carbon-based composite electrodes of supercapacitors and metal-based batteries.[77-79] Some preliminary investigations on the fabrication of porous electrodes for organic batteries with an ice-templating approach, the development of techniques for their morphological characterization, and first electrochemical measurements have been carried out in the previous master thesis by the author of this PhD thesis.[57]

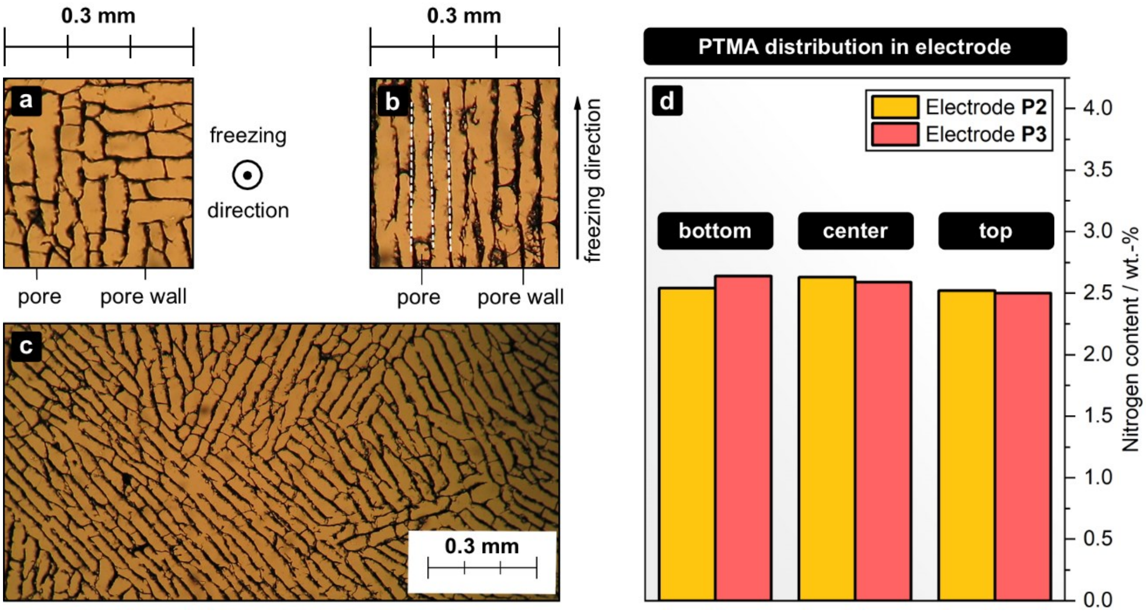

Figure 2.6. Photomicrographs of (a, c) cross-sections and (b) a longitudinal section of ice-templated porous electrode **P5**, respectively; (d) distribution of nitrogen obtained from elemental analysis of three pieces of the porous electrodes **P2** and **P3**, respectively, which demonstrate the homogeneous distribution of PTMA over the sample height.

This master thesis delivered ice-templated porous electrodes with a typical lamellar pore morphology (**Figure 2.6**). However, electrochemical cells utilizing these electrodes exhibited severe capacity decay. Consequently, a goal of this PhD thesis was the further electrochemical investigation of such porous electrodes and the optimization of their performance in organic batteries. Poly(2,2,6,6-tetramethylpiperidinyloxy-4-yl methacrylate) (PTMA) was chosen as the redox-active material for the preparation of the ice-templated porous electrodes due to its known stability, fast electron transfer kinetics, and former successful application in ORBs.[26] PTMA was prepared as described previously in literature,[40] except that a free radical polymerization was applied with the addition of 4 mol-% triethyleneglycol dimethacrylate as a crosslinker to further decrease the solubility of the polymer within the organic battery electrolyte. A subsequent oxidation yielded a degree of functionalization with nitroxide radicals of approximately 86 ± 3% as determined by EPR spectroscopy. Subsequently, the obtained polymer was ground with a planet ball mill using ZrO_2 balls (2 mm diameter) in a ZrO_2 cup. Slurries composed of vapor-grown carbon fibers (VGCF), carbon nano-particles (50 nm, CNP50), a binder component, the PTMA powder, and pure water were subsequently used to produce several ice-templated porous electrodes (**Table 2.1**) with a homogenous distribution of the redox-active material (**Figure 2.6d**). Constant cooling rates between 0.05 K s^{-1} and 0.4 K s^{-1} were used to drive the directional solidification. Only a negligible increase of the pore diameter over the sample height of ~2 cm was evident from the aforementioned experimental study,[57] which was attributed to the rather small height of the resulting samples. As a consequence, the application of the exponential cooling function discussed in **Chapter 2.1** was not necessary. Two types of binder components were investigated: Poly(3,4-ethylenedioxythiophene) polystyrene sulfonate (PEDOT:PSS) and carboxymethyl cellulose (CMC). Despite the promising electrical conductivity of PEDOT:PSS, porous electrodes produced with this binder were mechanically highly fragile and, hence, difficult to handle. In contrast to that, CMC turned out to provide a considerably higher mechanical stability without significant changes in the electrochemical behavior. Consequently, all electrodes used for the subsequent battery characterization exclusively contained CMC as binder material. Approximately ~1 mm thick slices of the ice-templated porous electrodes were extracted from the porous electrodes with a razor blade and carefully attached to graphite foil as conductive substrate with an adhesive graphite ink.

Table 2.1. Composition of the suspension/slurry used for the preparation of planar and porous electrodes as well as the mass of the final (dry) electrodes.

ID[(a)]	PTMA[(b)] wt.-%	VGCF[(b)] wt.-%	CNP50[(b)] wt.-%	Binder[(b)] wt.-%	H2O[(b)] wt.-%	Electrode mass mg
F1	59.2 ± 0.8	15.4 ± 0.3	20.6 ± 0.4	4.8 ± 0.1[(c)]	1,278	3.63 ± 0.02
F2	44.4 ± 0.6	22.3 ± 0.4	29.5 ± 0.5	3.8 ± 0.1[(c)]	1,278	2.50 ± 0.02
P1[(e, f)]	42.3 ± 0.2	19.8 ± 0.1	29.4 ± 0.1	8.4 ± 0.4[(d)]	2,956	-
P2[(f)]	42.7 ± 0.2	20.3± 0.1	28.2 ± 0.1	8.8 ± 0.4[(d)]	2,818	-
P3[(f)]	44.5 ± 0.1	22.3 ± 0.1	29.4 ± 0.1	3.8 ± 0.1[(c)]	2,915	-
P4[(f)]	44.6 ± 0.1	22.2 ± 0.1	29.3 ± 0.1	3.8 ± 0.1[(c)]	2,918	-
P5[(f)]	42 ± 2	21 ± 1	28 ± 1	9 ± 1[(d)]	2,795	-
P6[(f)]	45 ± 2	19 ± 1	27 ± 1	9 ± 1[(d)]	3,000	-
P7[(f)]	59.7 ± 0.2	15.1 ± 0.1	20.5 ± 0.1	4.8 ± 0.1[(c)]	2,886	6.8 ± 0.1

(a) **F** for flat/planar electrodes and **P** for porous electrodes; numbered consecutively.
(b) Weight-percent with respect to the total mass of all solids.
(c) Binder: CMC.
(d) Binder: PEDOT:PSS.
(e) Prepared with mortar ground PTMA.
(f) 2 mL suspension used.

Furthermore, conventional thin-film electrodes of equal composition were produced by doctor-blading of the slurry on a graphite foil and used as benchmark electrodes for the performance evaluation of the porous electrodes (**Table 2.1**).

For assessment of the battery performance, the electrodes were immersed in a 0.1 M $Zn(ClO_4)_2 \times 6\ H_2O$ ethylene carbonate (EC)/dimethyl carbonate (DMC) (3:7) electrolyte and cycled *versus* a zinc metal counter electrode in a beaker glass (**Figure 2.7**). Both electrode types exhibited a stable galvanostatic cycling behavior at 1 C and yielded a specific capacity of 104 ± 6 mAh g^{-1} (porous) and 111 ± 6 mAh g^{-1} (planar) as calculated from the measured total capacity and the known mass fraction of electrochemically active PTMA. For the porous electrodes, this represents a capacity utilization of 94 ± 5% of the theoretically expected specific capacity of 110.7 mAh g^{-1}. Furthermore, no significant capacity loss was observed over 25 cycles and the coulombic efficiency was higher than 95%. Hence, the porous electrodes obtained by the ice-templating approach delivered a stable performance with nearly full capacity utilization in a zinc-based electrolyte. The C-rate performance 1C, 5C, 10C, as well as 25C was also evaluated for both electrode types and the results are displayed in **Figure 2.7**. While both electrodes performed equally at 1C, a significant difference could be observed at higher C-rates. The planar electrode exhibited a recognizable specific discharge capacity even at rates of up to 25C, whereas nearly zero capacity retention was observed for the porous electrode at 10C and above. For a rate of 5C approximately 78 ± 4% (porous) and 92 ± 5% (planar) of the theoretical capacity were obtained, respectively. Hence, the planar electrode revealed a remarkably higher C-rate capability than the porous electrode. The cause for the significantly different performance was investigated by analysis of the DC resistances of both electrodes. The latter was estimated from the applied current and the overpotentials, which were obtained from the peak split of the charging and discharging peaks within the

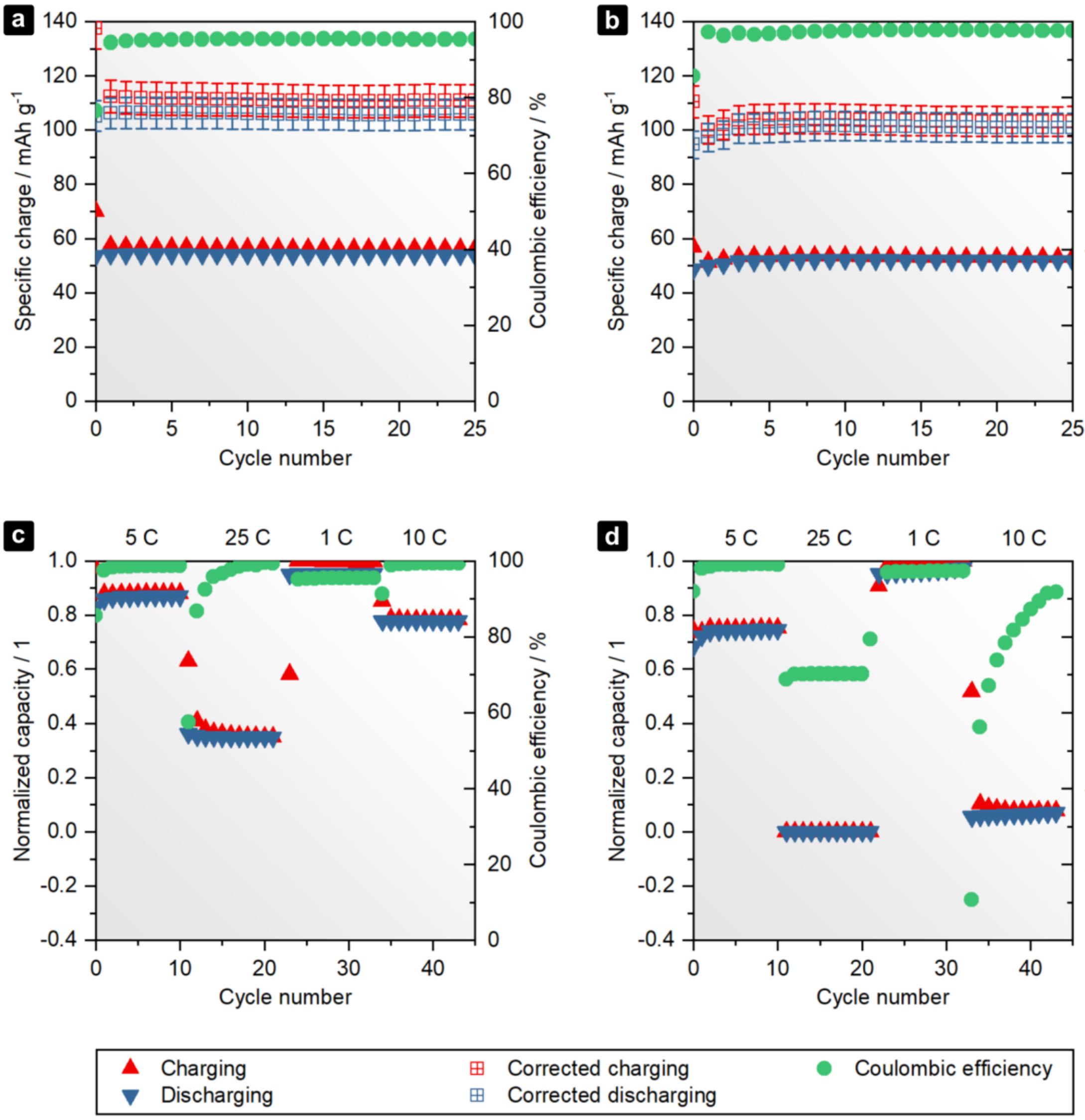

Figure 2.7. Cycling experiments at 1C for (a) the planar electrode **F1** and (b) the porous electrode **P7** in 0.1 M $Zn(ClO_4)_2 \times 6\ H_2O$ EC/DMC (3:7) with a zinc counter electrode in a beaker-type cell setup; (c, d) C-rate tests for the same electrodes at rates between 1C and 25C (capacities were normalized to 1C charge capacity (59 mAh g^{-1}) for better comparability).

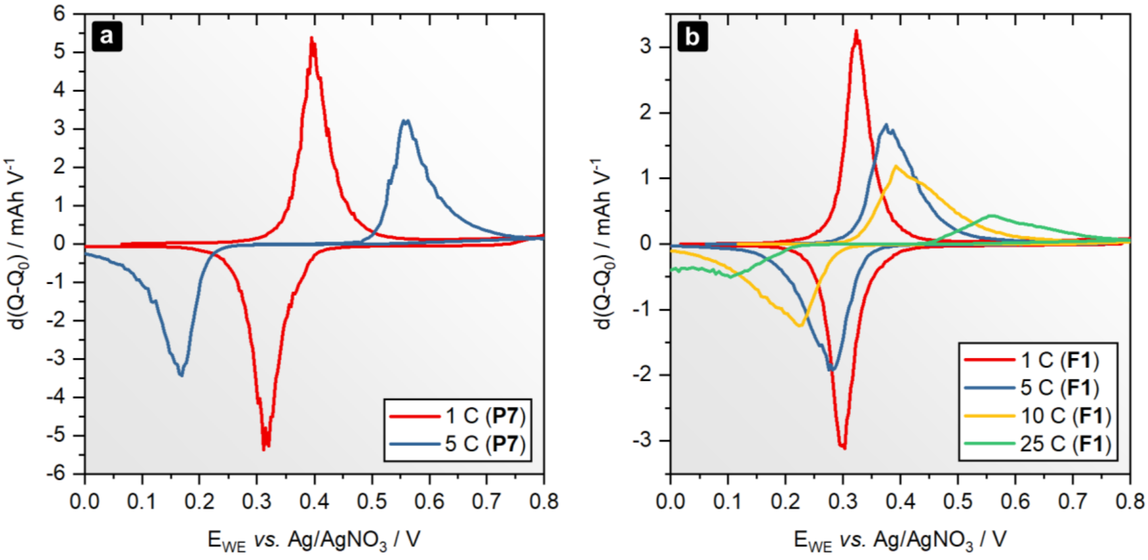

Figure 2.8. Derivatives of the capacity-potential curves recorded at different C-rates for (a) porous electrode **P7** and (b) planar electrode **F1** in 0.1 M $Zn(ClO_4)_2 \times 6\ H_2O$ EC/DMC (3:7) with a zinc counter electrode in a beaker-type cell setup.

derivatives of the capacity-potential curves (**Figure 2.8**). The mean resistance obtained for the porous electrode was 86 ± 7 Ω. In contrast to that, the planar electrode yielded an approximately two-fold lower resistance with a value of 39 ± 3 Ω. Consequently, the lower C-rate performance can be partially ascribed to the higher internal resistance of the porous system, which most-likely originates from a lower electronic conductivity within the porous scaffold and the low interfacial conductivity between the current collector and the electrode in comparison to thin film planar electrodes. Furthermore, it needs to be emphasized that a significant difference in the thicknesses of nearly two orders of magnitude existed between the porous electrodes (~1 mm) and the planar electrodes (~40 µm). This difference could not be mitigated in this study due to limitations in the film formation of thicker planar electrodes on the one hand and methodological restrictions in cutting thinner slices from the porous electrodes on the other hand.

3 Investigation of tubular cell designs for redox flow batteries

Parts of this chapter have been published in: **P3)** C. Stolze, C. Schmerbauch, C. Friebe, U. S. Schubert, *Energy Technol.* **2017**, *5*, 225–227. **P4)** C. Stolze, T. Janoschka, J. Winsberg, M. Strumpf, M. D. Hager, U. S. Schubert, *Energy Technol.* **2018**, *6*, 2296–2310.

As outlined so far, organic batteries represent promising candidates for a sustainable energy supply in mobile devices, smart packaging, wearables, and printed electronics. Unfortunately, their scalability is rather limited and, thus, they are not applicable for large-scale energy storage. However, the electrochemical principle of organic batteries has been successfully transferred to water- as well as organo-soluble polymers and small molecules for applications in redox flow batteries, recently.[30, 31, 80] This continuously evolving large-scale energy storage technology stands out from other battery types due to its decoupled capacity and power scalability. That is, its capacity is solely determined by the physico-chemical properties of the redox-active molecules, whereas its power density is strongly related to the design and number of the applied electrochemical reactors (*i.e.*, the flow cells).[34, 81, 82] Some remarkable progress has been achieved with regard to the energy density and the stability of inorganic and organic RFB chemistries, in particular due to the increased research interest in the past two decades.[35] However, the basic setup of a flow cell has not changed significantly since its invention by W. Kangro in the late 1940s.[32] They are usually constructed in the filter-press design, which basically consists of two cubic half-cells that are pressed on a separating membrane (**Figure 3.1a**).

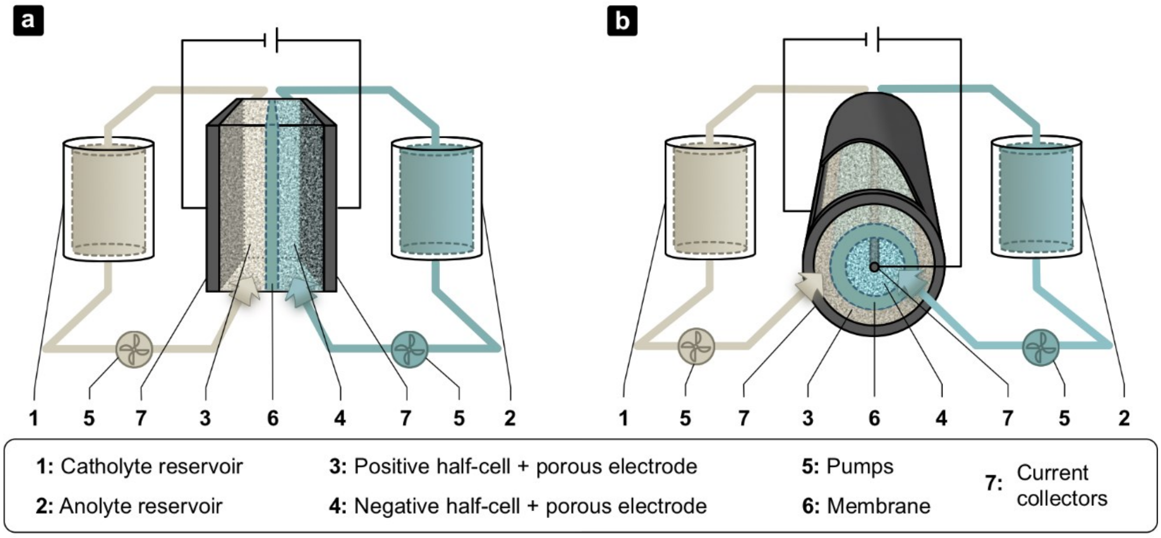

Figure 3.1. Schematic representation of (a) a conventional filter-press flow battery and (b) a tubular flow battery with the corresponding electrolyte tanks, pumps, and external circuits. The tubular cell is illustrated with a cut in the outer current collector only in order to allow insight into the inside of the cell.

In contrast to conventional batteries with solid electrodes, the membrane not only works as an insulating separator that prevents contact between the electron-conducting parts of the electrode. It also needs to prevent the passage of the dissolved redox-active molecules between the half-cells, while enabling the important exchange of the supporting electrolyte ions to ensure electroneutrality. The most significant advantage of the filter-press design is the ability to form cell stacks made up of identical flow cells, which are stacked on each other and, thus, are connected electrically in series and hydrodynamically in parallel. This represents a simple approach to increase the cell voltage and, thus, the absolute electrical power of a RFB. However, the power density of the RFB is basically defined by the power density of a single flow cell unit. While it is frequently argued that a high power density is not important for stationary energy storage where space is not a limiting factor, it is often overlooked that power density is also connected to material consumption and cost efficiency. That is, if a RFB with a defined power rating can be constructed with significantly smaller and lighter flow cells, this directly translates to, *e.g.*, lower material costs and reduced installation costs for the battery. Despite this simple fact, flow cell design improvements have been achieved mainly by comparatively small changes to the basic design concept over the decades. The last milestone was achieved with the introduction of flow fields known from the technologically similar fuel cells,[83] which resulted in a significant increase in the achievable power density and energy efficiency.[84-86] The material research efforts and the application of flow fields yielded a power density increase of more than one order of magnitude since the 1970s.[81] However, alternative design concepts which are fundamentally deviating from the conventional filter-press design are rarely found in literature. Although a high research effort is necessary to understand and to optimize the properties of such alternative cell designs, the few examples that were reported prior to the work performed in this PhD thesis[87-92] already demonstrated that a re-thinking of the conventional design choices can have a benefit for the performance or the costs of redox flow batteries. With regard to that, non-conventional flow cell designs represent an interesting and promising research topic that has not been sufficiently explored so far and deserves far more attention.

One of the main difficulties in flow cell design is the reliable sealing of the cell, which is required to prevent both electrolyte leakage and the permeation of oxygen into the cell over the desired life-time of the flow battery (*i.e.*, >20 years). The latter is important due to a variety of side-reactions that usually occur in the anolyte, if oxygen is present. While this can be easily achieved on laboratory scale, the increasing sealing area for increasing flow cell size renders this task more difficult for larger flow cells. With regard to this, in particular tubular flow cell designs (**Figure 3.1b**) can provide a significantly reduced sealing area. Additionally, they offer the applicability of membrane materials that are mechanical instable in large planar geometries – such as ceramics. The latter possess an unrivaled chemical inertness as well as superior thermal stability compared to other membrane materials and their utilization could help to enlarge the number of applicable solvents and molecules for the chemical design of RFB electrolytes. Tubular geometries also provide a better ratio between membrane area and cell volume, which exhibits an inverse relationship to the cell radius. Therefore, microtubular cell designs, which are characterized by tubular half-cell thicknesses below 1 mm, have already proven beneficial for the performance of fuel cells due to:[93-97]

- a significantly increased power density,
- a beneficial heat distribution,
- an enhanced cell design flexibility,
- an improved applicability to mobile applications, and
- a reduced capital cost.

Despite these theoretical advantages, only two tubular flow batteries were reported in literature prior to this work.[88, 90] One reason for the low number of publications in this field certainly is the lack of availability of tubular ion-exchange membranes. However, due to the invention of polymer-based aqueous RFBs by Janoschka *et al.* in 2015,[31] which enabled the utilization of size-exclusion membranes instead of the usual ion-exchange membranes, new opportunities arose.

Consequently, tubular and microtubular cell designs with size-exclusion membranes were investigated in this thesis concerning their viability, electrochemical properties, and battery performance in comparison to conventional filter-press flow cells (cFFC).

3.1 Redox flow cell with a macro-tubular ceramic membrane

A tubular flow cell for a polymer-based RFB consisting of concentric half-cells separated by a ceramic membrane (Fraunhofer IKTS, Germany) was constructed. The latter consists of an Al_2O_3 substrate with open porosity (30%, d_{50} = 3 µm), which was manufactured with a layer of porous ZrO_2 (d_{50} = 3 nm) on its exterior face functioning as a size-exclusion membrane with a molecular weight cut-off (MWCO) of 5 kDa. The current collector for the inner half-cell was a graphite rod (material-id: 2124, MERSEN Deutschland Suhl

GmbH, Germany) surrounded by a graphite felt (GFA6, SGL Carbon GmbH, Germany) as the porous electrode. The outer half-cell contained an identical graphite felt surrounding the ceramic membrane. A tube made from the same graphite material as the inner rod was utilized as current collector for the outer half-cell. Two copper wires were coiled around the end of the inner graphite rod and the outer graphite tube, respectively, to provide an electrical connection between the current collectors and the potentiostat. A polyvinyl chloride (PVC) tube was used as housing for the setup and caps were glued on both ends with silicon to seal the cell (**Figure 3.2a**). Important constructional parameters for the prototype are listed in **Table 3.1**.

Due to the tubular geometry, the sealing area for the flow cell design is independent from its length. This provides a simple route to upscaling by elongation of the cell parts, while maintaining a safe sealing even for larger flow cells. Furthermore, the application of a ceramic membrane is enabled due to the improved mechanical stability of this geometry when compared to rectangular membranes of the same geometric area. A 2,2,6,6-tetramethylpiperdine-1-oxyl (TEMPO) based polymer and a viologen-based polymer (**Figure 3.2b**) were utilized as redox-active species for the aqueous catholyte and anolyte, respectively. The active compounds were synthesized according to a previously published procedure.[98] Electrochemical impedance spectroscopy measurements and galvanostatic charging and discharging experiments were performed to characterize the performance of the tubular cell. The electrochemical impedance spectroscopy revealed an area resistance of 50 Ω cm^2 based on the membrane area and a volumetric resistance of 38 Ω cm^3 based on the cell volume without the current collectors (**Figure 3.3a**).

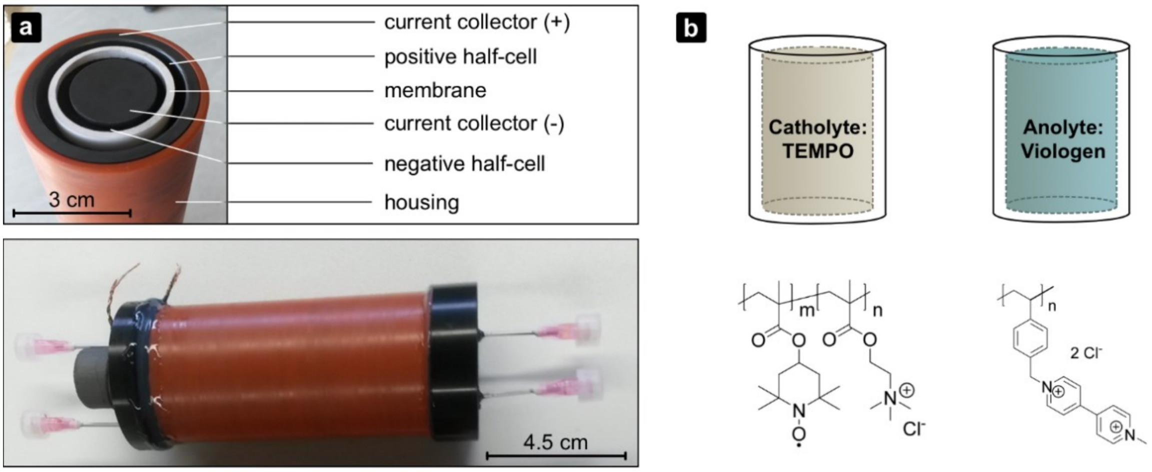

Figure 3.2. (a) Photographs of the laboratory prototype of a tubular redox flow battery with a ceramic membrane and (b) schematic representation of the chemical structure of the TEMPO-based polymer (catholyte) as well as the viologen-based polymer (anolyte).

Table 3.1. Cell dimensions and parameters for the tubular redox flow cell with a ceramic membrane.

Cell part	Inner diameter / mm	Outer diameter / mm	Thickness / mm	Length / mm
Graphite rod	–	22.5	22.5	130
Graphite tube	38.5	45	3.25	100
Graphite felt[a]	–	–	6	100
Ceramic membrane[b]	28.5	32.5	2	100

(a) Given thickness in uncompressed state.
(b) Substrate: Al_2O_3 (30% porosity); membrane: ZrO_2 (on exterior, d_{50} = 3 nm).

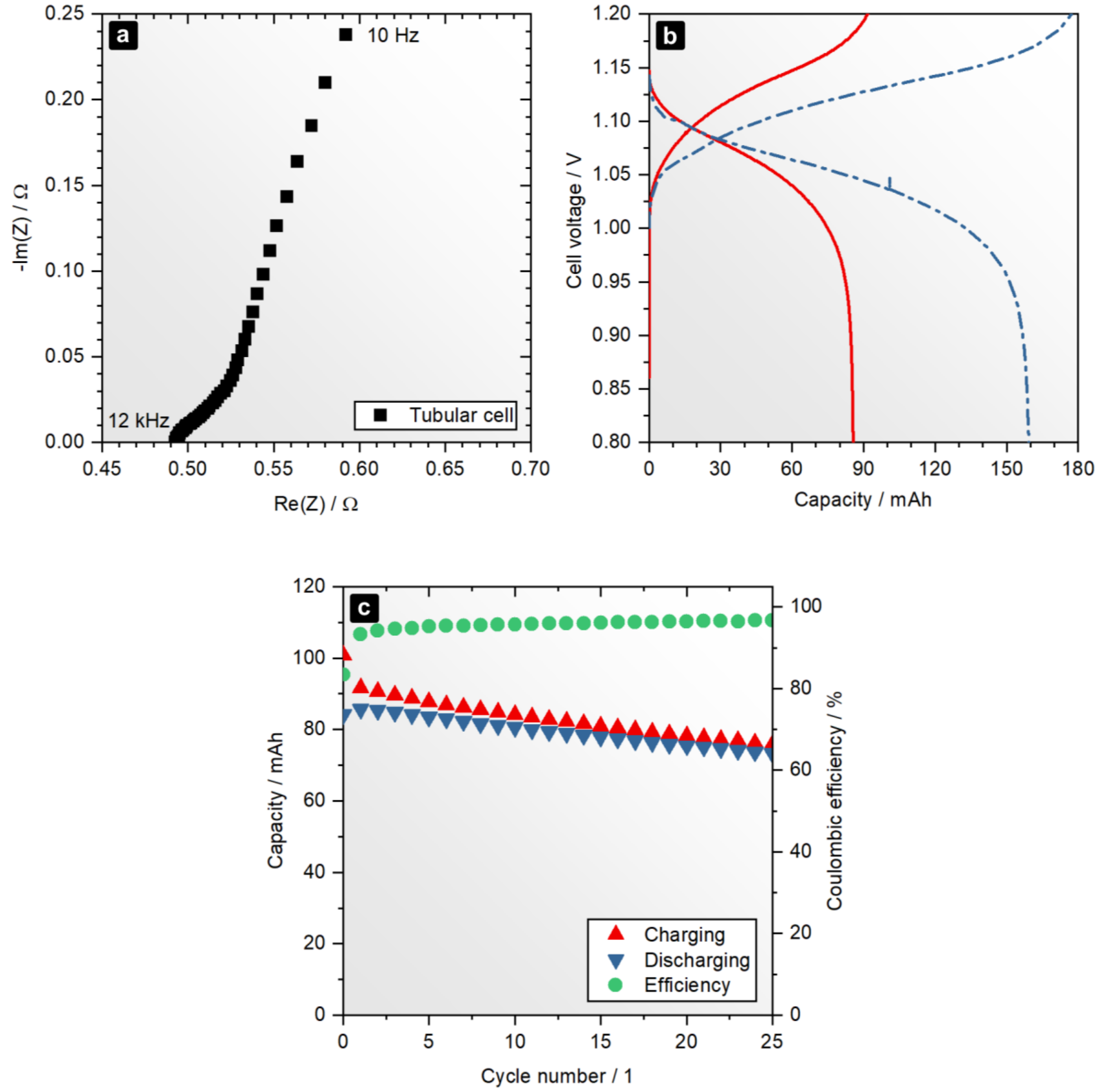

Figure 3.3. (a) Electrochemical impedance spectroscopy for the tubular cell; (b) potential-time curves for the 2nd cycle in both static (solid line) and pumped (dashed line) operation mode; (c) cycling behaviour during static operation mode for 25 consecutive galvanostatic cycles.

The rather high resistance is attributed to the thickness and the low porosity of the Al_2O_3 substrate of the ceramic membrane as well as the imperfect electrical contact between copper wire and graphite parts. In a second experiment, galvanostatic cycling at 100 mA was performed for two cycles in a pumped operation mode (**Figure 3.3b**) and over 25 consecutive cycles in a static mode (**Figure 3.3c**). A coulombic efficiency of above 90% was observed, which was significantly below the 96 to 99% reported for a conventional filter-press design with a cellulose-based dialysis membrane utilizing TEMPO- and viologen-based polymers.[31] While care was taken during the sealing of the housing, the utilization of silicone as sealing material clearly does not represent the most sophisticated assembly approach. Diffusion of oxygen into the cell and subsequent self-discharge of the anolyte can, therefore, not be excluded as cause for the low efficiency. However, although the battery performance clearly demands further optimization of the assembly procedure, the general viability of the first tubular redox flow battery with a ceramic size-exclusion membrane could be successfully demonstrated.

3.2 Microtubular flow cell design with commercial hollow-fiber membranes

The power density of the experimentally realized tubular flow battery presented in **Chapter 3.1** as well as a vanadium-based tubular flow battery published by Ressel *et al.* later[99] was significantly lower compared to that of conventional filter-press cells. While one approach to increase power densities is the perfection of manufacturing strategies and cell materials, another one is to decrease power losses by reduction of the cell diameter and half-cell thicknesses (= distance from current-collector to membrane). This approach aims at shorter charge carrier pathways and a further increase in the ratio between membrane area and cell volume. For conventional filter-press flow cells it was reported that the reduction of half-cell thicknesses from the upper to the lower millimeter or even micrometer range can lead to a significantly improved power density.[100-102] Consequently, a reduction of the half-cell thickness represents a logical step for tubular flow cells as well. The resulting tubular flow cells with half-cell thicknesses below 1 mm are termed microtubular flow cells (µTFC) throughout this PhD thesis.

While previously published tubular approaches currently prohibit further size reduction due to the utilization of ion-exchange membranes,[90, 99] the size-exclusion approach using polymer-based RFBs benefits from the commercial availability of microtubular dialysis membranes. Consequently, a hollow fiber dialysis membrane with an inner diameter of 1 mm and a MWCO of 3 kDa (modified polyether sulfone (mPES), Spectrum

Laboratories, Inc.) was utilized in this PhD thesis to construct a microtubular hybrid flow cell (**Figure 3.4**). The outer, positive half-cell was constructed for a poly(2,2,6,6-tetramethylpiperidin-4-yl methacrylate-*co*-poly(ethylene glycol)methyl ether methacrylate) (poly(TMA-*co*-PEGMA)) based electrolyte, while the inner, negative half-cell contained a zinc wire for utilization of the Zn/Zn^{2+} redox couple. The latter was chosen due to its oxygen insensitivity,[80] which simplified the manufacturing of the first prototype. While the work in this PhD thesis was focused on the investigation of cell performance, the synthesis and basic investigations on the utilized RFB chemistry was reported in earlier studies.[80] The performance of the µTFC was compared experimentally to the conventional filter-press design commonly utilized in our laboratory.[31, 80] A planar size-exclusion membrane (ZelluTrans dialysis membrane T1, regenerated cellulose, Carl Roth GmbH & Co. KG, Germany) having a MWCO of 3.5 kDa was used in this flow cell. Prior to the assembly of both cells, however, the properties of both membrane types were investigated. **Table 3.2** summarizes the measured electrolyte resistivities, membrane thicknesses, and membrane resistances as obtained in a dry state and a wet state, respectively. The wet state was prepared by storage in the corresponding electrolyte solution for at least 12 hours. The results indicate no interaction between the ions of the 1 M NH_4Cl and 1 M $ZnCl_2$ supporting electrolytes and the membrane materials. This was concluded from the identical ratios of the membrane area resistances obtained for the different membrane types in equal solutions (approximately 2.8 ± 0.1). This conclusion was additionally supported by the equality of the ratios between the free electrolyte resistivities and the ratios of the membrane resistances of the same membrane in the different solutions (approximately 1.2 ± 0.2).

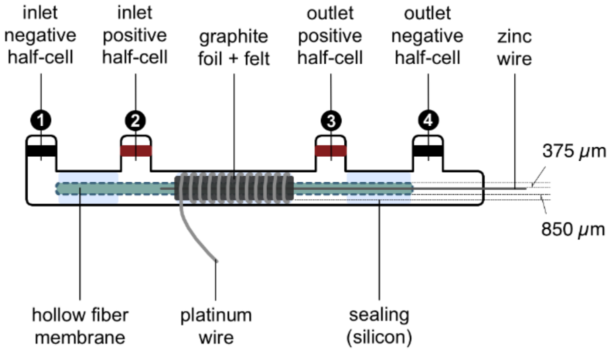

Figure 3.4. Schematic representation of the experimental setup of the µTFC prototype with one microtubular membrane, a positive (outer) half-cell with a thickness of 850 µm, and a negative (inner) half-cell with a thickness of 350 µm. The positive half-cell contains a graphite felt as porous electrode, while the negative half-cell contains a zinc wire only.

Table 3.2. Mean values and standard errors (95% confidence interval) obtained from measurements of electrolyte resistivity, membrane thicknesses, and membrane area resistances (with respect to the total membrane area) of conventional flat (regenerated cellulose, 3.5 kDa, ZelluTrans) and microtubular dialysis membranes (mPES, 3 kDa, SpectrumLabs) in aqueous electrolytes containing 1.00 ± 0.02 mol L^{-1} NH_4Cl and 1.00 ± 0.02 mol L^{-1} $ZnCl_2$.

Electrolyte	Electrolyte resistivity Ω cm	Membrane thickness µm		Membrane area resistance Ω cm^2	
	Free electrolyte solution	Flat	Microtubular	Flat	Microtubular
Dry	-	22.5 ± 0.6	140 ± 3	-	-
1 M NH_4Cl	9.22 ± 0.01	48 ± 2	154 ± 4	0.52 ± 0.03	0.19 ± 0.01
1 M $ZnCl_2$	11.49 ± 0.03	48 ± 2	154 ± 5	0.60 ± 0.07	0.21 ± 0.02

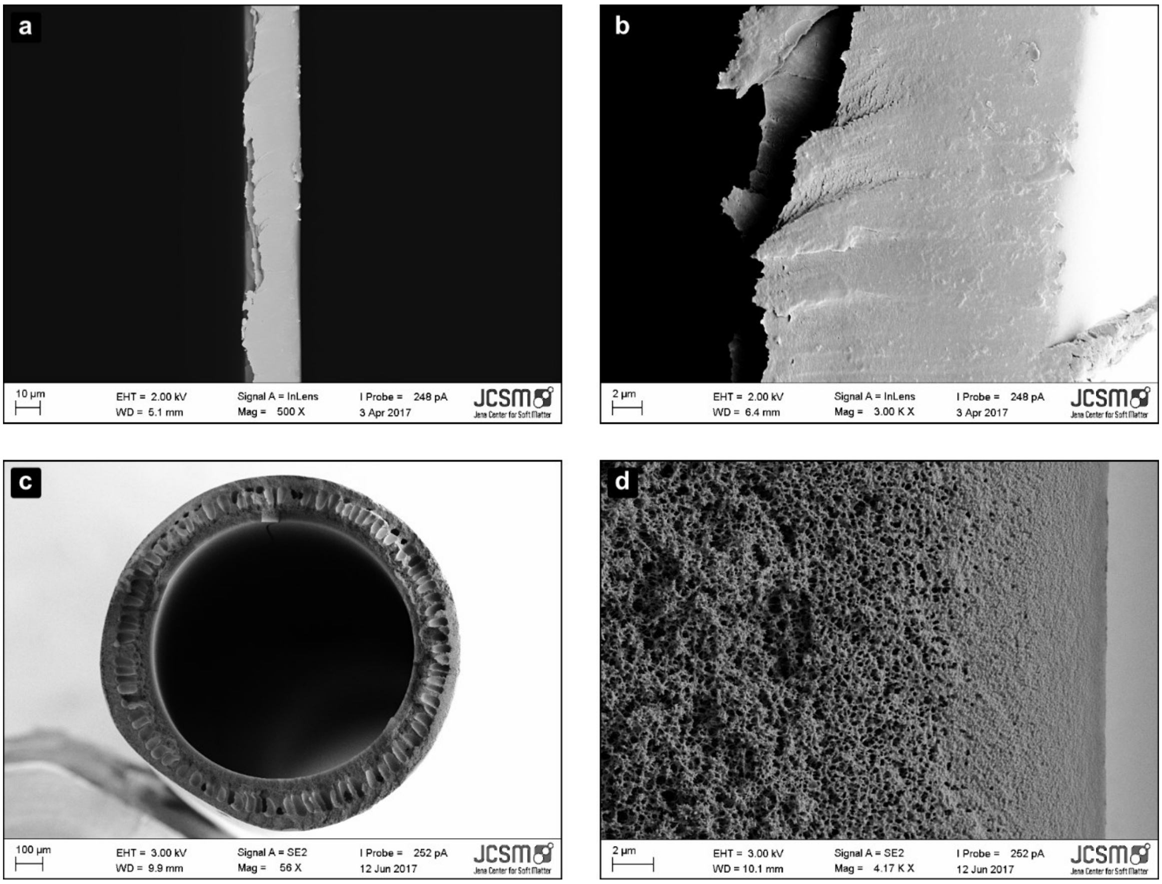

Figure 3.5. Scanning electron micrographs of the utilized (a, b) flat membrane type and (c, d) microtubular membrane type in different magnifications. The different manufacturing types are clearly visible with the flat membranes consisting completely of a very dense pore structure, while the microtubular membranes consist of a macro-porous supporting layer with a thin micro-porous separation layer on its inner side; (d) shows the dense separation layer of the microtubular membrane.

Any interaction mechanism between supporting electrolyte and membrane material would have caused different dwelling times for different ions as well as ion concentrations within the membrane and, as a consequence, different ratios would have been observed between the two membrane types. Thus, the permeation of supporting electrolyte ions through the membranes, which determines the membrane area resistance, is governed solely by the membranes' tortuosity and porosity. Despite the three-fold lower membrane thickness of the wet flat membrane, the microtubular membrane exhibited a significantly lower area resistance. Scanning electron microscopy of both membrane types revealed significant differences between the pore morphologies of the membranes, which are anticipated as the cause for this observation (**Figure 3.5**). The flat membrane exhibited a dense sub-micrometer pore structure throughout its whole thickness, while the microtubular membrane is made up mainly from a material layer with larger pores which seamlessly blends into a thin layer (< 5 µm) with sub-micrometer pores. The actual size-exclusion layer is, thus, by nearly one order of magnitude thinner in the microtubular membrane. Both the tubular geometry and the separation layer thickness result in a higher conductivity in this membrane type. This circumstance was also reflected by the electrochemical impedance spectroscopy measurements conducted for both flow cell types (**Figure 3.6**), where the cFFC yielded a volumetric resistance of 2.9 ± 0.5 Ω cm^3 and the µTFC gave a value of 0.3 ± 0.1 Ω cm^3. Hence, a difference of one order of magnitude was observed at similar compression rates (~25%) of the porous electrodes.

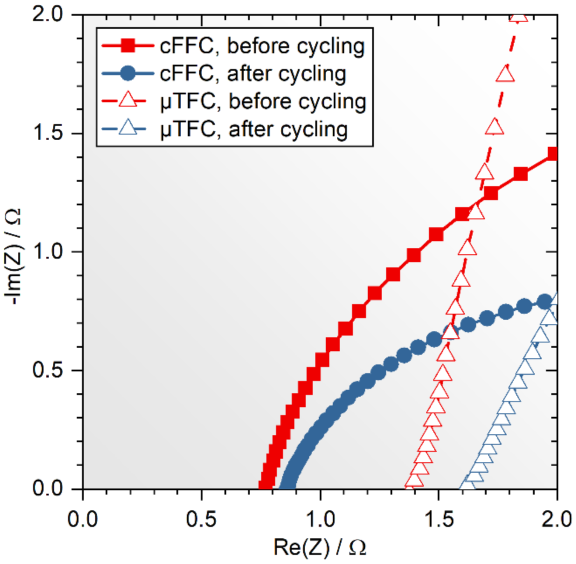

Figure 3.6. Electrochemical impedance spectra of the conventional filter-press flow cell and the microtubular flow cell prototype obtained at their initial state (directly after assembly) and after cycling experiments (60 cycles at 5 mA cm^{-3}). Only the high-frequency range is displayed.

Ressel *et al.* reported a value of 6.1 Ω cm^2 for their zero-gap vanadium-based (macro)tubular flow battery, which corresponds to a volumetric value of 0.7 Ω cm^3 and, hence, a more than two-fold higher volumetric resistance.[99] Compared to the benchmark setting quinone-bromine and all-vanadium cFFCs reported by Chen *et al.* and Zhou *et al.*,[102, 103] however, the volumetric resistance of the presented μTFC prototype is one order of magnitude higher. This is most-likely due to the optimized electrode materials and, in particular, the zero-gap cell architectures utilized for these studies. A zero-gap architecture could not be used within this first μTFC prototype due to the well-known dendrite formation of the utilized Zn/Zn^{2+} redox couple. A more reasonable comparison is, hence, obtained with regard to other zinc-based flow cells rather than zero-gap vanadium redox flow batteries. The lowest resistance reported for a conventional flat zinc-bromine RFB is approximately 0.6 Ω corresponding to a volumetric resistance of more than 0.8 Ω cm^3.[101, 104] Therefore, the μTFC presented in this PhD thesis yielded a more than two-fold lower value. Another verification of the improved cell resistance was revealed by the measurement of polarization curves (**Figure 3.7**).

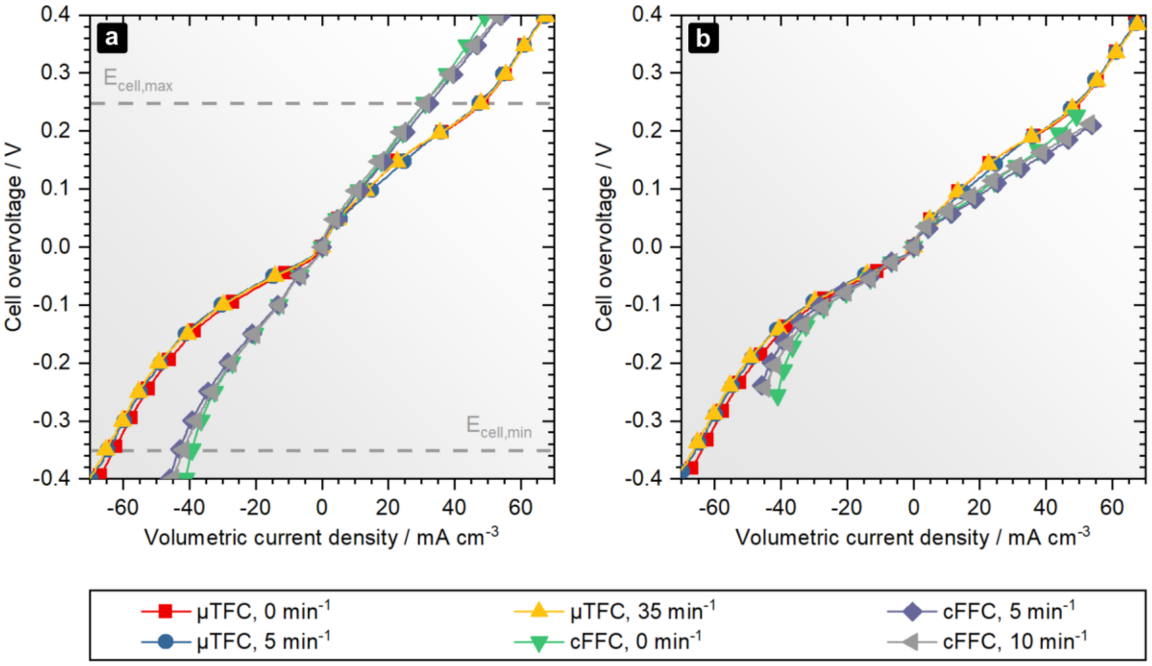

Figure 3.7. Polarization curves of a conventional filter-press flow cell and a microtubular flow cell as obtained in non-pumped and pumped operation mode for a state-of-charge of 50 ± 10% at a scan rate of 100 mV s^{-1}. Curves in (a) show the uncorrected form of the polarization curves where the dashed lines mark the upper and lower cell voltage limits used for galvanostatic charging and discharging, respectively. Curves in (b) show IR drop corrected data for which the ohmic overvoltages were removed according to the ohmic resistances measured by impedance spectroscopy (0.776 Ω (cFFC) and 1.370 Ω (μTFC)).

The cause of this difference was further analyzed by evaluation of the main contributions to the measured polarization overvoltage in the different current regimes, which are usually identified as activation (low current range), ohmic (medium current range), and concentration overvoltages (high current range).[100, 105] It is evident that activation overvoltages contribute equally to the cell polarization in both cell types. This is reasonable, since the same redox chemistries are utilized. The electrolyte convection through the half-cells only had a minor influence on the polarization behavior as well due to the missing porous electrode in the zinc half-cell, which consequently governed the mass-transfer polarization for both cells to a similar extend. After a correction of the IR drop using the resistance values obtained by electrochemical impedance spectroscopy presented before, the origin of the performance difference between both cells was clearly identified: Evaluated from the difference in limiting currents before and after correction, the ohmic resistance constitutes 40% of the polarization overvoltage in the conventional filter-press flow cell, while it only contributed 5% in the µTFC. In turn, it can be stated that the performance of the µTFC is strongly limited by activation and concentration overvoltages, which contribute 95% to the total cell overvoltage. These overvoltages can be attributed mainly to the limitations of the negative half-cell (missing porous electrode, sluggish kinetics of the Zn/Zn^{2+} couple, etc.) and, consequently, can be overcome by utilization of fully organic polymer-based µTFCs with porous electrodes in both half-cells. To realize such cells, however, a development of more sophisticated manufacturing procedures is required. Despite this issue, the low ohmic resistance of the µTFC would theoretically enable for limiting current densities as high as 1,000 mA cm^{-3} compared to a value of 100 mA cm^{-3} for the reference filter-press flow cell utilized in this study.

The impedance spectroscopy investigations and polarization curve investigations gave insight into the limits of cell performance in terms of applied voltages and volumetric current densities. Despite their obvious advantages, polarization curves cannot provide reliable information on the capacity retention at varying current densities or stability during continuous cycling, which are the most important practical parameters for battery applications. As a consequence, two more sets of experiments were performed to investigate these battery properties (**Figure 3.8**). For the current rating experiments, volumetric discharging current densities from 100 mA cm^{-3} to 1 mA cm^{-3} were applied in static flow cells. **Figure 3.8a** and **Figure 3.8b** display the same data normalized to the first cycle and the last cycle (both obtained at 1 mA cm^{-3}), respectively. Two major insights can be gained from the results of this experiment:

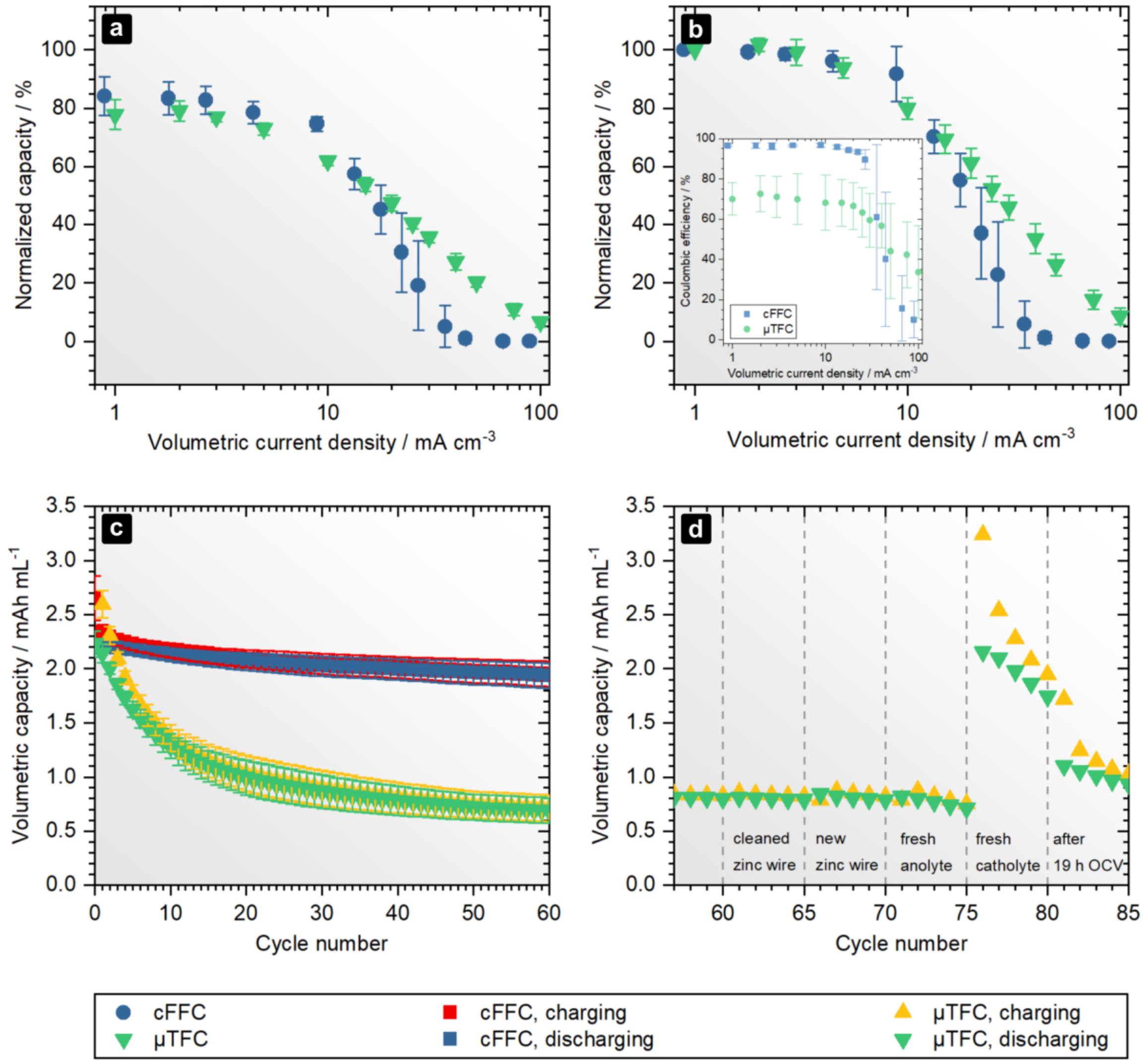

Figure 3.8. Capacity retention at different volumetric discharging current densities normalized to the capacity (obtained at 1 mA cm^{-3}) of (a) the first cycle and (b) the last cycle of the whole current rating experiment (charging currents were kept constant at 1 mA cm^{-3} during the experiment). Inset in (b) shows the coulombic efficiencies for both cell types. The results of subsequent charge-discharge cycles at a moderate charging/discharging current density of 5 mA cm^{-3} is provided in (c) in terms of volumetric capacities (normalized to positive half-cell volume of 2.5 mL (cFFC) and 114.5 µL (µTFC), respectively). The impact of subsequent cell part exchanges within the µTFC on the capacity retention are shown in (d).

First, the µTFC exhibited a superior capacity retention compared to the cFFC at current densities above 40 mA cm^{-3} (two-sided Welch's t-test, significance level: $< 5\%$). The µTFC enabled to extract roughly one fourth of its total capacity at 45 mA cm^{-3}, while the conventional filter-press flow cell delivered nearly zero capacity at the same current density. Second, a significant capacity decay during the experiments can be deduced from the differences between the two normalizations. This capacity fade is attributed to the utilized redox chemistry and the degradation of the electrolyte, respectively, which is known from a previous study.[80] Furthermore, a lower coulombic efficiency was observed for the µTFC (inset, **Figure 3.8b**). Although this has the undesirable effect of lowering the energy efficiency and stability of the system, it has to be pointed out that it does not dispute the conclusions drawn for the µTFCs decreased resistance and increased power density. The lack of efficiency could, in general, originate from a side reaction or from polymer cross-over through the membrane. However, any side reactions would occur equally in both types of flow cells and, consequently, a polymer cross-over or some kind of leakage between the half-cells inside the µTFC seems to be the more likely reason. This hypothesis was supported by the results of subsequent galvanostatic cycling experiments (**Figure 3.8c**). The conventional filter-press design exhibited a capacity retention of 73 ± 7% of the initial discharge capacity after 60 consecutive cycles at a moderate volumetric current density of 5 mA cm^{-3}. Under the same conditions, the µTFC yielded a value of only 19 ± 4%. Further insights into the causes of this different behavior were gathered by a step-by-step exchange of some cell parts of the µTFC after these 60 cycles. **Figure 3.8d** displays the impact of each exchange step on the capacity retention of the µTFC. Neither the cleaning or replacement of the zinc wire nor the exchange of the anolyte had a significant impact on the capacity retention. However, the replacement of the catholyte with fresh electrolyte led to a 100% recovery of the capacity. Subsequent cycling exhibited a nearly identical behavior to the initial cycling experiment. After five cycles, the µTFC was put to open-circuit at approximately 100% SOC. After 19 hours in this state, the galvanostatic cycling was continued and a severe capacity loss was observed. With regard to the previously discussed lower coulombic efficiency of the µTFC and the capacity loss observed after the plain resting period of 19 h, it can be concluded that polymer cross-over through the microtubular membrane or the sealing is the origin of the µTFC's inferior coulombic efficiency and cycle stability. Cross-over could be facilitated by the higher ion permeability and the higher membrane area per volume inherent to the microtubular membrane in comparison to the conventional membrane of the filter-press flow cell. Indubitably, this issue can be overcome in the future by a thorough design of the polymer electrolyte and optimization of the sealing approach. In particular, the polymer cross-over through the microtubular membrane can be mitigated by tuning of the molar mass of the utilized polymers or the utilization of membranes with a smaller MWCO. Despite that, the presented experiments represent a first proof-of-principle that microtubular flow cells are – in general – experimentally accessible with commercially available microtubular dialysis membranes.

4 State-of-charge monitoring for redox flow batteries

Parts of this chapter have been published in: **P5)** C. Stolze, M. D. Hager, U. S. Schubert, *J. Power Sources* **2019**, *423*, 60–67. **P6)** C. Stolze, J. P. Meurer, M. D. Hager, U. S. Schubert, *Chem. Mater.* **2019***, 31,* 5363–5369.

The variation of the electrode morphology and the re-design of the electrochemical cell discussed so far represent direct measures for the performance optimization of organic batteries, since they directly influence the physico-chemical properties of the system. Another approach to maximize performance properties, however, is the optimization of operational parameters. A battery management system is, therefore, usually installed with each type of battery to ensure maximum efficiency and safety under any combination of external conditions. With regard to this, redox flow batteries represent a highly complex battery system, whose performance parameters are influenced strongly by external parameters and interdependent physical properties of the rechargeable electrolytes. This includes properties such as density, conductivity, concentration, pH value, and viscosity which continuously vary during the battery operation due to changes in temperature, electrical loads, chemical composition (*e.g.*, due to side-reactions and cross-over), state-of-health, and state-of-charge (SOC). The latter relates the amount of charge, Q, that can be obtained from a battery at an arbitrary point in time to its maximum capacity, Q_{max}. For a RFB, SOCs can also be defined from the total concentrations, $c = c_{ox} + c_{red}$, of the redox species and the concentrations of its redox states for each of the two electrolytes:

$$SOC = \frac{Q}{Q_{max}} = \frac{c_{ox}}{c_{ox} + c_{red}} = \frac{c_{ox}}{c} \quad \text{and} \quad \overline{SOC} = \frac{\bar{Q}}{\bar{Q}_{max}} = \frac{\bar{c}_{red}}{\bar{c}_{ox} + \bar{c}_{red}} = \frac{\bar{c}_{red}}{\bar{c}}. \qquad (8)$$

Herein, the subscripts *ox* and *red* denote the oxidized and reduced form of the redox species, respectively. The variables marked with a bar represent the variables for anolytes, while those without a bar denote variables for a catholyte.

The state-of-charge represents an ideal monitoring parameter for a safe and efficient flow battery operation. Most of the physical properties of both anolyte and catholyte are dependent on the SOC. Consequently, with a changing SOC there are changes in the optimal operational conditions with regard to, *e.g.*, flow rate and current load. In addition, a lot of electrolytes exhibit increasingly strong side-reactions at extreme SOCs (*i.e.*, close to 0% or 100% SOC). Naturally, there is a high interest to push the battery as far as possible to these extreme SOCs to utilize the battery's maximum capacity without irreversibly damaging the system. A reliable and accurate state-of-charge monitoring method is, therefore, mandatory. Due to the aforementioned interrelationship of the SOC to nearly all electrolyte properties, a notable variety of methods utilizing different physico-chemical properties of the RFB electrolytes already exists. These methods are, *e.g.*, based on the spectral properties of the electrolytes,[106, 107] the electrolytes' electrical conductivities,[107-109] the electrolytes' densities,[110] the electrolytes' viscosities,[111] the transferred charge (coulomb counting),[110] the terminal voltage of the battery in combination with electrochemical models and online fitting procedures,[112-115] amperometric measurements,[116] and open-circuit voltages. [110, 117]

It can be summarized, however, that each of the reported methods struggles with a combination of several of the following disadvantages:

(1) Error accumulation over time;
(2) calibration and frequent, time-consuming re-calibration;
(3) dependencies on changing system parameters (*e.g.*, temperature, salt concentration, electrolyte capacity etc.);
(4) no individual electrolyte SOC prediction (*i.e.*, missing half-cell resolution);
(5) no real-time monitoring capability;
(6) mathematical complexity;
(7) complex and costly instrumentation;
(8) limitation to certain types of electrolytes.

As part of this PhD thesis, two methods have been investigated to mitigate these issues.

4.1 Symmetric open-circuit cells for the state-of-charge monitoring

In contrast to conventional batteries, RFBs have the advantage that additional electrochemical cells can be used to measure the open-circuit voltage (OCV) between both half-cells.[110, 117] This is due to the decoupling of the charge storage material and the electrochemical conversion unit in RFBs, which is unique among the battery technologies. Although most commercial RFB systems rely on this method, its missing half-cell resolution is highly problematic due to capacity imbalances that frequently occur in redox flow batteries.[118] Other OCV approaches, therefore, measure the equilibrium half-cell potentials of the electrolyte *versus* a standard reference electrode (*e.g.*, Ag/AgCl, Hg/Hg_2SO_4).[117] In that way, the individual SOC of both anolyte and catholyte can be predicted accurately and electrolyte imbalances can be safely detected. However, reference potential drift originating from unpredictable species cross-over between reference electrode and battery electrolyte also causes unpredictable errors over time. Due to this, frequent re-calibration is inevitable. While novel calibration methods are straight forward and reliable, they usually take hours for large-scale redox flow systems.[110]

In order to slow down cross-over induced potential drift and to enable a significantly faster (re-)calibration, a novel symmetric open-circuit cell without standard reference electrode was investigated as part of this PhD thesis. This cell takes its reference state from the equilibrium potential of a portion of the monitored flow battery electrolyte at a constant SOC. The proposed symmetric open-circuit cell consists of two T-piece LuerLock adapters that are connected with each other and enable an insertion directly into the flow path of the redox flow battery. A glass frit divides the reference electrolyte chamber from the flow battery electrolyte path. Two graphite rods that are immersed in the reference half-cell and the flow battery electrolyte, respectively, are used as electrode pair (**Figure 4.1**). The reference electrolyte is prepared *in-situ* by charging the flow battery electrolyte to approximately 50% SOC as determined by coulomb counting and, subsequently, inserting the electrolyte into the reference half-cell. Calibration and re-calibration of the open-circuit cell is performed according to the method reported by Ressel *et al.*, recently.[110] In brief, the measurable potential evolution of the open-circuit cell during a charging or discharging cycle is related to the transferred charge, Q, by coulomb counting and a fitting approach.

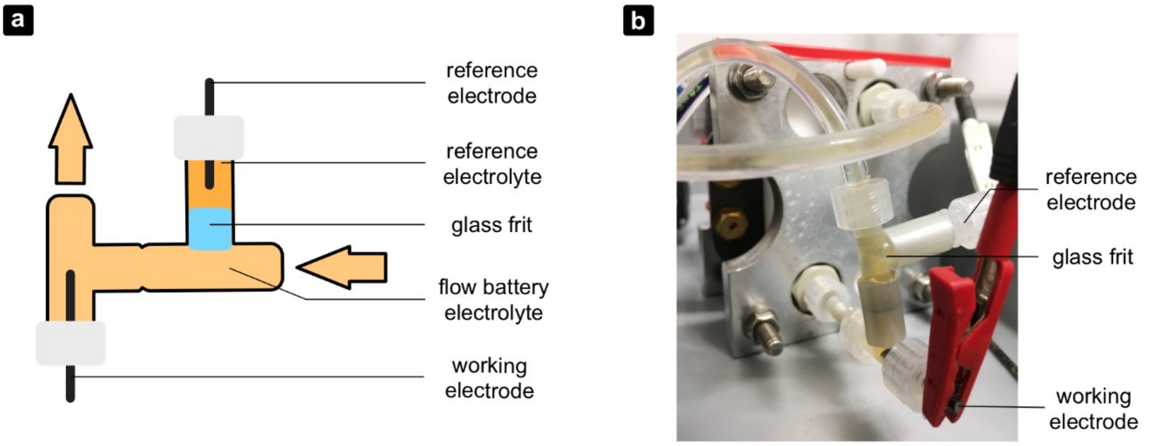

Figure 4.1. (a) Schematic representation and (b) photograph of the experimental setup of the conventional and the symmetric open-circuit cells, respectively. The silver wires used as reference electrodes for the conventional open-circuit cells had a diameter of 0.4 mm, whereas the graphite rods used for the symmetric open-circuit cell had a diameter of 2 mm; both had a length of approximately 1 cm (inside the reference compartment). The glass frits (blue in (a)) had a diameter of 3.2 mm, a height of 4 mm, and consisted of ion permeability porous glass according to the manufacturer (ALS Co, Ltd., Japan).

At a temperature, T, and for a n-electron redox reaction, the Nernst equation is:

$$E_{eq}(Q) = E_{ref} \pm \frac{RT}{nF} ln\left(\frac{SOC(Q)}{1 - SOC(Q)}\right) = E_{ref} \pm \frac{RT}{nF} ln\left(\frac{\frac{Q}{Q_{max}} + SOC_0}{1 - \frac{Q}{Q_{max}} - SOC_0}\right). \tag{9}$$

In this equation, to which the obtained data is fitted by the least-squares method, E_{ref} represents the reference potential of the open-circuit cell, Q_{max} the total capacity of the battery electrolyte, and SOC_0 its initial state-of-charge. While these are the fitting parameters, R is the universal gas constant and F is the Faraday constant. The different signs correspond to catholytes (plus) and anolytes (minus), respectively. For standard reference electrodes, E_{ref} equals the formal potential of the redox reaction under investigation and for the symmetric open-circuit cell the reference potential can be derived from the state-of-charge of the reference electrolyte. Consequently, if the reference potential was determined by the fitting approach, the SOC of the monitored electrolyte can be calculated from the measured open-circuit cell voltage by:

$$SOC(E_{eq}) = \frac{exp\left(\pm\frac{nF}{RT}(E_{eq} - E_{ref})\right)}{1 + exp\left(\pm\frac{nF}{RT}(E_{eq} - E_{ref})\right)}. \tag{10}$$

The online-monitoring capability was tested in an aqueous organic redox flow battery based on a *N,N,N*-2,2,6,6-heptamethylpiperidinyloxy-4-ammonium chloride (TEMPTMA) catholyte and a *N,N'*-dimethyl-4,4-bipyridinium dichloride (MV) anolyte. The SOC estimation capability of the symmetric approach was directly compared to that of a conventional open-circuit cell with Ag/AgCl reference electrode for the catholyte of the operating RFB (**Figure 4.2**).

The mean deviation between the SOC estimates of both cells, ΔSOC, was approximately −0.03 ± 0.29% directly after the calibration. However, due to the reference potential drift in both cells the deviation continuously increased during the course of six consecutive galvanostatic cycles. The origin of this increasing deviation was investigated in further experiments. To assess the reference potential drift rates, both open-circuit cells were re-calibrated every 5th cycle of the RFB. Linear regression of E_{ref} over time subsequently yielded the drift rate. The symmetric open-circuit cell exhibited a two-fold lower reference potential drift at a rate of 37 ± 18 µV h^{-1} in comparison to -87 ± 2 µV h^{-1} for the conventional open-circuit cell. Subsequent investigations on the cause of this reference drift in the symmetric open-circuit cell revealed that it is mainly caused by cross-over and not by self-discharge of the reference electrolyte. Therefore, the observed difference in drift rates can be attributed predominantly to the lower impact of species cross-over in the symmetric cell type in comparison to the conventional open-circuit cell. In turn, this is due to the chemical similarity of reference electrolyte and monitored electrolyte in symmetric cells and, hence, is an inherent advantage of this novel open-circuit cell type. As a consequence of the presented results, symmetric open-circuit cells offer a novel and fast method for re-calibration by using the following approach:

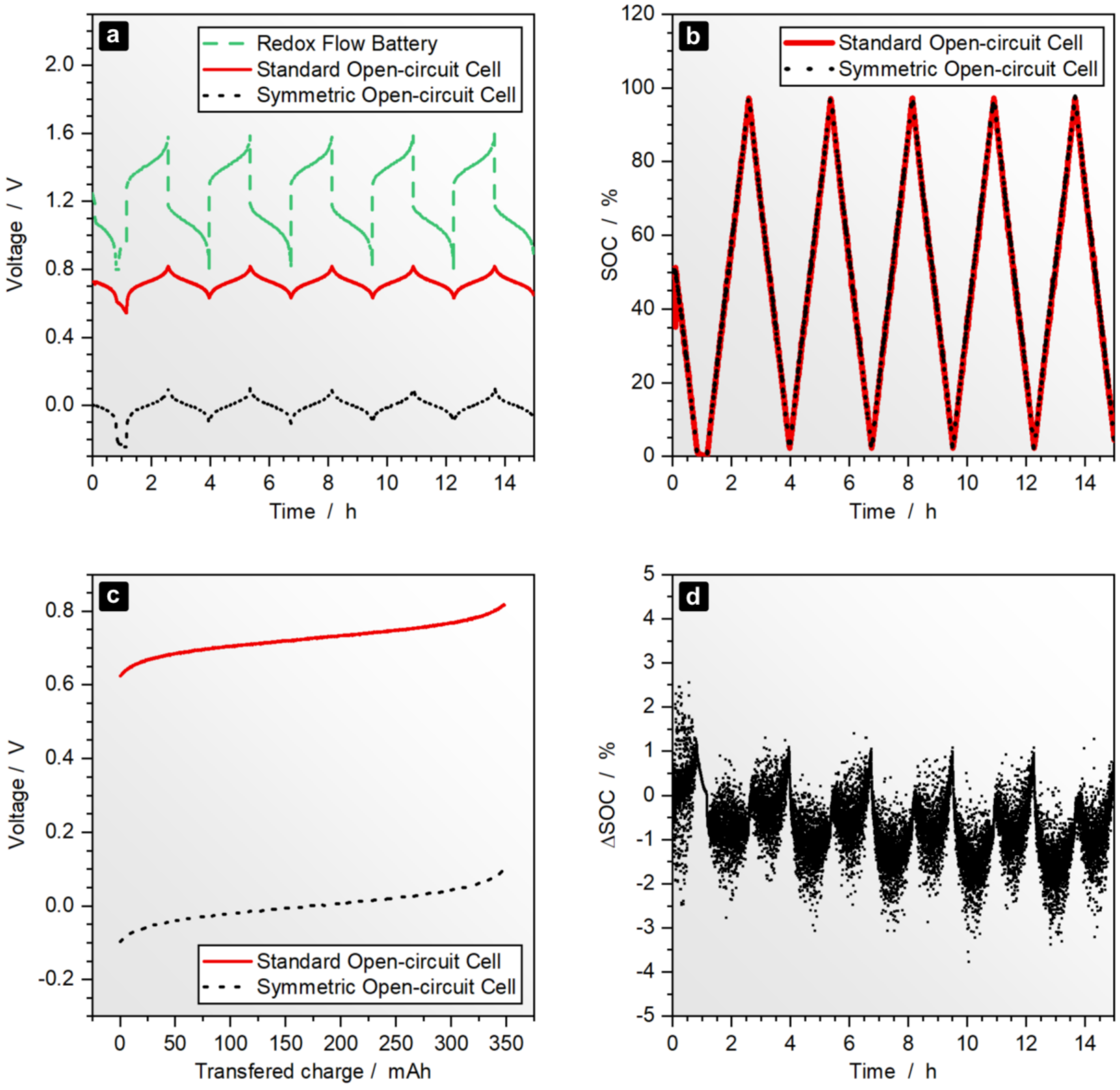

Figure 4.2. After *in-situ* production of the reference electrolyte at 50% SOC, (a) cell voltages of the TEMPTMA / MV redox flow battery and the corresponding open-circuit cells were monitored over five consecutive galvanostatic cycles at 50 mA cm^{-2}. The open-circuit voltages of (b) the first charging cycle were used for the calibration of the OCV-SOC relationship. The obtained calibration was used to monitor (c) the SOC of the catholyte over five successive cycles. The absolute difference in the SOC estimation between the both open-circuit cells is depicted in (d).

During the operation of the RFB, a specific amount of *in-situ* produced reference electrolyte can be stored in a separate reservoir. As soon as re-calibration of the open-circuit cell is required, the reference electrolyte can be exchanged with the reference electrolyte in the reservoir. While this exchange is theoretically possible for conventional open-circuit cells as well, the remarkable advantage of symmetric open-circuit cells is that the reference electrolyte can be produced *in-situ*, whenever it is required. In contrast to that, the application of this procedure to these cells would necessitate an external supply of, *e.g.*, saturated KCl-AgCl reference electrolyte once the reservoir is emptied. The proposed re-calibration method was investigated for a symmetric TEMPTMA/TEMPTMA RFB, which was operated for a period of 26 days. A larger amount of reference electrolyte was directly taken from the RFB tank and stored in a separate glass vial at day one. A reference potential value of −1.25 ± 0.06 mV was obtained during initial calibration at the same day and was used throughout all of the 26 days without re-calibration. Instead, the reference electrolyte of the symmetric open-circuit cell was exchanged three times within the course of this experiment. Furthermore, a conventional open-circuit cell with Ag/AgCl reference was operated in parallel and was frequently re-calibrated with the standard procedure. The SOC estimates of the conventional cell with standard re-calibration procedure and the symmetric cell with the novel reference electrolyte exchange procedure were compared for a reliability evaluation of this approach. **Figure 4.3a** summarizes the obtained SOC differences for each of the full charging cycles that followed directly after the four reference electrolyte exchanges. Each of the four data sets indicates that 95% of the measured data points within the corresponding cycle exhibit a deviation of less than ±3% from the SOC value obtained from the frequently re-calibrated conventional open-circuit cell. The average estimation error and its standard deviation calculated from the mean values of the four cycles is 0.07 ± 0.77%. Additionally, it was verified that the electrolyte exchange had a significant influence on the estimated SOC value of the symmetric open-circuit cell at all. To do so, the SOC estimation error was evaluated by re-calibrating the symmetric open-circuit cell with Ressel's method and comparing it to the not re-calibrated data. This was done for the charging cycles before and after each reference electrolyte exchange (**Figure 4.3b**). The results clearly indicate that both the novel re-calibration approach and the standard re-calibration approach deliver accurate results. However, the presented electrolyte exchange procedure is expected to be 100 to 10,000 times faster, in particular, if automated exchange mechanisms are installed within the battery.

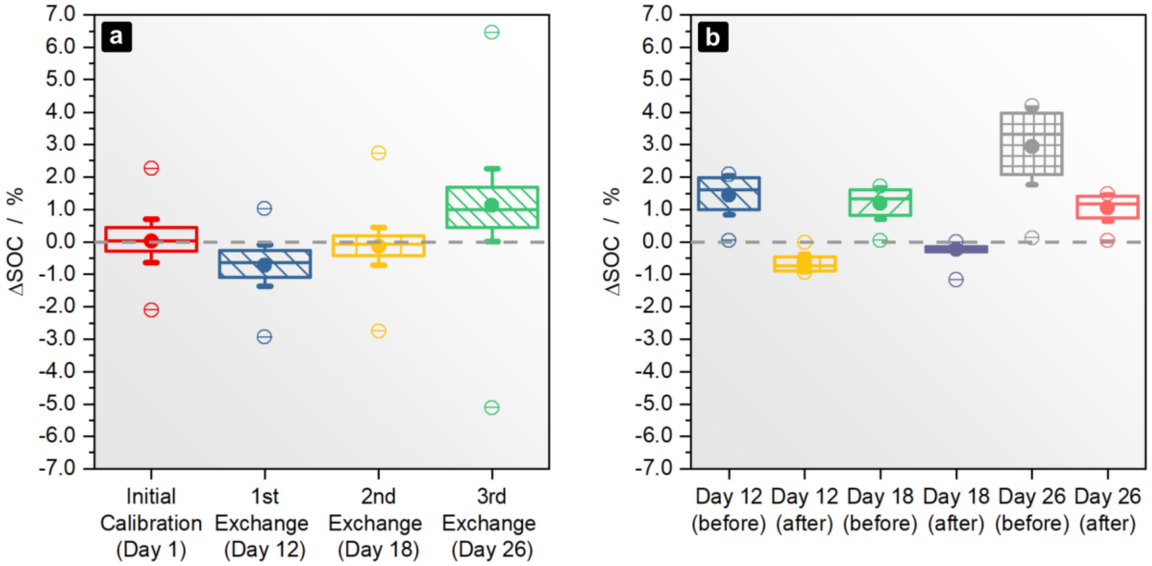

Figure 4.3. Box plots of the SOC estimation differences between (a) the data of the re-calibrated standard open-circuit cell with Ag/AgCl reference electrode and the data of the not re-calibrated symmetric open-circuit cell after the reference electrolyte exchange and (b) between the re-calibrated symmetric open-circuit cell data and the not re-calibrated symmetric open-circuit cell data before and after the reference electrolyte exchange. Each box plot represents the data for the full charging cycle. The boxes mark the 25th and 75th percentile, the whiskers represent one standard deviation, the circles within the box show the mean value, the horizontal lines represent the medians, and the outer circles show the minimum and maximum values within each data set. Observed variances originate mainly from the measurement noise of the cell voltage measurement.

4.2 Amperometric, calibration-free, and temperature-independent state-of-charge measurement

Although the symmetric open-circuit cell represents a major improvement of the open-circuit cell method for SOC monitoring, it still relies on calibration and is prone to variances in, *e.g.*, system temperature and electrolyte composition. Furthermore, an automated electrolyte exchange procedure requires additional hardware, which increases costs to a yet unknown extend. This method, therefore, still shares some of the disadvantages that were listed at the beginning of this chapter for current SOC monitoring methods: Calibration errors, dependence on system parameters, and costs.

However, during the work on this PhD thesis, a novel SOC monitoring method based on the measurement of currents under mass-transfer limiting conditions was invented that overcomes most – if not all – of the present issues related to the state-of-charge monitoring of redox flow batteries. A simple mathematical relationship between the SOC and the ratio of cathodic to anodic mass-transfer limited current was derived, which requires neither a calibration nor the knowledge about the temperature, the concentration, or any other system parameter. The new approach relies on the measurement of anodic and cathodic mass-transfer limiting currents, $i_{l,a}$ and $i_{l,c}$, which can be described in a mathematical form for a variety of electrode types by:[119]

$$i_{l,a} = nFAm_{red}c_{red} \quad \text{and} \quad i_{l,c} = -nFAm_{ox}c_{ox}. \tag{11}$$

In these equations, n, F, c_{red}, and c_{ox} have the previously introduced meanings, A represents the electrode area and $m_{red/ox}$ the so-called mass-transfer coefficients, which describe the type of mass-transport and the geometry of the electrode. By using the definition of the state-of-charge and the total concentration, one can derive a remarkably simple relationship between the SOC and the ratio of the anodic and cathodic limiting currents:

$$SOC = \frac{1}{1 - \frac{i_{l,a}}{i_{l,c}}\frac{m_{ox}}{m_{red}}} \quad \text{(for catholytes),} \tag{12}$$

$$\overline{SOC} = \frac{1}{1 - \frac{\bar{i}_{l,c}}{\bar{i}_{l,a}}\frac{\bar{m}_{red}}{\bar{m}_{ox}}} \quad \text{(for anolytes).} \tag{13}$$

While these equations already enable a state-of-charge measurement, the ratio of mass-transfer coefficients still needs to be determined separately. However, if the limiting currents are measured at two distinct times, t_1 and t_2, and if the time period between them is sufficiently short so that neither the total concentration nor the mass-transfer coefficients change, the ratio of mass-transfer coefficients can be evaluated from the current differences:

$$\frac{\Delta i_{l,c}}{\Delta i_{l,a}} \equiv \frac{i_{l,c}(SOC(t_2)) - i_{l,c}(SOC(t_1))}{i_{l,a}(SOC(t_2)) - i_{l,a}(SOC(t_1))} = \frac{nFAm_{ox}c\Delta SOC}{nFAm_{red}c\Delta SOC} = \frac{m_{ox}}{m_{red}}. \tag{14}$$

$$\frac{\Delta \bar{i}_{l,c}}{\Delta \bar{i}_{l,a}} \equiv \frac{\bar{i}_{l,c}(\overline{SOC}(t_2)) - \bar{i}_{l,c}(\overline{SOC}(t_1))}{\bar{i}_{l,a}(\overline{SOC}(t_2)) - \bar{i}_{l,a}(\overline{SOC}(t_1))} = \frac{\bar{n}F\bar{A}\bar{m}_{ox}\bar{c}\Delta\overline{SOC}}{\bar{n}F\bar{A}\bar{m}_{red}\bar{c}\Delta\overline{SOC}} = \frac{\bar{m}_{ox}}{\bar{m}_{red}}. \tag{15}$$

Combination of the two sets of equations yields the general parameter-independent relationship between the state-of-charge and the mass-transfer limiting currents:

$$SOC = \frac{1}{1 - \frac{i_{l,a}}{i_{l,c}}\frac{\Delta i_{l,c}}{\Delta i_{l,a}}} \quad \text{(for catholytes),} \tag{16}$$

$$\overline{SOC} = \frac{1}{1 - \frac{\bar{i}_{l,c}}{\bar{i}_{l,a}}\frac{\Delta \bar{i}_{l,a}}{\Delta \bar{i}_{l,c}}} \quad \text{(for anolytes).} \tag{17}$$

The derived relationships enable a simple, cost-efficient, and calibration-free state-of-charge monitoring on the half-cell level. It should be emphasized that equations (16) and (17) are independent from any system property including the temperature and the concentration of redox species. In addition, the relationship was derived without assumptions regarding the electrolyte properties. The suggested approach is, thus, theoretically applicable to a variety of aqueous/non-aqueous organic/inorganic electrolytes. A minor limitation of the general equations (16) and (17) is the requirement of a SOC difference between times t_1 and t_2 and, thus, they cannot be used during open-circuit periods of the RFB.

To the best of the author's knowledge, amperometric techniques for the state-of-charge monitoring of redox flow battery electrolytes have been reported only once in the scientific literature so far. Kroner *et al.* constructed a sensor based on an electrode which is covered with a porous ceramic gas diffusion layer (GDL) with a constant thickness δ.[116] The GDL is supposed to cause a stationary concentration profile, which limits the transport of the redox-active species from the bulk electrolyte to the electrode surface. While the authors' SOC monitoring method relies on a calibration approach, their reported sensor data also obeys equations (11) for which $m_{ox/red} = D_{ox/red}\,\delta^{-1}$ and $D_{ox/red}$ is the diffusion coefficient of the oxidized or reduced species. It is, therefore, a perfect candidate for the first verification of the derived equations. For this diffusion-limited process the SOC estimation equation can be written as:

$$SOC = \frac{1}{1 - \frac{i_{l,a}}{i_{l,c}} \frac{D_{ox}}{D_{red}}}. \tag{18}$$

The limiting currents for a 1.6 M vanadium catholyte obtained with the GDL-based sensor were extracted from Figure 6 of the aforementioned publication. A significant offset current was evident for both the anodic and the cathodic potential regimes at zero concentration; thus, all currents were corrected for this offset value. The SOC values were subsequently estimated in two ways: First, using equation (18) with the assumption that $D_{ox}D_{red}^{-1} \approx 1$, which is a good and frequently utilized assumption in electrochemistry literature. Second, equation (16) was used. Over all 10 offline samples investigated in the publication of Kroner *et al.,* the evaluation method proposed in this PhD thesis resulted in absolute root-mean-square deviations (RMSD) of 4% and 6% for the estimated SOCs.

The observed offset current in the data of Kroner and co-workers was anticipated to be an artifact of their sensor. To overcome this problem and due to the beneficial electrochemical properties of microelectrodes (*e.g.*, steady-state voltammograms, low non-faradaic currents, etc.), this kind of electrode was used for the further verification of the proposed method in own experiments. The mass-transfer limited currents at a microelectrode can be calculated by,[119]

$$i_{l,a} = 4nFrD_{red}c_{red} \quad \text{and} \quad i_{l,c} = -4nFrD_{ox}c_{ox}. \tag{19}$$

It is evident that these limiting currents yield the same SOC relationship, equation (18), that was derived for other diffusion-limited currents before.

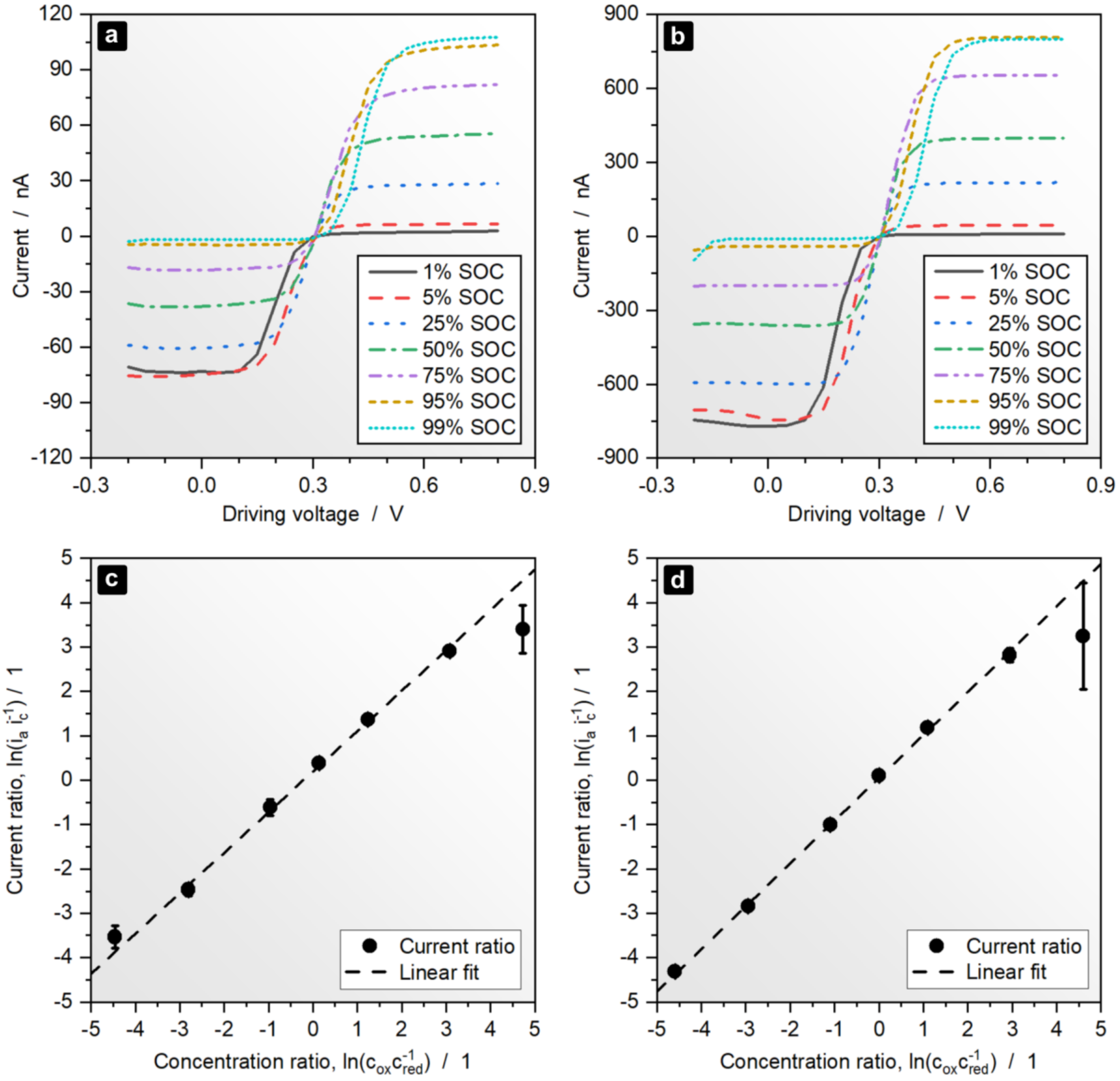

Figure 4.4. Exemplary steady-state voltammograms obtained at the gold microelectrode (diameter: 25 µm) for different SOCs of ferri-/ferrocyanide aqueous electrolytes with total concentrations of (a) 50 mM and (b) 500 mM. Current ratios of the limiting cathodic (at 0.8 V) and anodic (at –0.2 V) currents were obtained from (a) and (b). Their natural logarithmic values were plotted over the natural logarithmic values of the concentration ratios of ferricyanide and ferrocyanide for (c) the 50 mM electrolyte and (d) the 500 mM electrolyte (data points: average values of three repetitions; error bars: corresponding standard deviations).

In a first experimental approach, electrolytes containing different ratios of ferri- and ferrocyanide in an aqueous 0.5 M and 1 M KCl solution were prepared at total concentrations of 50 mM and 500 mM of the redox species. Due to the defined ratios of both redox states of the redox couple, the solutions resembled battery electrolytes with a known SOC. These "offline" samples (*i.e.*, samples measured outside an operating RFB) were investigated using a closed bipolar electrode setup with a reference electrolyte containing approximately equal amounts of ferri- and ferrocyanide in an aqueous 3 M KCl solution saturated with AgCl.[120-125] A AgCl-coated silver-wire was used as reference electrode in the reference compartment and a series-coupled gold microelectrode (diameter: 25 µm) was utilized as working electrode in the analysis half-cell. The current response at the microelectrode was recorded in an overpotential range from −0.5 V to +0.5 V *vs.* its equilibrium potential. **Figure 4.4** displays exemplary steady-state voltammograms for the prepared ferri-/ferrocyanide electrolytes. A significant dependence of the limiting currents on the SOC was observed as expected. Furthermore, the limiting current ratios exhibited a linear relationship with the known concentration ratios of oxidized and reduced species as predicted by equations (19).

Table 4.1. SOC estimates obtained from the derived amperometric equations for offline samples of the ferri-/ferrocyanide redox couple in aqueous 0.5 M and 1 M $KCl_{(aq)}$ solutions, respectively. Total concentrations of 50 mM and 500 mM were prepared and reference SOCs, SOC_{ref}, were determined from the weighed substance masses and the calculated concentrations. $\Delta SOC \equiv SOC - SOC_{ref}$ represents the deviation from the reference SOC.

	50 mM[(a)]		**50 mM**[(b)]			**500 mM**[(a)]		**500 mM**[(b)]	
$\boldsymbol{SOC_{ref}}$ **%**	SOC %	ΔSOC %	SOC %	ΔSOC %	$\boldsymbol{SOC_{ref}}$ **%**	SOC %	ΔSOC %	SOC %	ΔSOC %
1.1	3.3	2.2	-	-	**1.0**	1.3	0.3	-	-
5.7	8.3	2.6	−2.3	−7.9	**5.0**	5.6	0.6	−5.4	−10.4
27.7	34.6	6.9	21.5	−6.2	**25.0**	26.7	1.7	14.3	−10.7
53.5	60.5	7.1	52.5	−1.0	**50.0**	52.7	2.7	47.4	−2.6
77.5	81.3	3.8	75.3	−2.2	**75.0**	76.7	1.7	72.3	−2.7
95.6	95.3	−0.3	93.5	−2.1	**95.0**	94.2	−0.8	93.0	−2.0
99.1	97.0	−2.2	95.7	−3.4	**99.0**	94.5	−4.5	95.1	−3.9
RMSD	**4.3**		**4.5**			**2.2**		**6.5**	

(a) Calculated from equation (18) using the assumption $D_{ox}D_{red}^{-1} = 1$.
(b) Calculated from equation (16) using the current difference to the first current value.

Larger deviations were observed only at extreme SOCs due to expected measurement errors in the lower nanoampere measurement range. In contrast to the amperometric sensor constructed by Kroner *et al.*, the microelectrode exhibited only negligible offset currents. The obtained current ratios were used to calculate the state-of-charge using equations (16) and (18). For the latter, the assumption of equal diffusion coefficients for the oxidized and the reduced redox state was used again. **Table 4.1** summarizes the results of this evaluation. It is evident that the absolute RMSD of the SOC estimation for offline samples was well below 6.5% and, therefore, in the same range as observed for the aforementioned data of vanadium-based samples. The observed inaccuracies are attributed to the comparably low concentrations, measurement errors in the low current regime, and the rather small number of samples used to cover the full SOC range. The latter causes higher estimation errors for $\Delta i_{l,c}$ and $\Delta i_{l,a}$. These assumptions are supported experimentally by the higher estimation accuracies achieved for the online SOC monitoring of TEMPTMA electrolytes at higher concentrations in an operating flow battery. These experiments are presented later in this chapter. Prior to the online monitoring experiments, the theoretically predicted temperature independence of the approach was investigated using the ferri-/ferrocyanide redox couple and TEMPTMA. Both types of electrolytes were prepared at approximately 50% SOC and, subsequently, heated to different temperatures in an oil bath. **Figure 4.5** displays the anodic and cathodic limiting currents as well as their ratios obtained in a temperature range from approximately 25 to 50 °C using the microelectrodes. While the absolute current values increase with rising temperatures due to the higher ion mobilities in heated electrolytes, the ratio of anodic to cathodic current, $i_a i_c^{-1}$, stays constant. This observation implies a temperature independence of the ratio of the diffusion coefficients, $D_{ox} D_{red}^{-1}$. This implication for the ratio of the diffusion coefficients is theoretically expected from the Einstein-Stokes-Equation for two sorts of ions within the same electrolyte. The online SOC monitoring capability of the approach was tested in an operating symmetric TEMPTMA/TEMPTMA RFB according to the considerations about symmetric RFBs published by Goulet *et al.*, recently.[41] For the measurement, a carbon fiber microelectrode (diameter: 33 µm) was inserted directly into the catholyte tank of the RFB using the same closed bipolar electrode setup utilized for the offline experiments before. In order to minimize distortions by convective flux of redox species to the microelectrode surface, the electrolyte inlet and outlet were placed far away from the microelectrode.

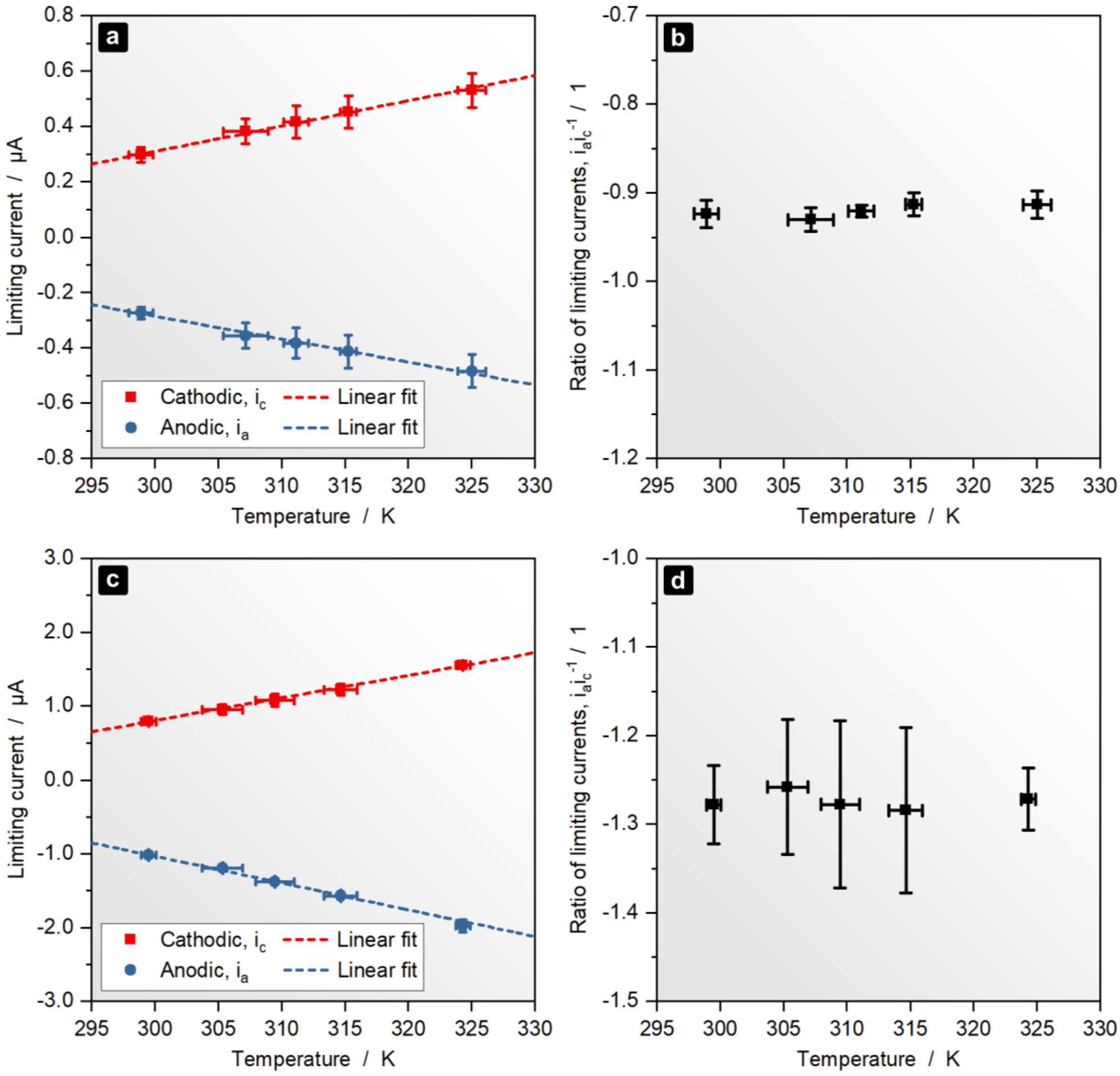

Figure 4.5. Cathodic and anodic limiting currents obtained in an electrolyte temperature range from 25 to 50 °C for (a, b) 500 mM ferri-/ferrocyanide in 0.5 M $KCl_{(aq)}$ and (c, d) 1.3 M aqueous TEMPTMA; absolute current values are presented as average values of (a) four and (c) three repetitions, respectively; (b, d) ratios of cathodic to anodic limiting current. All error bars represent the corresponding standard deviations.

Furthermore, a symmetric open-circuit cell, which was described in **Chapter 4.1**, was operated in parallel to monitor the SOC of the electrolyte with a known method for verification of the results. During the course of six consecutive charge-discharge cycles (**Figure 4.6a**), the limiting currents at the microelectrode exhibited a linearly increasing/decreasing behavior corresponding to the linearly varying SOC in this galvanostatic experiment (**Figure 4.6b**). The reference state-of-charge, SOC_{ref}, was evaluated from the symmetric open-circuit cell, which was calibrated in each half-cycle to obtain maximum accuracy. For the amperometric data, equations (16) and (18) were utilized to estimate the SOC. The qualitative analysis already showed an excellent agreement between the SOC estimates (**Figure 4.6c**), which was further verified by a statistical analysis of all SOC values (**Figure 4.6d**). The box plots display the differences, $\Delta SOC \equiv SOC - SOC_{ref}$, between the SOC estimates from the amperometric approach, SOC, and the reference state-of-charge, SOC_{ref}, obtained from the open-circuit cell for all data points obtained during the six full cycles of battery operation. It can be stated that 98% of the SOC estimates of both methods deviated by not more than ±5%.

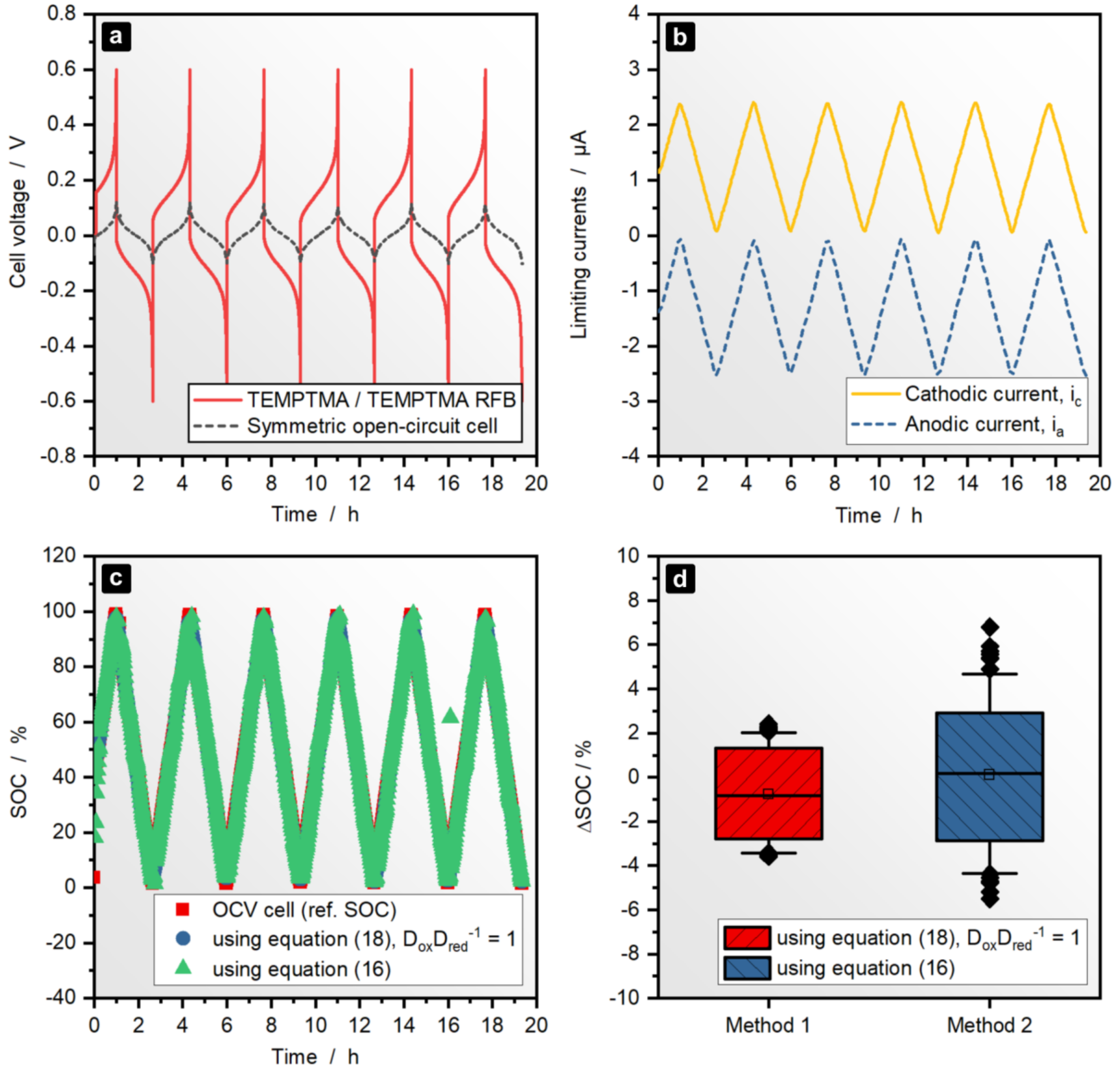

Figure 4.6. Real-time SOC monitoring experiment for a symmetric TEMPTMA / TEMPTMA RFB (1.3 M $TEMPTMA_{(aq)}$; galvanostatic cycling: ±200 mA): (a) Cell voltages of the RFB and an open-circuit cell connected to the capacity-limiting half-cell; (b) limiting currents measured by a closed bipolar carbon-fiber disk microelectrode (diameter: 33 µm; driving voltages: –0.2 V and 0.8 V); (c) SOC as determined from the open-circuit cell and the limiting currents; (d) box plots for the SOC estimation differences of open-circuit cell and amperometric approach, $\Delta SOC \equiv SOC - SOC_{ref}$ (box: 10 to 90% percentile; whiskers: 1 to 99% percentile; squares (☐): mean; line (—): median; diamonds (♦): outliers).

Indeed, the same 98% of SOC estimates exhibited an absolute deviation of less than ±3% if equal diffusion coefficients were assumed. The absolute RMSD for both amperometric evaluation approaches were 1.7% and 2.9%, respectively. It can be stated that the overall accuracy of the presented method is comparable to the open-circuit cell technique as the well-accepted standard approach for SOC estimation. The amperometric SOC monitoring method is, therefore, on par with all known state-of-the-art SOC monitoring techniques for redox flow batteries reported so far.[110, 111, 113, 117, 126, 127]

5 Summary

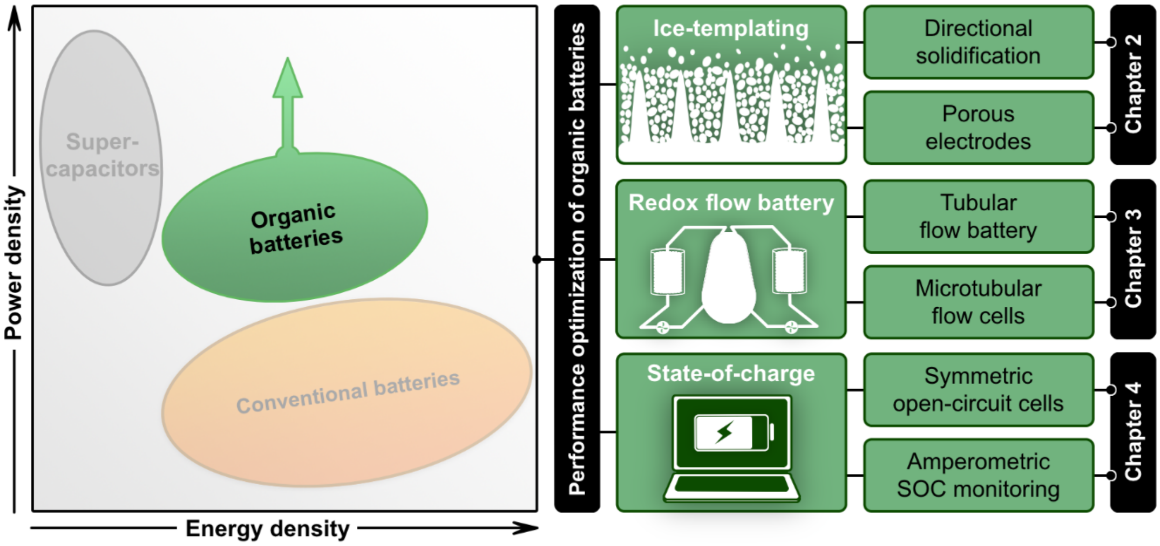

Figure 5.1. Graphical summary of the content presented in the Chapters 2 to 4 of this PhD thesis.

Organic compounds represent a highly promising material basis for the next generations of batteries. Due to the enormous flexibility synthetic approaches provide for the tailoring of material properties, organic redox-active molecules can be adjusted to perform as energy storage material in both solid electrodes for organic radical batteries (ORB) and in the electrolytes for redox flow batteries (RFB). In comparison to their conventional metal-based counterparts, organic electrode materials excel due to their non-abundant resource basis, fast redox reactions, potentially low cost, and outstanding versatility. Due to that, the recent years have witnessed a remarkable increase in the number of investigated redox units and a few very promising candidates have been found. Despite the already large number of investigated molecules, only a negligible fraction of the synthetic opportunities has been exploited. With regard to this, organic electrode materials are not limited by theoretically promising structures, but rather by the experimental workload for their realization and investigation. The advent of novel machine learning algorithms and automated laboratories will be remarkably beneficial in speeding up materials research in the upcoming years. Thus, there is no doubt that more and more viable redox chemistries will be discovered. After decades of research focusing on metal-based batteries, however, established electrode processing routines, battery cell designs, and characterization techniques are not yet optimized for the new opportunities and challenges experienced during the application and investigation of organic electrode materials. Consequently, there is a strong need for intensification of investigations in these areas to exploit all of the potential this highly interdisciplinary research field bears.

For that reason, non-conventional approaches for the fabrication of ORB electrodes, for the design of redox flow cells, and the online monitoring of redox flow battery electrolytes were investigated in this work.

The first results obtained in this PhD thesis contribute to an improved understanding of the directional solidification of water, which is the fundamental basis for fabrication of porous samples by ice-templating approaches. It was theoretically and experimentally demonstrated that an exponential cooling function leads to a solidification with constant ice front velocity. The demonstrated degree of accuracy between the predicted and the measured ice front velocity surpasses that of the quasi-stationary cooling function proposed in previous works. That renders the exponential cooling function an ideal tool for ice-templating approaches, for which pore dimensions commonly exhibit a defined dependency on this specific velocity. The achieved constancy of the velocity value guarantees homogenous pore diameters throughout the whole sample height of ice-templated porous materials. Furthermore, a supercooling effect was identified as the velocity-determining process at the initial phase of solidification. This helps to understand the small structural sizes commonly observed in the initial/transitional layers of ice-templated samples. With regard to the positive effects reported for meso- and microporous morphologies on the performance of electrodes, an ice templating approach was applied for the preparation of porous electrodes for ORBs containing carbon additives, a cellulose-based binder, and redox-active PTMA. These electrodes were investigated regarding their electrochemical performance in PTMA/zinc organic radical batteries. They exhibited no capacity decay over 25 cycles and a capacity utilization of approximately 94% of the theoretically expected value of 110.7 mAh g^{-1}. However, first electrochemical experiments for the comparison to conventional planar electrodes revealed a significantly lower C-rate capability of the porous electrodes. This observation was mainly attributed to the larger thicknesses of the porous electrodes and the lower electric conductivities of the porous scaffold. The first issue might be overcome by optimization of the cutting procedures for the porous electrodes to obtain thinner slices. The second might be addressed by optimization of the slurry formulation and the process parameters of the ice-templating process itself. The adjustment of the slurry's water content, for example, can lead to densified and thicker pore walls with a higher overall conductivity. Furthermore, the addition of conductive components or the embedding of inert conductive foams (metal or carbon) during the ice-templating could be beneficial to the electrode performance as well. Despite the identified obstacles, ice-templating successfully yielded stable porous electrodes with an excellent performance at 1C. The approach enables a novel variety of opportunities for the manipulation of the morphological properties of ORB electrodes and, thus, represents an interesting technique for further research.

Although ORBs represent promising candidates for applications in mobile devices, smart packaging, wearables, and the internet of things, they lack a sufficient scalability for stationary energy storage. However, due to the chemical tunability of organic redox units, the ORB principle was successfully transferred to the highly scalable redox flow battery technology within the recent years. Current research on RFBs is mostly focused on the improvement of energy density and measures for increasing the power density are rarely investigated. The latter is partly due to the wide-spread opinion that power density in terms of volume limitations is not of great importance for stationary batteries. However, it is frequently overlooked that it does matter in terms of resource and cost efficiency; *i.e.*, smaller flow cells with higher power densities automatically lead to a lower material consumption at equal absolute powers. In this context, non-conventional flow cell geometries have hardly been subject to investigations within the past decades. The thesis at hand contributes to fill this gap by a first investigation of tubular and microtubular organic redox flow batteries. The realization of tubular cells became viable with the invention of polymer-based RFBs, which utilize size-exclusion membranes instead of ion-exchange membranes, which are not readily available in a tubular shape. It was demonstrated at first that this new approach not only enables the realization of a tubular cell geometry, but also the utilization of ceramic size-exclusion membranes that are not applicable in conventional filter-press flow cells due to the increasing fragility of the material at larger planar sizes. The tubular cell exhibited a comparably low sealing area per volume and a stable cycling over 25 consecutive cycles. However, a rather high cell resistance of $50\,\Omega\,\text{cm}^2$ based on the membrane area and a volumetric resistance of $38\,\Omega\,\text{cm}^3$ as well as a significant capacity fade were observed. An improper sealing with silicone and the high thickness of the ceramic membrane are anticipated as the main cause for the observed performance issues. In a second approach, the volume and diameter of the cell were significantly reduced to exploit the high membrane area to volume ratio that can be achieved from a tubular geometry. The resulting microtubular flow cells were experimentally realized with commercially available hollow fiber dialysis membranes (MWCO: 3 kDa). A poly(TMA-*co*-PEGMA) / zinc hybrid flow battery represented a first simple approach for the preparation of such a μTFC, because the inner (negative) half-cell could be built up from a zinc wire and oxygen could not interfere the negative redox reaction. A direct comparison to a conventional filter-press flow cell utilizing the same materials revealed a ten-fold reduced volumetric resistance for the µTFC (0.3 ± 0.1 Ω cm^3). In a comparison to literature reports on other zinc-based flow cells, the presented µTFC yielded a two-fold lower ohmic resistance. The beneficial performance of the µTFC was further verified by polarization curve measurements, where ohmic resistances contributed by 40% of the total overvoltage in the filter-press design whereas it only constituted 5% of the overvoltage within the µTFC. The main limitations in the power density for the investigated µTFC, therefore, stems from activation and concentration overpotentials, which were attributed to the utilized redox chemistry and the missing porous electrode in the negative half-cell. Current rating experiments performed at volumetric discharging current densities ranging from 100 to 1 mA cm^{-3} also exhibited an improved capacity retention due to the microtubular cell design for current densities above 45 mA cm^{-3}. However, the aforementioned experiments and further consecutive galvanostatic cycling also revealed a low coulombic efficiency and a strong capacity decay over 60 cycles for the µTFC. The results of subsequent investigations suggest that polymer cross-over through the membrane or leakage at the membrane sealing are the most-likely causes for the observed problems. Future research efforts might overcome the remaining issues by an increase of the polymer's hydrodynamic volume, a decrease in the membranes MWCO, and the utilization of more sophisticated sealing approaches.

After this successful demonstration of the general viability of tubular and microtubular flow cell designs as direct non-conventional means for the improvement of flow batteries, indirect measures for their performance optimization were explored. With regard to this, two new approaches for the state-of-charge monitoring of redox flow batteries were investigated. First of all, the well-known open-circuit cell method for the online state-of-charge measurement of RFB electrolytes was modified. It was demonstrated that a portion of the monitored flow battery electrolyte itself in a fixed state-of-charge can provide a sufficiently stable reference potential, if it is used in the reference half-cell of the open-circuit cell instead of a conventional reference electrode. This symmetric open-circuit cell was compared to a conventional open-circuit cell with Ag/AgCl reference electrode during the operation of an aqueous organic TEMPTMA / MV RFB. A mean absolute difference of −0.03 ± 0.29% in the SOC estimates of both cells revealed identical accuracy for both cell types. However, due to the very similar composition of reference electrolyte and monitored electrolyte in the symmetric open-circuit cell, the measured reference potential drift was two-fold lower in comparison to the conventional open-circuit cell. Furthermore, the approach enables a 100 to 10,000 times faster re-calibration method, which is based on the exchange of the *in-situ* producible reference electrolyte. In a second approach, it was demonstrated that the state-of-charge of a large variety of redox flow battery electrolytes can be assessed with simple amperometric equations from the mass-transfer limited currents at different types of electrodes. The introduced approach performed equally well regardless of changes in temperature, concentration, and other system parameters. As the first absolute method for the measurement of the state-of-charge, the method does not rely on error-prone calibration procedures which are usually necessitated by other techniques. In first online monitoring experiments, the method delivered root-mean-square-deviations of below 3% in comparison to the open-circuit cell approach, which can be considered as the "gold standard" among SOC monitoring methods. Consequently, the accuracy of the presented amperometric approach is on par with all state-of-the-art techniques. Although all experiments presented in this thesis were carried out using commercial potentiostats, such complex and universal hardware is not required for the SOC measurements. On the contrary, a high cost-efficiency is indicated for this approach, which basically relies on technologically simple constant voltage sources and direct current measurements.

In conclusion, the general viability of ice-templated electrode morphologies and tubular redox flow cell designs was successfully demonstrated for organic batteries for the first time. Despite the promising potential of these approaches, it is, however, obvious that further research is required to obtain operational values that outperform conventional approaches and utilize their full potential. A different circumstance is met for the presented state-of-charge monitoring methods which outperform previous approaches and can be easily transferred to industrial RFBs. In particular, the amperometric SOC monitoring approach is expected to be highly beneficial to both industrial application and academic research in the near future. It overcomes most – if not all – of the present issues related to the SOC monitoring of redox flow battery electrolytes, while providing cost-efficiency, half-cell resolution, reliability, and technological simplicity at the same time. The availability of this first calibration-free, temperature-independent, and highly versatile method for the state-of-charge measurement will contribute not only to a safe and performance-optimized RFB operation, it will also help, *e.g.*, to assess the long-term stability of charged electrolytes, to understand degradation mechanisms, to investigate self-discharge processes, and to speed up research for both organic and metal-based redox flow batteries. Furthermore, the cost-efficiency of the presented approach will enable a wide-spread utilization of this method in industry and academia even in laboratories with strongly limited resources.

6 Zusammenfassung

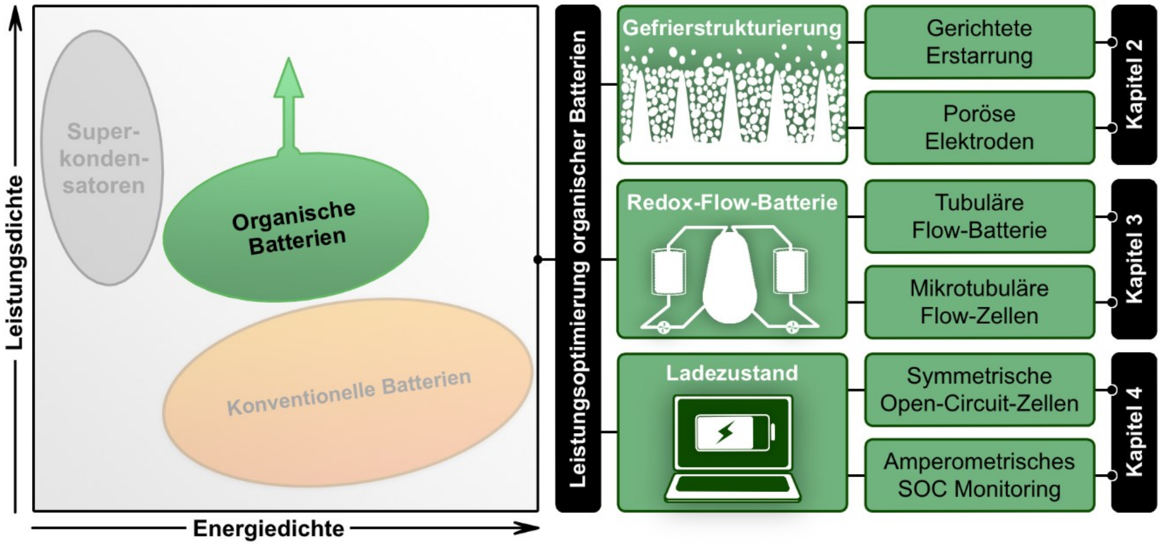

Figure 6.1. Grafische Zusammenfassung des in den Kapiteln 2 bis 4 präsentierten Inhalts dieser Doktorarbeit.

Organische Verbindungen stellen eine vielversprechende Materialbasis für zukünftige Batteriegenerationen dar. Aufgrund der enormen Flexibilität, die synthetische Ansätze für die Anpassung der Materialeigenschaften bieten, können organische redoxaktive Moleküle so angepasst werden, dass sie Anwendung als Energiespeichermaterial sowohl in Feststoffelektroden für organische Radikalbatterien (ORB) als auch in den Elektrolyten für Redox-Flow-Batterien (RFB) finden können. Im Vergleich zu Elektroden auf Metallbasis zeichnen sich organische Elektrodenmaterialien durch einen geringen Ressourcenverbrauch, schnelle Redoxreaktionen, potenziell niedrige Kosten und eine hohe Flexibilität aus. In den letzten Jahren ist die Zahl der untersuchten Redox-Einheiten daher erheblich angestiegen und es wurden einige sehr vielversprechende Kandidaten gefunden. Trotz der großen Anzahl bereits untersuchter Moleküle konnte bisher nur ein vergleichsweise geringer Teil der Synthesemöglichkeiten ausgeschöpft werden. Diesbezüglich sind organische Elektrodenmaterialien nicht durch die Anzahl theoretisch vielversprechender Strukturen beschränkt, sondern vor allem durch den experimentellen Aufwand für deren Realisierung und Charakterisierung. In diesem Zusammenhang wird die Einführung neuartiger Algorithmen für maschinelles Lernen und Automatisierung von Laboren in den kommenden Jahren die Materialforschung vermutlich erheblich beschleunigen. Somit besteht kaum Zweifel, dass zukünftig eine Vielzahl anwendbarer Materialien entdeckt werden. Nach jahrzehntelanger Forschung im Bereich metallbasierter Batterien sind etablierte Routinen für die Elektrodenverarbeitung, das Design von Batteriezellen und Techniken für die Charakterisierung jedoch noch nicht für die neuen

Möglichkeiten und Herausforderungen optimiert, die sich aus der Anwendung und Untersuchung organischer Elektrodenmaterialien ergeben. Infolgedessen ist eine Intensivierung der Untersuchungen in diesen Bereichen dringend erforderlich, um das gesamte Potenzial dieses interdisziplinären Forschungsbereichs auszuschöpfen. Aus diesem Grund wurden in dieser Arbeit neue und unkonventionelle Ansätze zur Herstellung von ORB-Elektroden, zum Design von Redox-Flow-Zellen und zur Online-Überwachung von Redox-Flow-Batterieelektrolyten untersucht.

Die ersten Ergebnisse dieser Dissertation tragen zu einem besseren Verständnis der gerichteten Erstarrung von Wasser bei, welche die Grundlage für die Herstellung poröser Proben mithilfe der sogenannten Gefrierstrukturierung (engl.: Ice-Templating) bildet. Es wurde sowohl theoretisch als auch experimentell gezeigt, dass eine exponentielle Kühlfunktion zu einer Erstarrung mit konstanter Eisfrontgeschwindigkeit führt. Der erzielte Genauigkeitsgrad zwischen vorhergesagter und gemessener Eisfrontgeschwindigkeit übertrifft den der in früheren Arbeiten vorgeschlagenen quasistationären Kühlfunktion. Dies macht die exponentielle Kühlfunktion zu einem idealen Werkzeug für Ice-Templating-Ansätze, bei denen die Porendimensionen üblicherweise eine definierte Abhängigkeit von dieser spezifischen Geschwindigkeit aufweisen. Die erreichte Konstanz des Geschwindigkeitswertes garantiert homogene Porendurchmesser über die gesamte Probenhöhe der resultierenden porösen Materialien. Weiterhin wurde ein Unterkühlungseffekt in der Anfangsphase der Erstarrung als der geschwindigkeitsbestimmende Prozess identifiziert. Diese Erkenntnis trägt dazu bei, die kleinen Strukturgrößen zu verstehen, die üblicherweise in den Anfangs- / Übergangsschichten poröser Proben, die mittels Ice-Templating hergestellt wurden, beobachtet werden. In Bezug auf die positiven Effekte auf die Leistungsfähigkeit von Elektroden, die für meso- und mikroporöse Morphologien in der wissenschaftlichen Literatur vermerkt wurden, wurde ein Ice-Templating-Ansatz zur Herstellung poröser Elektroden für ORBs angewendet. Diese Elektroden enthielten Kohlenstoffadditive, ein Bindemittel auf Cellulosebasis sowie das redoxaktive PTMA und wurden hinsichtlich ihrer elektrochemischen Leistungsfähigkeit in PTMA/Zink-ORBs untersucht. Diese zeigten über 25 Lade-Entlade-Zyklen hinweg keinen nennenswerten Kapazitätsabfall sowie eine Kapazitätsauslastung von ca. 94% des theoretisch erwarteten Wertes von 110,7 mAh g^{-1}. Erste elektrochemische Experimente zum Vergleich mit herkömmlichen planaren Elektroden ergaben jedoch eine deutlich geringere C-Raten-Fähigkeit der porösen Elektroden. Diese Beobachtung wurde hauptsächlich auf die größeren Dicken der porösen

Elektroden und die geringeren elektrischen Leitfähigkeiten der Porenstrukturen zurückgeführt. Die erste Einschränkung könnte durch Optimierung der Schneidverfahren für die porösen Elektroden behoben werden, um dünnere Elektrodenschichten zu erhalten. Die zweite Limitierung könnte durch Optimierung der Zusammensetzung der ursprünglichen Suspension und der Prozessparameter des Ice-Templating-Prozesses selbst angegangen werden. Beispielsweise kann die Anpassung des Wassergehalts der Suspension zu verdichteten und dickeren Porenwänden mit einer höheren Gesamtleitfähigkeit führen. Darüber hinaus könnte die Zugabe von leitfähigen Komponenten oder das Einbetten von inerten leitfähigen Schäumen (Metall oder Kohlenstoff) während des Ice-Templatings auch für die Elektrodenleistung von Vorteil sein. Trotz der festgestellten Hindernisse lieferte das Ice-Templating-Verfahren stabile poröse Elektroden mit einer hervorragenden Leistung bei 1C. Der Ansatz bietet eine Vielzahl von Möglichkeiten zur Manipulation der morphologischen Eigenschaften von ORB-Elektroden und stellt somit eine interessante Technik zur weiteren Erforschung dar.

Obwohl ORBs vielversprechende Kandidaten für Anwendungen in mobilen Geräten, intelligenten Verpackungen, sogenannten Wearables und dem Internet der Dinge sind, fehlt ihnen eine ausreichende Skalierbarkeit für die Anwendung als stationäre Energiespeicher. Aufgrund der chemischen Flexibilität organischer Redoxeinheiten konnte das ORB-Prinzip in den letzten Jahren jedoch erfolgreich auf die hochskalierbaren Redox-Flow-Batterietechnologie übertragen werden. Die aktuelle Forschung zu RFBs konzentriert sich hauptsächlich auf die Verbesserung der Energiedichte und Maßnahmen zur Erhöhung der Leistungsdichte werden selten untersucht. Letzteres kann der weit verbreiteten Meinung zugeschrieben werden, dass die Leistungsdichte für stationäre Batterien auf Grund geringer Volumenbeschränkungen nicht von großer Bedeutung ist. Es wird jedoch häufig übersehen, dass sie im Hinblick auf Ressourcen- und Kosteneffizienz durchaus relevant ist. Kleinere Redox-Flow-Zellen mit höheren Leistungsdichten führen automatisch zu einem geringeren Materialverbrauch bei gleichen absoluten Leistungen. In diesem Zusammenhang wurden unkonventionelle Geometrien von Redox-Flow-Zellen in den letzten Jahrzehnten kaum untersucht. Die vorliegende Arbeit trägt dazu bei, diese Lücke durch eine erste Untersuchung von tubulären und mikrotubulären organischen Redox-Flow-Batterien zu schließen. Die Realisierung solcher tubulären Zellen wurde mit der Erfindung von polymerbasierten RFBs möglich, die Größenausschlussmembranen anstelle von Ionenaustauschmembranen verwenden. Letztere sind in tubulärer Form nicht ohne weiteres verfügbar. Es wurde zunächst gezeigt, dass dieser neuartige Ansatz nicht nur die

Realisierung einer tubulären Zellgeometrie ermöglicht, sondern auch die Verwendung von keramischen Größenausschlussmembranen, die aufgrund der zunehmenden Zerbrechlichkeit des Materials bei großflächigen Filterpress-Zellen nicht anwendbar sind. Die realisierte tubuläre Zelle zeigte eine vergleichsweise geringe Versiegelungsfläche pro Volumen und eine prinzipielle Zyklierbarkeit in 25 aufeinanderfolgenden Lade-Entlade-Zyklen. Es wurden jedoch ein relativ hoher Zellwiderstand von 50 Ω cm^2 (bezogen auf die Membranfläche) und ein Volumenwiderstand von 38 Ω cm^3 (bezogen auf das Zellvolumen) sowie eine signifikante Kapazitätsabnahme beobachtet. Die Abdichtung mit Silikon und die hohe Dicke der Keramikmembran sind hierbei vermutlich die Hauptursache für die beobachteten Leistungsprobleme. In einem zweiten Ansatz wurden das Volumen und der Durchmesser der Zelle signifikant reduziert, um das für die Leistungsdichte vorteilhafte hohe Verhältnis von Membranfläche zu Volumen auszunutzen, welches mit einer tubulären Geometrie erzielt werden kann. Die resultierenden mikrotubulären Redox-Flow-Zellen (µTFC) wurden experimentell mit kommerziell erhältlichen Hohlfaserdialysemembranen (MWCO: 3 kDa) realisiert. Eine Poly(TMA-*co*-PEGMA)/Zink-Hybrid-RFB stellte einen ersten einfachen Ansatz für die Herstellung einer solchen µTFC dar, da die innere (negative) Halbzelle aus einem Zinkdraht aufgebaut werden konnte und Sauerstoff für diese Zellchemie keinen Störfaktor darstellt. Ein direkter Vergleich mit einer herkömmlichen RFB im Filterpressen-Design unter Verwendung der gleichen Materialien ergab einen um das Zehnfache verringerten Volumenwiderstand für die µTFC (0,3 ± 0,1 Ω cm^3). Im Vergleich zu Literaturangaben über andere zinkbasierte RFBs ergab die vorgestellte µTFC einen um den Faktor zwei verringerten ohmschen Widerstand. Die vorteilhafte Leistung der µTFC wurde durch Polarisationskurvenmessungen zusätzlich bestätigt, bei denen die ohmschen Widerstände etwa 40% der gesamten elektrochemischen Überspannung in der Filterpressen-RFBs verursachten, während sie nur 5% der Überspannung innerhalb der µTFC ausmachten. Die Hauptbeschränkungen der Leistungsdichte für die untersuchte µTFC resultieren daher aus Aktivierungs- und Konzentrationsüberpotentialen, die auf die verwendete Redoxchemie und die fehlende poröse Elektrode in der negativen Halbzelle zurückgeführt wurden. Strombelastbarkeitstests, die bei volumetrischen Entladestromdichten im Bereich von 100 bis 1 mA cm^3 durchgeführt wurden, zeigten auch einen verbesserten Kapazitätserhalt aufgrund des mikrotubulären Designs für Stromdichten oberhalb von 45 mA cm^3. Die zuvor genannten Experimente und weitere aufeinanderfolgende galvanostatische Zyklen zeigten jedoch für die µTFC auch eine niedrige Coulomb-Effizienz und einen starken Kapazitätsabfall über 60 Zyklen hinweg.

Die Ergebnisse nachfolgender Untersuchungen legen nahe, dass Diffusion von redoxaktiven Molekülen durch die Membran oder Dichtungsfehler an der Membranabdichtung die wahrscheinlichsten Ursachen für die beobachteten Probleme sind. Zukünftige Forschungsanstrengungen könnten diese Probleme durch eine Erhöhung des Molekulargewichts der Polymere, eine Verringerung des MWCO der Membranen und die Verwendung eleganterer Dichtungsansätze überwinden.

Nach dieser erfolgreichen Demonstration der allgemeinen Realisierbarkeit von tubulären und mikrotubulären Flow-Zellen als direktes, nicht konventionelles Mittel zur Verbesserung von RFBs, wurden indirekte Maßnahmen zur Leistungsoptimierung erforscht. In diesem Zusammenhang wurden zwei neue Ansätze zur Ladezustandsüberwachung von Redox-Flow-Batterien untersucht. Zunächst wurde das bekannte Open-Circuit-Cell-Verfahren zur Online-Ladezustandsmessung von RFB-Elektrolyten modifiziert. Es wurde gezeigt, dass ein Teil des Batterieelektrolyten selbst in einem festen Ladezustand ein ausreichend stabiles Referenzpotential liefern kann, wenn er in der Referenzhalbzelle der Open-Circuit-Zelle anstelle einer herkömmlichen Referenzelektrode verwendet wird. Eine solche symmetrische Open-Circuit-Zelle wurde während des Betriebs einer wässrigen organischen TEMPTMA/MV-RFB mit einer herkömmlichen Open-Circuit-Zelle mit Silber-Silberchlorid-Referenzelektrode verglichen. Eine mittlere absolute Differenz von −0,03 ± 0,29% in den SOC-Abschätzungen beider Open-Circuit-Zellen ergab für beide Zelltypen eine nahezu identische Genauigkeit. Aufgrund der sehr ähnlichen Zusammensetzung von Referenzelektrolyt und überwachtem Batterieelektrolyten in der symmetrischen Open-Circuit-Zelle war der gemessene Referenzpotentialdrift im Vergleich zur herkömmlichen Open-Circuit-Zelle jedoch um einen Faktor zwei geringer. Darüber hinaus ermöglicht der Ansatz eine 100- bis 10.000-mal schnellere Rekalibrierungsmethode, die auf dem Austausch des *in situ* produzierbaren Referenzelektrolyten basiert. In einem zweiten Ansatz wurde gezeigt, dass der Ladezustand einer Vielzahl von Redox-Flow-Batterieelektrolyten mit einfachen amperometrischen Gleichungen aus den massentransferbegrenzten Strömen verschiedener Elektrodentypen bestimmt werden kann. Der vorgestellte Ansatz zeigte eine Unabhängigkeit von Änderungen der Temperatur, der Konzentration und anderer Systemparameter. Als erstes absolutes Verfahren zur Bestimmung des Ladezustands beruht diese Methode nicht auf fehleranfälligen Kalibrierungsverfahren, die normalerweise erforderlich sind. In ersten Online-Monitoring-Experimenten lieferte die Methode im Vergleich zum Open-Circuit-Cell-Ansatz, der als „Goldstandard“ unter den SOC-Monitoring-Methoden angesehen werden kann, absolute quadratische Mittelwertabweichungen von unter 3%. Folglich ist die Genauigkeit des vorgestellten amperometrischen Ansatzes allen bisher bekannten Techniken ebenbürtig. Obwohl die in dieser Arbeit vorgestellten Experimente mit kommerziellen Potentiostaten durchgeführt wurden, ist für die SOC-Messungen keine derart komplexe und universelle Hardware erforderlich. Tatsächlich zeichnet sich für diesen Ansatz, der im Wesentlichen auf einfachen Konstantspannungsquellen und einfacher Gleichstrommessung beruht, eine hohe Kosteneffizienz ab.

Es lässt sich zusammenfassen, dass in dieser Arbeit zum ersten Mal die allgemeine Realisierbarkeit von gefrierstrukturierten Elektrodenmorphologien und tubulären Redox-Flow-Zellen für organische Batterien demonstriert werden konnten. Trotz des vielversprechenden Potenzials dieser Ansätze ist es jedoch offensichtlich, dass weitere Forschung erforderlich ist, um Leistungswerte zu erzielen, die konventionelle Ansätze übertreffen und eine industrielle Anwendbarkeit ermöglichen. Im Gegensatz dazu übertreffen die vorgestellten, neuen Ladezustandsüberwachungsmethoden alle bisherigen Ansätze und lassen sich leicht auf industrielle RFBs übertragen. Insbesondere der Ansatz der amperometrischen SOC-Überwachung dürfte in naher Zukunft sowohl für die industrielle Anwendung als auch für die akademische Forschung von großem Nutzen sein. Sie überwindet die meisten – wenn nicht alle – der gegenwärtigen Probleme im Zusammenhang mit der SOC-Überwachung von RFB-Elektrolyten und bietet gleichzeitig eine hohe Kosteneffizienz, Halbzellenauflösung, Zuverlässigkeit und eine bemerkenswerte technologische Einfachheit. Die Verfügbarkeit dieser ersten kalibrierungsfreien, temperaturunabhängigen und äußerst vielseitigen Methode zur Ladezustandsmessung wird nicht nur zu einem sicheren und optimierten RFB-Betrieb führen, sondern auch dazu beitragen, die Langzeitstabilität geladener Elektrolyte zu untersuchen, das Verständnis von Zersetzungsprozessen zu verbessern, die Untersuchung von Selbstentladungsmechanismen zu erleichtern und die Forschung sowohl für organische als auch für metallbasierte Redox-Flow-Batterien zu beschleunigen. Darüber hinaus wird die Kosteneffizienz des vorgestellten Ansatzes eine breite Anwendung dieser Methode sowohl im industriellen Umfeld als auch im akademischen Bereich bis hin zu Laboratorien mit begrenzten Ressourcen ermöglichen.

7 References

[1] WWF, *Living Planet Report - 2018: Aiming Higher*, M. Grooten, R. E. A. Almond, Gland, Switzerland, **2018**.

[2] IPCC, *Climate Change 2013: The Physical Science Basis. Contribution of Working Group I to the Fifth Assessment Report of the Intergovern-Mental Panel on Climate Change*, T. F. Stocker, D. Qin, G.-K. Plattner, M. Tignor, S. K. Allen, J. Boschung, A. Nauels, Y. Xia, V. Bex, P. M. Midgley, Cambridge, United Kingdom and New York, NY, USA, **2013**.

[3] NOAA National Centers for Environmental Information, *Global Climate Report – Annual 2019*, https://www.ncdc.noaa.gov/sotc/global/201913 (Retrieved on January 22, 2020), **2019**.

[4] E. Dlugokencky, P. Tans, *Noaa/Esrl: Global Monthly Mean Co$_2$*, https://www.esrl.noaa.gov/gmd/ccgg/trends/global.html (Retrieved on January 22, 2020), **2019**.

[5] United Nations Framework Convention on Climate Change (UNFCCC), *Paris Agreement*, Paris, **2016**.

[6] IRENA, *Global Energy Transformation: A Roadmap to 2050 (2019 Edition)*, Abu Dhabi, **2019**.

[7] T. M. Gür, *Energy Environ. Sci.* **2018**, *11*, 2696-2767.

[8] IRENA, *Electrification with Renewables: Driving the Transformation of Energy Services*, Abu Dhabi, **2019**.

[9] G. L. Soloveichik, *Annu. Rev. Chem. Biomol. Eng.* **2011**, *2*, 503-527.

[10] M. Sanders, C. Pillot, *The Rechargeable Battery Market and Main Trends 2016 to 2025*, Michigan, USA, **2017**.

[11] C. Vaalma, D. Buchholz, M. Weil, S. Passerini, *Nat. Rev. Mater.* **2018**, *3*, 18013.

[12] B. Faber, B. Krause, R. S. De La Sierra, *Artisanal Mining, Livelihoods, and Child Labor in the Cobalt Supply Chain of the Democratic Republic of Congo*, **2017**.

[13] C. Banza Lubaba Nkulu, L. Casas, V. Haufroid, T. De Putter, N. D. Saenen, T. Kayembe-Kitenge, P. Musa Obadia, D. Kyanika Wa Mukoma, J. M. Lunda Ilunga, T. S. Nawrot, O. Luboya Numbi, E. Smolders, B. Nemery, *Nat. Sustain.* **2018**, *1*, 495-504.

[14] G. E. Blomgren, *J. Electrochem. Soc.* **2016**, *164*, A5019-A5025.

[15] D. B. Agusdinata, W. Liu, H. Eakin, H. Romero, *Environ. Res. Lett.* **2018**, *13*, 123001.

[16] E. Cantatore, *Applications of Organic and Printed Electronics*, Springer, Boston, MA, **2013**.

[17] P. Friederich, A. Fediai, S. Kaiser, M. Konrad, N. Jung, W. Wenzel, *Adv. Mater.* **2019**, *31*, 1808256.

[18] D. MacInnes, M. A. Druy, P. J. Nigrey, D. P. Nairns, A. G. MacDiarmid, A. J. Heeger, *J. Chem. Soc., Chem. Commun.* **1981**, 317-319.

[19] L. W. Shacklette, M. Maxfield, S. Gould, J. F. Wolf, T. R. Jow, R. H. Baughman, *Synth. Met.* **1987**, *18*, 611-618.

[20] L. W. Shacklette, T. R. Jow, M. Maxfield, R. Hatami, *Synth. Met.* **1989**, *28*, 655-662.

[21] A. G. Macdiarmid, J.-C. Chiang, W. Huang, B. D. Humphrey, N. L. D. Somasiri, *Mol. Cryst. Liq. Cryst.* **2011**, *125*, 309-318.

[22] T. Janoschka, M. D. Hager, U. S. Schubert, *Adv. Mater.* **2012**, *24*, 6397-6409.

[23] P. Novák, K. Müller, K. S. V. Santhanam, O. Haas, *Chem. Rev.* **1997**, *97*, 207-282.

[24] K. Mizushima, P. C. Jones, P. J. Wiseman, J. B. Goodenough, *Mater. Res. Bull.* **1980**, *15*, 783-789.

[25] M. S. Whittingham, *Science* **1976**, *192*, 1126-1127.

[26] H. Nishide, S. Iwasa, Y.-J. Pu, T. Suga, K. Nakahara, M. Satoh, *Electrochim. Acta* **2004**, *50*, 827-831.

[27] K. Nakahara, S. Iwasa, M. Satoh, Y. Morioka, J. Iriyama, M. Suguro, E. Hasegawa, *Chem. Phys. Lett.* **2002**, *359*, 351-354.

[28] S. Muench, A. Wild, C. Friebe, B. Haupler, T. Janoschka, U. S. Schubert, *Chem. Rev.* **2016**, *116*, 9438-9484.

[29] T. B. Schon, B. T. McAllister, P. F. Li, D. S. Seferos, *Chem. Soc. Rev.* **2016**, *45*, 6345-6404.

[30] B. Huskinson, M. P. Marshak, C. Suh, S. Er, M. R. Gerhardt, C. J. Galvin, X. Chen, A. Aspuru-Guzik, R. G. Gordon, M. J. Aziz, *Nature* **2014**, *505*, 195-198.

[31] T. Janoschka, N. Martin, U. Martin, C. Friebe, S. Morgenstern, H. Hiller, M. D. Hager, U. S. Schubert, *Nature* **2015**, *527*, 78-81.

[32] W. Kangro, Germany, **1949**, DEP47135A.

[33] M. Skyllas-Kazacos, L. Cao, M. Kazacos, N. Kausar, A. Mousa, *ChemSusChem* **2016**, *9*, 1521-1543.

[34] L. F. Arenas, C. Ponce de León, F. C. Walsh, *J. Energy Storage* **2017**, *11*, 119-153.

[35] J. Winsberg, T. Hagemann, T. Janoschka, M. D. Hager, U. S. Schubert, *Angew. Chem. Int. Ed.* **2017**, *56*, 686-711.

[36] J. Luo, B. Hu, M. Hu, Y. Zhao, T. L. Liu, *ACS Energy Lett.* **2019**, *4*, 2220-2240.

[37] A. Hollas, X. Wei, V. Murugesan, Z. Nie, B. Li, D. Reed, J. Liu, V. Sprenkle, W. Wang, *Nat. Energy* **2018**, *3*, 508-514.

[38] T. Janoschka, N. Martin, M. D. Hager, U. S. Schubert, *Angew. Chem. Int. Ed.* **2016**, *55*, 14427-14430.

[39] S. Jin, Y. Jing, D. G. Kwabi, Y. Ji, L. Tong, D. De Porcellinis, M.-A. Goulet, D. A. Pollack, R. G. Gordon, M. J. Aziz, *ACS Energy Lett.* **2019**, *4*, 1342-1348.

[40] T. Janoschka, A. Teichler, B. Häupler, T. Jähnert, M. D. Hager, U. S. Schubert, *Adv. Energy Mater.* **2013**, *3*, 1025-1028.

[41] M.-A. Goulet, M. J. Aziz, *J. Electrochem. Soc.* **2018**, *165*, A1466-A1477.

[42] K. Sakaushi, E. Hosono, G. Nickerl, T. Gemming, H. Zhou, S. Kaskel, J. Eckert, *Nat. Commun.* **2013**, *4*, 1-9.

[43] R. Liu, J. Duay, S. B. Lee, *Chem. Commun.* **2011**, *47*, 1384-1404.

[44] Z. Lei, W. Wei-kun, W. An-bang, Y. Zhong-bao, C. Shi, Y. Yu-sheng, *J. Electrochem. Soc.* **2011**, *158*, A991-A996.

[45] Y. Kim, C. Jo, J. Lee, C. W. Lee, S. Yoon, *J. Mater. Chem.* **2012**, *22*, 1453-1458.

[46] J.-K. Kim, *J. Power Sources* **2013**, *242*, 683-686.

[47] J.-K. Kim, J. Scheers, J.-H. Ahn, P. Johansson, A. Matic, P. Jacobsson, *J. Mater. Chem. A* **2013**, *1*, 2426-2430.

[48] Z. Zhu, J. Chen, *J. Electrochem. Soc.* **2015**, *162*, A2393-A2405.

[49] H.-G. Wang, S. Yuan, D.-L. Ma, X.-B. Zhang, J.-M. Yan, *Energy Environ. Sci.* **2015**, *8*, 1660-1681.

[50] D. O. Carlsson, A. Mihranyan, M. Strømme, L. Nyholm, *RSC Adv.* **2014**, *4*, 8489-8497.

[51] D. O. Carlsson, G. Nyström, Q. Zhou, L. A. Berglund, L. Nyholm, M. Strømme, *J. Mater. Chem.* **2012**, *22*, 19014-19024.

[52] H. Olsson, D. O. Carlsson, G. Nyström, M. Sjödin, L. Nyholm, M. Strømme, *J. Mater. Sci.* **2012**, *47*, 5317-5325.

[53] S. Deville, *Adv. Eng. Mater.* **2008**, *10*, 155-169.

[54] U. G. K. Wegst, M. Schecter, A. E. Donius, P. M. Hunger, *Philos. Trans. R. Soc., A* **2010**, *368*, 2099-2121.

[55] S. Deville, *J. Mater. Res.* **2013**, *28*, 2202-2219.

[56] S. Deville, E. Saiz, R. K. Nalla, A. P. Tomsia, *Science* **2006**, *311*, 515-518.

[57] C. Stolze, Master thesis, Friedrich Schiller University Jena **2013**.

[58] H. Schoof, L. Bruns, A. Fischer, I. Heschel, G. Rau, *J. Cryst. Growth* **2000**, *209*, 122-129.

[59] T. Fukasawa, M. Ando, T. Ohji, S. Kanzaki, *J. Am. Ceram. Soc.* **2001**, *84*, 230-232.

[60] H. Schoof, J. Apel, I. Heschel, G. Rau, *J. Biomed. Mater. Res.* **2001**, *58*, 352-357.

[61] S. Deville, E. Saiz, A. P. Tomsia, *Acta Mater.* **2007**, *55*, 1965-1974.

[62] T. Waschkies, R. Oberacker, M. J. Hoffmann, *J. Am. Ceram. Soc.* **2009**, *92*, S79-S84.

[63] T. Waschkies, R. Oberacker, M. J. Hoffmann, *Acta Mater.* **2011**, *59*, 5135-5145.

[64] S. Deville, E. Maire, A. Lasalle, A. Bogner, C. Gauthier, J. Leloup, C. Guizard, *J. Am. Ceram. Soc.* **2009**, *92*, 2497-2503.

[65] J. Stefan, *Aus den Sitzungeber. der kais. Acad. d. Wiss. in Wien* **1889**, *89*, 269-286.

[66] B. Rubinsky, E. G. Cravahlo, *Int. J. Heat Mass Transfer* **1981**, *24*, 1987-1989.

[67] B. Rubinsky, E. G. Cravalho, *Cryobiology* **1984**, *21*, 303-320.

[68] J. Yoo, B. Rubinsky, *Numer. Heat Transfer* **2007**, *6*, 209-222.

[69] S. Deville, E. Maire, A. Lasalle, A. Bogner, C. Gauthier, J. Leloup, C. Guizard, *J. Am. Ceram. Soc.* **2009**, *92*, 2489-2496.

[70] S. Flauder, U. Gbureck, F. A. Müller, *Key Eng. Mater.* **2012**, *529-530*, 129-132.

[71] S. Flauder, U. Gbureck, F. A. Müller, *Acta Biomater.* **2014**, *10*, 5148-5155.

[72] O. M. Alifanov, *Inverse Heat Transfer Problems*, 1st ed., Springer, Berlin, **1994**.

[73] H. E. Sweers, *J. Hydrol.* **1976**, *30*, 375-401.

[74] A. Lasalle, C. Guizard, J. Leloup, S. Deville, E. Maire, A. Bogner, C. Gauthier, J. Adrien, L. Courtois, H. E. Kim, *J. Am. Ceram. Soc.* **2012**, *95*, 799-804.

[75] S. Deville, E. Maire, A. Lasalle, A. Bogner, C. Gauthier, J. Leloup, C. Guizard, *J. Am. Ceram. Soc.* **2010**, *93*, 2507-2510.

[76] H. D. Baehr, K. Stephan, *Wärme- Und Stoffübertagung*, 8th ed., Springer Berlin, **2013**.

[77] K. H. Lee, Y. W. Lee, S. W. Lee, J. S. Ha, S. S. Lee, J. G. Son, *Sci. Rep.* **2015**, *5*, 1-10.

[78] X. Zhang, C. Li, Y. Luo, *Langmuir* **2011**, *27*, 1915-1923.

[79] Y. Huang, D. Wu, J. Jiang, Y. Mai, F. Zhang, H. Pan, X. Feng, *Nano Energy* **2015**, *12*, 287-295.

[80] J. Winsberg, T. Janoschka, S. Morgenstern, T. Hagemann, S. Muench, G. Hauffman, J. F. Gohy, M. D. Hager, U. S. Schubert, *Adv. Mater.* **2016**, *28*, 2238-2243.

[81] B. R. Chalamala, T. Soundappan, G. R. Fisher, M. R. Anstey, V. V. Viswanathan, M. L. Perry, *Proc. IEEE* **2014**, *102*, 976-999.

[82] A. Z. Weber, M. M. Mench, J. P. Meyers, P. N. Ross, J. T. Gostick, Q. Liu, *J. Appl. Electrochem.* **2011**, *41*, 1137-1164.

[83] T. R. Ralph, *Platinum Met. Rev.* **1997**, 102-113.

[84] D. S. Aaron, Q. Liu, Z. Tang, G. M. Grim, A. B. Papandrew, A. Turhan, T. A. Zawodzinski, M. M. Mench, *J. Power Sources* **2012**, *206*, 450-453.

[85] R. M. Darling, M. L. Perry, *J. Electrochem. Soc.* **2014**, *161*, A1381-A1387.

[86] Q. Xu, T. S. Zhao, C. Zhang, *Electrochim. Acta* **2014**, *142*, 61-67.

[87] M. Duduta, B. Ho, V. C. Wood, P. Limthongkul, V. E. Brunini, W. C. Carter, Y.-M. Chiang, *Adv. Energy Mater.* **2011**, *1*, 511-516.

[88] B. Fang, Y. Wei, T. Arai, S. Iwasa, M. Kumagai, *J. Appl. Electrochem.* **2003**, *33*, 197-203.

[89] E. C. Montoto, G. Nagarjuna, J. Hui, M. Burgess, N. M. Sekerak, K. Hernandez-Burgos, T. S. Wei, M. Kneer, J. Grolman, K. J. Cheng, J. A. Lewis, J. S. Moore, J. Rodriguez-Lopez, *J. Am. Ceram. Soc.* **2016**, *138*, 13230-13237.

[90] M. Park, D. S. Shin, J. Ryu, M. Choi, N. Park, S. Y. Hong, J. Cho, *Adv. Mater.* **2015**, *27*, 5141-5146.

[91] M. Yue, Q. Zheng, F. Xing, H. Zhang, X. Li, X. Ma, *AIChE J.* **2018**, *64*, 782-795.

[92] Q. Zheng, F. Xing, X. Li, T. Liu, Q. Lai, G. Ning, H. Zhang, *J. Power Sources* **2015**, *277*, 104-109.

[93] F. Calise, G. Restucccia, N. Sammes, *J. Power Sources* **2010**, *195*, 1163-1170.

[94] K. S. Howe, G. J. Thompson, K. Kendall, *J. Power Sources* **2011**, *196*, 1677-1686.

[95] S. M. Jamil, M. H. D. Othman, M. A. Rahman, J. Jaafar, A. F. Ismail, K. Li, *J. Eur. Ceram. Soc.* **2015**, *35*, 1-22.

[96] V. Lawlor, *J. Power Sources* **2013**, *240*, 421-441.

[97] V. Lawlor, S. Griesser, G. Buchinger, A. G. Olabi, S. Cordiner, D. Meissner, *J. Power Sources* **2009**, *193*, 387-399.

[98] T. Janoschka, S. Morgenstern, H. Hiller, C. Friebe, K. Wolkersdörfer, B. Häupler, M. D. Hager, U. S. Schubert, *Polym. Chem.* **2015**, *6*, 7801-7811.

[99] S. Ressel, A. Laube, S. Fischer, A. Chica, T. Flower, T. Struckmann, *J. Power Sources* **2017**, *355*, 199-205.

[100] Q. Chen, M. R. Gerhardt, M. J. Aziz, *J. Electrochem. Soc.* **2017**, *164*, A1126-A1132.

[101] M. Wu, T. Zhao, R. Zhang, H. Jiang, L. Wei, *Energy Technol.* **2018**, *6*, 333-339.

[102] X. L. Zhou, Y. K. Zeng, X. B. Zhu, L. Wei, T. S. Zhao, *J. Power Sources* **2016**, *325*, 329-336.

[103] Q. Chen, M. R. Gerhardt, L. Hartle, M. J. Aziz, *J. Electrochem. Soc.* **2016**, *163*, A5010-A5013.

[104] M. C. Wu, T. S. Zhao, H. R. Jiang, Y. K. Zeng, Y. X. Ren, *J. Power Sources* **2017**, *355*, 62-68.

[105] D. Aaron, Z. Tang, A. B. Papandrew, T. A. Zawodzinski, *J. Appl. Electrochem.* **2011**, *41*, 1175-1182.

[106] S. Rudolph, U. Schröder, I. M. Bayanov, K. Blenke, D. Hage, *J. Electroanal. Chem.* **2013**, *694*, 17-22.

[107] M. Skyllas-Kazacos, M. Kazacos, *J. Power Sources* **2011**, *196*, 8822-8827.

[108] S. Corcuera, M. Skyllas-Kazacos, *Eur. Chem. Bull.* **2012**, *1*, 511-519.

[109] K. Ngamsai, A. Arpornwichanop, *J. Power Sources* **2015**, *298*, 150-157.

[110] S. Ressel, F. Bill, L. Holtz, N. Janshen, A. Chica, T. Flower, C. Weidlich, T. Struckmann, *J. Power Sources* **2018**, *378*, 776-783.

[111] X. Li, J. Xiong, A. Tang, Y. Qin, J. Liu, C. Yan, *Appl. Energy* **2018**, *211*, 1050-1059.

[112] J. Kalawoun, K. Biletska, F. Suard, M. Montaru, *J. Power Sources* **2015**, *279*, 694-706.

[113] Z. Wei, A. Bhattarai, C. Zou, S. Meng, T. M. Lim, M. Skyllas-Kazacos, *J. Power Sources* **2018**, *390*, 261-269.

[114] Z. Wei, T. M. Lim, M. Skyllas-Kazacos, N. Wai, K. J. Tseng, *Appl. Energy* **2016**, *172*, 169-179.

[115] Z. Wei, R. Xiong, T. M. Lim, S. Meng, M. Skyllas-Kazacos, *J. Power Sources* **2018**, *402*, 252-262.

[116] I. Kroner, M. Becker, T. Turek, *Batteries* **2019**, *5*, 5.

[117] M. R. Mohamed, H. Ahmad, M. N. Abu Seman, *Elektron. Elektrotech.* **2013**, *19*, 37-42.

[118] D. Reynard, H. Vrubel, C. R. Dennison, A. Battistel, H. Girault, *ChemSusChem* **2019**, *12*, 1222-1228.

[119] A. J. Bard, L. R. Faulkner, *Electrochemical Methods: Fundamentals and Applications*, 2nd ed., John Wiley & Sons, Inc., **2001**.

[120] J. T. Cox, J. P. Guerrette, B. Zhang, *Anal. Chem.* **2012**, *84*, 8797-8804.

[121] S. M. b. Fakhruddin, K. Y. Inoue, R. Tsuga, T. Matsue, *Electrochem. Commun.* **2018**, *93*, 62-65.

[122] S. E. Fosdick, K. N. Knust, K. Scida, R. M. Crooks, *Angew. Chem. Int. Ed.* **2013**, *52*, 10438-10456.

[123] J. P. Guerrette, S. M. Oja, B. Zhang, *Anal. Chem.* **2012**, *84*, 1609-1616.

[124] C. A. C. Sequeira, D. S. P. Cardoso, M. L. F. Gameiro, *Chem. Eng. Commun.* **2016**, *203*, 1001-1008.

[125] P. Zhong, P. Yu, K. Wang, J. Hao, J. Fei, L. Mao, *Analyst* **2015**, *140*, 7154-7159.

[126] Y.-S. Chou, N.-Y. Hsu, K.-T. Jeng, K.-H. Chen, S.-C. Yen, *Appl. Energy* **2016**, *182*, 253-259.

[127] C. Stolze, M. D. Hager, U. S. Schubert, *J. Power Sources* **2019**, *423*, 60-67.

Abbreviations

cFFC	Conventional filter-press flow cell
CMC	Carboxymethyl cellulose
CNP50	Carbon nano particles (50 nm)
DMC	Dimethyl carbonate
EC	Ethylene carbonate
GDL	Gas diffusion layer
IRENA	International renewable energy agency
IKTS	(Fraunhofer) Institut für Keramische Technologien und Systeme
mPES	Modified polyether sulfone
MV	Methyl viologen
MWCO	Molecular weight cut-off
OCV	Open-circuit voltage
ORB	Organic radical battery
PEDOT:PSS	Poly(3,4-ethylenedioxythiophene) polystyrene sulfonate
PEGMA	Poly(ethylene glycol) methacrylate
ppm	Parts per million
PTMA	Poly(TEMPO methacrylate)
RFB	Redox-flow battery
RMSD	Root-mean-squared deviation
SOC	State-of-charge
TEMPO	2,2,6,6-Tetramethylpiperdine-1-oxyl
TEMPTMA	*N,N,N*-2,2,6,6-Heptamethylpiperidin-1-oxy 4-ammonium chloride
TMA	TEMPO methacrylate
β-TCP	β-Tricalcium phosphate
μTFC	Microtubular flow cell

Symbols

Chapter 2

c	Specific heat capacity
f_{min}	Lower temperature limit of the setup
f	Time-dependent temperature of the cooling plate
h_f	Specific latent heat of solidification
k	Thermal diffusivity
k_s	Thermal diffusivity
L	Sample height in an ice-templating experiment
L_{max}	Maximum sample height with constant ice front velocity
s	Time-dependent position of the ice front
t	Time
T_0	Freezing temperature of the liquid
T_e	Temperature of the environment
T_p	Initial temperature of the liquid
T_s	Temperature distribution in the solid phase
v_f	Ice front velocity
α	Heat transfer coefficient between sample liquid and environment
λ	Thermal conductivity
λ_s	Thermal conductivity of the solid phase
ρ	Density
ρ_s	Density of the solid phase
ϑ_0	Freezing temperature as a function of ice front temperature

Chapter 4

A	Electrode area
c	Total concentration of redox species
c_{ox}	Concentration of oxidized form of redox species
c_{red}	Concentration of reduced form of redox species
D_{ox}	Diffusion coefficient of the oxidized species
D_{red}	Diffusion coefficient of the reduced species
E_{eq}	Equilibrium potential of the electrolyte *versus* reference electrode (open-circuit)
E_{ref}	Reference potential
F	Faraday constant
$i_{l,a}$	Anodic limiting current
$i_{l,c}$	Cathodic limiting current
m_{ox}	Mass-transfer coefficient of the oxidized species
m_{red}	Mass-transfer coefficient of the reduced species
n	Number of electrons taking part in redox reaction
Q	Amount of charge in the battery
Q_{max}	Maximum capacity
r	Radius of microelectrode
R	Universal gas constant
SOC	State-of-charge of the electrolyte
SOC_0	Initial state-of-charge of the electrolyte
T	Temperature

Publication list

Peer-reviewed publications

[1] C. Stolze, J. Meurer, M. D. Hager, U. S. Schubert, “An Amperometric, Temperature-independent, and Calibration-free Method for the Real-time State-of-Charge Monitoring of Redox Flow Battery Electrolytes”, *Chem. Mater.* **2019**, *31*, 5363-5369.

[2] C. Stolze, M. D. Hager, U. S. Schubert, “State-of-Charge Monitoring for Redox Flow Batteries: A Symmetric Open-circuit Cell Approach”, *J. Power Sources* **2019**, *423*, 60-67.

[3] T. Hagemann, M. Strumpf, E. Schröter, C. Stolze, M. Grube, I. Nischang, M. D. Hager, U. S. Schubert, “A Novel (2,2,6,6-Tetramethylpiperidin-1-yl)oxyl-Containing Zwitterionic Polymer as a Catholyte Species for High-capacity Aqueous Polymer Redox Flow Batteries”, *Chem. Mater.* **2019**, *31*, 7987-7999.

[4] C. Stolze, T. Janoschka, J. Winsberg, M. Strumpf, M. D. Hager, U. S. Schubert, “Microtubular Flow Cell Design Utilizing Commercial Hollow Fiber Dialysis Membranes for Size-exclusion Based Flow Batteries”, *Energy Technol.* **2018**, *6*, 2296-2310.

[5] C. Stolze, C. Schmerbauch, C. Friebe, U. S. Schubert, “A Tubular Polymer Redox Flow Battery with a Ceramic Membrane”, *Energy Technol.* **2017**, *5*, 225–227.

[6] J. Winsberg, C. Stolze, A. M. Schwenke, S. Muench, M. D. Hager, U. S. Schubert, “Aqueous 2,2,6,6–Tetramethylpiperidine–*N*–oxyl catholytes for a High-capacity and High-current Density Oxygen-insensitive Hybrid Flow Battery”, *ACS Energy Lett.* **2017**, *2*, 411-416.

[7] C. Stolze, T. Janoschka, S. Flauder, F. A. Müller, M. D. Hager, U. S. Schubert, “Investigation of Ice-templated Porous Electrodes for Application in Organic Batteries” *ACS Appl. Mater. Interfaces* **2016**, *8*, 23614-23623.

[8] C. Stolze, T. Janoschka, U. S. Schubert, F. A. Müller, S. Flauder, “Directional Solidification with Constant Ice Front Velocity in the Ice-templating Process”, *Adv. Eng. Mater.* **2016**, 18, 111-119.

[9] J. Winsberg, C. Stolze, S. Muench, F. Liedl, M. D. Hager, U. S. Schubert, “TEMPO/phenazine Combi-molecule: A Redox-active Material for Symmetric Aqueous Redox Flow Batteries”, *ACS Energy Lett.* **2016**, *1*, 976-980.

[10] A.M. Schwenke, T. Janoschka, C. Stolze, N. Martin, S. Hoeppener, U. S. Schubert, “Microwave-assisted Preparation of Carbon Nanofiber-functionalized Graphite Felts as Electrodes for Polymer-based Redox Flow Batteries”, *J. Power Sources* **2016**, *335*, 155-161.

[11] D. Schmidt, B. Häupler, C. Stolze, M. D. Hager, U.S. Schubert, “Poly[N-(10-oxo-2-vinylanthracen-9(10H)-ylidene)cyanamide] as a Novel Cathode Material for Li-Organic Batteries”, *J. Polym. Sci., Part A: Polym. Chem.* **2015**, *53*, 2517-2523.

Poster presentations & mini-papers

[1] C. Stolze, J. P. Meurer, M. D. Hager, U. S. Schubert, “A Calibration-free, Temperature-independent, Amperometric State-of-Charge Monitoring Method”, *International Flow Battery Forum 2019*, Lyon (France), July **2019**.

[2] C. Stolze, J. P. Meurer, M. D. Hager, U. S. Schubert, “A Calibration-free, Temperature-independent, Amperometric State-of-charge Monitoring Method”, *The International Flow Battery Forum: Conference Book of Papers* **2019**, 138.

Patents

[1] C. Stolze, C. Schmerbauch, T. Janoschka, U. Martin, N. Martin, U. S. Schubert, M. Maly-Schreiber, “Redox-Flow-Batterie zur Speicherung elektrischer Energie mit radial angeordneten Hohlfasermembranen”, WO2018091042A1, **2017**.

[2] C. Stolze, C. Schmerbauch, T. Janoschka, U. Martin, N. Martin, U. S. Schubert, M. Maly-Schreiber, “Redox-Flow-Batterie zur Speicherung elektrischer Energie mit Hohlfasermembranen”, DE102016122284A1, **2016**.

[3] C. Schmerbauch, C. Stolze, T. Janoschka, U. Martin, N. Martin, U. S. Schubert, “Redox-Flow-Zelle zur Speicherung elektrischer Energie in tubulärer Bauform”, DE 102016122283A1, **2016**.

Non-peer-reviewed research studies

[1] C. Stolze, L. Gollmer, M. D. Hager, U. S. Schubert, J. Liebe, M. Ehrich, B. Jelinek, M. Ammon, L. Fahmy, “Forschungs- und Entwicklungspotenziale der Thüringer Energiespeicherbranche“, **2019**.

[2] C. Stolze, M. D. Hager, U. S. Schubert, “Machbarkeitsstudie: Organische und Polymer-Redox-Flow-Batterie”, **2018**.

Acknowledgements

This work would not have been possible in its current form without the continuous support, advice, and help of several people. First, I wish to express my sincere appreciation to Prof. Ulrich S. Schubert for giving me the opportunity to work in his group on a highly interesting and interdisciplinary research field. Thank you for giving me as a physicist the time to adjust to the different working environment and procedures in the chemical sciences, for providing an excellent research infrastructure, and the tremendous freedom to find and to pursue my own scientific ideas.
Furthermore, I am very grateful to Dr. Martin Hager for all the invaluable background work that helps to keep and to continuously extend this group's research environment. I thank you for the many advices I got from you throughout the years and for always finding a free spot in your tight schedule when I needed to discuss questions concerning this work or the various other tasks.

I also would like to express my gratitude to all my colleagues within the Schubert group who helped me throughout the years. Although I cannot name all here, I particularly appreciate the pioneering work on organic batteries that Dr. Tobias Janoschka, Dr. Bernhard Häupler, Dr. Andreas Wild, Dr. Jan Winsberg, Dr. Christian Friebe, Dr. Daniel Körfer, Dr. Tino Hagemann, Simon Münch, and Christoph Schmerbauch performed for this research group. I wish to express my special gratitude to Dr. Tobias Janoschka for his many advices and kind help especially during the beginning of my PhD time. I am also very thankful for the support by Rene Burges, Maria Strumpf, Hannes Hiller, Sabine Morgenstern, and Kristin Schreyer and for all the effort they have put into the everyday lab work and in keeping our labs organized.

I am thankful to Prof. Dr.-ing. Frank Müller for the interesting cooperation on the investigation of the ice-templating process and the general physics of directional solidification with constant ice-front velocity. With regard to this, I am particularly indebted to Dr. Stefan Flauder for all the interesting discussions and his invaluable practical support during this cooperation. Your devotion to your work and your high scientific standards have been inspiring to me. Furthermore, I am also grateful to PD Dr. Reimar Krieg and Diana Mierzwa for their very kind and selfless support during their introduction into the micro-sectioning of my ice-templated samples.

I would like to pay my special regards to the colleagues from the JenaBatteries GmbH not only for providing me with the electrolyte samples and designing the redox flow battery cells used in a lot of my experiments. I also whole-heartedly appreciate the many fruitful discussions with Dr. Norbert Martin, Carsten Oder, Udo Martin, and Jeanette Stammer and the inspiring time I got to spent with them. Thanks, to all of you!

I deeply value Franca Frister, Sylvia Braunsdorf, Ulrike Kaiser, Doreen Küchler, and Mandy Hendreich for all the administrative work they did in the background and their open ears and help whenever I had an organizational question.

My very personal and deep gratitude goes to my parents, my brother and his wonderful family, and my friends for their unconditional support, acceptance, and the many occasions to find the necessary distraction from this PhD thesis in the time we have spent together. Thank you!

Last but not least, my dear Jonas, I want to thank you. I know the past years have been challenging in many respects for both of us. I am deeply grateful that we managed all this together, for your understanding throughout this time, your perpetual support and your love. Thank you so much!

Declaration of Authorship / Selbstständigkeitserklärung

I certify that the work presented here is, to the best of my knowledge and belief, original and the result of my own investigations, except as acknowledged, and has not been submitted, either in part or whole, for a degree at this or any other university.

(Ich erkläre, dass ich die vorliegende Arbeit selbstständig und unter Verwendung der angegebenen Hilfsmittel, persönlichen Mitteilungen und Quellen angefertigt habe.)

Jena, der 06.08.20

…………………………….
Christian Stolze

Publications P1 to P6

Publication P1

Directional Solidification with Constant Ice Front Velocity in the Ice-Templating Process

C. Stolze, T. Janoschka, U. S. Schubert, F. A. Müller, S. Flauder,
Adv. Eng. Mater. **2016**, *18*, 111-119.

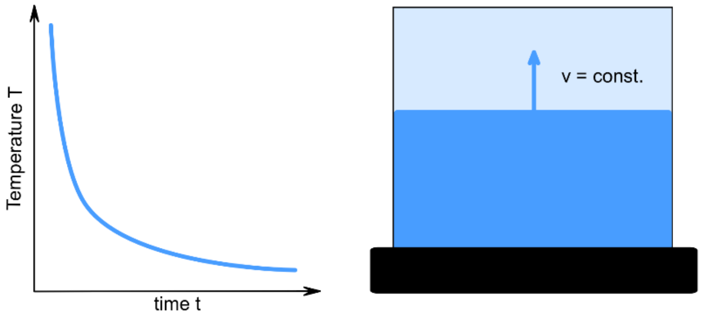

ADVANCED ENGINEERING MATERIALS

DOI: 10.1002/adem.201500235

Directional Solidification with Constant Ice Front Velocity in the Ice-Templating Process**

By *Christian Stolze, Tobias Janoschka, Ulrich S. Schubert,* Frank A. Müller* and *Stefan Flauder*

An exponential cooling function for the directional solidification of liquids with constant ice front velocities is investigated with respect to an enhanced control over the ice-templating process. It is mathematically derived and set into relation to other cooling functions found in literature. A theoretical limit of applicability is discussed and a mathematical expression for the maximum sample size realizable with this new approach is derived. Experimental results from the time-resolved direct measurement of the ice front evolution during the directional solidification of pure water and a ceramic β-tricalcium phosphate (β-TCP) suspension in a cooling room environment are presented. These results are compared to the results of numerical simulations. Ice front velocities from 10 to 50 μm s^{-1} are realized.

1. Introduction

Ice-templating, also referred to as freeze-casting, is a simple method to prepare porous materials with aligned pores. An aqueous suspension and/or solution is cooled from one side in order to initiate a directional solidification. Within the solidification process lamellar ice crystals grow in the opposite direction of the heat flux, rejecting the particles suspended/dissolved in the liquid phase during the phase transition. As a result, particles accumulate between the ice lamellae forming a separate solid phase, which remains as a porous structure after the ice has been removed via a freeze-drying process. This method has been applied to produce various porous materials for biomedical application.[1,2] It is also of particular interest for a variety of other applications like, for example, electrode materials, filters, or membranes.

Although there is a qualitative understanding of the underlying physical processes, a lot of details are not fully understood yet. However, this method holds a variety of options to control the resulting structural sizes, mainly by the composition of the sample liquids and the thermodynamic conditions applied to drive the directional solidification.[1,3–5] The present study focuses on the latter aspect. It has been shown that for ceramic suspensions, the resulting pore dimensions are directly related to the ice front velocity during the solidification.[5–8]

The directional solidification of water is the thermodynamically relevant process for ice-templating and the evolution of the ice front. The latter has been studied long before applications like ice-templating arose. In his original work from 1889, J. Stefan theoretically investigated the formation of ice in the polar oceans. The process was mathematically described by the heat equation on a domain of water cooled from only one side by the atmosphere.[9] With his study, Stefan presented the first mathematical treatment of a simple directional solidification process without convection. Since a phase change occurs in the material domain, this kind of boundary value problem naturally includes a moving boundary, the ice front. As a consequence of this publication, the class of moving boundary value problems is often referred to as *Stefan problems*. Stefan already presented two analytical solutions and showed that they fulfill the Stefan problem.

---

[*] *Prof. U. S. Schubert, C. Stolze, T. Janoschka
Laboratory of Organic and Macromolecular Chemistry (IOMC), Friedrich Schiller University Jena, Humboldtstr. 10, D-07743 Jena, Germany
C. Stolze, T. Janoschka, Prof. U. S. Schubert
Center for Energy and Environmental Chemistry Jena (CEEC Jena), Friedrich Schiller University Jena Philosophenweg 7a, D-07743 Jena, Germany
E-mail: ulrich.schubert@uni-jena.de
Prof. F. A. Müller, S. Flauder
Otto-Schott-Institute of Materials Research, Friedrich Schiller University Jena, Löbdergraben 32, D-07743 Jena, Germany*

[**] *The authors wish to thank the European Social Fund (ESF), the Thüringer Aufbaubank (TAB), the Thüringer Ministeriumfür Wirtschaft, Wissenschaft und digitale Gesellschaft (TMWWdG), and the European Commission (SMILEY project under contract no. FP7-NMP-2012-SMALL-6-310637) for the financial support.*

The paper was amended 9 October 2015 after initial publication: wrong author titles were removed and formula 2c was updated. Also Supporting Information was supplied.

However, he did not provide a strict derivation for them. They represented two cases of directional solidification: (1) the ice front position develops proportional to the square root of time, if a constant temperature is applied as cooling function and (2) the ice front position evolves proportional to time, i.e., with a constant ice front velocity, if an exponential cooling function is applied.

Intense investigations in order to control and understand directional solidification of water were conducted with respect to cryobiology. Rubinsky et al. developed numerical procedures to calculate the ice front evolution for Stefan problems describing directional solidification of water with different cooling functions applied to one boundary.[10,11] Using those methods, the authors presented a numerically motivated approximation for a linear cooling function to induce a directional solidification with constant ice front velocity.[12] Waschkies et al. derived an analytical formula as a quasi-stationary (approximate) solution to a Stefan problem, which allows to calculate a linear cooling function from the material parameters of the solid phase and a desired constant velocity of directional solidification. By doing so, they implicitly gave an analytical derivation for the results obtained by Rubinsky et al. before.[8]

Recently, Flauder et al. presented a study utilizing the exponential cooling function given by Stefan in ice-templating processes and showed that the application of this cooling function leads to homogeneous pore sizes throughout the whole sample height of frozen ceramic suspensions.[13,14] The present study focuses on the theoretical derivation, investigation, and discussion of this analytical cooling function.

2. Theory

The physics of directional solidification can be mathematically formulated as a Stefan problem. For this purpose, it has to be considered that there are two phases, a liquid and a solid one, for which the heat equation

$$\frac{\partial T(\vec{r},t)}{\partial t} = \Delta(k\,T(\vec{r},t)), \tag{1}$$

has to be solved. Here, $T(\vec{r},t)$ is the temperature distribution and k is the thermal diffusivity defined by $k = \lambda/\rho c$ with the thermal conductivity, λ, the density, ρ, and the specific heat capacity, c, of the domain material. The present study is focused on the one-dimensional case, which allows an analytical treatment. The one-dimensional Stefan problem for the directional solidification can be mathematically formulated as follows:

$$\begin{aligned} &\frac{\partial T_s(z,t)}{\partial t} = k_s \frac{\partial^2 T_s(z,t)}{\partial z^2}\ \forall z \leq s(t) \quad \text{and} \\ &\frac{\partial T_l(z,t)}{\partial t} = k_l \frac{\partial^2 T_l(z,t)}{\partial z^2}\ \forall z \geq s(t) \end{aligned} \tag{1a}$$

$$T_s(0,t) = f(t), \tag{1b}$$

$$\left.\frac{\partial T_l(z,t)}{\partial z}\right|_{z=L} = 0, \tag{1c}$$

$$T_s(s(t),t) = T_l(s(t),t) = T_0, \tag{1d}$$

$$\lambda_s \left.\frac{\partial T_s(z,t)}{\partial z}\right|_{z=s(t)} - \lambda_l \left.\frac{\partial T_l(z,t)}{\partial z}\right|_{z=s(t)} = h_f \rho_s \frac{ds(t)}{dt}, \tag{1e}$$

$$T_l(z,0) = T_p, \tag{1f}$$

$$s(0) = 0. \tag{1g}$$

Equations 1b–g are the boundary and initial conditions under which the heat Equation 1a have to be solved. The indices l and s denote the parameters and variables in the liquid (l) and solid (s) phase, $s(t)$ is the position of the ice front (i.e., the boundary between the liquid and solid phase) at time t, $f(t)$ the time-dependent temperature at the cooled boundary and L denotes the height of the frozen sample. T_0 is the liquidus temperature of the liquid, T_p the initial temperature of the liquid and h_f is the specific latent heat of solidification. While Equations 1b–e are the spatial boundary conditions, Equations 1f–g represent the initial conditions. The latter express that initially no solid phase is present and that the liquid phase has the constant temperature T_p. Equation 1b represents the fact that the temperature is controlled at the boundary $z = 0$ and follows the time-dependent temperature function $f(t)$, while Equation 1c expresses a thermal insulation on the other system boundary $z = L$. Finally, Equations 1d and e describe the conditions at the moving phase boundary. Since the transition from liquid to solid phase takes place at this boundary, its temperature is at the liquids temperature T_0. Equation 1e is the so-called *Stefan condition*, which describes the heat flux across the phase boundary taking into account the latent heat released per infinitesimal time step dt. The formulation of this Stefan problem in one dimension is justified for liquids whose solidification takes place with a planar ice front and in the case that the material parameters can be treated as scalar constants. Due to the one-dimensionality of this problem, all effects taking place at boundaries parallel to the direction of solidification are neglected.

Further simplification of the mathematical treatment can be achieved if the temperature of the liquid phase is assumed to be $T_l(z,t) = T_0$ throughout the whole process. As a consequence, only the heat equation for the solid phase has to be solved and the simplified Stefan problem describing an evolution of a planar ice front can be written as

$$\frac{\partial T_s(z,t)}{\partial t} = k_s \frac{\partial^2 T_s(z,t)}{\partial z^2}\ \forall z \leq s(t), \quad \forall t \in \mathbb{R} \tag{2a}$$

$$T_s(0,t) = f(t), \tag{2b}$$

$$\left.\frac{\partial T_s(z,t)}{\partial z}\right|_{z=L} = 0, \tag{2c}$$

$$T_s(s(t),t) = T_0, \tag{2d}$$

$$\lambda_s \frac{\partial T_s(z,t)}{\partial z}\bigg|_{z=s(t)} = h_f \rho_s \frac{ds(t)}{dt} = h_f \rho_s v_f, \tag{2e}$$

$$s(0) = 0. \tag{2f}$$

Since processes with constant ice front velocity $ds/dt = v_f =$ const. are the ones of special interest for ice-templating, the function pair ($T_s(z,t)$; $f(t)$) is referred to as the solution of this moving boundary value problem. This solution is the answer to the question, what temperature $f(t)$ has to be applied to the cooled boundary of the sample liquid in order to achieve a directional solidification with constant ice front velocity v_f. Since $f(t)$ is the unknown function and not $s(t)$, an inverse Stefan problem is treated here. Analytically, it can be solved with a power series expansion (Taylor series) around (z_0,t_0),

$$T(z,t) = \sum\nolimits_{m=0}^{\infty} \sum\nolimits_{n=0}^{\infty} a_{m,n} (z - z_0)^m (t - t_0)^n. \tag{3}$$

Using this approach, (z_0,t_0) is reasonably chosen to be (0,0) since the function of interest is the cooling function $f(t) = T_s(0,t)$. The further mathematical treatment to determine the coefficients a_{mn} and, thus, to solve this Stefan problem is quite extensive, but straightforward. The main steps for the derivation of the solution are documented in the supplementary part of this publication. The solution is an exponential function which represents the temperature distribution in the solid phase at time t as follows:

$$T_s(z,t) = T_0 + \frac{h_f}{c_s}\left[1 - \exp\left(\frac{v_f^2}{k_s} t - \frac{v_f}{k_s} z\right)\right]. \tag{4}$$

At $z = 0$, the solution is identical to the cooling function $f(t)$ according to Equation 2b, which results in

$$f(t) = T_0 + \frac{h_f}{c_s}\left[1 - \exp\left(\frac{v_f^2}{k_s} t\right)\right]. \tag{5}$$

Equations 4 and 5 represent the unique solution to the presented moving boundary value problem with constant ice front velocity. It was shown by Alifanov that a solution to an inverse Stefan problem is unique, if it exists.[15] Therefore, the derived cooling function, Equation 5, is theoretically the only cooling function available to achieve a directional solidification with constant ice front velocity under the assumed conditions.

3. Materials and Methods

3.1. Materials

Directional solidification experiments have been conducted using deionized water. A small amount of about 1 mg Al_2O_3 particles (diameter: 280 nm, Ceralox High Purity Alumina APA-0.5, Sasol North America, Inc., USA) was added to support heterogeneous crystal nucleation during the initial phase of solidification. Additionally, an aqueous suspension was prepared from 20 vol% phase-pure β-tricalcium phosphate (β-TCP) powder and a solution of poly(vinyl alcohol)-binder (1 wt% dry powder mass, $M_n = 22{,}000\ \mathrm{g\ mol^{-1}}$, ≥98%; VWR), anionic polyelectrolyte dispersant polyacrylic acid (1 wt% of dry powder mass, $M_n = 56{,}220\ \mathrm{g\ mol^{-1}}$; Dolapix PC 21, Zschimmer und Schwarz, Germany) and sodium pyrophosphate decahydrate (2 mg in 1 g of water) in deionized and degassed water as described in ref.[14] The β-TCP particles have been obtained by synthesizing a phase-pure β-TCP powder, which was wet-milled resulting in irregular-shaped particles with an average Feret diameter of 0.3 μm and a BET surface of 8 $\mathrm{m^2\ g^{-1}}$.[14]

3.2. Directional Solidification

Basically, the same experimental setup was used as described in detail by Flauder et al.[13,14] This setup enables the control of temperature at the bottom of a sample liquid and, hence, the application of the theoretical cooling function derived above. Some non-negligible adjustments had to be made to this setup, however, in order to measure the ice front evolution over time throughout the whole process. Instead of a cylindrical PTFE mold, a transparent cuboid mold with an attached scale with millimeter resolution was used as a sample vessel for the liquid. The mold was left open at the top and four miniature thermocouples (type T, TC Mess- und Regeltechnik, Germany) were introduced into the mold at distances of about 5 mm to each other (Figure 1). Temperatures were measured with a four channel temperature data logger (YC-747UD, YCT, China). In contrast to the preceding experiments of Flauder et al., the mold was not thermally insulated from the environment with a vacuum chamber in order to be able to measure the ice front evolution visually. However, to keep the influence of heat exchange between environment and sample as small as possible, the experiments were conducted in a cooling room with an environmental

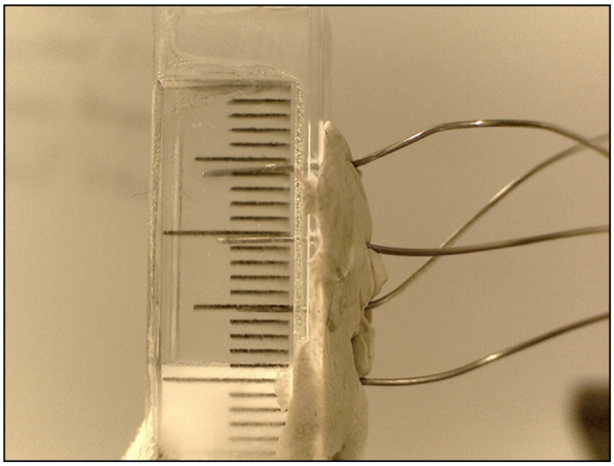

Fig. 1. Sample mold containing partly frozen sample liquid during directional solidification. A defined ice front can be identified. A millimeter scale is attached for the time-resolved observation of the ice front position and four temperature sensors reach into the sample liquid to measure the temperature distribution inside the sample.

temperature of 5 °C. The ice front evolution of water samples was measured at onset velocities of 10, 25, and 50 $\mu m\,s^{-1}$, respectively. For the β-TCP suspension, a velocity of 20 $\mu m\,s^{-1}$ was chosen. A USB digital microscope (PCE-MM200, PCE instruments, China) and a laptop were used for the measurement of the ice front evolution with photos taken every 5 s for a velocity of 50 $\mu m\,s^{-1}$and every 10 s for all other ice front velocities, respectively. The ice front position over time was then evaluated from the photos using the computer software Axio Vision LE 4.8 achieving a resolution of 0.1 mm in the measured ice front position. Water samples and the suspension were subjected to a controlled temperature evolution at their bottom according to the theoretical cooling function, Equation 5. This was calculated using the material parameters shown in Table 1. In order to take into account the composition of the suspension and the formation of domains of pure ice and concentrated particles with different thermal properties during the ice-templating process, averaged values of the parameters were calculated. These calculations incorporate the composition of the suspension, as well as the composition and geometric form of the different phases in the frozen suspension.[14] Additionally, one measurement was undertaken with water using a linear cooling function with a slope of 0.1 $K\,s^{-1}$. This was done in order to compare the ice front evolution using the exponential cooling function presented in this study with the linear cooling function derived by Waschkies et al.[8]

Since the modifications of the setup described above represent a deviation from the conditions formulated by the analytically solved Stefan problem, slight deviations from the theoretically calculated ice front evolution can be expected. Therefore, a numerical model was developed describing a Stefan problem which takes into account effects neglected by the analytical model.

3.3. Numerical Analysis

The numerical analysis was performed with the following more complex Stefan problem:

$$\frac{\partial T_s(z,t)}{\partial t} = k_s \frac{\partial^2 T_s(z,t)}{\partial z^2}\ \forall z \leq s(t) \quad \text{and} \\ \frac{\partial T_l(z,t)}{\partial t} = k_l \frac{\partial^2 T_l(z,t)}{\partial z^2}\ \forall z \geq s(t), \tag{6a}$$

$$T_s(0,t) = f(t), \tag{6b}$$

$$T_s(s(t),t) = T_l(s(t),t) = \vartheta_0(T_s(s(t),t)), \tag{6c}$$

$$\left.\frac{\partial T_l(z,t)}{\partial z}\right|_{z=L} = \alpha(T_l(L,\,t) - T_e), \tag{6d}$$

$$\lambda_s \left.\frac{\partial T_s(z,t)}{\partial z}\right|_{z=s(t)} - \lambda_l \left.\frac{\partial T_l(z,t)}{\partial z}\right|_{z=s(t)} = h_f \rho_s \frac{ds(t)}{dt}, \tag{6e}$$

$$T_l(z,\,0) = T_p,\ s(0) \leq z \leq L, \tag{6f}$$

$$s(0) = 0. \tag{6g}$$

Here, T_p is the initial temperature of the liquid, T_e is the constant environmental temperature and α is the assumed heat transfer coefficient between the sample liquid and the surrounding air. The value of α is approximated as $\alpha = 10\,W\,(m^2 K)^{-1}$ for a water/air interface with a temperature difference of 1–10 K in still air.[16]

$\vartheta_0(T_s(s(t),t))$ represents the freezing temperature as a function of the current ice front temperature, which models the temperature at the ice front. It takes into account that the necessary temperature for sufficient ice crystal nucleation may be below the liquid's standard freezing temperature. Consequently, the liquid near the cooling finger might be supercooled at the beginning of the process allowing the formation of thermodynamically stable ice crystal nuclei. At that point, a rapid growth of crystal nuclei and, thus, solidification arises. Subsequently, the temperature at the ice front increases quickly until it reaches the liquids standard freezing temperature T_0, which is sufficient to drive the further crystal growth. Hence, for $\vartheta_0(T_s(s(t),t))$ a step function is chosen that is smoothed over a time range of 25 s. Apart from that the boundary value problem takes into account the heat conduction in the liquid phase and heat exchange with the environment.

This moving boundary value problem is solved on an interval of length L, which is divided into two subdomains at the point of the moving ice front. For the computational work, COMSOL Multiphysics 4.4 with the Heat Transfer, ODE, and Deformed Geometry modules was used with the standard solver settings. The mesh consisted of 200 elements with 100 on each subdomain.

4. Results and Discussion

4.1. Evolution of Ice Front and Temperature Distribution with Preset Cooling Functions

Figure 2 shows the temperature evolution in a pure water sample measured at five different positions and the ice front

Table 1. Material parameters of the solid phase used to calculate the theoretical cooling function for the experiments.

Sample	λ_s [$W\,K^{-1}\,m^{-1}$]	h_f [$kJ\,K^{-1}$]	c_s [$kJ\,kg^{-1}\,K^{-1}$]	ϱ_s [$kg\,m^{-3}$]	v_f [$\mu m\,s^{-1}$]
Water	2.2	333.4	2.04	920	10, 25, 50
Suspension	1.898	188.71	1.447	1321	20

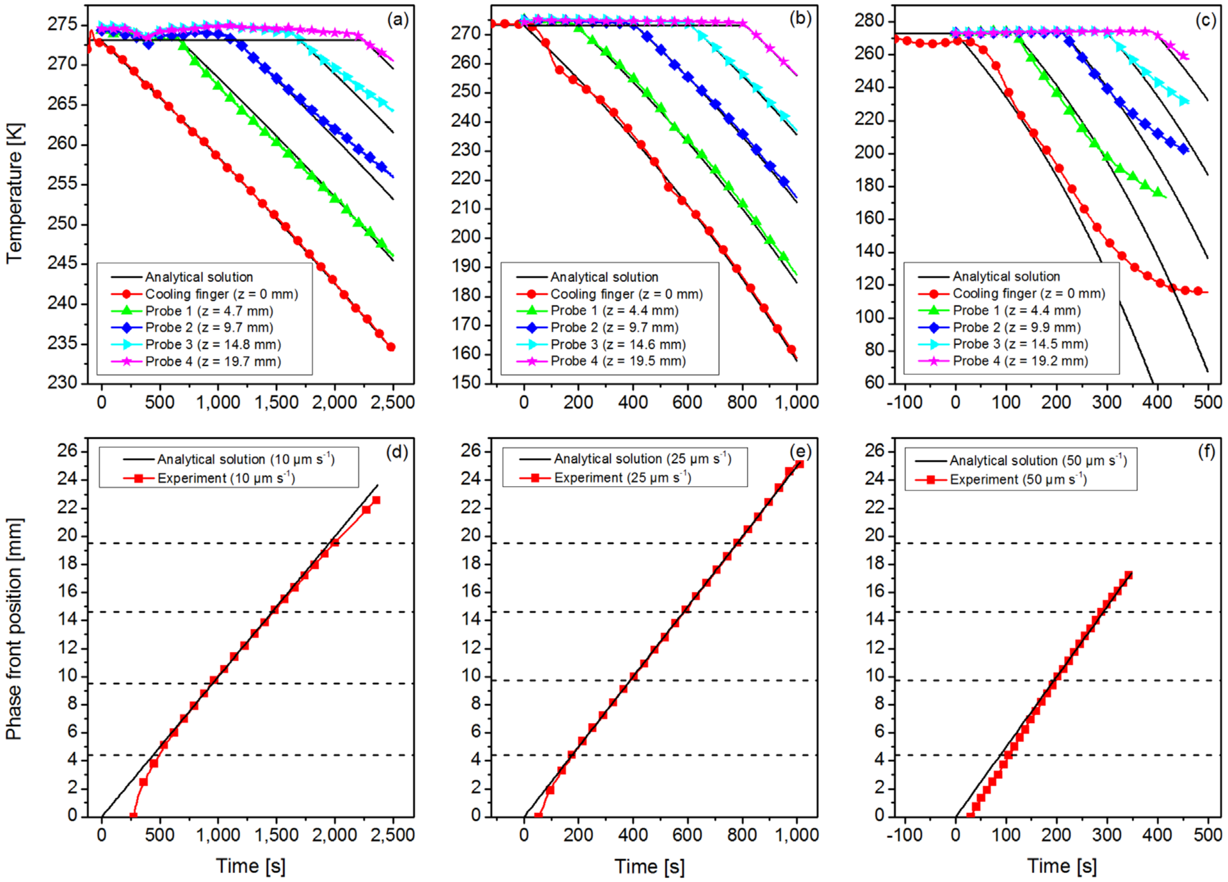

Fig. 2. Temperature evolution in the sample and at the cooling finger for $v_f = 10\,\mu m\,s^{-1}$ (a), $25\,\mu m\,s^{-1}$ (b), and $50\,\mu m\,s^{-1}$ (c), as well as experimental and theoretical ice front evolution for the same velocities (d–f). Dotted lines in the lower graphs mark the positions of the temperature probes.

evolution over time for preset cooling functions calculated from Equation 5 for ice front velocities, v_f, of 10, 25, and $50\,\mu m\,s^{-1}$ compared to the analytical solution. While the theoretical cooling function could be realized for the two lower velocities, it was technically difficult to achieve the same degree of matching for the $50\,\mu m\,s^{-1}$ sample due to the necessary high cooling rates particularly in the lower temperature range. Regarding the temperature evolution inside the sample, the theoretically expected and the experimentally observed evolution were in good agreement for the $25\,\mu m\,s^{-1}$ sample. However, for the $10\,\mu m\,s^{-1}$ sample more remarkable deviations have been measured, which are highest for the temperature probe close to the liquid–air-interface.

Looking at Figure 2d–f, the measured ice front evolution over time is in good agreement with the theoretical expectation over the major time range. Deviations from the theoretically expected, linear evolution are observed for the $10\,\mu m\,s^{-1}$ sample only at the beginning and the end of the process. The $25\,\mu m\,s^{-1}$ sample is in very good agreement with the theory, except for a remarkable deviation during the first 100 s and minor deviations at the end of the process, where the velocity tends to increase. Due to the larger deviations of the experimentally realized cooling function toward the end of the process for the $50\,\mu m\,s^{-1}$ sample, higher deviations have been expected and observed regarding the ice front evolution. However, even for this sample an acceptable agreement between the theoretical and experimental ice front evolution was observed. This can be explained by the fact that in the necessary time frame of 300 s, the cooling function was sufficiently realized and the stronger deviations occurred only after 300 s.

4.2. Numerical Simulation and Discussion of Observed Experimental Deviations

Although strict measures were taken to keep the external influences to a minimum, not all conditions, on which the analytical solution is based, were strictly met during the experiment. Therefore, the observed deviations may be due to a combination of the following reasons: (1) missing thermal insulation from the environment and, hence, heat transfer from the environment to the system, (2) liquid initially not at its freezing temperature T_0, (3) supercooling of the liquid at the beginning of the process (necessary nucleation temperature lower than later crystal growth temperature), and (4) heat transport by convection in the liquid.

Using the computational model presented in Section 3.3, the Stefan problem for the investigated system was modified in order to include some of the aforementioned experimental conditions, namely conditions (1)–(3), and to study their effects on the theoretical ice front evolution. The model was computed using the experimentally realized cooling functions $f(t)$ for each velocity as input, while the ice front evolution was calculated as solution of the boundary value problem. Figure 3 illustrates the ice front evolution according to the numerical solution compared to the experimental measurements and the analytical solution for each of the three ice front velocities. The simulation and experiment have proven to be in good agreement. The numerical calculations have shown that the accelerated ice front evolution over the first few millimeters can be explained by assuming supercooling of the liquid at the beginning of the process to up to 7 K below the standard freezing temperature of 273.15 K. This delays the initiation of the solidification until a specific temperature is reached at which thermodynamically stable and growing crystallization nuclei are generated leading to a spontaneous and fast solidification of the whole supercooled area. This finding helps to understand the structure formation in the initial layer of porous samples produced by ice-templating processes utilizing directional solidification. In these layers, smaller structures than in the rest of the samples are commonly reported and mostly attributed to higher ice front velocities.[17,18–20] Lasalleet al. already performed experimental investigations on the supercooling effect and suggested it to be the main cause for the initial layer of ice-templated samples, which is termed transitional zone. So far, this is in agreement with the results presented here. However, the authors also reported supercooling of up to 22 K (pure distilled water).[20] The results of the numerical calculations presented here gave an excellent correspondence to the experimentally measured ice front evolution when assuming supercooling temperatures of up to 7 K.

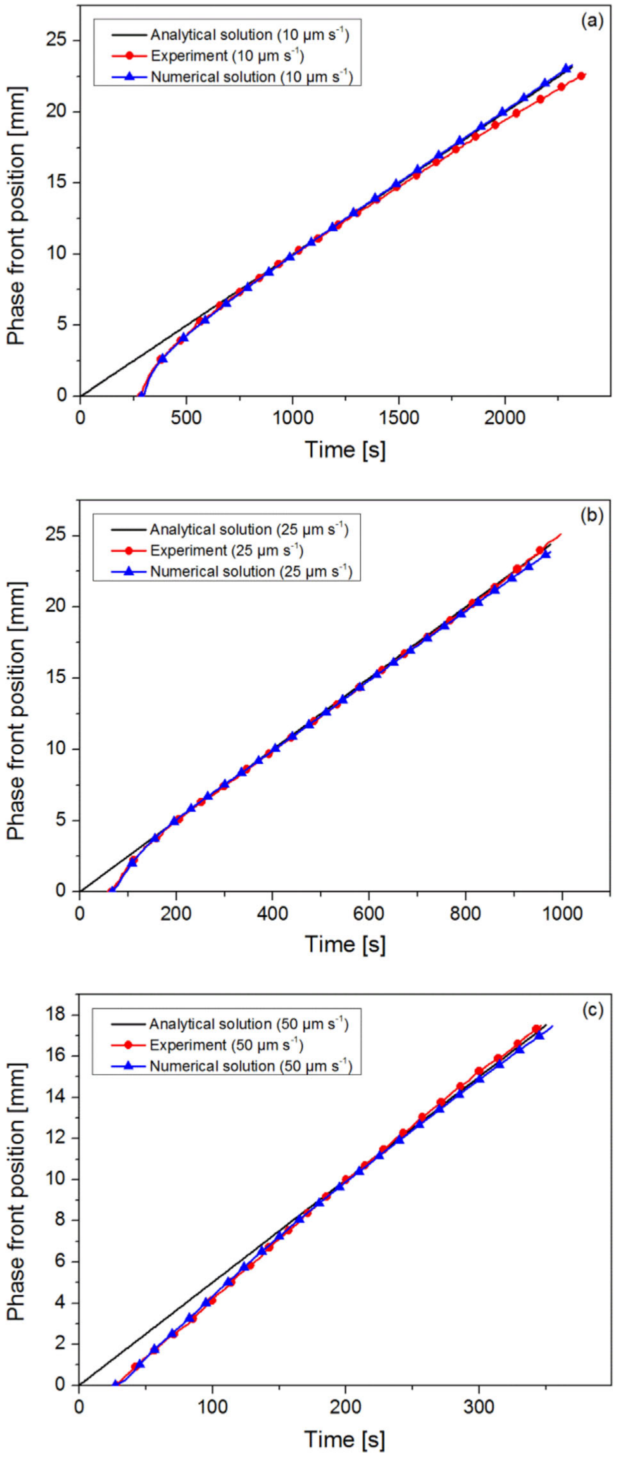

Fig. 3. Comparison of analytically and numerically calculated with the experimentally measured ice front evolution for $v_f = 10\,\mu m\,s^{-1}$ *(a),* $25\,\mu m\,s^{-1}$ *(b), and* $50\,\mu m\,s^{-1}$ *(c).*

Parameter variations in the simulations indicate that for the $10\,\mu m\,s^{-1}$samples, the tendency of the decreasing ice front velocity at the end of the process can be qualitatively reproduced by the numerical model for artificially increased heat transfer from the environment to the liquid across the liquid–air interface. This means that the heat transfer coefficient at the water/air interface was artificially increased. The heat transfer into the system has a higher influence the slower the solidification takes place. That is why the decrease is observed for the $10\,\mu m\,s^{-1}$ only. It has to be taken into account that heat exchange occurred across all system boundaries of the sample vessel, which could not be included in a one-dimensional model that only considers the upper liquid–air-boundary. A two-dimensional model would be required for this purpose. In other words, the one-dimensional model neglects all system boundaries parallel to the direction of solidification.

Deviations at the beginning, which were shown to be due to a period of time during which the liquid is supercooled for up to 7 K, are hard to be circumvented. However, efforts to support the formation of crystallization germs should weaken this effect. For example, the effect of a roughened cooling finger surface on the initial supercooling could be investigated. The aforementioned results obtained by Lasalle et al. suggest that the supercooling temperatures can be influenced by adding different dispersants to the liquid.[20] For suspension based systems also the modification of particle sizes might have an impact on the degree of supercooling.[21]

4.3. Relevance for Ice-Templating of Porous Samples

So far, the results presented in this work rely on the directional solidification of water. This pure liquid generally solidifies with a planar ice front, which is in accordance with the theoretical assumptions of the presented Stefan problem. With respect to the application of the analytical cooling function in ice-templating processes with, e.g., ceramic suspensions, there is no such planar ice front. Instead, the planar ice front is perturbed and grows in form of parallel-aligned lamellae, which reject the particles formerly suspended resulting in a layered structure of ice and particles, which are accumulated between the lamellae. However, it is reasonable to assume that each lamella grows at the same velocity like its neighbor in a homogenous suspension. Hence, the envelope of the lamella tips represents a line equivalent to a planar ice front, as illustrated in Figure 4. It was recently shown that the application of the presented analytical cooling function in an ice-templating process leads to homogeneous pore structures throughout the whole sample height of ice-templated β-TCP suspensions.[14] While these results can be understood as an indirect proof for an ice front evolution with constant ice front velocity, a direct measurement of the ice front evolution in such suspensions is missing up to now. Therefore, the same experimental procedure used to measure the ice front evolution for the water samples was applied to a β-TCP suspension for a theoretical ice front evolution with $v_f = 20\,\mu\mathrm{m\,s^{-1}}$. The measured ice front evolution is presented in Figure 5. A linear regression was performed on the experimental data, which confirmed the expectation of a constant ice front velocity during the solidification. The slope of the linear curve fit and, hence, the ice front velocity was $18.2 \pm 0.1\,\mu\mathrm{m\,s^{-1}}$. This value is close to the theoretically expected velocity of $20\,\mu\mathrm{m\,s^{-1}}$ set by the chosen cooling function. The deviation of about $2\,\mu\mathrm{m\,s^{-1}}$ is partly due to the aforementioned experimental conditions. However, the linear regression was performed taking into account all measured data points. Just like it was observed for the water samples, the last data points deviate from a linear behavior due to missing thermal insulation. If a linear regression is performed only on the data points up to 12 mm ice front position and, thus, in the linear regime of the ice front evolution, an ice front velocity of $18.9 \pm 0.1\,\mu\mathrm{m\,s^{-1}}$ is obtained.

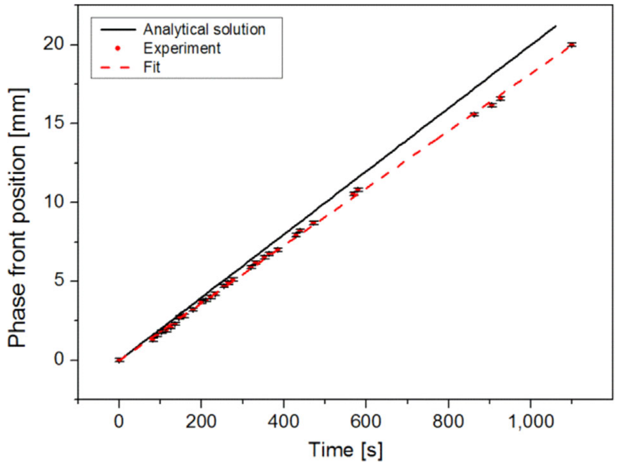

Fig. 5. Ice front evolution of a β-TCP suspension subjected to a directional solidification with a theoretical ice front velocity of $v_f = 20\,\mu m\,s^{-1}$. The experiment is compared to the analytical solution and a linear regression was performed, revealing a slope of $18.2 \pm 0.1\,\mu m\,s^{-1}$.

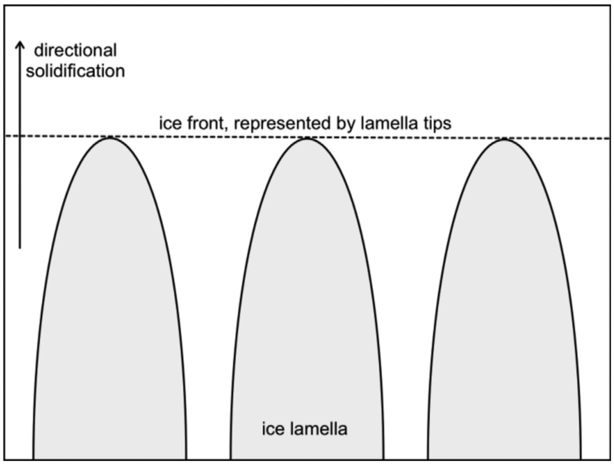

Fig. 4. Schematic illustration of the ice front during an ice-templating process, where the envelope of the lamella tip positions approximately gives a line representing the overall ice front position of the process.

The fact that the cooling function used in this experiment relies on the material constants of the frozen suspension (thermal diffusivity, heat capacity, specific latent heat) represents another source of deviations. These parameters have been calculated from the parameters known for pure tricalcium phosphate and pure ice at 273 K and, thus, are only an approximation for the real parameters of the solidified suspension.[14] Furthermore, the model does not take into account the potential accumulation of particles ahead of the ice front and any particle-related effects like, for example, the influence of particle concentration on the freezing temperature of the suspension, which might cause a change in freezing temperature throughout the process under certain circumstances.

Despite the slight deviations observed, the experiment confirms the applicability of the analytical cooling function for ice-templating of aqueous β-TCP suspensions with constant ice front velocity. Since the theoretical model relies on the macroscopic thermal material properties of the suspension only, it is reasonable to assume that the results can be applied to an extensive range of different suspensions and solutions.

4.4. Physical Limitations of the Process

The solution of the inverse Stefan problem, Equation 5, attains negative absolute temperatures after a certain time, which depends on the material parameters and the ice front velocities. Since negative absolute temperatures are physically impossible, the cooling function is physically limited to $f = 0\,\mathrm{K}$ and the directional solidification will not proceed with a constant ice front velocity, as soon as this natural temperature limit is reached. However, the experimental effort which has to be made in order to reach temperatures close to 0 K is by far too complex for this kind of process and, thus, the ice front velocity will change much earlier depending on the lowest temperature a particular experimental setup is able to reach. A further limiting factor is that the experimental setup has to provide an appropriate heat flux to reproduce the temperature profile of Equation 5. The minimum temperature that can be reached under this condition will be denoted as $f_{\min}$ and the time necessary to reach this temperature will be referred to as τ. It may be pointed out, that providing the appropriate heat flux experimentally is the most challenging task for reaching higher ice front velocities. However, assuming that these conditions are met, the value of τ can be calculated by

$$f_{\min} = f(\tau) = T_0 + \frac{h_f}{c_s}[1 - \exp\left(\frac{v_f^2}{k_s}\tau\right)], \tag{7}$$

which results in

$$\tau = \frac{k_s}{v_f^2}\ln(1 - \frac{c_s}{h_f}[f_{\min} - \mathrm{T}_0]). \tag{8}$$

Furthermore, the time τ corresponds to a thickness $L_{\max} = s(\tau) = v_f\tau$ of the solid phase that has been formed with constant ice front velocity, v_f, during this time interval. This consequently leads to the equation for the maximum sample thickness, which can be produced under constant ice front velocity conditions

$$L_{\max} = v_f\tau = \frac{k_s}{v_f}\ln(1 - \frac{c_s}{h_f}[f_{\min} - \mathrm{T}_0]). \tag{9}$$

For a specific material composition, Equation 9 states that the maximum size of a sample produced by directional solidification with constant ice front velocity is inversely proportional to the ice front velocity v_f. With respect to ice-templating, this equation enables to predict the maximum height of a sample with a homogeneous pore diameter across the sample height. Using the physical parameters for the β-TCP suspension (Table 1) and the theoretical temperature limit $f_{\min} = 77\,\mathrm{K}$ of the experimental setup used in this work, the maximum sample height for $v_f = 20\,\mu\mathrm{m\,s^{-1}}$ is 45.6 mm. In comparison, the maximum height for pure water is 94.1 mm at $v_f = 10\,\mu\mathrm{m\,s^{-1}}$ and 18.8 mm at $v_f = 50\,\mu\mathrm{m\,s^{-1}}$.

4.5. Thermal Contact Resistance and Quasi-Stationary Approximation

Equation 5 was derived by neglecting the thermal contact resistance between the solidified phase and the cooling finger. To take this effect into account, the heat flux is evaluated at the interface $z = 0$ by using Fourier's law and the equation for heat transfer at interfaces,[22]

$$\frac{dq}{dt} = -\lambda_s \left.\frac{\partial T_s}{\partial z}\right|_{z=0} = -\alpha_s(T_s(0,t) - g(t)) = -\alpha_s(f(t) - g(t)). \tag{10}$$

In this equation, λ_s denotes the thermal conductivity of the solid and α_s the thermal contact conductivity (the reciprocal of the thermal contact resistance) between the solid phase and the cooling finger, while $f(t)$ and $g(t)$ are the temperature of the solid at $z = 0$ and the temperature of the cooling finger surface, respectively. Hence, the boundary condition Equation 2b can be rewritten as

$$T_S(0,t) = f(t) = \frac{\lambda_s}{\alpha_s}\left.\frac{\partial T_s}{\partial z}\right|_{z=0} + g(t). \tag{11}$$

For vanishing thermal contact resistance, i.e., $\alpha_s^{-1} \cong 0$, Equation 10 simplifies to the initial approximation $f(t) = g(t)$. Using Equation 4 results in

$$\left.\frac{\partial T_s}{\partial z}\right|_{z=0} = \frac{h_f}{c_s}\frac{v_f}{k_s}\exp\left(\frac{v_f^2}{k_s}t\right). \tag{12}$$

Finally, Equations 5 and 12 can be inserted into Equation 11 which leads to the temperature $g(t)$ that needs to be applied in order to guarantee the temperature $f(t)$ at the bottom of the solid phase,

$$\begin{aligned} g(t) &= f(t) - \frac{\lambda_s}{\alpha_s}\left.\frac{\partial T_s}{\partial z}\right|_{z=0} \\ &= T_0 + \frac{h_f}{c_s}(1 - \exp\left(\frac{v_f^2}{k_s}t\right) - \frac{\lambda_s}{\alpha_s}\frac{v_f}{k_s}\exp\left(\frac{v_f^2}{k_s}t\right). \end{aligned} \tag{13}$$

Waschkies et al. published a quasi-stationary solution to the Stefan problem represented by Equations 2a–f.[8] This quasi-stationary solution applies for cases where the phase-transition number,

$$\mathrm{Ph} = \frac{h_f}{c_s(T_0 - g(t))}, \tag{14}$$

i.e., the ratio between the latent heat and the difference in inner energy of the solid phase at temperatures T_0 and $g(t)$, is higher than 7. The latter is valid for arbitrarily low $g(t)$ only, if c_s is sufficiently small. In other words, the solution by Waschkies et al. is a good approximation only for vanishing specific heat capacity, $c_s \to 0$.

Since $g(t)$ is the unique and exact solution to the boundary value problem (with contact resistance), the quasi-stationary approximation can be derived from it as follows: using the definition of the thermal diffusivity $k_s = \lambda_s/\rho_s c_s$ and the Taylor-series expression of the exponential function around $c_s = 0$, the cooling function $g(t)$ can be written as

$$\begin{aligned} g(t) &= T_0 + \frac{h_f}{c_s} - \frac{h_f}{c_s}\left(1 + \frac{v_f\rho_s c_s}{\alpha_s}\right)\sum\nolimits_{n=0}^{\infty}\frac{1}{n!}\left(\frac{v_f^2\rho_s t}{\lambda_s}c_s\right)^n \\ g(t) &= T_0 + \frac{h_f}{c_s} - \frac{h_f}{c_s}\sum\nolimits_{n=0}^{\infty}\frac{1}{n!}\left(\frac{v_f^{2n}\rho_s^n t^n}{\lambda_s^n}c_s^n + \frac{v_f^{2n+1}\rho_s^{n+1}t^n}{\alpha_s\lambda_s^n}c_s^{n+1}\right) \\ g(t) &= T_0 - h_f\rho_s\frac{v_f}{\alpha_s} - \sum\nolimits_{n=1}^{\infty}\frac{1}{n!}\left(h_f\frac{v_f^{2n}\rho_s^n t^n}{\lambda_s^n}c_s^{n-1} + \frac{v_f^{2n+1}\rho_s^{n+1}t^n}{\alpha_s\lambda_s^n}c_s^n\right). \end{aligned} \tag{15}$$

For $c_s \rightarrow 0$ all terms with $n > 1$ vanish and $g(t)$ simplifies to

$$g(t) \approx T_0 - h_f\rho_s\left(\frac{v_f}{\alpha_s}+\frac{v_f^2}{\lambda_s}t\right) = g_{qs}(t), \qquad (16)$$

which is the cooling function for the quasi-stationary case, $g_{qs}(t)$, as derived by Waschkies et al. earlier. Figure 6 illustrates the relative difference Δg between the exact analytical cooling function g and the quasi-stationary cooling function g_{qs},

$$\Delta g = \frac{|g - g_{qs}|}{g}, \qquad (17)$$

over the sample height, s, and the normalized sample height, respectively, for the directional solidification of water with the ice front velocities $v_f = 10$, 25, and 50 µm s^{-1}, respectively. It is evident that for increasing ice front velocities, the relative difference increases with respect to the sample height. Further investigation of the relative difference $\Delta g(t)$ reveals that it grows above 5% for water samples larger than 59% of $L_{\max}$, where $L_{\max}$ is calculated according to Equation 9 using $f_{\min} = 77$ K (theoretical temperature limit of the experimental setup). The error value of 5% was chosen as a marking point, since it corresponds to a noticeable deviation and the relative difference rapidly increases from there until it ends up at about 25%.

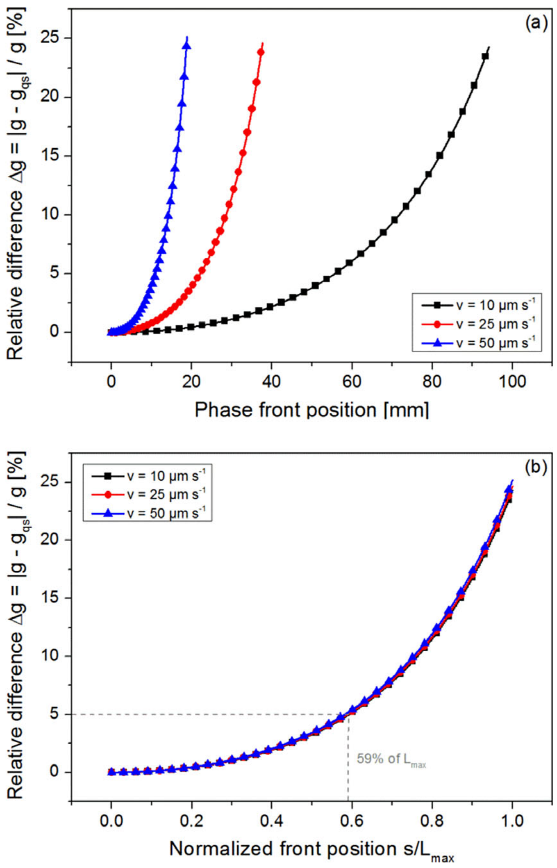

Fig. 6. Relative difference between exact and quasi-stationary cooling function over (a) the sample height and (b) the sample height normalized to L_{max} for $v_f = 10$, 25, and 50 µm s^{-1}.

Furthermore, Figure 7 illustrates the experimental ice front evolution of two water samples. The first was solidified using the exponential cooling function with $v_f = 25$ µm s^{-1}. The second represents the data for a sample solidified using a linear cooling function with a slope of 0.1 K s^{-1}, which corresponds to an ice front velocity of $v_f \cong 27$ µm s^{-1} according to the quasi-stationary solution, Equation 16. For increasing time, t, the ice front velocity for the sample frozen with the linear cooling function falls below the velocity of the sample solidified using the exponential cooling function, although it is associated with a higher theoretical ice front velocity. The sample height at the end of the process was 2.5 cm for the exponential cooling function, which corresponds to 66.7% of the maximum sample height $L_{\max} = 3.8$ cm as calculated from Equation 9 for water and an ice front velocity of $v_f = 25$ µm s^{-1}. Using Equation 17 or looking at Figure 6, one can easily evaluate that a difference of 6.8% is expected between the cooling functions and, hence, the phase front positions of both approaches for $v_f = 25$ µm s^{-1} at that sample height. Experimentally, a difference of 4.7% is observed at the end of the process in Figure 7. Bearing in mind the slightly different velocities of both approaches and the general experimental deviations discussed, this comparative measurement is in an acceptable agreement with the expectations derived mathematically in form of the relative difference (see Equation 17).

The accuracy of the quasi-stationary approximation for a certain sample height depends significantly on the ratio of the specific latent heat, h_f, and specific heat capacity, c_s. However, for water-based systems our investigations indicate a rather limited range of validity for the literature-known quasi-stationary approximation compared to the exact cooling function presented here.

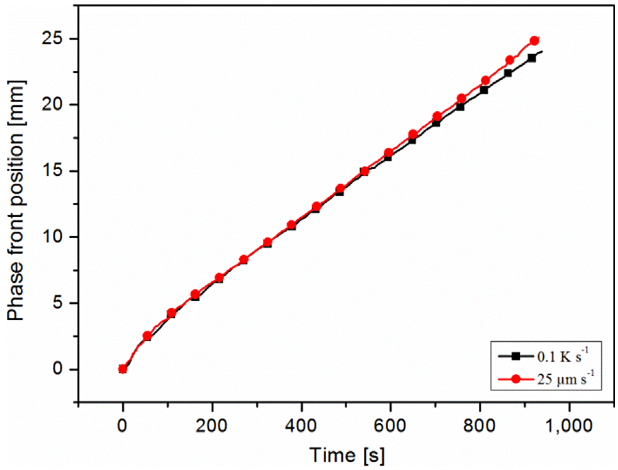

Fig. 7. Comparison of the ice front evolution over time between one water sample frozen using a linear cooling function (0.1 K s^{-1}) and the other frozen using the exponential cooling function (25 µm s^{-1}).

5. Conclusions

A one-dimensional inverse Stefan problem was presented and analytically solved using a series expansion. This results in an exponential cooling function which is necessary to achieve a directional solidification with constant ice front velocity in a thermally insulated system cooled only on one system boundary. Additionally, a theoretical limit for the maximum sample height realizable with this approach was mathematically derived. The theoretical approach was validated by experiments with pure water and a β-tricalcium phosphate suspension for different ice front velocities. The presented exponential cooling function enables a more accurate control of solidification during the ice-templating processes than previous attempts with linear cooling functions. Hence, constant pore sizes can be obtained even at higher velocities or for larger samples. The improved control of ice-templating processes will be advantageous with respect to custom-tailored porous materials for bone tissue engineering or porous electrodes for energy storage, for example. A better understanding of the initial phase of solidification was achieved. High initial ice front velocities can be attributed to supercooling of the liquid at the beginning of the cooling phase. This effect can explain the small structural sizes in the first layers of ice-templated suspensions.

Article first published online: September 10, 2015
Manuscript Revised: June 29, 2015
Manuscript Received: May 6, 2015

---

[1] S. Deville, *Adv. Eng. Mater.* **2008**, *10*, 155.
[2] U. G. K. Wegst, M. Schecter, A. E. Donius, P. M. Hunger, *Phil. Trans. R. Soc. A* **2010**, *368*, 2099.
[3] H. Schoof, L. Bruns, A. Fischer, I. Heschel, G. Rau, *J. Cryst. Growth* **2000**, *209*, 122.
[4] H. Schoof, J. Apel, I. Heschel, G. Rau, *J. Biomed. Mater. Res.* **2001**, *58*, 352.
[5] T. Fukasawa, M. Ando, T. Ohji, S. Kanzaki, *J. Am. Ceram. Soc.* **2001**, *84*, 230.
[6] S. Deville, E. Saiz, R. Nalla, A. P. Tomsia, *Science* **2006**, *311*, 515.
[7] S. Deville, E. Saiz, R. Nalla, A. P. Tomsia, *Acta Mater.* **2007**, *55*, 1965.
[8] T. Waschkies, R. Oberacker, M. J. Hoffmann, *J. Am. Ceram. Soc.* **2009**, *92*, S79.
[9] J. Stefan, *Sitzungsber. der kais. Acad. d. Wiss.* **1889** *98*, 269.
[10] B. Rubinsky, E. G. Cravahlo, *Int. J. Heat Mass Transfer* **1981**, *24*, 1987.
[11] J. Yoo, B. Rubinsky, *Numer. Heat Transfer* **1983**, *6*, 209.
[12] B. Rubinsky, E. G. Cravahlo, *Cryobiology* **1984**, *21*, 303.
[13] S. Flauder, U. Gbureck, F. A. Müller, *Key Eng. Mater.* **2013**, *529–530*, 129.
[14] S. Flauder, U. Gbureck, F. A. Müller, *Acta Biomater.* **2014**, *10*, 5148.
[15] O. M. Alifanov, in *Inverse Heat Transfer Problems*, Springer, Berlin, Germany **1994**, Ch. 2.
[16] H. E. Sweers, *J. Hydrol.* **1976**, *30*, 375.
[17] A. Bareggi, E. Maire, A. Lasalle, S. Deville, *J. Am. Ceram. Soc.* **2011**, *94*, 3570.
[18] S. Deville, E. Maire, A. Lasalle, A. Bogner, C. Gauthier, J. Leloup, C. Guizardz, *J. Am. Ceram. Soc.* **2009**, *92*, 2489.
[19] B. Delattre, H. Bai, R. O. Ritchie, J. Coninck, A. P. Tomsia, *ACS Appl. Mater. Interfaces* **2014**, *6*, 159.
[20] A. Lasalle, C. Guizard, J. Leloup, S. Deville, E. Maire, A. Bogner, C. Gauthier, J. Adrien, L. Courtois, *J. Am. Ceram. Soc.* **2012**, *95*, 799.
[21] S. Deville, E. Maire, A. Lasalle, A. Bogner, C. Gauthier, J. Leloup, C. Guizard, *J. Am. Ceram. Soc.* **2010**, *93*, 2507.
[22] H. D. Baehr, K. Stephan, in *Wärme- und Stoffübertragung*, 6th ed. Springer, Bochum/Stuttgart,Germany **2008**.

Directional Solidification with Constant Ice Front Velocity and the Ice-Templating Process

By *C. Stolze*, *T. Janoschka*, *U. S. Schubert**, *F. A. Müller, S. Flauder*

[*] E-Mail: ulrich.schubert@uni-jena.de

Supporting Information: Analytical solution of the Stefan problem

The one-dimensional Stefan problem describing a directional solidification with constant solid/liquid phase front velocity of a planar phase front can be written as

$$\frac{\partial T_s(z,t)}{\partial t} = k_s \frac{\partial^2 T_s(z,t)}{\partial z^2} \qquad \forall\, z \le s(t),\ \ \forall\, t \in \mathbb{R} \tag{S1a}$$

$$T_s(0,t) = f(t), \tag{S1b}$$

$$\left.\frac{\partial T_s(z,t)}{\partial z}\right|_{z=L} = 0, \tag{S1c}$$

$$T_s(s(t),t) = T_0, \tag{S1d}$$

$$\lambda_s \left.\frac{\partial T_s(z,t)}{\partial z}\right|_{z=s(t)} = h_f \rho_s \frac{ds(t)}{dt} = h_f \rho_s v_f, \tag{S1e}$$

$$s(0) = 0. \tag{S1f}$$

Its solution can be derived analytically using a Taylor series expansion,

$$T_s(z,t) = \sum_{m=0}^{\infty} \sum_{n=0}^{\infty} a_{m,n}\, (z - z_0)^m\, (t - t_0)^n. \tag{S2}$$

Using this approach, *(z_0,t_0)* is reasonably chosen to be *(0,0)* since the function of interest is the cooling function *$f(t) = T_s(0,t)$*, leading to

$$T_s(z,t) = \sum_{m=0}^{\infty} \sum_{n=0}^{\infty} a_{m,n}\, z^m\, t^n. \tag{S3}$$

Equation (S3) is inserted into all the equations (S1a) to (S1f), each leading to a different equation with a polynomial series expression for the variables *z* and *t*. The coefficients on both sides of these series expressions are equated for each equation separately and the resulting expression is resolved for the coefficient. This eventually leads to the following conditions for the coefficients $a_{m,n}$:

$$a_{0,0} = T_0 \tag{S4a}$$

$$a_{1,0} = \frac{h_f}{c_s}\frac{v_f}{k_s} \tag{S4b}$$

$$a_{0,n} = -\frac{n-1}{2k} a_{0,n-1} v_f^2 - a_{1,n-1} v_f$$

$$-\sum_{m=2}^{\frac{n-n \, mod \, 2}{2}} \frac{(n-m)!}{(n-2m)!(2m-1)!} \frac{1}{k_s^{m-1}} v_f^{2m-1} \left[\frac{a_{0,n-m}}{2m}\frac{v_f}{k_s} + \frac{a_{1,n-m}}{n-2m+1}\right]$$

$$-\sum_{m=1+\frac{n-n \, mod \, 2}{2}}^{\frac{n+n \, mod \, 2}{2}} 2m \frac{(n-m)!}{(n-2m+1)!(2m-1)!} \frac{1}{k_s^{m-1}} v_f^{2m-1} a_{1,n-m} v_f^{2m-1} \tag{S4c}$$

$$a_{1,n} =$$

$$-\sum_{m=1}^{\frac{n-n \, mod \, 2}{2}} \frac{(n-m)!}{(n-2m)!(2m)!} \frac{1}{k_s^{m}} v_f^{2m-1} \left[\frac{2m(n-m+1)}{(n-2m+1)} a_{0,n-m+1} + a_{1,n-m} v_f\right]$$

$$-\sum_{m=1+\frac{n-n \, mod \, 2}{2}}^{\frac{n+n \, mod \, 2}{2}} \frac{(n-m+1)!}{(n-2m+1)!(2m)!} \frac{1}{k_s^{m}} v_f^{2m-1} a_{0,n-m+1} v_f^{2m-1} \tag{S4d}$$

$$a_{m,n} = \begin{cases} \frac{(n+\frac{1}{2}(m-1))!}{n!m!} \left(\frac{1}{k_s^m}\right)^{\frac{m-1}{2}} a_{1,n+\frac{m.-1}{2}} & , \ m \text{ uneven} \\ \\ \frac{(n+\frac{m}{2})!}{n!m!} \left(\frac{1}{k_s^m}\right)^{\frac{m}{2}} a_{0,n+\frac{m.}{2}} & , \ m \text{ even} \end{cases} \tag{S4e}$$

Equations (S4c) to (S4e) are valid for $n \geq 1$. All coefficients $a_{0,n}$ and $a_{1,n}$ can be determined from equations (S4a) to (S4d), which results in:

$$a_{0,n} = -\frac{h_f}{c_s}\frac{1}{n!}\left(\frac{v_f^2}{k_s}\right)^n \quad , \tag{S5a}$$

$$a_{1,n} = -\frac{h_f}{c_s}\frac{1}{n!}\left(\frac{v_f^2}{k_s}\right)^n \frac{v_f}{k_s} \quad . \tag{S5b}$$

Finally, equations (S5a) and (S5b) can be inserted into equation (S4e), which leads to an expression for all of the coefficients $a_{m,n}$. For both, even and uneven m, the same expression is found except for a factor (-1)$^{m+1}$. Together with equation (S4a) all the coefficients $a_{m,n}$ are then defined by

$$a_{m,n} = \begin{cases} T_0 & , \quad m = n = 0 \\ & \\ (-1)^{m+1} \frac{h_f}{c_s} \frac{1}{m!n!} \left(\frac{v_f}{k_s}\right)^m \left(\frac{v_f^2}{k_s}\right)^n & , \quad \text{else} \end{cases} \tag{S6}$$

Equation (S3) and (S6) can be put together and give an expression for the initial power series as follows:

$$T_s(z,t) = \sum_{m=0}^{\infty} \sum_{n=0}^{\infty} a_{m,n}\, z^m\, t^n$$

$$= T_0 + \frac{h_f}{c_s}\left(1 - \sum_{m=0}^{\infty} \sum_{n=0}^{\infty} \frac{1}{m!}\left(-\frac{v_f}{k_s} z\right)^m \frac{1}{n!}\left(\frac{v_f^2}{k_s} t\right)^n\right). \tag{S7}$$

The series in this expression represents the well-known power series for the exponential function with two variables, which has an infinite radius of convergence, and is the exact temperature distribution for the whole domain and throughout the whole duration of the process. Thus, equation (S7) can finally be written as

$$T_s(z,t) = T_0 + \frac{h_f}{c_s}\left[1 - \exp\left(\frac{v_f^2}{k_s} t - \frac{v_f}{k_s} z\right)\right]. \tag{S8}$$

At $z = 0$ the solution is identical to the cooling function $f(t)$ according to equation (S1b), which results in

$$f(t) = T_0 + \frac{h_f}{c_s}\left[1 - \exp\left(\frac{v_f^2}{k_s} t\right)\right]. \tag{S9}$$

Equations (S8) and (S9) represent the unique solution to the presented Stefan problem.

Publication P2

Investigation of Ice-Templated Porous Electrodes for Application in Organic Batteries

C. Stolze, T. Janoschka, S. Flauder, F. A. Müller, M. D. Hager, U. S. Schubert,
ACS Appl. Mater. Interfaces **2016**, *8*, 23614-23623.

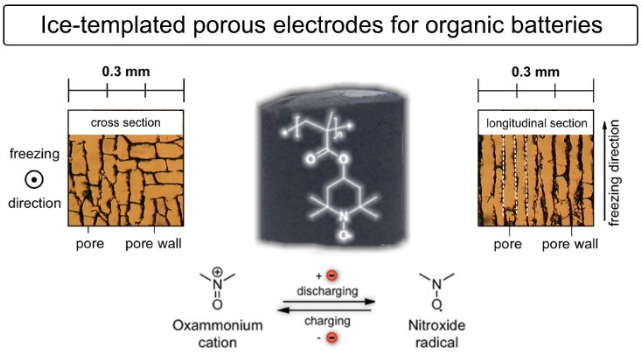

ACS APPLIED MATERIALS & INTERFACES
Research Article
www.acsami.org

Investigation of Ice-Templated Porous Electrodes for Application in Organic Batteries

Christian Stolze,[†,‡] Tobias Janoschka,[†,‡] Stefan Flauder,[§,⊥] Frank A. Müller,[‡,§] Martin D. Hager,[†,‡] and Ulrich S. Schubert*,[†,‡]

[†]Laboratory of Organic and Macromolecular Chemistry (IOMC), Friedrich Schiller University Jena, Humboldtstrasse 10, 07743 Jena, Germany

[‡]Center for Energy and Environmental Chemistry Jena (CEEC Jena), Friedrich Schiller University Jena, Philosophenweg 7a, 07743 Jena, Germany

[§]Otto-Schott-Institute of Materials Research (OSIM), Friedrich Schiller University Jena, Löbdergraben 32, 07743 Jena, Germany

Supporting Information

ABSTRACT: Application and investigation of porous composite electrodes for organic batteries fabricated by an ice-templating method are reported for the first time. The possibility to produce polymer composite electrodes with highly aligned, parallel pores is demonstrated and electrochemical investigations are presented to examine their suitability for application in organic batteries. The performance of such ice-templated porous electrodes is experimentally compared with planar electrodes of similar composition against zinc and lithium counter electrodes, respectively. Fundamental properties limiting the performance of ice-templated porous electrodes are discussed and further means to overcome those limitations are proposed.

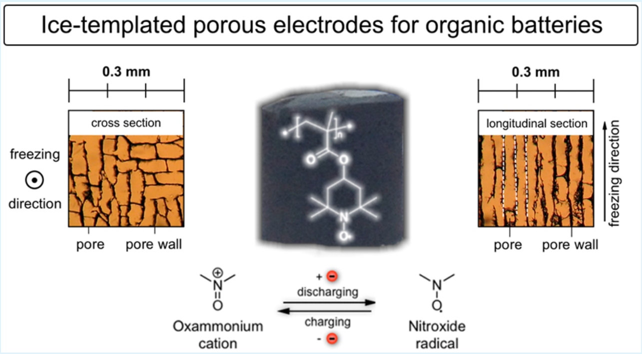

KEYWORDS: *ice-templating, freeze casting, energy storage, organic batteries, porous electrodes, TEMPO, PTMA, ORB*

1. INTRODUCTION

Organic batteries have become an intensively studied research area over the past decades, because of their potential for a low-cost, efficient, high-performance, environmentally benign, and durable battery technology.[1,2] Redox reactions of organic molecules are utilized in such batteries in contrast to the majority of commercially available systems, which are based on metals and metal compounds. Although significant theoretical and experimental efforts have been focused onto developing and optimizing suitable organic chemical structures,[3−9] comparably few investigations have been carried out regarding the geometric structure of electrodes for organic batteries and its influence on the battery performance. The geometric structure of an electrode, however, has without any doubt an important impact on the properties of any electrochemical system. Although standard planar electrodes are confined to their two-dimensional character, porous electrodes provide opportunities for totally different cell designs, e.g., three-dimensional interpenetrating electrodes. Different studies have already demonstrated the benefits provided by nano- to macroporous electrodes for organic batteries.[10−20] Except for Olsson et al. and Carlsson et al., who fabricated porous electrodes from cellulose and polypyrrole with a thickness of 0.9 to 1.3 mm, nearly all studies have in common that only thin-film electrodes in the range of micrometer thicknesses and random pore structures have been fabricated. Nevertheless, it was demonstrated that porosity can have a significantly positive influence on the electrochemical performance, which the authors attributed mainly to the presence of a high number of counterions within the pores of highly porous electrodes and the short counterion paths resulting from that. However, all these studies reported random pore structures.

Hence, although there are some investigations that utilize different methods for the preparation of random pore structures with increased surface area for organic battery electrodes, nearly no investigations were conducted for obtaining defined pore geometries. One technique for achieving such defined pore structures is the ice-templating method, which relies on the directional solidification of aqueous suspensions or solutions as well as the physical properties of the anisotropic growth of ice crystals. For porous ceramics, this method has been shown to be simple in terms of experimental operation, while offering a considerable control over the pore structure of the resulting sample because of the direct relationship between the velocity of the ice front during solidification and the resulting pore diameters.[21,22] Various

Received: April 27, 2016
Accepted: July 22, 2016
Published: August 29, 2016

Table 1. Mass, Composition, and Amount of Water Used for Preparation of Planar and Porous Electrodes

sample[a]	PTMA (wt%)[b]	VGCF (wt%)[b]	CNP50 (wt%)[b]	binder (wt%)[b]	H_2O (wt%)[b]	electrode mass (mg)
F1	59.2 ± 0.8	15.4 ± 0.3	20.6 ± 0.4	4.8 ± 0.1[c]	1278	3.63 ± 0.02
F2	44.4 ± 0.6	22.3 ± 0.4	29.5 ± 0.5	3.8 ± 0.1[c]	1278	2.50 ± 0.02
P1[e,f]	42.3 ± 0.2	19.8 ± 0.1	29.4 ± 0.1	8.4 ± 0.4[d]	2956	
P2[f]	42.7 ± 0.2	20.3 ± 0.1	28.2 ± 0.1	8.8 ± 0.4[d]	2818	
P3[f]	44.5 ± 0.1	22.3 ± 0.1	29.4 ± 0.1	3.8 ± 0.1[c]	2915	
P4[f]	44.6 ± 0.1	22.2 ± 0.1	29.3 ± 0.1	3.8 ± 0.1[c]	2918	
P5[f]	42 ± 2	21 ± 1	28 ± 1	9 ± 1[d]	2795	
P6[f]	45 ± 2	19 ± 1	27 ± 1	9 ± 1[d]	3000	
P7[f]	59.7 ± 0.2	15.1 ± 0.1	20.5 ± 0.1	4.8 ± 0.1[c]	2886	6.8 ± 0.1
P8[g,h]	44.7 ± 0.1	22.2 ± 0.1	29.3 ± 0.1	3.8 ± 0.1[c]	2860	8.7 ± 0.2

[a] **F** for flat/planar electrodes and **P** for porous electrodes; numbered consecutively. [b] Weight-percent with respect to the total mass of all solids. [c] Binder: CMC. [d] Binder: PEDOT:PSS. [e] Prepared with mortar ground PTMA. [f] 2 mL of suspension used. [g] 0.25 mL of suspension used. [h] Nickel foam embedded.

temperature−time evolution functions can be applied to the cooled boundary of the suspension in order to achieve specific pore diameters or pore shapes over the direction of the solidification.[23−25] Total porosities of the resulting samples are also very dependent on the solids content of the suspension and can be controlled in a wide range from at least 10 to 90%.[26] Hitherto, few studies dealt with utilizing this technique for carbon-based composite electrodes; only selected examples of the fabrication of supercapacitors or metal-based batteries were described.[27−29] To the best of our knowledge, no application of the ice-templating method to the production of porous electrodes for organic batteries has been published so far in the open literature.

Consequently, the present study utilizes an ice-templating method to provide a new approach in the fabrication of nonplanar polymer/carbon composite electrodes for organic batteries for the first time. Porous electrodes with highly aligned, parallel pores were prepared and a structural investigation is presented to demonstrate the applicability of this method for polymer/carbon suspensions. Electrochemical investigations of such porous electrodes against zinc and lithium counter electrodes are compared to those of planar electrodes of similar composition in beaker-type battery setups and a coin-cell setup, respectively. Differences between the electrode types are discussed in detail, providing a fundamental basis for further investigations and optimizations on ice-templated porous organic electrodes.

2. EXPERIMENTAL SECTION

2.1. Materials. Triethylene glycol dimethacrylate (95%, Sigma-Aldrich Chemie GmbH), 2,2,6,6-tetramethyl-4-piperidinyl methacrylate (*TCI Deutschland GmbH*), 4,4′-azobis(4-cyanovaleric acid) (98%, Sigma-Aldrich Chemie GmbH) and sodium tungstate dihydrate (99%, Sigma-Aldrich Chemie GmbH) were used as received without further purification for the synthesis of cross-linked poly(2,2,6,6-tetramethylpiperidinyloxy-4-yl methacrylate-*co*-triethylene glycol dimethacrylate) (PTMA, see section 2.3) as electrochemically active species. Vapor grown carbon nanofibers (VGCF, 100 nm × 20−200 μm, Sigma-Aldrich Chemie GmbH) as well as carbon nanopowder (CNP50, 50 nm particle diameter, Sigma-Aldrich Chemie GmbH) were applied as conductive additives for the electrodes and carboxymethyl cellulose (CMC, 3.85 wt% in aqueous solution) or poly(3,4-ethylenedioxythiophene) polystyrenesulfonate (PEDOT:PSS, 1.3 wt% aqueous solution, Sigma-Aldrich Chemie GmbH) as binder material. Paraplast Plus (paraffin wax, Sigma-Aldrich Chemie GmbH) and Entellan (Merck Millipore) were used to prepare sample sections for structural characterization. Ethylene carbonate (Alfa Aesar GmbH), dimethyl carbonate (Acros Organics), zinc perchlorate hexahydrate and lithium perchlorate (Sigma-Aldrich Chemie GmbH) were applied as electrolyte mixtures. Graphite foil (0.5 mm, 99.8% metal based) and graphite conductive adhesive (alcohol based) were purchased from Alfa Aesar GmbH. Nickel foam (90% porosity, 1200 μm mean pore diameter, 2.9 mm thick, Alantum Europe GmbH) was used as alternative current collector. Commercial CR2032 coin cell casings and Li-ion battery separators (25 μm thick, trilayer polypropylene-polyethylene-polypropylene, Celgard LLC.) were obtained from MTI Corporation. Zinc foil (250 μm thick, 99.98% metals basis, Alfa Aesar GmbH) and metallic lithium (cut from rod, 99.9% metals basis, Sigma-Aldrich Chemie GmbH) were used as counter electrode materials.

2.2. Characterization and Instrumentation. Particle size measurements were performed via light scattering using an Analysette 22 (Fritsch GmbH) and a CoulterCounter LS230 (Beckman Coulter), respectively. Structure investigations were carried out with a light microscope and a mountable digital camera (Canon PowerShot G5). Pore dimensions were determined using ImageJ, version 1.46r. The shorter width of each rectangular pore in a cross-section was measured and will be denoted as the pore diameter of a pore throughout this study. Either 100, 300, or 450 pores were measured for each section to obtain a mean pore diameter and the corresponding standard deviation of the pore size distribution. Random measurement uncertainties mainly caused by the finite wall thickness of a pore were estimated by repeating the measurement of one pore a hundred times yielding a standard deviation of the mean of ±0.2 μm for a 10-fold magnification. However, the standard deviation of the pore size distribution was by one or two magnitudes larger than the measurement uncertainty and, therefore, the latter was negligible. BET measurements were carried out on a Quantachrome Autosorb iQ with nitrogen as adsorbate (adsorption cross section: 16.2 Å^2, temperature: 77.350 K). Elemental analysis was performed using a λ-EuroVector EuroEA3000 system to investigate the material distribution in the porous electrodes. Electron spin resonance (ESR) spectra were acquired on an EMXmicro CW-EPR spectrometer (EMX micro EMM-6/1/9-VT control unit, ER 070 magnet, EMX premium ER04 X-band microwave bridge equipped with EMX standard resonator, EMX080 power unit) by Bruker Corporation. The samples were investigated at room temperature and the data handling was done on the Bruker Xenon software package, version 1.1b86. The SpinCount software module was used for quantitative measurements. The spectrometer was calibrated using TEMPO (99% purity, Sigma-Aldrich Chemie GmbH) as a reference standard and, hence, no internal reference was present during sample measurement. Eight ESR tubes (3 mm diameter) were prepared with ground PTMA powder and each sample was measured three times. The standard deviation of all measurements was σ_x = 8%. The mean value and its standard deviation of the mean were taken as best estimate for the true degree of functionalization. Electrochemical investigations were performed using a VMP3-based 16-channel-potentiostat from BioLogics Scientific Instruments. A three-electrode setup was applied for beaker-type cells utilizing an Ag/$AgNO_3$ reference electrode (RE-7S, 0.01 M $AgNO_3$

and 0.1 M TBAP in acetonitrile, BAS Inc.). Coin cells were assembled using a MTI MSK-160D Electrical Crimping Machine in a glovebox under argon atmosphere having water and oxygen levels below 0.1 ppm.

2.3. Preparation of Poly(2,2,6,6-tetramethylpiperidinyloxy-4-yl methacrylate-*co*-triethylene glycol dimethacrylate), PTMA. 4,4′-Azobis(4-cyanovaleric acid) (1.94 g, 6.9 mmol) was added to a solution of 2,2,6,6-tetramethyl-4-piperidinyl methacrylate (30 g, 133.1 mmol) and triethylene glycol dimethacrylate (1.5 g, 5.3 mmol) in a mixture of methanol and water (3:1, 92 mL). The mixture was deaerated by flushing with argon for 30 min and subsequently heated to 70 °C for 24 h. After cooling to room temperature the reaction mixture was transferred to a ChemSpeed A100 robotic platform, sodium tungstate dihydrate (1.25 g, 3.8 mmol) as well as hydrogen peroxide (30%, 30 mL) were added and the reaction mixture was vigorously mixed by a twisted blade stirrer. After 24 h hydrogen peroxide (30%, 30 mL) was added a second time and the reaction was stirred for 24 h. Subsequently, the polymer gel was separated from the solvent, washed with methanol, further purified by Soxhlet extraction with acetonitrile and dried in vacuo. The title compound was obtained as an orange solid (25 g, 78% yield, ATR-FTIR $\nu_{\max}$ ($\mathrm{cm^{-1}}$): 2976 (m), 2938 (m), 1723 (s), 1465 (m), 1363 (m), 1239 (m), 1141 (s), 1006 (w), 982 (w), 965 (m), 752 (w), 685 (w); elemental analysis: 63.7% (C), 9.1% (H), 5.6% (N)).

Subsequently, two small amounts of this polymer were ground with either mortar and pestle or a planet ball mill (Pulverisette 7, Fritsch GmbH) using ZrO_2 balls (2 mm diameter) in a ZrO_2 cup for 20 min. The obtained particle batches were used for investigation of electrode structure and material distribution. Furthermore, a larger batch of PTMA was ground with the planet ball mill under the same conditions, but with an additional filtering step after the grinding (40 μm metal filter).

2.4. Preparation of Planar Electrodes. Planar electrodes were prepared from VGCF, CNP50, PTMA, binder (CMC) and water (rf. Table 1) by first mixing the dry components with pestle and mortar. In a second step, the CMC solution was mixed with pure water and, subsequently, mortar and pestle were used to blend this aqueous phase with the dry components until a homogeneous slurry was obtained. The slurry was spread on graphite foil sheets of 1−1.5 cm in width and 2−2.5 cm in length, which was subsequently dried in an oven at 60 °C for 4 h. Resulting planar electrodes had an average thickness of approximately (40 ± 20) μm as determined using a caterpillar from three planar electrodes with 10 measurements at different positions for each of the electrodes.

2.5. Preparation of Porous Electrodes. The setup for ice-templating of polymer/carbon suspensions was the same as used by Flauder et al. for the application of ice-templating on ceramic suspensions.[22] The interested reader is referred to this publication for further details. All suspensions for the ice-templating of porous electrodes were prepared by mixing VGCF, CNP50 and PTMA using pestle and mortar followed by the addition of the aqueous binder solution as well as deionized water (*rf.* Table 1). Homogenization of the mixture was achieved utilizing an Ultra-Turrax T25 (Janke & Kunkel GmbH/IKA Labortechnik) at 8000 to 9000 rpm for approximately 20 min. Suspensions prepared in that way were used to produce porous samples in an ice-templating step. Two different binder materials were tested: PEDOT:PSS was chosen because of its intrinsic electrical conductivity and earlier use in ice-templating.[28] CMC was utilized because it was already successfully applied as binder material for organic batteries.[30] However, in principle, all porous samples were prepared in the following four steps: (1) Precooled suspension (refrigerator) with a temperature of roughly 273 K was dispersed in a sonic bath for at least 1 min and shaken by hand, before an amount of either 0.25 or 2 mL of the suspension was filled into the ice-templating setup; (2) for a duration of 120 s the suspension was precooled to 273 K inside the evacuated setup to ensure a constant temperature near to the suspension's freezing point; (3) the suspension was cooled from its bottom with a constant cooling rate of 0.05 $\mathrm{K\ s^{-1}}$, 0.2 $\mathrm{K\ s^{-1}}$, or 0.4 $\mathrm{K\ s^{-1}}$, stopping the process at 200 K for the 0.25 mL samples and at 130 K for the 2 mL samples; (4) the frozen sample was extracted and lyophilized for 24 h at a pressure of 1 mbar to remove the ice completely. The 2 mL samples were cut into thin longitudinal sections (∼1 mm thick, cutting direction parallel to the pore direction) using a razor blade. Each piece was glued onto a piece of graphite foil using a conductive graphite ink (Figure S4). Porous samples with an embedded nickel foam current collector (**P8**, ∼3 mm thick, see section 3.3.3) for optimization experiments were built into the coin cells without further preprocessing.

2.6. Sample Preparation for Investigation of Pore Structure and Material Distribution. For the investigation of the distribution of PTMA within the porous sample, a cylindrical sample was cut into three pieces along the original solidification direction (bottom, center, top, each ∼0.4 cm thick). Consequently, each piece was chopped up and subjected to elemental analysis separately. Porous electrodes were prepared for investigation of their structure by infiltrating each sample with molten Paraplast Plus at 70 °C, which subsequently cooled down and hardened at room temperature. Embedded samples were cut into ∼5 μm thick long and cross-sections using a microtome. Each section was floated onto a water drop located on an object slide having a temperature of 35 °C, in order to obtain smooth sections. After drying the sections for a minimum of 5 h, they were immersed into xylene for ∼1.5 min until the paraffin was washed out without destroying the structure. The sample was then covered with Entellan and a cover glass. Photomicrographs of sample sections were obtained via light microscopy.

2.7. Electrochemical Performance Investigations. Constant-current chronopotentiometric studies for the investigation of the charge/discharge behavior and the C-rate capability of planar and porous electrodes were carried out on electrodes with a PTMA content of 60% (**F1**, **P7**) and 45% (**F2**, **P8**), respectively. Beaker-type electrochemical cells were built with zinc as counter electrode in 0.1 M $Zn(ClO_4)_2 \times 6\ H_2O$ EC/DMC (3:7) electrolyte and with an AgCl/Ag reference electrode, whereas coin cell experiments were carried out in 1 M $LiClO_4$ containing EC/DMC (3:7) using lithium as counter electrode with a commercial Li-ion separator. Cyclability tests were performed over 25 cycles at a C-rate of 1C, which corresponds to one charge or one discharge cycle performed in 1 h. C-rate capability tests for the evaluation of the electrodes under different power loads were carried out at 5C, 25C, 1C and 10C in this specific order. All current values applied for different C-rates in this study rely on theoretical calculations carried out using Faraday's law of electrolysis with the assumption that 100% of the PTMA (molar mass of repetition unit: $M = 242.08\ \mathrm{g\ mol^{-1}}$) in each electrode were electrochemically active. The total charge and discharge capacity for each electrode—as obtained by integration of the applied current over time—was normalized to the total electrode mass including the conductive additives and the binder material. This weight-based value was used to compare different electrodes with each other. It will be referred to as uncorrected specific capacity throughout this study. However, to gain a reliable value for the specific capacity, which can be compared with the theoretically expected value of 110.7 mAh $\mathrm{g^{-1}}$ for the cross-linked PTMA, two values need to be known: the amount of PTMA in the electrode and its degree of functionalization, i.e., the fraction of electrochemically active units. The first value is known from the total mass and the composition of the electrode (Table 1), whereas the second was determined by ESR measurements. Division of the uncorrected specific capacity by this value and the mass fraction of PTMA in an electrode yields an experimental measure for the specific capacity based on the electrode's active material only. This value will be denoted as corrected specific capacity. Measurement uncertainties for uncorrected specific capacities arose from uncertainty in the electrode mass determination only. Current and time measurements exhibited a negligible measurement error. This is also true for the values of the corrected specific capacities; however, an additional uncertainty was included by error propagation of the ESR measurement uncertainty.

3. RESULTS AND DISCUSSION

3.1. Material Distribution. The redox-active polymer poly(2,2,6,6-tetramethylpiperidinyloxy-4-yl methacrylate-*co*-triethylene glycol dimethacrylate) (PTMA) was successfully synthesized in a 78% yield by free radical polymerization bearing a degree of functionalization of (86 ± 3)% as determined by ESR measurements.

Figure 1a shows the results of particle size measurements as determined by light scattering in both volume and number distributions of two differently prepared PTMA powders, which were obtained from the same batch of synthesized polymer either using a planet ball mill or mortar and pestle. Comparison of both types of distribution data revealed that both powders consisted of a large amount of smaller particles and a few significantly larger particles. PTMA ground with a planet ball mill exhibited a volume fraction based d_{50} diameter of d_{50} = 12 μm, whereas particles prepared via grinding with mortar and pestle yielded a 2-fold higher value of d_{50} = 27 μm. The number fraction based value of PTMA ground using the planet ball mill, d_{50} = 80 nm, was by a factor of approximately four smaller than the number fraction based value determined for the other particle batch. The observed differences had a significant impact on the material distribution within the ice-templated porous electrodes, which were prepared from these two powder batches.

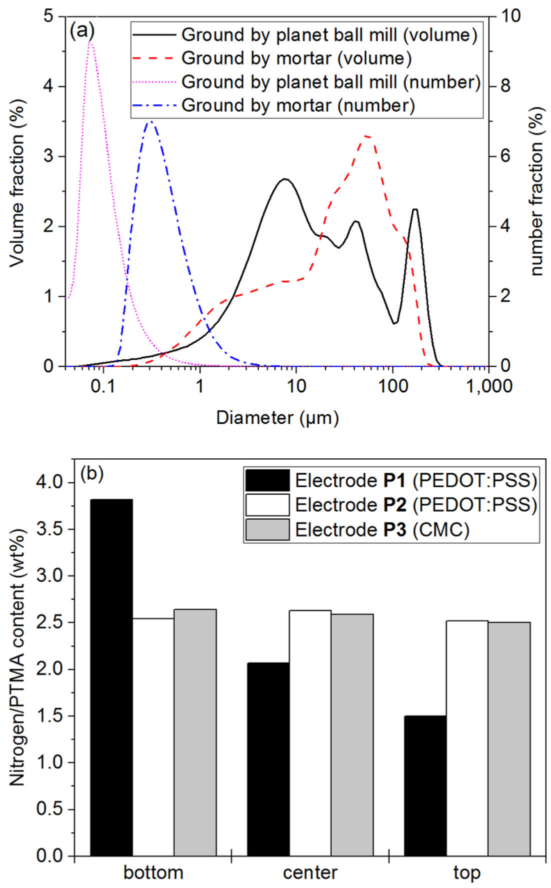

Figure 1. (a) Particle size distributions of PTMA powders, which were obtained employing a planet ball mill or mortar and pestle; (b) nitrogen content in pieces of porous electrodes made from compositions **P1**, **P2**, and **P3** as determined by elemental analysis.

Figure 1b shows the content of nitrogen in each sample region of porous electrodes prepared from compositions P1 (PEDOT:PSS binder, mortar particles), P2 (PEDOT:PSS binder, planet ball mill particles) and P3 (CMC binder, planet ball mill particles) as determined by elemental analysis. The complete data of the elemental analyses is also available in the Figure S5. However, the content of nitrogen in each sample region was directly proportional to the PTMA content, since nitrogen was an exclusive indicator for PTMA in the electrodes. As evident from the data, the particle batch prepared with mortar and pestle included larger particles, which gave rise for stronger sedimentation during ice-templating with composition P1. This resulted in an accumulation of PTMA and, hence, nitrogen in the bottom part of this electrode. On the other hand, a homogeneous distribution of the polymer along the direction of solidification could be observed for P2, where each sample region contained approximately the same amount of nitrogen. To rule out any influence of the binder material on the polymer distribution, the same experiment was conducted with an electrode ice-templated from composition P3, which evidently exhibited the same homogeneity as obtained for P2.

Consequently, it can be concluded that small sized particles are required for a homogeneous material distribution within the ice-templated porous electrode, while the two different binder materials have no recognizable influence. Because of the positive effect of small particles, a larger batch of polymer was

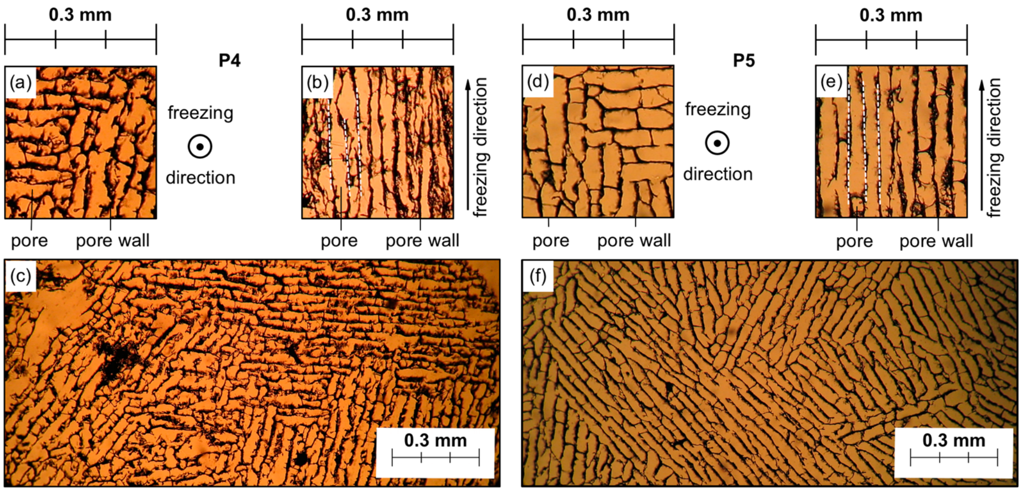

Figure 2. Photomicrographs of a (a, d) cross-section, (b, e) longitudinal section and (c, f) a larger image section of the cross-section of porous electrodes (a−c) **P4** and (d−f) **P5**.

subsequently ground using the planet ball mill and applying an additional filtering step. Particles obtained from that batch were exclusively used for all electrodes, which were investigated by electrochemical experiments throughout this study. The particle size distribution of this batch is shown in Figure S3.

3.2. Structural Investigation of the Porous Electrodes. Figure 2 shows both cross- and longitudinal sections of porous samples made from **P4** and **P5** in order to study the topology of the ice-templated electrodes. The pore structure is clearly visible for both compositions. Structure artifacts, like abnormally large pores and fuzzy wall shapes in sections of **P4**, can be primarily ascribed to the preparation method used for the sections, because some minor dissolution of the water-soluble binder materials during the floating step and slight damaging of the structure during wax infiltration and the washing with xylene could not always be prevented.

The result of the statistical evaluation of the pore dimensions for a cooling rate of 0.2 K s^{-1} at different positions in a sample (**P5**) as well as for different cooling rates of 0.05, 0.2, and 0.4 K s^{-1} (**P6**) are listed in Table 2. Pore size distributions obtained from the same measurements are available in the Figure S6. It is evident from the data that mean diameters measured from the same sample at different positions do not differ significantly, which indicates a negligible variation of the pore diameters over the whole height of one sample (**P5**). However, an inversely proportional relationship between pore diameter and cooling rate is observed for porous electrodes ice-templated at different cooling rates (**P6**). Both results are in agreement with previous findings regarding ice-templating of (ceramic) particle suspensions.[21,22,24] The latter effect can be used to control the pore sizes and shapes of porous electrodes for organic polymer batteries. In addition, it was shown before that varying the solids content of a suspension allows tailoring the total porosity of ice-templated samples in a range from at least 10 to 90%.[26] The porosity of porous electrodes in the present study was estimated to be at least 65% by determining the ratio of the sum of the bright areas (pores) to the total area in photomicrographs like those shown in Figure 2. Because this is the porosity value for specific cross sections, we regard this value only as an estimate for the overall porosity of the whole sample. BET analysis carried out on the nitrogen adsorption isotherm of a porous sample revealed a specific surface area of 8 m^2 g^{-1} and a macro-porous pore structure (Figure S7).

Table 2. Comparison of the Mean Pore Diameters at Different Cross-Sectional Positions in Electrodes of Composition P5 and P6 Ice-Templated at Cooling Rates of 0.05, 0.2, or 0.4 K s^{-1}, Respectively[a]

cooling rate (K s^{-1})	sample position	mean diameter (μm)	standard deviation (μm)
0.2[b]	bottom	31[d]	10[d]
0.2[b]	center	30[e]	5[e]
0.2[b]	top	35[e]	5[e]
0.05[c]	top	48[f]	12[f]
0.2[c]	top	30[f]	6[f]
0.4[c]	top	23[f]	5[f]

[a]Pore size distributions are available in the Figure S6. [b]**P5**. [c]**P6**. [d]Data of 300 pores. [e]Data of 450 pores. [f]Data of 100 pores.

Although the resulting structures were well-defined for both types of binder materials, the use of PEDOT:PSS resulted in highly fragile porous electrodes, which were very difficult to handle experimentally. Furthermore, preliminary comparative studies with porous electrodes made with these different binders exhibited no performance difference. Because of their considerably higher mechanical stability, all electrodes used for electrochemical experiments presented throughout this study exclusively contained CMC as binder material.

3.3. Electrochemical Investigations. The following sections contain the results of the electrochemical investigations of the ice-templated porous electrodes, including cycle stability tests, *C*-rate capability tests, and the comparison of the electrochemical performance of porous ice-templated electrodes with planar electrodes.

3.3.1. Electrochemical Stability and Specific Capacity. Figure 3a shows the chemical structure of the redox-active PTMA polymer, its formal redox reaction and cyclic voltammograms of both porous and planar electrodes, which exhibit clear redox reactions at 0.4 V vs $Ag/AgNO_3$ corresponding to the well-known standard potential of the TEMPO moiety.[1,6] In addition, Figure 3b, c show 25 charge and discharge cycles for each electrode type with zinc as counter electrode in 0.1 M $Zn(ClO_4)_2 \times 6\ H_2O$ EC/DMC (3:7). Both electrode types exhibited stable cycling at (53 ± 2) mAh g^{-1} and (57 ± 1) mAh g^{-1} of uncorrected specific capacity (triangles), respectively, with no capacity loss over 25 cycles. The Coulombic efficiency was higher than 95% indicating stable and chemically reversible reactions. Corrected specific capacities (squares with error bars) are shown in Figure 3 as well, yielding values of (104 ± 6) mAh g^{-1} for porous and (111 ± 6) mAh g^{-1} for planar electrodes. It can be stated that the experimental result is in agreement with the theoretically expected specific capacity of 110.7 mAh g^{-1} within the measurement accuracy. Hence, (94 ± 5)% of the theoretically available capacity could be utilized for the porous electrode at 1*C*. This result proves the basic viability of porous ice-templated electrodes based on organic polymers.

3.3.2. C-Rate Capability. An exemplary charging and discharging curve of each electrode (25th cycle) is shown in Figure 4a. It can be clearly seen that the porous electrode reveals a higher overpotential compared to the planar electrode as can be evaluated from the voltage difference between the charging and discharging plateaus. Impact of this high overvoltage on the battery performance was investigated further by performing C-rate experiments at various power loads. Figure 4b, c shows a comparison of a C-rate capability of porous electrode **P7** and planar electrode **F1** in 0.1 M $Zn(ClO_4)_2 \times 6\ H_2O$ EC/DMC (3:7) with a zinc counter electrode in a beaker-type cell setup. For better comparability, capacities were normalized to the maximum 1C charge capacity obtained during the C-rate test for each electrode, which was roughly (59 ± 2) mAh g^{-1} of uncorrected or (115 ± 6) mAh g^{-1} of corrected specific capacity for both electrodes.

This slightly higher value at 1*C* in comparison to the experimental results illustrated in Figure 3 can be attributed to increased swelling of the polymer during the *C*-rate experiments. Although both electrodes performed equally at 1*C*, a significant difference could be observed at higher *C*-rates. The planar electrode exhibited a recognizable specific discharge capacity even at rates of up to 25*C*, whereas the porous electrode exhibited a nearly full capacity loss at 10*C*. For a rate of 5*C* about (78 ± 4)% and (92 ± 5)% of the theoretical capacity were obtained for the porous and the planar electrode, respectively. Hence, the planar electrode revealed a remarkably higher *C*-rate capability than the porous electrode. Although a

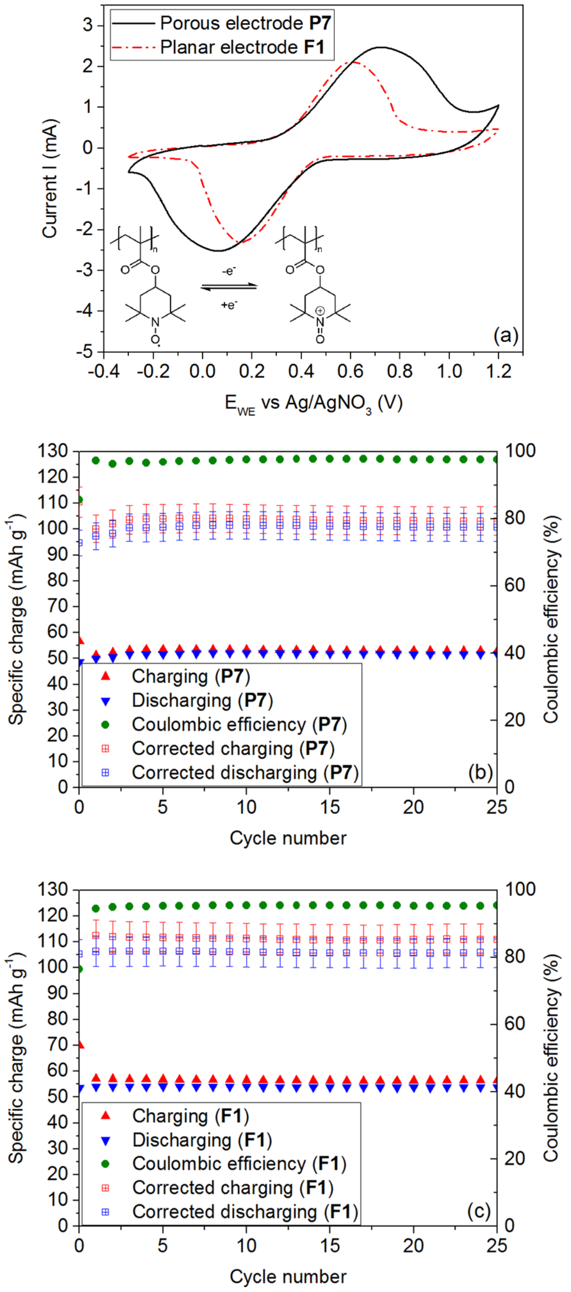

Figure 3. (a) Cyclic voltammetry of porous and planar electrodes made from compositions **P7** and **F1**, respectively. The inset shows a schematic representation of the chemical structure of PTMA and its formal redox reaction. Charging and discharging test at 1C for (b) porous electrode **P7** and (c) planar electrode **F1** in 0.1 M Zn(ClO$_4$)$_2$ × 6 H$_2$O EC/DMC (3:7) with a zinc counter electrode in a beaker-type cell setup.

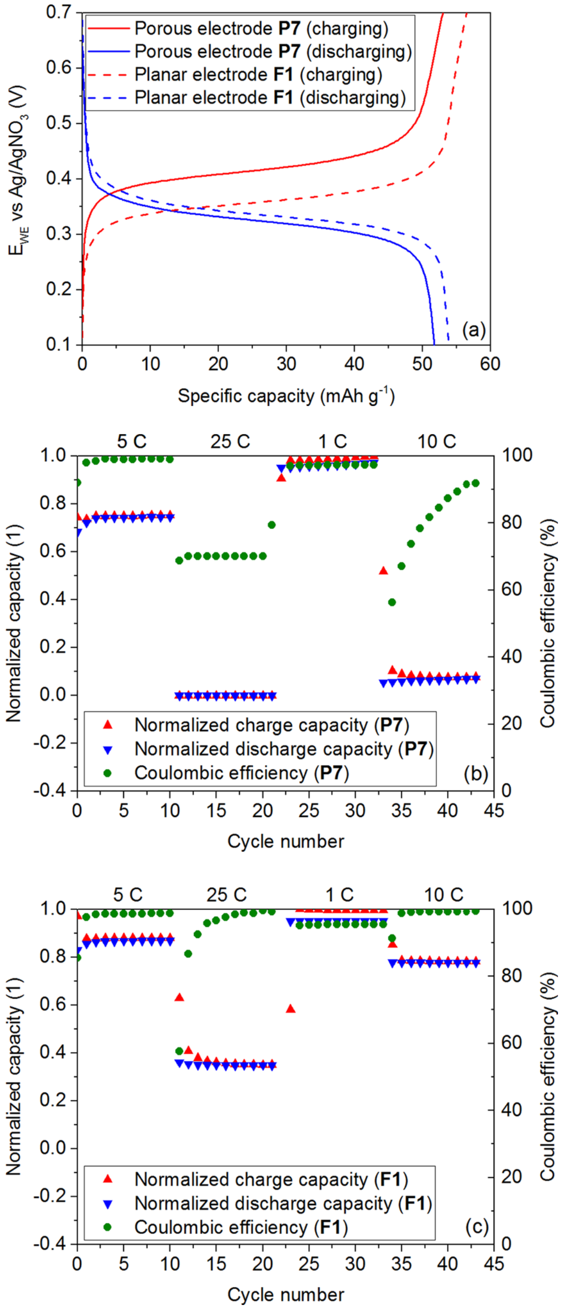

Figure 4. (a) Potential−capacity diagram (25th cycle) and C-rate tests for electrodes (b) **P7** and (c) **F1** in 0.1 M Zn(ClO$_4$)$_2$ × 6 H$_2$O EC/DMC (3:7) with a zinc counter electrode in a beaker-type cell. Capacities in (b) and (c) were normalized to a 1C charge capacity (59 mAh g^{-1}).

higher absolute active mass of **P7** compared to **F1** (rf. Table 1) required a higher absolute current for the same C-rate and, hence, caused an inherently higher overpotential, a better C-rate performance would have been expected with respect to the increased intrinsic surface area and porosity of the porous electrode. Carlsson et al. and Olsson et al. demonstrated before that porosity has a positive influence on the redox performance of electrochemical systems.[18−20] However, they verified this only for single electrodes (no batteries) and conducting polymers, which fully covered a microporous fibrous cellulose network with a random pore-structure. These properties represents some remarkable differences in comparison to the porous electrodes reported in the present study, which consist of aligned macropores made up from graphite and polymer particles. Further analysis was carried out on planar and porous electrodes in order to investigate the origin for the observed discrepancy.

3.3.3. *Investigation of Performance Differences.*

Electrochemical impedance spectroscopy measurements were carried out on the electrodes aiming at the evaluation of ohmic resistances. However, no well-defined impedance spectra were obtained in the experiments due to interfering, not yet understood, stray impedances and, thus, no convenient conclusions could be drawn. Therefore, a nonstandard approach for the approximate evaluation of the internal resistances was chosen: The numerical derivative of each capacity-potential diagram was calculated for each of the electrodes **P7** and **F1** (Figure 5).

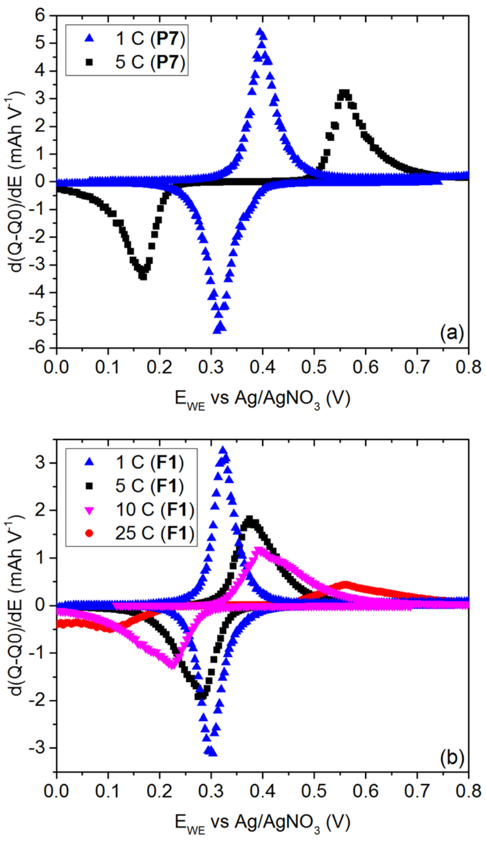

Figure 5. Derivatives of the potential−capacity curves for (a) porous electrode **P7** and (b) planar electrode **F1** in 0.1 M $Zn(ClO_4)_2 \times 6\ H_2O$ EC/DMC (3:7) with a zinc counter electrode in a beaker-type cell setup at different C-rates.

Comparing the peak splits of these curves, which are related to the overpotential η of the redox reaction during a charge and discharge cycle, a significant difference can be observed at different *C*-rates for both electrodes. The overpotential for each *C*-rate was evaluated from the peak split, ΔE, using eq 1

$$\eta = \frac{\Delta E}{2} = \frac{|E_{max} - E_{min}|}{2} \quad (1)$$

wherein E_{max} and E_{min} are the both peak potentials of each curve. According to Ohm's law the measured overpotential can be translated into a resistance, $R_\eta = \eta/I$, which was calculated for all available peak splits. The results are summarized in Table 3 and the obtained resistance values only represent an approximation for the low frequency impedance of the system. Measurement uncertainties arising from numerical differentiation with the nonequidistant data points caused varying values for the apparent formal potentials obtained from the derivatives in Figure 5. Their maximum deviation from the mean value was 8%. Since this uncertainty also corresponds to the uncertainty in the measured peak splits, this value was taken as a measure for the maximum uncertainty in the measured overpotentials. Uncertainties in the current measurements were negligible. Hence, the total uncertainty in resistance values determined by this method was estimated to be ~8%. The mean resistance obtained for the porous electrode was (86 ± 7) Ω and (39 ± 3) Ω for the planar electrode. Therefore, the porous electrode exhibited a 2-fold higher internal ohmic resistance. Apart from that, the following possible causes for the different performances observed at higher *C*-rates suggest themselves to be (1) a low electrolyte conductivity, (2) a low conductivity in the porous scaffold, (3) a low interfacial conductivity between the current collector and the electrode in comparison to thin film planar electrodes and/or (4) a significant difference in thickness by nearly 2 orders of magnitude between the porous (~1 mm) and the planar electrodes (~40 μm).

Table 3. Internal Ohmic Resistance, R_η, of Porous and Planar Electrode As Obtained from Overpotential Measurements, η, from Capacity−Potential Derivatives Shown in Figure 5

	I (mA)	C-rate	η (mV)	R_η (Ω)
P7	0.453[a]	1	39 ± 3	85 ± 7
P7	2.270	5	197 ± 16	87 ± 7
F1	0.240[a]	1	10.0 ± 0.8	42 ± 3
F1	1.200	5	47 ± 4	39 ± 3
F1	2.400	10	88 ± 7	37 ± 3
F1	6.000	25	230 ± 18	38 ± 3

[a] Value corresponds to 1*C* for this electrode.

The influence of the electrolyte resistance on the system performance strongly depends on the concentration of the supporting electrolyte and the distance between the working and counter/reference electrode. Due to their inherently smaller system size, coin cells are particularly suitable for minimizing the electrode distance and, therefore, were used on this zinc-based battery system. However, the data is not included in this study because a very limited lifetime caused by strong dendrite formation at the zinc electrode and the lack of a trustworthy method to verify that the porous electrode was not destroyed (compressed) during coin cell assembly, did not allow drawing convenient conclusions from such coin cell experiments yet. Future experiments may focus on the development of suitable methods to assemble zinc based coin cells without the risk of destroying the porous electrode. Measures to suppress or slow down the dendrite formation are reported in literature and suggest an optimistic perspective for the creation of an enduring zinc-based coin cell system.[31,32]

To investigate the influence of points (2) and (3), however, porous electrodes with an embedded nickel foam were ice-templated. The purpose of using a metal foam was to increase the overall conductivity in the porous electrode and, hence, to increase the scaffold conductivity and to facilitate electron transport from the current collector to the redox active units and vice versa.

This approach has already been successfully applied by Lee et al. yielding a significant capacity increase for ice-templated porous supercapacitor electrodes with embedded nickel foams.[27] Due to the improved mechanical stability the nickel foam provided for the porous electrode, coin cells could be built using lithium instead of zinc as a counter electrode and 1 M $LiClO_4$ in EC/DMC (3:7) as electrolyte. A high supporting electrolyte concentration was chosen to counteract the suspected influence of low electrolyte conductivity as mentioned in point (1). In order to increase the scaffold conductivity electrodes with a lower amount of PTMA (45 wt%) were ice-templated. C-rate tests were performed for both porous and planar electrodes with this polymer content. Results of these measurements for electrodes **P8** and **F2**, respectively, are presented in Figure 6. A significantly lower uncorrected specific capacity ((30 ± 1) mAh g^{-1} at 1C) was observed for both types of electrodes in this lithium coin cell setup, which might be due to the different electrolyte system or a remarkable influence of the counter electrode. However, since this study was focused on a relative comparison of planar and porous electrodes under similar circumstances, this performance discrepancy is of secondary importance. Two interesting aspects are evident from the C-rate experiments: The porous electrode with the embedded nickel foam does perform slightly better than the planar electrode at 5C. Nevertheless, it does also show a significant capacity loss during cycling. Regarding the latter observation, this might be caused by a side reaction, e.g., with the nickel foam. Because of the lower standard potential of nickel, redox reaction of the foam with the oxidized TEMPO is, at least theoretically, possible. With respect to point (4), the thickness of the porous electrodes (~1 mm) might be another cause for the higher overpotentials compared to significantly thinner planar electrode (40 μm), since charge carries in thicker electrodes have longer charge carrier paths in the electrode material as well as in the electrolyte. Larger thicknesses consequently also increase the mean distance between counter and working electrode. Deeper investigation on the influence of this parameter requires fundamental improvements in the cutting procedure used to obtain thin porous electrode pieces first and will be part of future investigations.

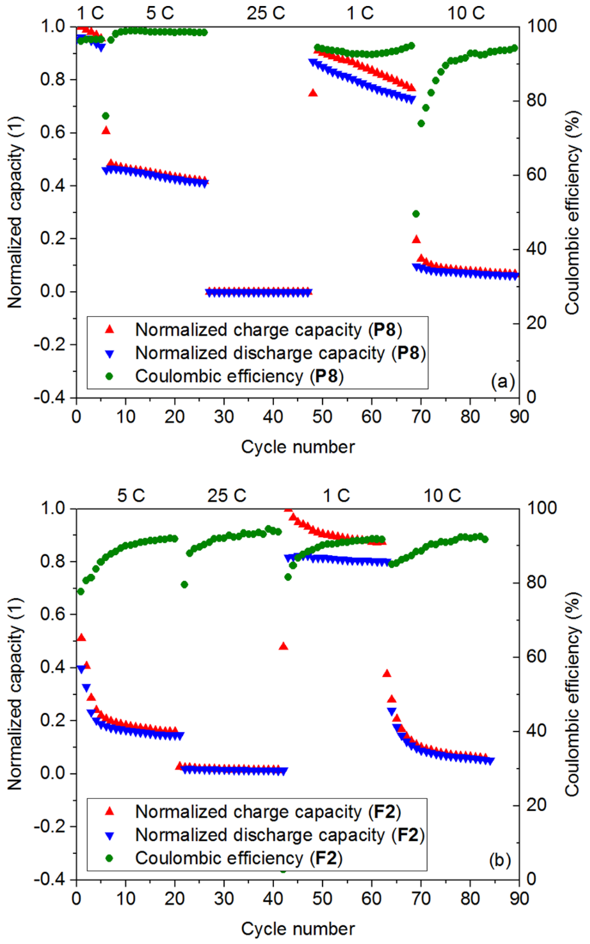

Figure 6. C-rate performances in 1 M $LiClO_4$ EC/DMC (3:7) of (a) porous electrode **P8** with embedded nickel foam (1C, 5C, 25C, 1C, 10C) and (b) planar electrode **F2** (5C, 25C, 1C, 10C) vs Li counter electrode. The capacities are normalized to 1C charge capacity (30 mAh g^{-1}).

3.4. Future Perspectives for Performance Optimizations. To overcome the revealed performance limitations of the ice-templated porous electrodes, different options are available for future investigations. Suspensions can be prepared with different conductive additives to increase the scaffold conductivity. The variation of the amount of water used for the suspension in combination with a variation of the cooling rate could lead to thicker and more densified pore walls, which should have a similarly positive impact on scaffold conductivity due to an increased particle−particle contact in the scaffold. In addition, embedding conductive foams, as implied by one of the experiments presented in this study, can be an interesting option for further optimization approaches. Moreover, using water-soluble polymers for the ice-templating, which uniformly precipitate on the conductive scaffold during solidification, might represent a fundamental source for performance gains as well. Problems arising from the inherently larger distances between thick porous electrodes and their counter electrode may be solved by producing interpenetrating porous electrodes with appropriate separator layers. Optimization potential rests also in the interface between current collector and porous electrode. Embedded conductive foams represent one possible first step for solving this issue.

4. CONCLUSION

For the first time porous electrodes for organic batteries were produced by an ice-templating approach. Microscopy investigations revealed that the pores were well structured and aligned in parallel. Pore diameters were measured for samples ice-templated at different cooling rates. These investigations provided evidence for a direct relationship between pore diameters and the cooling rate as well as for the highly operative control that the ice-templating method enables. However, first electrochemical experiments for comparison of standard planar and porous electrodes of similar composition in 0.1 M $Zn(ClO_4)_2 \times 6\,H_2O$ EC/DMC (3:7) with a zinc counter electrode revealed a lower C-rate capability of the porous electrodes. It was demonstrated that this could be attributed to the significantly larger dimensions of porous electrodes in combination with their lower scaffold conductivity. Approaches for further performance improvements were pointed out including a change in the conductive additives, the amount of water used in the suspensions or embedding porous conductive materials. In summary, ice-templating allows for a great variety of opportunities in manipulating the properties of organic battery electrodes and, hence, in optimizing their performance. New battery setups like, for example, interpenetrating porous cathodes and anodes, suggest themselves and promise new interesting geometric approaches.

ASSOCIATED CONTENT

Supporting Information

The Supporting Information is available free of charge on the ACS Publications website at DOI: 10.1021/acsami.6b05018.

IR spectrum of PTMA, sample photographs of porous electrodes, ESR spectrum of solid PTMA powder, complete elemental analyses data of porous electrodes, particle size distribution of ground PTMA, pore size distributions, and N_2 adsorption/desorption isotherms (PDF)

AUTHOR INFORMATION

Corresponding Author

*E-mail: ulrich.schubert@uni-jena.de. Fax: (+)49 3641 948202. Homepage: www.schubert-group.com.

Present Address

$^{\perp}$S.F. is currently at Ceramic Materials Engineering, University of Bayreuth, Ludwig-Thoma-Strasse 36 b, 95447 Bayreuth, Germany

Author Contributions

The manuscript was written through contributions of all authors. All authors have given approval to the final version of the manuscript.

Notes

The authors declare no competing financial interest.

ACKNOWLEDGMENTS

The authors thank the European Regional Development Fund (ERDF), the Thüringer Ministerium für Wirtschaft, Wissenschaft und Digitale Gesellschaft (TMWWDG), and the European Commission (SMILEY project under Contract FP7-NMP-2012-SMALL-6-310637) for the financial support. The kind help provided by PD Dr. R. Krieg and D. Mierzwa from the Institute of Anatomy II of the Friedrich Schiller University with respect to equipment use and methodological training in preparation of microtome sections for the porous electrodes is thankfully acknowledged, as well as Dr. A. Koschella and Prof. T. Heinze from the Institute of Organic Chemistry and Macromolecular Chemistry for access to an appropriate light microscope for the investigation of the sample sections. Finally, we want to thank Prof. P. Adelhelm and Dipl.-Ing. B. Fähndrich for BET measurements at our porous electrodes.

REFERENCES

(1) Nishide, H.; Koshika, K.; Oyaizu, K. Environmentally Benign Batteries Based on Organic Radical Polymers. *Pure Appl. Chem.* **2009**, *81*, 1961−1970.

(2) Nyholm, L.; Nyström, G.; Mihranyan, A.; Strømme, M. Toward Flexible Polymer and Paper-Based Energy Storage Devices. *Adv. Mater.* **2011**, *23*, 3751−3769.

(3) Novák, P.; Müller, K.; Santhanam, K. S. V.; Haas, O. Electrochemically Active Polymers for Rechargeable Batteries. *Chem. Rev.* **1997**, *97*, 207−282.

(4) Li, C.; Bai, H.; Shi, G. Conducting Polymer Nanomaterials: Electrosynthesis and Applications. *Chem. Soc. Rev.* **2009**, *38*, 2397−409.

(5) Gómez-Romero, P.; Ayyad, O.; Suárez-Guevara, J.; Muñoz-Rojas, D. Hybrid Organic−Inorganic Materials: From Child's Play to Energy Applications. *J. Solid State Electrochem.* **2010**, *14*, 1939−1945.

(6) Nakahara, K.; Oyaizu, K.; Nishide, H. Organic Radical Battery Approaching Practical Use. *Chem. Lett.* **2011**, *40*, 222−227.

(7) Poizot, P.; Dolhem, F. Clean Energy New Deal for a Sustainable World: From Non-Co2 Generating Energy Sources to Greener Electrochemical Storage Devices. *Energy Environ. Sci.* **2011**, *4*, 2003−2019.

(8) Janoschka, T.; Hager, M. D.; Schubert, U. S. Powering up the Future: Radical Polymers for Battery Applications. *Adv. Mater.* **2012**, *24*, 6397−409.

(9) Häupler, B.; Wild, A.; Schubert, U. S. Carbonyls: Powerful Organic Materials for Secondary Batteries. *Adv. Energy Mater.* **2015**, *5*, 11402034.

(10) Sakaushi, K.; Hosono, E.; Nickerl, G.; Gemming, T.; Zhou, H.; Kaskel, S.; Eckert, J. Aromatic Porous-Honeycomb Electrodes for a Sodium-Organic Energy Storage Device. *Nat. Commun.* **2013**, *4*, 1485.

(11) Liu, R.; Duay, J.; Lee, S. B. Heterogeneous Nanostructured Electrode Materials for Electrochemical Energy Storage. *Chem. Commun.* **2011**, *47*, 1384−404.

(12) Lei, Z.; Wei-kun, W.; An-bang, W.; Zhong-bao, Y.; Shi, C.; Yu-sheng, Y. A Mc/Aq Parasitic Composite as Cathode Material for Lithium Battery. *J. Electrochem. Soc.* **2011**, *158*, A991−A996.

(13) Kim, Y.; Jo, C.; Lee, J.; Lee, C. W.; Yoon, S. An Ordered Nanocomposite of Organic Radicalpolymer and Mesocellular Carbon Foam as Cathode Material in Lithium Ion Batteries. *J. Mater. Chem.* **2012**, *22*, 1453−1458.

(14) Kim, J.-K. Micro-Fibrous Organic Radical Electrode to Improve the Electrochemical Properties of Organic Rechargeable Batteries. *J. Power Sources* **2013**, *242*, 683−686.

(15) Kim, J.-K.; Scheers, J.; Ahn, J.-H.; Johansson, P.; Matic, A.; Jacobsson, P. Nano-Fibrous Polymer Films for Organic Rechargeable Batteries. *J. Mater. Chem. A* **2013**, *1*, 2426−2430.

(16) Zhu, Z.; Chen, J. Review—Advanced Carbon-Supported Organic Electrode Materials for Lithium (Sodium)-Ion Batteries. *J. Electrochem. Soc.* **2015**, *162*, A2393−A2405.

(17) Wang, H.-G.; Yuan, S.; Ma, D.-L.; Zhang, X.-B.; Yan, J.-M. Electrospun Materials for Lithium and Sodium Rechargeable Batteries: From Structure Evolution to Electrochemical Performance. *Energy Environ. Sci.* **2015**, *8*, 1660−1681.

(18) Carlsson, D. O.; Mihranyan, A.; Strømme, M.; Nyholm, L. Tailoring Porosities and Electrochemical Properties of Composites Composed of Microfibrillated Cellulose and Polypyrrole. *RSC Adv.* **2014**, *4*, 8489−8497.

(19) Carlsson, D. O.; Nyström, G.; Zhou, Q.; Berglund, L. A.; Nyholm, L.; Strømme, M. Electroactive Nanofibrillated Cellulose Aerogel Composites with Tunable Structural and Electrochemical Properties. *J. Mater. Chem.* **2012**, *22*, 19014−19024.

(20) Olsson, H.; Carlsson, D. O.; Nyström, G.; Sjödin, M.; Nyholm, L.; Strømme, M. Influence of the Cellulose Substrate on the Electrochemical Properties of Paper-Based Polypyrrole Electrode Materials. *J. Mater. Sci.* **2012**, *47*, 5317−5325.

(21) Deville, S. Freeze-Casting of Porous Ceramics: A Review of Current Achievements and Issues. *Adv. Eng. Mater.* **2008**, *10*, 155−169.

(22) Flauder, S.; Gbureck, U.; Muller, F. A. Structure and Mechanical Properties of Beta-Tcp Scaffolds Prepared by Ice-Templating with Preset Ice Front Velocities. *Acta Biomater.* **2014**, *10*, 5148−55.

(23) Stefan, J. Über Die Theorie Der Eisbildung Insbesondere Über Die Eisbildung Im Polarmeere. *Aus den Sitzungsber. kais. Acad. Wiss. Wien* **1889**, *89*, 269−286.

(24) Waschkies, T.; Oberacker, R.; Hoffmann, M. J. Control of Lamellae Spacing During Freeze Casting of Ceramics Using Double-Side Cooling as a Novel Processing Route. *J. Am. Ceram. Soc.* **2009**, *92*, S79−S84.

(25) Stolze, C.; Janoschka, T.; Schubert, U. S.; Müller, F. A.; Flauder, S. Directional Solidification with Constant Ice Front Velocity in the Ice-Templating Process. *Adv. Eng. Mater.* **2016**, *18*, 111−120.

(26) Deville, S.; Bernard-Granger, G. Influence of Surface Tension, Osmotic Pressure and Pores Morphology on the Densification of Ice-Templated Ceramics. *J. Eur. Ceram. Soc.* **2011**, *31*, 983−987.

(27) Lee, K. H.; Lee, Y. W.; Lee, S. W.; Ha, J. S.; Lee, S. S.; Son, J. G. Ice-Templated Self-Assembly of Vopo4-Graphene Nanocomposites for Vertically Porous 3d Supercapacitor Electrodes. *Sci. Rep.* **2015**, *5*, 13696.

(28) Zhang, X.; Li, C.; Luo, Y. Aligned/Unaligned Conducting Polymer Cryogels with Three-Dimensional Macroporous Architectures from Ice-Segregation-Induced Self-Assembly of Pedot-Pss. *Langmuir* **2011**, *27*, 1915−23.

DOI: 10.1021/acsami.6b05018

(29) Huang, Y.; Wu, D.; Jiang, J.; Mai, Y.; Zhang, F.; Pan, H.; Feng, X. Highly Oriented Macroporous Graphene Hybrid Monoliths for Lithium Ion Battery Electrodes with Ultrahigh Capacity and Rate Capability. *Nano Energy* **2015**, *12*, 287−295.

(30) Yoshihara, S.; Isozumi, H.; Kasai, M.; Yonehara, H.; Ando, Y.; Oyaizu, K.; Nishide, H. Improving Charge/Discharge Properties of Radical Polymer Electrodes Influenced Strongly by Current Collector/Carbon Fiber Interface. *J. Phys. Chem. B* **2010**, *114*, 8335−8340.

(31) Banik, S. J.; Akolkar, R. Suppressing Dendritic Growth During Alkaline Zinc Electrodeposition Using Polyethylenimine Additive. *Electrochim. Acta* **2015**, *179*, 475−481.

(32) Nakata, A.; Arai, H.; Yamane, T.; Hirai, T.; Ogumi, Z. Preserving Zinc Electrode Morphology in Aqueous Alkaline Electrolytes Mixed with Highly Concentrated Organic Solvent. *J. Electrochem. Soc.* **2016**, *163*, A50−A56.

Supporting Information

Investigation of Ice-templated Porous Electrodes for Application in Organic Batteries

Christian Stolze,[1,2] *Tobias Janoschka,*[1,2] *Stefan Flauder,*[3,†] *Frank A. Müller,*[2,3] *Martin D. Hager,*[1,2] *Ulrich S. Schubert*[1,2,]*

[1] Laboratory of Organic and Macromolecular Chemistry (IOMC), Friedrich Schiller University Jena, Humboldtstr. 10, 07743 Jena, Germany

[2] Center for Energy and Environmental Chemistry Jena (CEEC Jena), Friedrich Schiller University Jena, Philosophenweg 7a, 07743 Jena, Germany

[3] Otto-Schott-Institute of Materials Research (OSIM), Friedrich Schiller University Jena, Löbdergraben 32, 07743 Jena, Germany

[†] Ceramic Materials Engineering, University of Bayreuth, Ludwig-Thoma-Str. 36 b, 95447 Bayreuth, Germany

Corresponding Author

*Fax: (+)49 3641 948202, E-mail: ulrich.schubert@uni-jena.de, Homepage: www.schubert-group.com

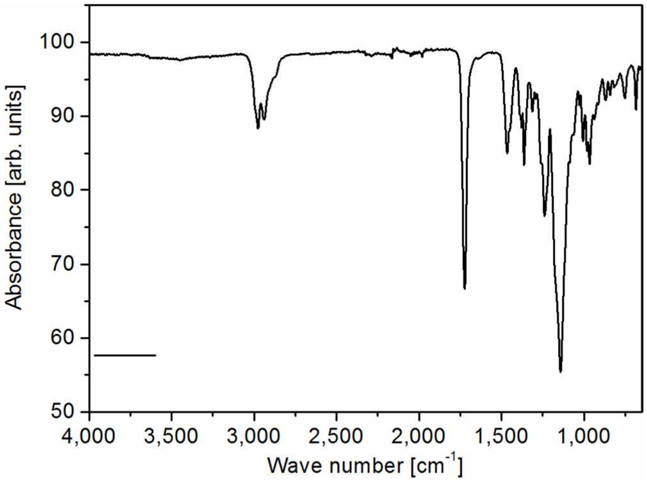

Figure S1. ATR-FTIR spectrum of PTMA with ν_{max} (cm^{-1}): 2976 (m), 2938 (m), 1723 (s), 1465 (m), 1363 (m), 1239 (m), 1141 (s), 1006 (w), 982 (w), 965 (m), 752 (w), 685 (w).

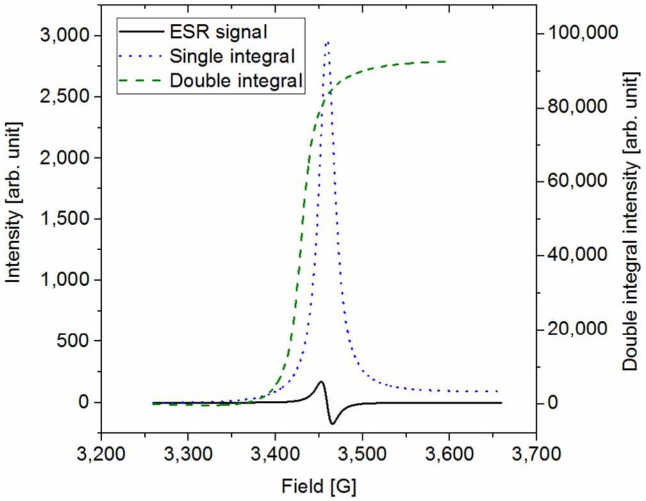

Figure S2. ESR signal of solid PTMA powder with integral and double integral of the signal.

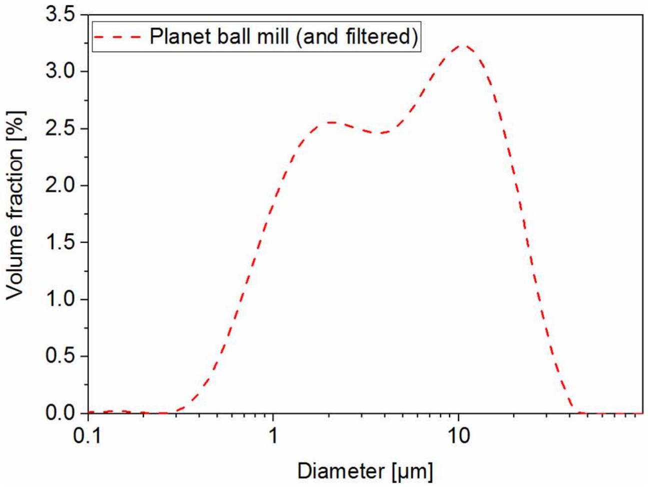

Figure S3. Particle size distribution for PTMA powder, prepared with a planet ball mill and additional filtering (40 µm filter) determined by light scattering.

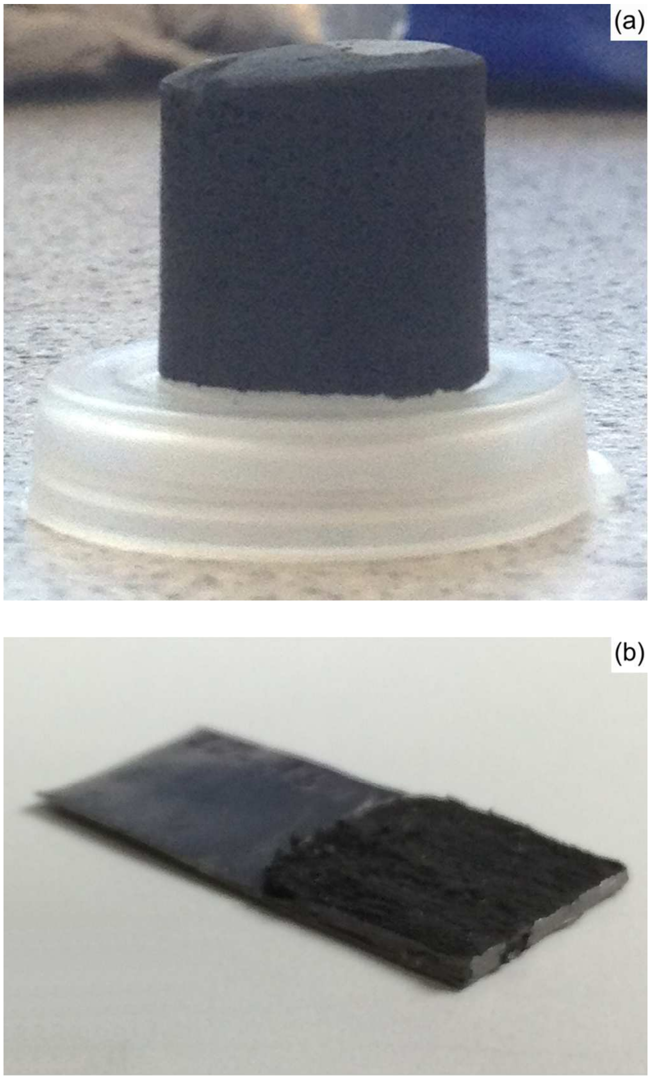

Figure S4. (a) Porous electrode as obtained after ice-templating. (b) Thin piece of a porous electrode glued on graphite foil current collector as used for beaker-type cells.

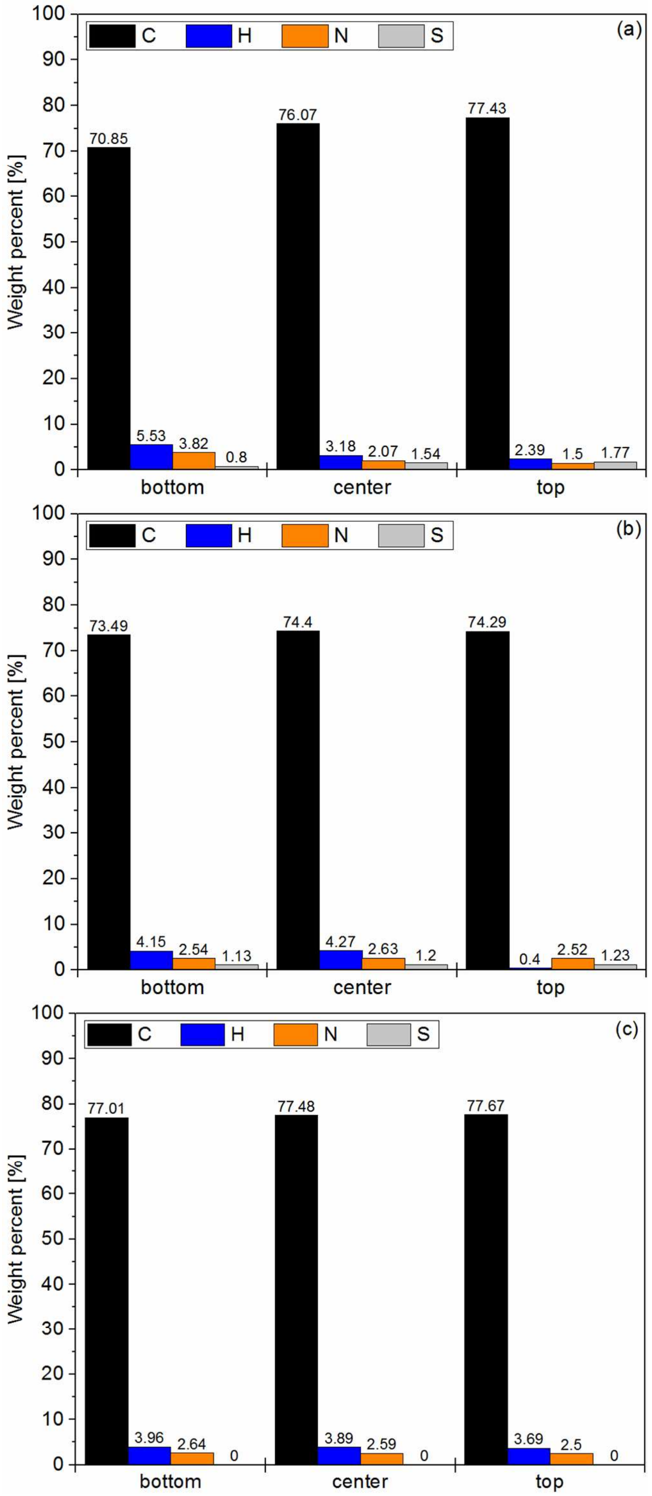

Figure S5. Complete elemental analysis results of porous electrodes made from compositions (a) **P1**, (b) **P2** and (c) **P3**.

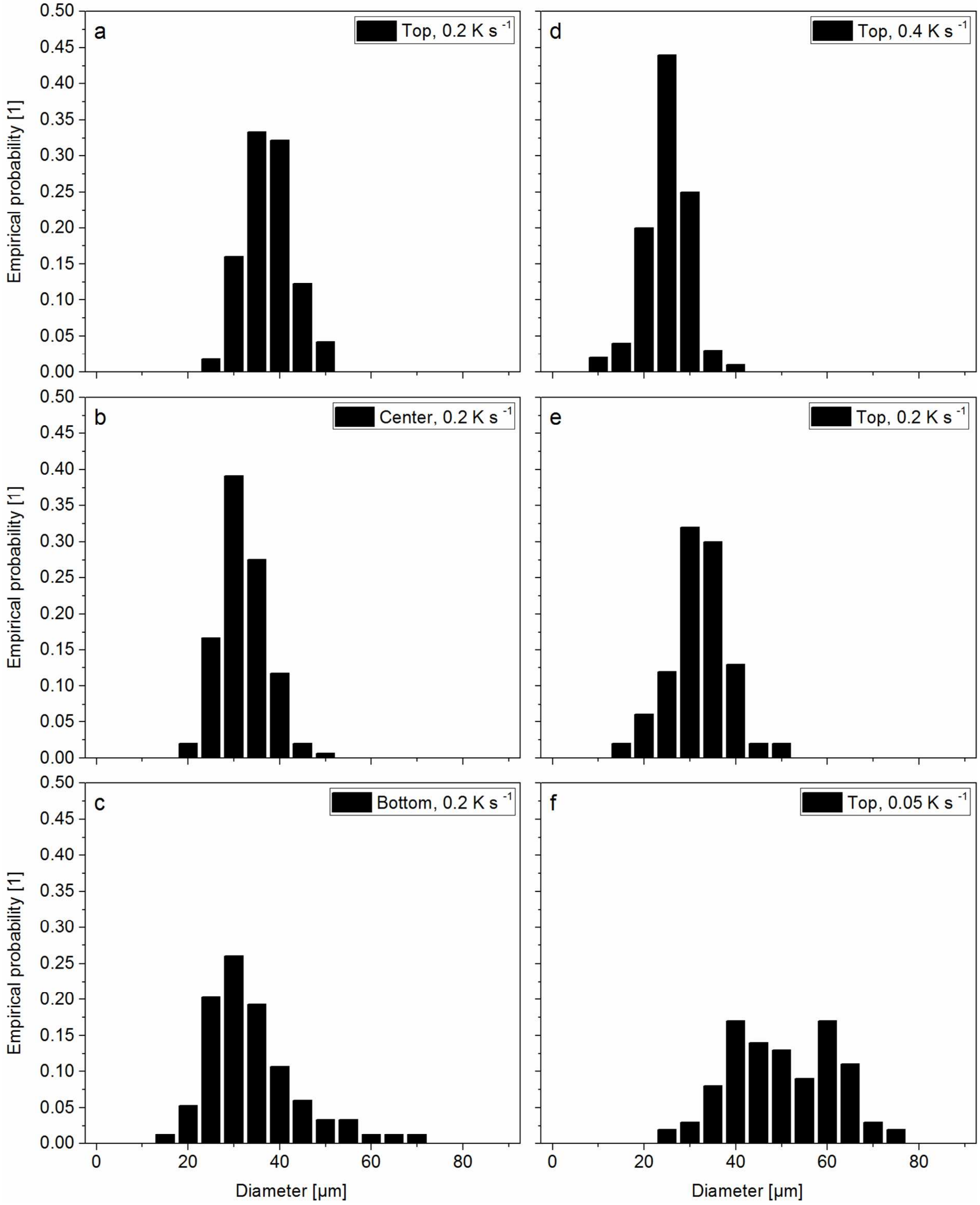

Figure S6. Distribution of pore diameters in porous electrodes made from compositions (a - c) **P5** and (d - f) **P6** at cooling rates of 0.05, 0.2 or 0.4 K s^{-1}, respectively as determined by evaluation of microscopic images of horizontal sections of the samples at three different positions (see also Table 2).

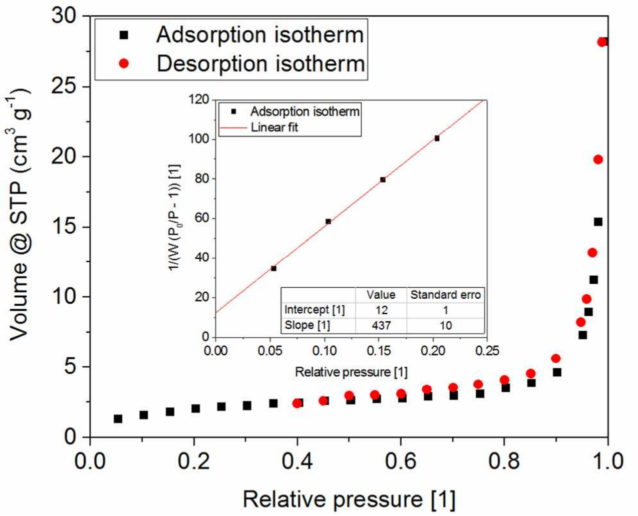

Figure S7. N_2 adsorption isotherm of a porous electrode made from composition **P7** with linear fit of the low-pressure part of the isotherm for BET analysis (slope: (440 ± 10) g^{-1}; intercept: (12 ± 1) g^{-1}).

Publication P3

A Tubular Polymer Redox Flow Battery with a Ceramic Membrane

C. Stolze, C. Schmerbauch, C. Friebe, U. S. Schubert,

Energy Technol. **2017**, *5*, 225-227.

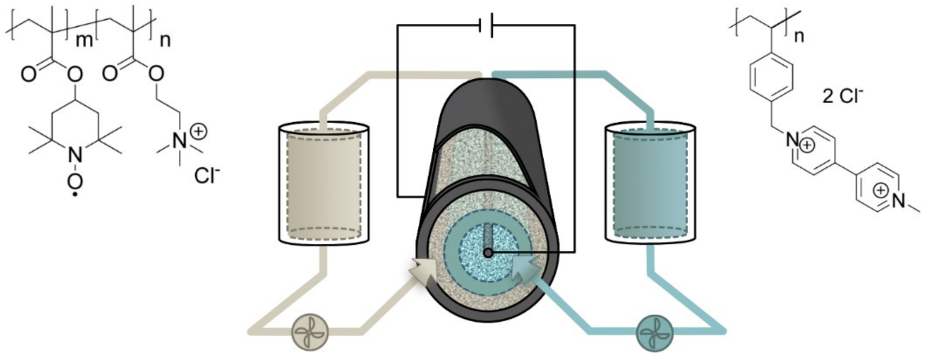

Energy Technology DOI: 10.1002/ente.201600304 **COMMUNICATION**

A Tubular Polymer Redox Flow Battery with a Ceramic Membrane

Christian Stolze,[a, b] Christoph Schmerbauch,[a, b] Christian Friebe,[a, b] and Ulrich S. Schubert*[a, b]

A tubular cell design for redox flow batteries is introduced utilizing chemically, mechanically, and thermally stable ceramic membranes. The basic viability of this new cell design is demonstrated via static and pumped charge and discharge experiments with a laboratory prototype. Electrochemical impedance spectroscopy measurements are presented for the investigation of the internal Ohmic resistance. The technological benefits of a tubular cell design as well as its limitations are discussed.

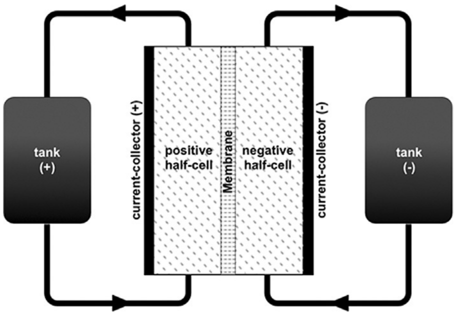

Figure 1. Schematic representation of an RFB with flat cell design.

An increased sensibility for the necessity of a global energy economy capable of providing a cost-efficient and sustainable response to humanity's ever-growing energy consumption has led to remarkable technological advances in the past decades. While particularly the utilization of renewable energy sources seems to be the solution for the energy generation problem, these sources naturally lack the inherently important reliability for powering an energy grid's base load. Hence, new energy storage systems are required to store wind, solar, and water energy when it is available but not consumed and vice versa. Redox flow batteries (RFBs) have become promising candidates providing both the energy capacity as well as the power density that is necessary for this technological challenge.[1] These batteries are based on electrochemically active molecules dispersed in liquid solutions, which serve as anode and cathode materials. They are stored in separate tanks and are pumped through an electrochemical cell consisting of two half-cells, which are separated by a membrane (Figure 1). Due to this technological design, they allow for an independent scaling of energy capacity (defined by tank size) and power density (defined by cell size and design). However, while a lot of effort was put into finding efficient, sustainable, and/or environmentally benign chemicals,[1b,c] introducing flow fields,[2] and improving different parts of the cell (e.g., electrodes, membrane),[1a] only few scientific studies have been conducted on fundamental improvements in the design of the electrochemical cell itself.[3] The by far most common approach is to use a flat cell, which consists of two rectangular half-cells that are stacked onto each other and whose cell volumes are separated by a flat membrane (Figure 1). The obvious advantage of this flat design is the simple ability of stacking identically manufactured cell units, which are, thus, connected in parallel hydrodynamically and in series electrically, leading to an increased system voltage and, consequently, a decrease in necessary current density to reach a certain power density.

A flat cell, however, can be scaled up efficiently only by increasing its basis area rather than its thickness,[2c] because only this approach also leads to an increase of the important membrane area while maintaining short charge-carrier paths between the half-cells. On the other hand, increasing the cell area is accompanied by increasing the area that needs to be sealed to avoid leakage. For many redox systems used for RFBs, oxygen is an additional disturbing factor, which has to be kept out of the cell by appropriate sealing. Another disadvantage of flat redox flow cells is their limitation regarding the choice of membrane types. While polymer-based cation- or anion-conducting membranes[1c] and size-exclusion membranes[4] can be easily applied, the important class of ceramic membranes cannot be practically utilized in flat redox flow cells. This fact is mainly due to the inherent mechanical properties of porous ceramic materials, which show an increasing probability for mechanical failure with increasing area. Nevertheless, ceramics provide unrivaled chemical inertness as well as superior mechanical and thermal stability compared to other membrane materials. These advantages can be utilized to enlarge the number of applicable solvents and molecules and, therefore, provide totally new opportunities for the chemical design of RFB electrolytes.

Certainly, the typical cell design needs to be rethought completely. Among the imaginable alternatives, a tubular cell design particularly suggests itself due to the mechanical nature of ceramics. While there is a significant increase of probability for mechanical failure with increasing area for flat porous ceramic objects, it is negligible for tubular ones whose area is increased by lengthening. In addition, ceramic tubes can be easily produced in nearly arbitrary length by simple extrusion processes.

---

[a] *C. Stolze, C. Schmerbauch, Dr. C. Friebe, Prof. Dr. U. S. Schubert*
Laboratory of Organic and Macromolecular Chemistry (IOMC)
Friedrich Schiller University Jena
Humboldtstr. 10, 07743 Jena (Germany)
E-mail: ulrich.schubert@uni-jena.de

[b] *C. Stolze, C. Schmerbauch, Dr. C. Friebe, Prof. Dr. U. S. Schubert*
Center for Energy and Environmental Chemistry Jena (CEEC Jena)
Friedrich Schiller University Jena
Philosophenweg 7a, 07743 Jena (Germany)

Consequently, this Communication presents a novel approach in both cell design and utilized membrane materials for redox flow batteries. It aims particularly at the demonstration of the basic viability of a tubular cell design with ceramic membranes.

The tubular cell design realized for this study consists of concentric cylinders. At the interior, a graphite rod is used as current collector for the inner half-cell. This rod is surrounded by a graphite felt, which is the porous electrode of the inner half-cell, and the tubular ceramic membrane. The latter consists of an Al_2O_3 substrate with open porosity (30 %, $d_{50}=3$ μm), which was manufactured with a layer made of porous ZrO_2 ($d_{50}=3$ nm) on its exterior face. The ZrO_2 layer is the actual membrane layer, which functions as a size-exclusion membrane (5 kDa). The outer half-cell contains an identical graphite felt surrounding the membrane. A graphite tube is utilized as current collector for the outer half-cell. This setup is encapsulated by a poly(vinyl chloride) (PVC) tube and circular caps are glued on the top and bottom with silicon to seal the cell. Two syringe needles for each half-cell integrated into the caps form the inlet (top) and outlet (bottom) for the electrolytes. Copper wire coiled around the inner graphite rod and outer graphite tube is utilized to connect the cell electrically to the electrochemical setup (Figure 2).

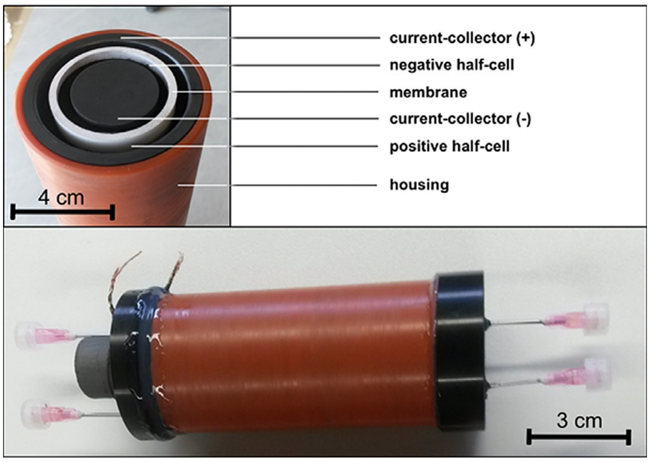

Figure 2. Photographs of the laboratory prototype of a tubular redox flow battery with ceramic membrane.

Such a tubular cell setup is easily scalable by increasing the cell length. While, as it was already pointed out before, an upscaling would increase the sealing area for a flat cell, an upscaling of a tubular cell clearly would keep this area constant because the only areas to be sealed are the caps. Important constructional parameters for the prototype are listed in Table 1.

Electrochemical impedance spectroscopy (EIS) measurements and constant-current charging and discharging experiments were performed to characterize the tubular cell electrochemically. All experiments were carried out in a four-point measurement mode in order to compensate for the non-ideal electrical contact between the copper wires and graphite parts. The studies were executed using a TEMPO-based polymer and a viologen-based polymer (Figure 3) as electrochemically active species for the positive and negative half-cell, respectively. Both compounds are water-soluble and have been synthesized as described in previous studies.[5] Sodium chloride was used as the supporting electrolyte. In order to compensate for transfer of water between the two half-cells due to osmotic and hydrodynamic pressure gradients across the membrane, 1 M NaCl was added to the electrolyte in the negative half-cell, while 3 M NaCl was used for the positive half-cell.

Table 1. Cell dimensions and parameters for the tubular redox flow cell.

Cell part	Inner diameter [mm]	Outer diameter [mm]	Thickness [mm]	Length [mm]
graphite rod	–	22.5	22.5	130
graphite tube	38.5	45	3.25	100
graphite felt[a]	–	–	6	100
ceramic membrane[b]	28.5	32.5	2	100

[a] Given thickness in uncompressed state. [b] Substrate: Al_2O_3 (30 % porosity); membrane: ZrO_2 (on exterior, $d_{50}=3$ nm).

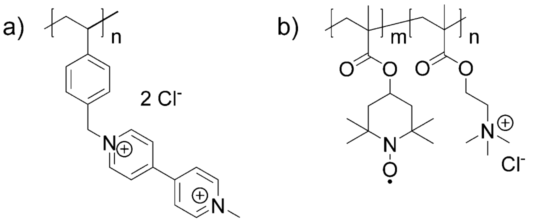

Figure 3. Schematic representation of a) the viologen-based polymer for the positive half-cell and b) the TEMPO-based polymer for the negative half-cell.

Electrochemical impedance spectroscopy was carried out to determine the total internal Ohmic resistance of the cell (Figure 4 a), which yielded a value of 50 $\Omega\,cm^2$ with respect to the membrane area. This rather high resistance is attributed to the thickness and low porosity of the aluminum oxide substrate of the ceramic membrane. Hence, these parameters of the membrane material have to be further optimized. Charging and discharging experiments at 100 mA over 25 cycles in a static and two cycles in a pumped operation mode successfully verified the general viability of the tubular cell design (Figure 4 b), exhibiting capacities of up to 85 mAh, Coulombic efficiencies above 90 %, and energy efficiencies above 83 %. However, while the first data are promising, optimization potential is clearly apparent in the cycling stability and current density of the battery. Performance drawbacks are most likely due to bad electrical contacts and non-ideal sealing materials, which might allow slow diffusion of oxygen into the cell. Improvement of these parameters will be part of future work.

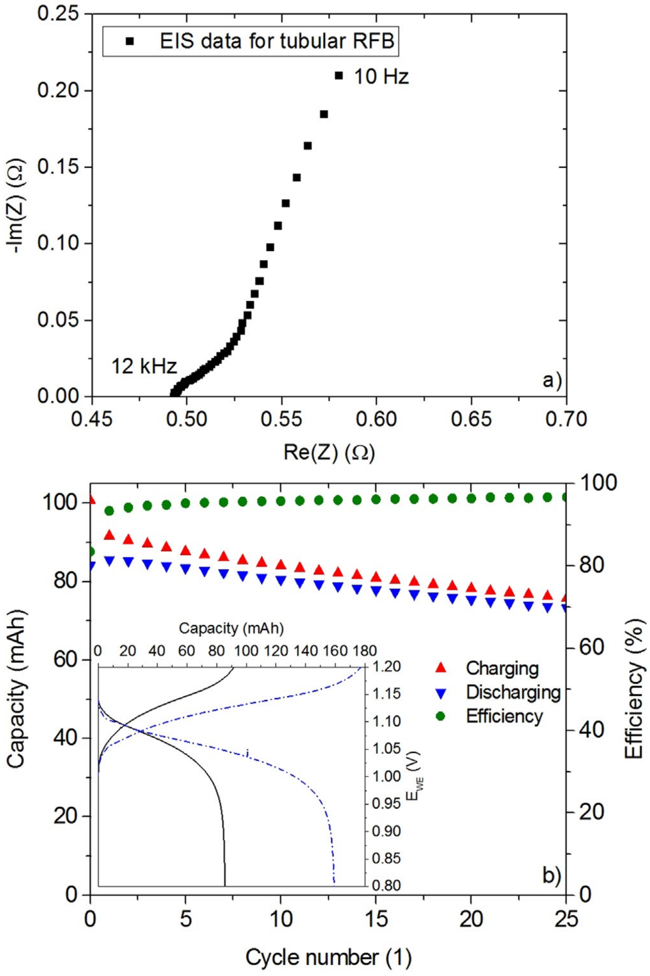

Figure 4. a) EIS for the tubular cell; b) charge and discharge cycles in static operation mode. Inset shows potential-time curves for 2nd cycle in static (solid line) and pumped (dashed line) operation mode.

In summary, a novel tubular cell design concept for redox flow batteries is introduced utilizing, for the first time, ceramic membranes in such a battery. The chemical, thermal, and mechanical stability of ceramic materials and the simple scalability of tubular cells promise new opportunities in the technological development of redox flow batteries (RFBs). The general viability of this new concept is demonstrated experimentally by construction of a laboratory prototype and by electrochemical characterization of the cell loaded with polymer electrolytes via impedance spectroscopy and constant-current measurements in a static and in a pumped operation mode. Strong improvements of the cell performance compared to the ones achieved with the first prototype are expected by optimization of the contact between electrically conductive parts (e.g., felts, current collectors, copper wires), the sealing, and the choice of specific graphite materials.

Experimental Section

Materials

Graphite rod and tube were used as current collectors and were obtained from MERSEN Deutschland Suhl GmbH. Graphite felts (GFA6) were utilized as porous electrodes and were purchased from SGL Carbon SE. The ceramic membrane was tailor-made and obtained from Fraunhofer IKTS Hermsdorf. Silicone was used as sealing material. Deionized water, sodium chloride (Sigma Aldrich GmbH), poly(4-methacryloyloxy-2,2,6,6-tetramethylpiperidine-1-oxyl-*co*-2-(methacryloyl-oxy)-*N*,*N*,*N*-trimethylethane ammonium chloride) and poly(1-methyl-1′-(4-vinylbenzyl)-[4,4′-bipyridine]-1,1′-diium dichloride) (synthesized according to literature reports[5]) were used as electrolytes.

Electrochemical characterization

A VMP3-based 16-channel-potentiostat controlled with EC-Labs software package from BioLogics Scientific Instruments was utilized for the electrochemical measurements. A two-electrode setup with four-point measurement was used for both constant-current and EIS experiments. Galvanostatic measurements were conducted at 100 mA, while EIS was measured at 0.85 V cell voltage with a sinoidal potential signal having an amplitude of 5 mV in a frequency range of 10 Hz to 500 kHz. The high-frequency intercept with the abscissa was used as a measure for the internal cell resistance.

Acknowledgements

The authors thank the European Regional Development Fund (ERDF), the Thüringer Aufbaubank (TAB), and the Thüringer Ministerium für Wirtschaft, Wissenschaft und Digitale Gesellschaft (TMWWDG) for financial support.

Keywords: ceramics · charge carriers · electrochemistry · membranes · redox flow batteries

[1] a) B. R. Chalamala, T. Soundappan, G. R. Fisher, M. R. Anstey, V. V. Viswanathan, M. L. Perry, *Proc. IEEE* **2014**, *102*, 976–999; b) P. Leung, X. Li, C. Ponce de León, L. Berlouis, C. T. J. Low, F. C. Walsh, *RSC Adv.* **2012**, *2*, 10125–10156; c) A. Z. Weber, M. M. Mench, J. P. Meyers, P. N. Ross, J. T. Gostick, Q. Liu, *J. Appl. Electrochem.* **2011**, *41*, 1137–1164.

[2] a) J. Houser, J. Clement, A. Pezeshki, M. M. Mench, *J. Power Sources* **2016**, *302*, 369–377; b) S. Kumar, S. Jayanti, *J. Power Sources* **2016**, *307*, 782–787; c) Q. Xu, T. S. Zhao, C. Zhang, *Electrochim. Acta* **2014**, *142*, 61–67.

[3] a) M. Park, D. S. Shin, J. Ryu, M. Choi, N. Park, S. Y. Hong, J. Cho, *Adv. Mater.* **2015**, *27*, 5141–5146; b) Q. Zheng, F. Xing, X. Li, T. Liu, Q. Lai, G. Ning, H. Zhang, *J. Power Sources* **2015**, *277*, 104–109; c) O. David, Y. Gendel, M. Wessling, *J. Membr. Sci.* **2014**, *461*, 139–145.

[4] T. Janoschka, N. Martin, U. Martin, C. Friebe, S. Morgenstern, H. Hiller, M. D. Hager, U. S. Schubert, *Nature* **2015**, *527*, 78–81.

[5] T. Janoschka, S. Morgenstern, H. Hiller, C. Friebe, K. Wolkersdörfer, B. Häupler, M. D. Hager, U. S. Schubert, *Polym. Chem.* **2015**, *6*, 7801–7811.

Received: May 12, 2016
Revised: June 29, 2016

Publication P4

Microtubular Flow Cell Design Utilizing Commercial Hollow Fiber Dialysis Membranes for Size-Exclusion Based Flow Batteries

C. Stolze, T. Janoschka, J. Winsberg, M. Strumpf, M. D. Hager, U. S. Schubert,

Energy Technol. **2018**, *6*, 2296-2310.

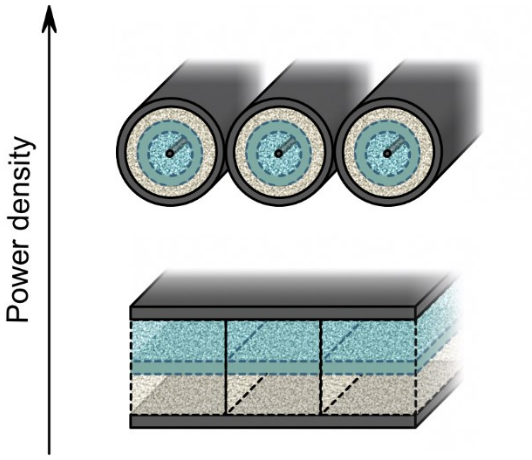

Energy Technology DOI: 10.1002/ente.201800183 FULL PAPER

Micro-Tubular Flow Cell Design Utilizing Commercial Hollow Fiber Dialysis Membranes for Size-Exclusion Based Flow Batteries

C. Stolze,[a, b] T. Janoschka,[a, b] J. Winsberg,[a, b] M. Strumpf,[a, b] M. D. Hager,[a, b] and U. S. Schubert*[a, b]

A micro-tubular flow cell (μTFC) is presented as a novel approach for flow cell design, which differs from previous tubular approaches by its lower cell diameter (3 mm) and half-cell thicknesses (≤850 μm). Analytical expressions for the ohmic resistances of both micro-tubular and conventional filter-press flow cells (cFFC) are derived, which imply that optimized μTFCs can be expected to have an at least two-fold lower ohmic resistance compared to equally sized cFFCs in the future. The theoretical findings motivate the experimental realization of a first μTFC single-cell unit to investigate the basic feasibility of this approach. This investigation is enabled by the utilization of a redox-active polymer in conjunction with a commercially available micro-tubular dialysis membrane (diameter: 1 mm). Aqueous solutions of poly(2,2,6,6-tetramethylpiperidin-4-yl methacrylate-*co*-poly(ethylene glycol)methyl ether methacrylate) (positive half-cell) and the Zn/Zn^{2+} redox couple (negative half-cell) are utilized as model electrolytes to examine the electrochemical performances of this first μTFC prototype. Furthermore, the common usage of area current densities based on the geometric area of the flow cell is critically discussed. A current density based on the cell volume is suggested as a less ambiguous and, hence, a more reliable parameter for performance evaluation.

Introduction

The first recorded reference to flow batteries as a feasible concept for energy storage dates back to the 1940s.[1] A lot of progress regarding the cell performance characteristics and the utilized redox chemistries has been made since then, in particular due to the increased research efforts in the past two decades.[2] These research efforts are, in general, rather focused on the improvement of the utilized materials for the different cell parts. However, the basic setup of a flow cell has not changed significantly over the past decades. A milestone in flow cell design research was the application of flow field concepts that had been previously known from fuel cells. Flow fields drastically reduce the pressure drop within the flow cell and, hence, increase the power and the energy efficiency of the whole system.[3] The material research efforts and the application of flow fields resulted in a power density increase of more than one order of magnitude since the 1970s.[3b] Despite that, a fundamental deviation from the conventional filter-press design has occurred only in a few cases.

One recent example for a fundamentally new cell design approach is the development of tubular flow cells.[4] Figure 1 schematically illustrates the basic setup of a tubular flow battery in comparison to a conventional filter-press flow battery (cFFB). Tubular cell designs entail a variety of advantages compared to filter-press designs such as a reduced sealing area, the applicability of ceramic membranes, a higher membrane area to volume ratio, and a fundamentally new design flexibility. However, the power density of experimentally realized tubular flow batteries is still inferior to that of cFFBs and demands further research and development efforts. While one approach to achieve higher power densities is the perfection of manufacturing strategies and cell materials, another one is to decrease power losses by reduction of the cell diameter and half-cell thicknesses (= distance from current-collector to membrane). The reduction of half-cell thicknesses from the upper to the lower millimeter or even micrometer range has already proven to drastically increase the power density for conventional filter-press flow cells (cFFC).[3a,5] Thus, thickness reduction is a logical step for tubular flow cells as well. For differentiation of such – not yet realized – smaller tubular flow cells from the literature-known tubular flow cells,[4] the term micro-tubular flow cells (μTFC) is suggested. It is used throughout this study to designate tubular flow cells with half-cell thicknesses ≤1 mm and cell diameters ≤4 mm. Micro-tubular approaches have already proven beneficial for fuel cells, namely due to[6]

- a significantly increased power density,
- a beneficial heat distribution,

---

[a] C. Stolze, T. Janoschka, J. Winsberg, M. Strumpf, Dr. M. D. Hager, Prof. Dr. U. S. Schubert
Laboratory of Organic and Macromolecular Chemistry (IOMC)
Friedrich-Schiller-University Jena
Humboldtstr. 10, 07743 Jena (Germany)
E-mail: ulrich.schubert@uni-jena.de

[b] C. Stolze, T. Janoschka, J. Winsberg, M. Strumpf, Dr. M. D. Hager, Prof. Dr. U. S. Schubert
Center for Energy and Environmental Chemistry Jena (CEEC Jena)
Friedrich-Schiller-University Jena
Philosophenweg 7a, 07743 Jena (Germany)

Supporting information for this article is available on the WWW under https://doi.org/10.1002/ente.201800183

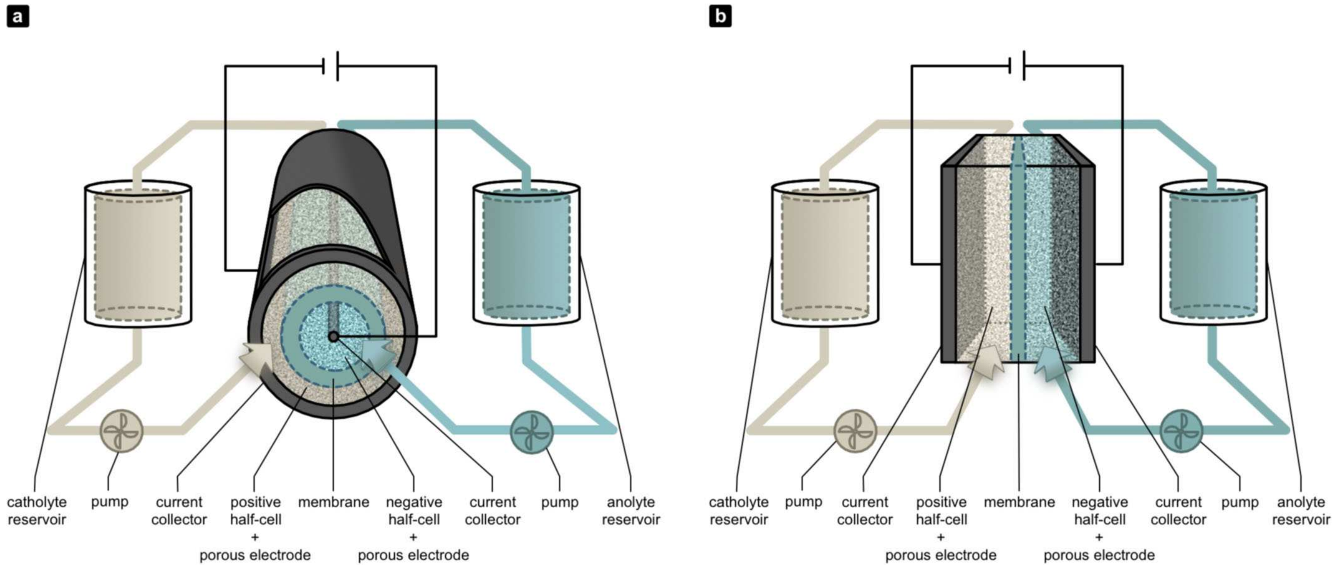

Figure 1. Schematic representation of (a) a µTFB and (b) a cFFB with corresponding electrolyte tanks, pumps and external circuits. The µTFC is illustrated with a cut in the outer current collector only in order to allow insight into the inside of the cell.

- a quicker start-up capability,
- an enhanced cell design flexibility,
- an improved applicability to mobile applications, and
- a reduced capital cost.

Both single-cell devices and stack designs have been successfully demonstrated for micro-tubular fuel cells. Therefore, the investigation of micro-tubular approaches for flow cells, which are in many aspects technologically comparable to fuel cells, seems highly interesting. Due to the lack of tubular ion-exchange membranes with diameters ≤ 2 mm, however, micro-tubular flow batteries have not been realized yet. Hence, the tubular flow cells reported so far had half-cell thicknesses in the medium to lower millimeter range and cell thicknesses in the upper millimeter range. The smallest tubular flow cell was reported by Park *et al.* and had a cell diameter of 7 mm and a membrane diameter of roughly 5 mm.[4b] The authors demonstrated a hybrid flow cell for which only the positive half-cell could be pumped and their design approach most-likely prohibits further significant reduction of both half-cell thickness and cell diameter. Ressel *et al.* reported a tubular cell with a slightly larger outer dimension of 9 mm and a membrane diameter of 5 mm. With half-cell thicknesses of 1 mm and 1.2 mm, respectively.[4c] While further reduction of half-cell thickness might be achieved for their design, further reduction of the membrane and cell diameter is strongly limited by the applicability of the contact welding approach, which the authors used for production of the tubular membrane from a flat Nafion membrane. Consequently, no feasible approach for micro-tubular flow cells is known so far. With the invention of aqueous polymer-based flow batteries,[7] however, micro-tubular flow cells with both low outer and inner dimensions have become a realistic technological approach. This is due to the fact, that simple dialysis membranes can be used, which are also readily available in a micro-tubular form with diameters ≤ 1 mm.

The study at hand makes use of this circumstance to investigate the first micro-tubular approach for flow batteries. In a first part, important theoretical aspects of a micro-tubular flow cell geometry are investigated and discussed. An analytical approximation for the lower limit of ohmic resistance and overvoltage reduction compared to cFFCs is mathematically derived and the theoretical feasibility of upscaling is discussed to elucidate the practical prospects of a micro-tubular cell design approach. In a second part, a first single-cell unit prototype of a µTFC is investigated experimentally to verify the feasibility of a size-exclusion based micro-tubular flow battery approach. This single-cell unit is characterized by a cell diameter of 3 mm, a membrane diameter of 1 mm, and half-cell thicknesses of about 375 µm (negative inner half-cell) and 850 µm (positive outer half-cell). It is, thus, the first micro-tubular flow cell reported in literature. The previously examined and oxygen-insensitive redox active polymer poly(2,2,6,6-tetramethylpiperidin-4-yl methacrylate-*co*-poly(ethy-lene glycol)methyl ether methacrylate) (poly(TMA-*co*-PEGMA)) is utilized along with the Zn/Zn^{2+} redox couple[8] as simple and easy-to-handle model electrolytes for all cell tests.

Theoretical Aspects of Micro-Tubular Flow Cells

Preceding the experimental analysis of a first micro-tubular flow cell prototype, this section elucidates the theoretical impact of a micro-tubular geometry on the performance limiting ohmic resistance of a flow cell. Furthermore, the theoretical challenges and approaches for upscaling of µTFCs are thoroughly discussed to evaluate the future practicability of µTFBs. Additionally, a general reasoning on the performance comparison of flow cells based on volumetric current densities instead of area current densities is detailed.

Cell overvoltages

The ohmic overpotential and, consequently, the corresponding ohmic resistance usually represents the largest fraction of a flow cell's overpotential and its impedance, respectively, in modern flow batteries.[5a,9] The ohmic cell resistance depends on the geometric properties of the cell parts and can be approximated analytically by some simple mathematical considerations. In order to compare cFFCs and µTFCs with respect to their ohmic resistances, an equal unit volume, $V_{cell} = D^2L$, is assumed. This volume is considered to have height and width, D, and a length, L. Figure 2a and Figure 2b illustrate how both cell types are placed into this well-defined volume. If identical materials are assumed for the cell parts of both cell types, the ohmic resistance, R_i, of the i^{th} cell part can be calculated from the specific resistances, ρ_i, of the cell part and its cross-sectional area, A_i, by integration over its thickness in the direction of current flow:

$$\int dR_i = \int \frac{\rho_i(l)}{A_i(l)} dl. \tag{1}$$

All specific resistances can be treated as constants, because homogeneous materials are utilized in modern flow batteries. Assuming highly-conductive current collectors, which is a reasonable assumption for state-of-the-art flow cells as well, only the porous electrodes, the electrolytes, and the membrane contribute significantly to the cell's ohmic resistance. Furthermore, high-power flow cells utilize a zero-gap architecture,[3a,5c,10] in which porous electrodes completely fill the space between the current collector and the membrane in each half-cell. Hence, the half-cell volume can be treated mathematically as a homogeneous mixed phase consisting of the porous solid electrode, which is soaked with the liquid electrolyte. For the calculation, an apparent specific conductivity can be assigned to the mixed phase in each half-cell. Subsequently, the overall ohmic resistance, R_{cell}, of each flow cell can be expressed by

$$R_{cell} = \rho_E^{neg} \int \frac{1}{A_E^{neg}(l)} dl + \rho_M \int \frac{1}{A_M(l)} dl + \rho_E^{pos} \int \frac{1}{A_E^{neg}(l)} dl. \tag{2}$$

The superscripts *neg* and *pos* denote the variables for the negative and the positive half-cell, respectively, while the subscripts E and M denote the variable for the electrode/electrolyte mixed phase (E) and the membrane (M). For the conventional filter-press flow cell, the cross-sectional areas that are perpendicular to the current flow are constant and equal for all cell parts and correspond to the geometric area calculated from the cell's width, D, and its length, L. In contrast to that, the cross-sectional area of a micro-tubular cell changes along the direction of current flow (radial direction). Considering both of these facts, the integral of equation (2) can be readily calculated for the cFFB and the µTFB, which results in the following equations for their ohmic resistances:

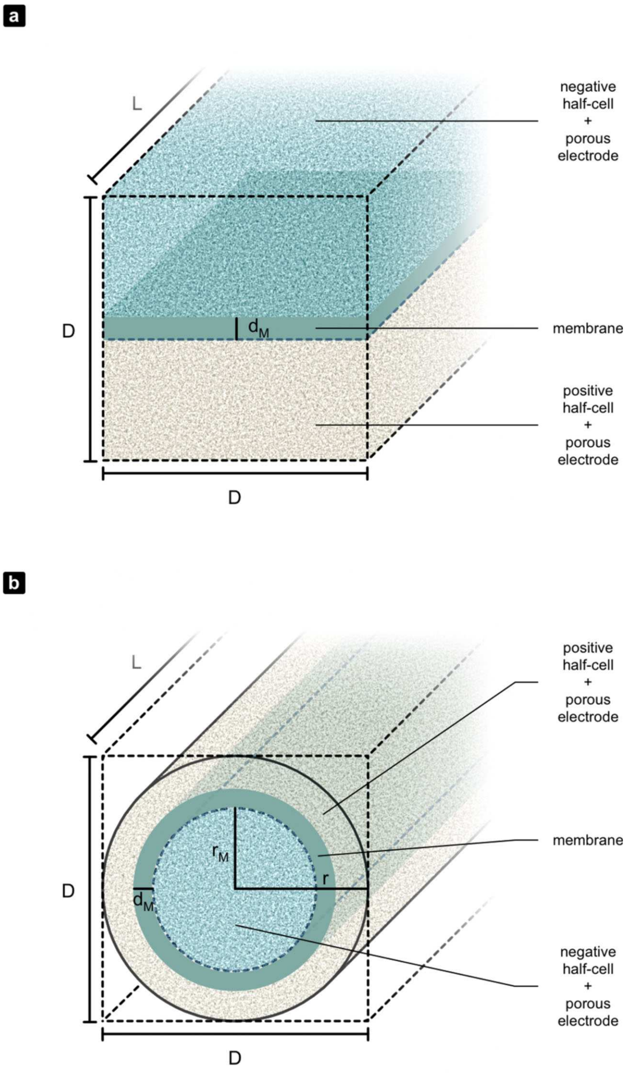

Figure 2. Schematic representation of the geometric models used for the approximation of ohmic resistances of (a) a cFFB and (b) a µTFC. Both cell types are placed in a cell volume of equal outer dimensions D×D×L. Only the membrane and the half-cells with porous electrodes, but without current collectors, are considered.

$$R_{cFFB} = \frac{1}{L}\left[\rho_E^{neg}\frac{d_E^{neg}}{D} + \rho_M\frac{d_M}{D} + \rho_E^{pos}\frac{d_E^{pos}}{D}\right], \tag{3}$$

$$R_{\mu TFB} = \frac{1}{2\pi L}\left[\rho_E^{neg}\ln\left(1+\frac{d_E^{neg}}{r_E^{neg}}\right) + \rho_M\ln\left(1+\frac{d_M}{r_M}\right) + \rho_E^{pos}\ln\left(1+\frac{d_E^{pos}}{r_E^{pos}}\right)\right]. \tag{4}$$

In these equations, the $d_i^{pos/neg}$ denote the thickness and the $r_i^{pos/neg}$ denote the inner radius of the corresponding cell part. Three considerations allow to derive a lower limit for the ratio of the ohmic resistance of a cFFC to the ohmic resistance of a µTFC:

(i) It can be stated that $\rho_E^{neg} \approx \rho_E^{pos} \equiv \rho_E \ll \rho_M$ for state-of-the-art flow batteries.
(ii) A series expansion of the natural logarithm allows the approximation $\ln(1+x) \leq x$.
(iii) For equal half-cell volumes, a given cell diameter, and a given membrane thickness, the radius of the membrane is defined by $r_M = 0.5D\sqrt{0.5 - d_M^2 D^{-2}} - 0.5 d_M$.

Application of assumptions (i) and (ii) to equations (3) and (4) yields the expressions:

$$R_{cFFB} \approx \frac{\rho_M}{L}\frac{d_M}{D}, \tag{5}$$

$$R_{\mu TFB} \approx \frac{1}{2\pi}\frac{\rho_M}{L}\ln\left(1+\frac{d_M}{r_M}\right) \leq \frac{1}{2\pi}\frac{\rho_M}{L}\frac{d_M}{r_M} \approx \frac{1}{2\pi}\frac{D}{r_M}R_{cFFB}. \tag{6}$$

Consequently, the lower limit for the ratio of the ohmic cell resistances of both cell types can be approximated by rearrangement of inequation (6) and utilization of assumption (iii),

$$\frac{R_{cFFB}}{R_{\mu TFB}} \geq 2\pi\frac{r_M}{D} = \pi\left(\sqrt{\frac{1}{2}-\frac{d_M^2}{D^2}} - \frac{d_M}{D}\right). \tag{7}$$

Modern flow cell membranes are characterized by thicknesses of roughly 50 µm. Half-cell thicknesses of high-performance cFFCs are usually in the range of 900 µm.[5a,10–11] Using these reasonable values for d_M and D, inequation (7) yields a ratio of above two. According to this approximation, a µTFC is able to achieve an at least two-fold lower resistance than a cFFC, if equal conditions (materials, outer dimensions, flow rate, etc.) are assumed. In other words, if the same amount of current is applied to both cell types, the ohmic overpotential of the µTFC will be at least two-fold lower than that of a comparable cFFC. The physical reasons for these difference are, basically,

- the shorter charge carrier pathways within the electrodes and the electrolytes of the micro-tubular geometry and
- the higher membrane area to volume ratio of the µTFC.

It needs to be pointed out that the discussion above is based on a single-cell unit level. Additional ohmic overvoltages will naturally occur during upscaling. This is true, however, for both cFFC and µTFC. On the other hand, the obtained minimum of a two-fold decrease in ohmic overvoltage results from very conservative assumptions that are already in favor of the cFFC. In particular, assessment (ii) represents an overestimation which consequently causes an underestimation of the real performance benefit of the µTFCs. Thus, it is likely that even higher performance gains can be expected from a well-designed micro-tubular cell setup; even, if upscaling is considered.

Upscaling approaches for micro-tubular flow cells

While upscaling of micro-tubular cells is clearly beyond the scope of this first proof-of-principle study, the theoretical opportunities for upscaling need to be elucidated in order to motivate research efforts in this novel field and to evaluate critically, whether the µTFC represents a feasible concept for the future of flow batteries. In particular, following questions arise, if upscaling of micro-tubular flow cells is considered:

- Can µTFCs only be upscaled by varying their length?
- Will current flow along the axial direction of the tube cause ohmic overvoltages that render upscaling of this cell type infeasible?
- Can stacking of cells, i.e., electrical series connection be realized in an efficient manner?

In general, flow cell upscaling from the laboratory scale to a "real battery" scale commonly includes two distinct steps, which have to be considered separately:

(i) Increasing single-cell size from laboratory scale to achieve a sufficient power per single-cell.
(ii) Stacking of large single-cells to achieve a high overall battery voltage.

Increasing the length of µTFCs for the purpose of upscaling has two remarkable disadvantages. First, a longer cell necessitates transport of current over a larger distance along the axial direction, which would cause a higher ohmic resistance. Second, lengthening also increases pressure drop. Therefore, extending the µTFC to arbitrary lengths represents no feasible option for upscaling. For cFFCs, the first upscaling step is achieved by increasing the geometric area of all components (membrane, electrodes, current collectors, etc.) from a few cm^2 (laboratory scale) to a value between 0.1 and 1 m^2 (battery scale). Looking at this upscaling process from an abstract point of view, increasing the geometric area of a cFFC is physically equivalent to connecting several small single-cell units in parallel. Such an upscaling process is illustrated schematically in Figure 3a. This approach is also feasible for µTFCs: Instead of increasing the length of a µTFC, upscaling can be achieved by parallel connection of several micro-tubular single-cell units as illustrated schematically by Figure 3b. The increase of single-cell size by simple parallel connection of identical single-cell units leads to an increase in cell size without significant increase in cell resistance. The electrical parallel connection reduces the total resistance, R_{cell}, of the upscaled cell in accordance with Kirchhoff's law, $R_{cell}^{-1} = \sum_j R_j^{-1}$. For N identical single-cell units with the equal resistance, R_u, it follows directly that $R_{cell} = R_u\, N^{-1}$. The total area, A_{cell}, and the total volume, V_{cell}, of a cell composed of these N single-cell units with an area A_u and a volume V_u is $A_{cell} = A_u\, N$ and $V_{cell} = V_u\, N$. As a consequence, it can be stated that the products of the resistance with the geometric area and the volume, respectively, are independent from the overall cell size:

$$R_{cell}\, A_{cell} = R_u\, A_u \text{ and } R_{cell}\, V_{cell} = R_u\, V_u. \tag{8}$$

These considerations already provide an answer to the

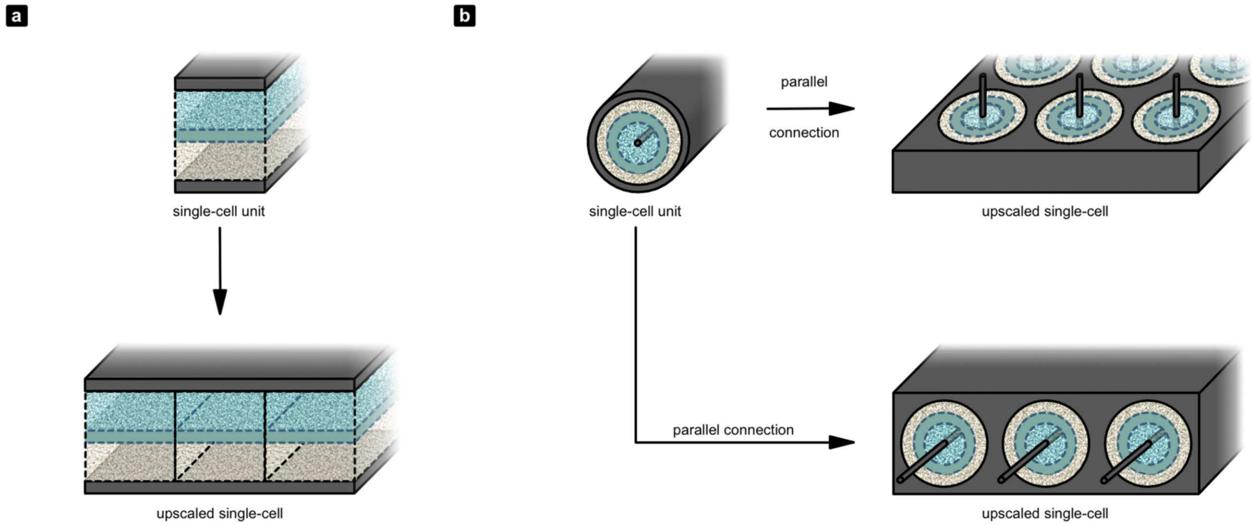

Figure 3. Theoretical principal for the first upscaling step: Enlarging single-cell size by parallel connection of small single-cell units illustrated for both (a) cFFCs and (b) μTFCs. The μTFC single-cell units are embedded in a conductive matrix, which forms the current collector for the positive (outer) half-cells. Inner current collectors are connected with each other externally (not depicted).

first and the second question considered at the beginning of this section: Upscaling of a μTFC does not necessitate to increase its length at all. Additionally, since parallel connection does not impose any requirements on the cell length, the micro-tubular cells can be kept sufficiently short to mitigate additional voltage drops caused by current flow in axial direction of the cell (see Figure 3b, upper upscaling path).

The second upscaling step involves electrical series connection of the larger cell units obtained from the first upscaling step. For cFFCs this step is achieved by utilization of bipolar plates and a simple stacking procedure.[3b] With regard to μTFCs, a stacking procedure is not as readily available and development of a stacking procedure will indubitably be one of the more challenging tasks of future research in this new research field of micro-tubular flow cell design. However, the validity of micro-tubular upscaling approaches has already been demonstrated successfully for micro-tubular fuel cells.[6c–e] Due to the similarity of flow cell and fuel cell technologies, it is, therefore, very likely that the upscaling approaches of micro-tubular fuel cells can be adapted for micro-tubular flow cells. Another aspect of upscaling involves the system costs. The small diameters of all cell parts clearly increase the assembling complexity. At a first glance, this might imply higher costs for the manufacturing of flow cells of this novel type compared to cFFCs. On the other hand, this cost increase might be compensated by the increased power density, the decreased system size, the reduced material demand, and is also a question of technological realization of fabrication in a large scale industrial approach. That is, industrial production might, e.g., allow compact extrusion based processes for the tubular cell parts, which can significantly reduce the manufacturing costs for the single-cell units. However, any economic estimation would be unrealistic at this early stage of development and, clearly, this topic demands further attention in the future, when the technological challenges are solved.

Resistance and current normalization

Finally, some general thoughts on the comparability of flow cell performances need to be emphasized prior to the experimental evaluation of the first μTFC prototype. The electrochemical response of a cell or half-cell to an applied current or an applied potential is always dependent on the surface area of the electrode. Therefore, it is common sense to normalize currents to the surface area of the electrode to compare different electrochemical systems. This, however, is difficult in terms of porous electrodes whose real intrinsic and electrochemically active surface area is often hard to determine. Due to this difficulty, currents in flow battery research are commonly normalized to the geometric area of the flow cell. Similarly, resistance values are often normalized by multiplication with the geometric area. The applicability of this product parameter is justified by its size-independence, which was already elucidated by the derivation of equation (8) in the previous section. Despite that mathematical justification, this area-based normalization has a few major downsides, in particular, if non-planar flow cell geometries like tubular cells are involved. These disadvantages are, e.g., that

- the choice of reference geometric area for a flow cell is ambiguous, if the cross-sectional area changes in the direction of current flow (e.g., as for tubular cells where current flows radially and cross-sectional area changes in radial direction),

- equal area current densities for different cell thicknesses result in different utilization factors of the electrolyte, and
- area current densities do not capture different absolute electrode surface areas resulting from different cell thicknesses.

Needless to mention that the situation is complicated even more by the complex interplay of performance determining overvoltage changes originating from cell thickness differences.[5a] Direct comparison of flow cell performance at equal geometric area current densities is, thus, in many cases not really meaningful. Therefore, the authors of the study at hand believe that a better way of current normalization is to use the flow cell volume as reference for flow cell comparison, which results in volumetric current densities and volumetric resistances. These have the advantage that for flow cells of different cell volume and, in particular, different geometries equal amounts of charge are inserted per unit of volume at equal volumetric current densities. This ensures that flow cells of different volumes have the same utilization factor at equal volumetric current densities (if equal electrolyte exchange rates are assumed). Furthermore, volumetric current densities ensure equal area current densities with respect to the real (intrinsic) surface area of the porous electrode, if cells of different geometry and thicknesses (but for equal electrode materials) are compared. Consequently, volumetric current densities are utilized in the present study to evaluate the performance of a μTFC prototype. Nevertheless, all necessary cell dimensions are stated throughout this study and allow the calculation of conventional area current densities.

Results and Discussion

A first μTFC prototype was developed (see Figure 7 and experimental section for details) and the experimental investigations conducted on this prototype are presented in this section. A flow-through cFFC without flow fields was used as a reference cell for all performance experiments. While this cFFC was utilized in the majority of literature-known aqueous polymer-based flow batteries, it needs to be emphasized that it is not optimized with respect to high-power applications. Nevertheless, the direct comparison of the μTFC prototype to this reference cell provides valuable information that enable, e.g., to differentiate between effects related to the model electrolyte and effects related to the cell setup.

Ohmic resistances

Ohmic resistances of both cell types were investigated by means of electrochemical impedance spectroscopy. Figure 4 shows exemplary impedance spectra for both cell types obtained before and after galvanostatic cycling at 5 mA cm^{-3} for 60 cycles. The absolute ohmic cell resistances of cells filled with fresh electrolytes were 0.6±0.1 Ω (average of seven measurements and their standard deviation) for the conventional filter-press flow cell and 2.0±0.7 Ω (average of seven measurements and their standard deviation) for the micro-tubular one. Impedance measurements were performed after fresh assembly of the cells, after cleaning of the cells with distilled water, and/or after exchange of the zinc wire (only μTFB). The observed standard deviations indicate that cell resistances of both cell types are quite sensitive to these procedures. In order to obtain a value which can be compared between the two different cell designs, the different cell volumes need to be considered. As thoroughly discussed, the product of cell volume and resistance, equation (8), is a reasonable parameter for the comparison of cells of different size and different geometries. The volumetric resistance of both cells yielded a value of 2.9±0.5 Ω cm^3 for the cFFC and a value of 0.3±0.1 Ω cm^3 for the μTFC. Hence, a difference of one order of magnitude was observed between the μTFC and the cFFC reference at similar compression rates of the porous electrodes in both cell types (25 % for cFFC, 28 % for μTFC). With respect to the previously reported larger tubular cells, a comparison with the cell of Park *et al.* is not possible as no series resistance was stated in their study at all.[4b] Ressel *et al.* reported a value of 6.1 Ω cm^2 for their zero-gap vanadium-based tubular flow battery, which corresponds to a volumetric value of 0.7 Ω cm^3 and, hence, a more than two-fold higher volumetric resistance.[4c] Compared to the benchmark setting quinone-bromine and all-vanadium cFFCs reported by Chen *et al.* and Zhou *et al.*,[5c,10] however, the volumetric resistance of the presented μTFC prototype is one order of magnitude higher. This difference is attributed to the optimized electrode materials and, in particular, the zero-gap cell architectures utilized by these cFFCs. A zero-gap architecture could not be used within this first μTFC prototype due to the well- known dendrite formation of the utilized Zn/Zn^{2+} redox couple.

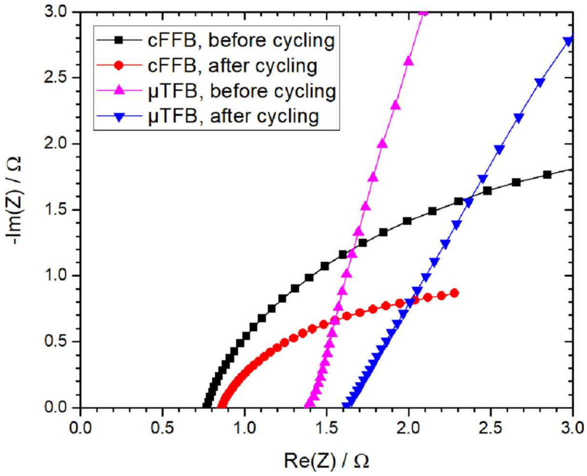

Figure 4. Electrochemical impedance spectra of the cFFC reference and the μTFC prototype obtained at the initial state and after cycling experiments (60 cycles at 5 mA cm^{-3}). Only the high-frequency range is shown.

The latter, however, was chosen due to its oxygen insensitivity,[8] which simplified the construction of this first prototype. Therefore, it is more reasonable to compare this μTFC to other zinc-based flow cells rather than zero-gap vanadium redox flow batteries. Compared to zinc-bromine

Table 1. Mean values and standard errors (95 % confidence interval) obtained from measurements of electrolyte resistivity, membrane thicknesses, and membrane area resistances (with respect to the total membrane area) of flat (regenerated cellulose, 3.5 kDa, ZelluTrans) and micro-tubular dialysis membranes (mPES, 3 kDa, SpectrumLabs) in aqueous electrolytes containing 1.00±0.02 mol L^{-1} NH_4Cl and 1.00±0.02 mol L^{-1} $ZnCl_2$.

Electrolyte	Electrolyte resistivity/Ω cm	Membrane thickness/μm		Membrane area resistance/Ω cm^2	
	Free electrolyte solution	Flat	Micro-tubular	Flat	Micro-tubular
Dry	–	22.5±0.6	140±3	–	–
1 M NH4Cl	9.22±0.01	48±2	154±4	0.52±0.03	0.19±0.01
1 M ZnCl2	11.49±0.03	48±2	154±5	0.60±0.07	0.21±0.02

cFFCs, the lowest resistance reported to the best of our knowledge, so far, is approximately 0.6 Ω,[5b,12] which corresponds to a volumetric resistance of more than 0.8 Ω cm^3. This resistance is more than two times higher than the one achieved with the μTFC presented in the study at hand. For a verification of the causes of the lower resistance obtained for the μTFC, the utilized membranes were characterized in terms of their contribution to the cell resistance; apart from that, polarization curves were measured for both flow cell types.

Membrane characterization

Although both membrane types utilized in this study had a similar molecular weight cut-off (MWCO) of 3 kDa (hollow fiber type) and 3.5 kDa (flat type), respectively, a difference in the membrane properties could not be precluded due to the different materials of both membranes. Therefore, the most important membrane characteristics were investigated and compared for both membrane types in order to quantify the influence of membrane choice.

While the flat membranes had thicknesses of 22.5±0.6 μm in the dry state and thicknesses of 48±2 μm when soaked with aqueous electrolyte, the micro-tubular membranes exhibited wall thicknesses of 140±3 μm in the dry and 154±5 μm in the wet state. However, while the flat membrane completely consists of a dense pore structure, the micro-tubular one has a thin separation layer on the inner side, which defines its MWCO, and a macro-porous supporting layer on the outer side. This structural difference is evident from scanning electron micrographs shown in Figure S4 of the supporting information. The two layers of the micro-tubular membranes do not have a sharp separation, but gradually transition into each other (see Figure S4f). The given wall thickness values for the hollow fiber membranes, thus, do not correspond to the actual separation layer thickness; the latter can be roughly estimated for the dry state from the SEM images and is within the same magnitude as the dry flat membrane (≈10 to 20 μm). Most important for the performance of the flow battery is the membrane area resistance, which is related to the membrane's permeability for the ions of the supporting electrolyte. Due to the pore structure, the porosity, and possible microscopic interactions between permeating ions and membrane material, the apparent diffusion coefficient of an ion in a swollen membrane is always smaller than in the free electrolyte. Therefore, also the ionic conductivity of the swollen membrane of a flow cell is lower than that of the free solution.

Table 1 summarizes the measured electrolyte resistivities, membrane thicknesses, and membrane resistances. As additional information, Figure S5 of the supporting information shows the statistical evaluation of the obtained area resistances (with respect to the membrane area) of the measurement setups with and without membrane for all combinations of the two membrane types and the two electrolytes as box plots. The experimental results indicate no significant interaction of the ions with the membrane materials. This can be infered from calculating the ratios of the membrane area resistances in the same solution for different membrane types, which results in the equal values of 2.7±0.1 and 2.8±0.1 for NH_4Cl and $ZnCl_2$, respectively. Comparison of the ratios of the membrane resistances of the same membrane in the two different solutions results in a value of 1.1±0.2 ($ZnCl_2$ to NH_4Cl ratio) for both membranes. The same ratio for the specific resistances of the free aqueous solutions of 1.00±0.02 mol L^{-1} $ZnCl_2$ and 1.00±0.02 mol L^{-1} NH_4Cl is 1.247±0.003. Hence, the corresponding ratios are in agreement with each other within their uncertainty. Despite the different membrane materials, the equality of these ratios strongly indicates that there is no significant material specific interaction of the ion pairs of $ZnCl_2$ and NH_4Cl with the membrane material. Any interaction mechanism would have caused different dwelling times for different ions as well as ion concentrations within the membrane and, as a consequence, different ratios would have been observed between the two membrane types. Thus, the ion permeation is determined solely by the tortuosity and porosity of the membranes. It is evident that the lower value observed for the ohmic resistance of the μTFC is not solely due to the cell geometry, but is also caused by the three-fold lower resistance of the utilized micro-tubular membrane as compared to the flat membrane. However, this difference is not due to the materials of the membranes, but to the different porosity and tortuosity of the membrane types. The latter is, in turn, the result of the distinct manufacturing procedures necessary for the production of the two membrane geometries.

Polarization curves

Figure 5a shows the results of polarization measurements obtained from linear voltage sweeps at an electrolyte state of charge (SOC) of 50±10 % for both the μTFC prototype and

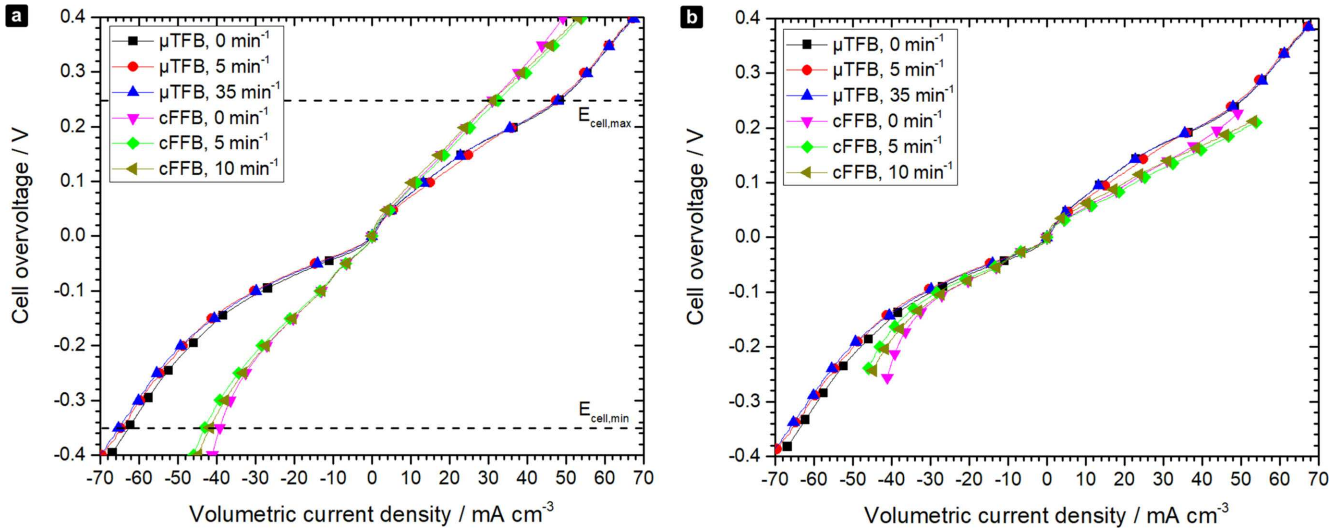

Figure 5. Polarization curves of conventional filter-press flow cell and micro-tubular flow cell as obtained in non-pumped and pumped operation mode for a SOC of 50±10% at a scan rate of 100 mV s^{-1}. Curves in (a) show the uncorrected form of polarization curves where the dashed lines mark the upper and lower cell voltage limits used for galvanostatic charging and discharging, respectively. Figure (b) shows IR drop corrected data for which the ohmic overvoltages were removed according to the ohmic resistances measured by impedance spectroscopy (0.776 Ω (cFFC) and 1.370 Ω (μTFC)).

the cFFC reference cell. The main contributions to the measured polarization overvoltage in the different current regimes are usually identified as activation, ohmic, and concentration overvoltages.[5a,9] Activation overvoltage can be evaluated most conveniently at low currents. For both investigated cell types, the activation overvoltage is small and contributes similarly to the overall overvoltage due to the identical redox chemistries and electrode materials used in both flow cells. The mass-transfer limited regime can be identified by the distinctly steeper slope in the polarization curve at high current values and is apparent for both anodic and cathodic overvoltages. Pumped cell tests revealed a positive but small impact of forced convection on the cell overvoltages, as the latter slightly decreased with increasing electrolyte flow rates. Limiting volumetric current densities as obtained at the limiting cell voltage of 1.3 V (cathodic process) and 1.9 V (anodic process) for the cFFC and the μTFC, respectively, are summarized in Table 2. The cFFC exhibited an increase of 10% for the limiting cathodic current due to forced convection by pumping. In contrast, the limiting anodic current did not change at all within the limiting cell voltage. For the μTFC, both limiting currents only revealed an insignificant alteration as response to the pumped operation mode. Furthermore, the maximum limiting current values were already reached at a moderate electrolyte exchange rate of 5 min^{-1} for both cell types and no additional performance benefit could be gained from further increase of the flow rate. This is most-likely due to the missing porous electrode in the negative half-cell of both flow cell types. Assuming laminar flow, the electrolyte velocity is always small in vicinity to the cell walls and, consequently, also at the surface of the planar zinc electrode. An increase in flow rate leads to a strong increase of velocity in the channel center but only to a minor velocity increase at the zinc electrode's surface. Hence, the flow rate has a small impact on the mass-transport to and from the zinc electrode, which results in the observed behavior. However, the formation of dendrites prevents the proper zero-gap utilization of porous electrodes in the negative half-cell and, therefore, this problem can be overcome only by utilization of a different redox system. Ohmic resistance values were obtained from impedance spectroscopy measurements and were used to calculate the contribution of ohmic overvoltages to the polarization. Data corrected for the IR drop is presented in Figure 5b. Comparison with Figure 5a reveals that ohmic overvoltages are negligible for the μTFC; even at the limiting currents the ohmic contribution to the overall cell overvoltage is below 5%. In contrast to this, the ohmic overvoltage constitutes over 40% of the cell's overvoltage for the cFFC at the limiting cell voltages. Hence, the utilized model electrolyte does not allow for the full utilization of the real performance capabilities of the μTFC due to non-ohmic overvoltages.

Table 2. Limiting volumetric currents of both cFFC and μTFC as obtained from polarization curves (Figure 5a) at the limiting cell voltages of 1.9 V (anodic) and 1.3 V (cathodic) at a scan rate of 100 mV s^{-1}.

Flow Rate[a]/min^{-1}	Limiting anodic current/ mA cm^{-3}		Limiting cathodic current/ mA cm^{-3}	
	cFFC	μTFC	cFFC	μTFC
0	31	51	39	62
5±1	32	50	43	64
10±1	32	–	42	–
35±1	–	52	–	64

[a] Flow rates are normalized to the total inner cell volumes (4.5 mL (cFFC) and 141.4 μL (μTFC)).

Indeed, the low ohmic resistance of the µTFC would enable for limiting current densities as high as 1,000 mA cm^{-3} compared to a value of 100 mA cm^{-3} for the reference cFFC. However, only values of approximately 64 mA cm^{-3} (µTFC) and 43 mA cm^{-3} (cFFC) were observed. The performance of the µTFC is strongly limited by activation and concentration overvoltages, which contribute 95 % to the total cell overvoltage. These overvoltages can be attributed mainly to the limitations of the negative half-cell (missing porous electrode, sluggish kinetics of the Zn/Zn^{2+} couple, etc.). Nevertheless, the polarization experiments demonstrated 50 % higher limiting power densities of 65 W L^{-1} (anodic) and 83 W L^{-1} (cathodic) for the µTFC compared to 42 W L^{-1} (anodic) and 56 W L^{-1} (cathodic) for the cFFC. It is evident from the considerations above that this can be attributed to the smaller ohmic resistance of the µTFC. As detailed in a previous section, the latter is due to the lower electrical area resistance of the micro-tubular membranes, the increased membrane area per volume, and the shorter charge carrier pathways within the µTFC.

Current rating

The polarization curve investigations gave insight into the limits of cell performance in terms of applied voltages and volumetric current densities. Despite their obvious advantages, polarization curves cannot provide reliable information on the capacity retention at varying current densities, which is one of the most important practical parameters for battery application. Consequently, current rating tests were performed on both cell types in a static non-pumped operation mode for volumetric discharging current densities up to 100 mA cm^{-3}. Pumped current rating tests were not performed due to the insignificant influence of pumping revealed by the results of the polarization experiments before. Since both cells performed equally in pumped and non-pumped polarization experiments, no increased scientific insight can be expected from pumped current rating tests.

The results of these experiments are shown in Figure 6 for both types of cells. The same data is presented in two forms in order to emphasize on two important aspects. Figure 6a displays the obtained data normalized to the initial capacity at 1 mA cm^{-3} (first cycle of the current rating test), while Figure 6b presents the same data normalized to the capacity of the last cycle of the current rating test which was performed at 1 mA cm^{-3}, as well. Statistical evaluation of the capacity retention data with a two-sided Welch's t-Test (Table S1, supporting information) revealed a significant difference for current densities above 40 mA cm^{-3} between both cell types at a significance level of below 5 %. Regarding these high currents, a capacity retention of 0 % was observed for the cFFC at a current density of 100 mA cm^{-3}, while the µTFC still provided a capacity retention of 7.6 ± 0.4 % at the same current density. The largest difference was observed at 45 mA cm^{-3} yielding a capacity retention of 24 ± 2 % (µTFC) compared to 1 ± 2 % (cFFC). In other words, the µTFC enabled to extract roughly one fourth of its total capacity at 45 mA cm^{-3}, while the cFFC delivered nearly no charge at all at the same current density. However, the difference between Figure 6a and Figure 6b indicates a strong capacity decay for both cell types over the course of the experiment. In consideration of the results obtained for the utilized electrolyte system in a previous study, this capacity decay is attributed to the utilized redox chemistry and degradation of the electrolyte, respectively.[8] Apart from the undesirable effect of lowering the energy efficiency, it has to be pointed out that the lower coulombic efficiency observed for the µTFC does not dispute the conclusions drawn for its decreased resistance and its increased power density. The latter are additionally verified by the results of the polarization experiments discussed in the previous section. Regarding the lower coulombic efficiencies observed for the µTFC, these could, in general, originate from a side reaction or from polymer cross-over through the membrane. However, any side reactions would be expected to occur equally in both cell types and, therefore, polymer cross-over is a more likely reason. This hypothesis was supported by the results of subsequent cycle stability experiments as discussed in the following section.

Cycle stability

Cycle stability experiments were performed at a moderate charging and discharging current density of 5 mA cm^{-3} in a non-pumped operation mode for both cell types in galvanostatic experiments. Pumped cycle stability experiments were not conducted for the same reasons stated in the previous section. It is evident from the capacity-cycle diagram, Figure 6c, that the cycle stability for the cFFC is significantly higher than that of the µTFC. After 60 cycles, the cFFC yielded a discharging capacity retention of 73 ± 7 % of the initial charging capacity, while the µTFC gave a value of 19 ± 4 %. Further insight into the causes for the stronger capacity decay observed for the µTFC was gathered by a step-by-step exchange of cell parts of the µTFC after the 60 cycles. The impact of each step on the cycling behavior and the capacity retention is shown in Figure 6d. First, extraction of the zinc wire, wiping it with a dry tissue, and reinserting it into the same cell without alteration of the electrolyte brought no significant improvement in successive cycling for another six cycles. In a second step, the zinc wire was replaced by a new unused one. Although a recognizable capacity recovery from 25 to 32 % of the initial capacity was observed, the zinc wire could be excluded as the main cause of the low cycle stability. Subsequently, the electrolyte in the negative half-cell was replaced by fresh electrolyte. This had no significant effect either. The exchange of the positive electrolyte in a last step finally recovered the capacity to its initial value. During subsequent cycling for another five cycles the cell exhibited the same behavior as in the beginning of the cycling experiment. In a last experiment, the cell was put to open circuit and was allowed to rest without any alteration for 19 h. After

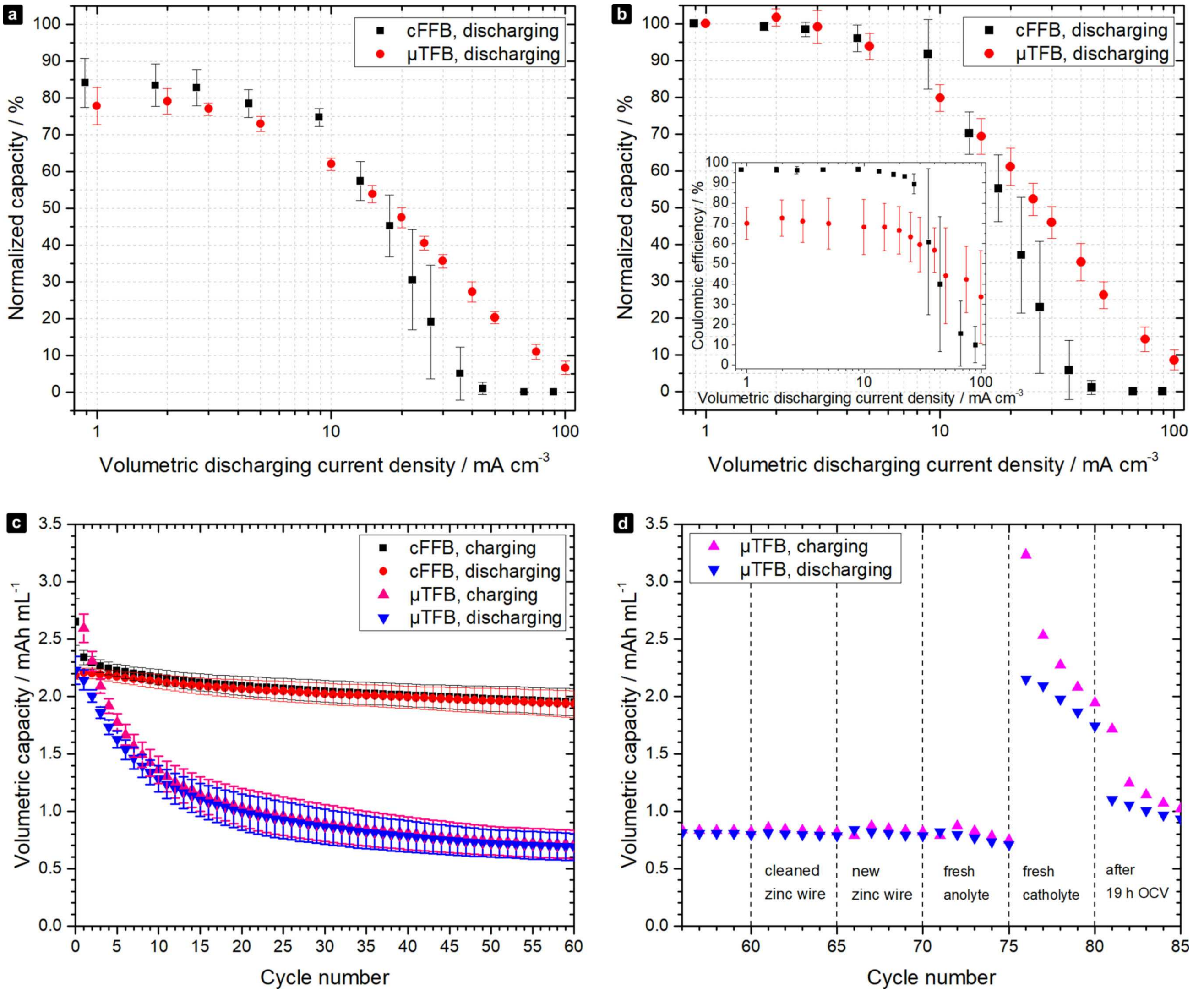

Figure 6. Capacity retention at different volumetric discharging current densities normalized to the capacity (obtained at 1 mA cm^{-3}) of the first cycle (a) and the last cycle (b) of the whole current rating experiment, respectively (charging currents were kept constant at 1 mA cm^{-3} during the experiment). Inset in (b) shows the coulombic efficiencies. The results of subsequent charge-discharge cycles at a moderate charging/discharging current density of 5 mA cm^{-3} is provided in (c) in terms of volumetric capacities (normalized to positive half-cell volume of 2.5 mL (cFFC) and 114.5 µL (µTFC), respectively). Impact of subsequent cell part exchanges within the µTFC on the capacity retention are shown in (d).

this resting period, it was charged and discharged again for another five cycles. A strong capacity loss compared to the last cycle before the open circuit period was observed. Altogether, it can be concluded from the results of these experiments that the capacity decay is not due to irreversible degradation of cell parts (current collectors, electrodes, membrane), but is fully due to some kind of capacity loss within the positive electrolyte. Taking into consideration the lower coulombic efficiency of the µTFC discussed in the previous section and the capacity loss observed after a plain resting period of 19 h, it is reasonable to assume that polymer cross-over through the micro-tubular membrane is the main reason for the µTFC's inferior coulombic efficiency and cycle stability. This cross-over is facilitated by the higher ion permeability (Table 1) and the higher membrane area per volume of the micro-tubular membrane in comparison to the flat membrane of the cFFC. Indubitably, this issue can be overcome in the future by a thorough design of the polymer electrolyte. In particular, the polymer cross-over through the micro-tubular membrane can be mitigated by tuning of the molar mass of the utilized polymers or using membranes with smaller MWCOs. However, tuning of the electrolyte would not have been meaningful for the present study, because the poly(TMA-*co*-PEGMA)/zinc system was only used as a model electrolyte to verify the general feasibility of the micro-tubular approach with an oxygen-insensitive and easy-to-handle anolyte. Future studies will focus on fully organic µTFCs with electrolytes optimized for the specific micro-tubular membranes.

Regarding the coulombic efficiencies in the cycle stability experiments (Figure S6), the µTFC revealed values of up to 96.7 %, while the cFFC revealed values of up to 99.1 %, which reflects the same tendency towards lower efficiencies for the µTFC in comparison to the cFFC. However, in contrast to the results obtained during the current rating tests, the coulombic efficiencies of both cells showed a significantly smaller difference. This is attributed to the different cycling modes. During the current rating experiments, a low constant charging current density of 1 mA cm^{-3} and varying discharging current densities were applied, while during the cycle stability experiments 5 mA cm^{-3} were used for both charging and discharging. As a consequence, the different coulombic efficiencies in both experiments originate from the different time scales during the charging processes. The polymer cross-over indicated by the previously discussed results, can occur to a larger extent during the slow charging in the current rating experiments than it can during the five-fold faster charging in the cycling stability experiments.

Conclusions

In this study, the first micro-tubular approach for tubular flow cells (µTFC) was introduced and investigated both theoretically and experimentally. This novel flow cell type is characterized by a tubular geometry with diameters in the lower millimeter range and half-cell thicknesses in the micrometer range. The theoretical examinations gave important insights into the benefits and properties that can be expected from emphasizing further research efforts on µTFCs. It was reasoned that

- micro-tubular flow cells can achieve an at least two-fold lower ohmic resistance compared to equally sized conventional filter-press flow cells (cFFC),
- upscaling of µTFCs is possible without increasing the length of single-cell units, and
- additional ohmic resistances from current flow into the axial direction can likely be mitigated by utilization of short identical micro-tubular single-cell units connected in parallel.

Motivated by these promising theoretical prospects, a micro-tubular laboratory prototype with a length of 2 cm, an inner cell diameter of 3 mm, and a membrane diameter of 1 mm was constructed to investigate experimentally the feasibility of this micro-tubular approach in a single-cell unit. A previously investigated aqueous poly(TMA-*co*-PEGMA) catholyte was utilized together with a zinc-based anolyte as an oxygen-insensitive model redox system for the performance evaluations. It was the polymer-based electrolyte and the commercial availability of micro-tubular dialysis membranes that enabled the experimental realization of this first µTFC. Within the experiments, the µTFC prototype was compared directly to the test cFFC utilized for the majority of the literature-known aqueous polymer-based flow batteries. The experimental performance of the µTFC was characterized by

- a volumetric resistance of $0.3 \pm 0.1\ \Omega\,\mathrm{cm}^3$ corresponding to a potential limiting current density of 1,000 mA cm^{-3},
- limiting volumetric current densities of 52 mA cm^{-3} (charging process) and 64 mA cm^{-3} (discharging process) in potentiodynamic experiments at a scan rate of 100 mV s^{-1},
- an above-zero capacity retention for current densities higher than 100 mA cm^{-3} in galvanostatic discharge experiments,
- columbic efficiencies of $\leq 70\,\%$ during galvanostatic discharge experiments at constant charging current densities (1 mA cm^{-3}) and varying discharge current densities (up to 100 mA cm^{-3}),
- columbic efficiencies of up to 96.7 % during galvanostatic discharge experiments at equal charging and discharging current densities of 5 mA cm^{-3}, and
- a significant capacity decay within the first 15 cycles of galvanostatic discharge experiments at equal charging and discharging current densities of 5 mA cm^{-3}.

In conclusion, this first µTFC prototype obtained an ohmic resistance that was ten-fold lower than the resistance of the reference cFFC,[8] two-fold lower than the lowest resistance value reported for tubular flow cells so far,[4c] and more than two times lower than the lowest resistance reported for zinc-bromine cFFCs.[5b,12] The reduced ohmic losses of this µTFC prototype can be attributed mainly to the increased membrane area to volume ratio, shorter charge carrier pathways, and the lower area resistance of the micro-tubular dialysis membrane. Despite the promising reduction of the ohmic resistance, the full performance potential of the µTFC for current densities of up to 1,000 mA cm^{-3} could not be realized experimentally, due to kinetic and mass transport limitations caused by the utilization of a zinc-based model anolyte and the absence of a porous electrode within the negative half-cell. The low coulombic efficiencies can be attributed to polymer cross-over as verified by successive exchange of cell-parts and electrolytes after galvanostatic long-term cycling.

Based on this proof-of-concept study and the detailed characterization and investigation of the first µTFC single-cell unit prototype at hand, several remaining challenges were identified that need to be addressed by future research efforts, i. e.,

- the mitigation of polymer cross-over to increase the coulombic efficiency,
- the replacement of expensive (e.g., platinum wire) and fragile (e.g., graphite foil) cell materials,
- the adjustment of half-cell volume ratios to a value close to one,
- the transition to a zero-gap architecture with a porous electrode for the inner half-cell,
- the development and demonstration of feasible upscaling approaches, and
- the development of cost-efficient production and assembly procedures.

These challenges will be overcome most-likely by decreasing the cell length, increasing the molar mass of the polymers, decreasing the membrane's MWCO, a thorough re-evaluation of the assembly procedure, development of mechanically and chemically stable graphite current collectors, further reduction of the outer cell diameter to achieve equal half-cell volumes, and the transition from a hybrid flow battery to an all-organic redox flow battery. Upscaling needs to be achieved in two steps, i.e., increasing single-cell size by parallel connection of short micro-tubular single-cell units and, subsequently, by the development of stacking procedures by suitable series connection of the larger single-cells obtained from the first upscaling step. Both steps have already been demonstrated successfully for micro-tubular fuel cells[6c–e] and, thus, there is little doubt that similar approaches will be successful for the upscaling of µTFCs as well. If all theoretically possible performance benefits are realized by means of future research activities, the increased power density of µTFCs can contribute to the flow battery technology by a significant decrease of stack size and a reduced stack cost per kW compared to cFFC stacks, which can originate from the lower material consumption required by smaller cell stacks with higher power density and compact extrusion based production steps for the micro-tubular cell parts.

Due to the commercial availability of micro-tubular dialysis membranes, µTFCs will be especially interesting for polymer- and suspension-based flow battery systems in the near future. The proper development of ion-exchange membranes in a micro-tubular form will, however, indubitably make this approach also feasible for other common flow battery redox chemistries, which are based, e.g., on vanadium or small organic molecules. Similar to their micro-tubular fuel cell counterparts, micro-tubular flow cells can be expected to provide both new prospects for performance improvements of flow batteries and a rich area for future research.

Experimental Section

Polymer synthesis & characterization

Materials. All reagents for the polymer synthesis were purchased from Sigma-Aldrich and TCI and were used as received without further purification. ^{1}H NMR spectra were measured on a FOURIER 300 from Bruker. Chemical shifts are reported in parts per million (ppm, δ scale) relative to the residual signal of the deuterated solvent. For dialysis, a cellulose-based dialysis membrane with a MWCO of 6 to 8 kDa (Spectra/Por 1, Spectrum Laboratories, USA) was employed.

Synthesis. 2,2,6,6-Tetramethylpiperidin-4-yl methacrylate (5 g; 22 mmol) was dispersed in a solution of poly(ethylene glycol) methyl ether methacrylate ($M_n = 950$ g mol^{-1}; 21 g; 22 mmol) in water (22 mL). After the addition of hydrochloric acid (37 %; 1.8 mL), the mixture was heated to 50 °C in order to fully dissolve the monomers. 4,4′-Azobis(4-cyanovaleric acid) (75 wt-%; 40 mg; 0.11 mmol) and 4-cyano-4-(phenylcarbonothioylthio)pentanoic acid (120 mg; 0.43 mmol) were added and the mixture was deaerated by flushing with argon for 60 min. After stirring at 80 °C for 24 h, the solution was cooled to room temperature (analyzed by ^{1}H NMR, Figure S1) and, subsequently, the oxidation was performed in three steps. First, sodium tungstate (163 mg; 0.55 mmol) was added and the pH value was adjusted to 12.1 with aqueous sodium hydroxide solution (29 wt-%; 2 mL). While a vigorous formation of foam was observed, hydrogen peroxide (30 %; 9.1 mL) was added in portions of 1 mL over the course of 20 min. The pH value was adjusted to 11.1 by the addition of 1.5 mL sodium hydroxide solution and the mixture was stirred for 20 h. Afterwards, hydrogen peroxide (9.1 mL) was added in four portions and the solution was stirred for 24 h. After a third addition of hydrogen peroxide (9.1 mL) in four portions and an additional reaction time of 24 h, the orange solution was dialyzed against water (MWCO = 6 to 8 kDa) for two days. Finally, the solution was lyophilized to yield an orange powder (13.3 g). ^{1}H NMR (D_2O, 300 MHz) δ: ppm 0.25–2.5 (26H, br), 3.3 (3H, s, $-CH_3$), 3.6 (80H, br, $-OC_2H_4-$), 4.2 (2H, br, COO–CH_2–), 5.1 (1H, br, –COO–CH); specific capacity of oxidized polymer: 15.8 mAh g^{-1} (determined by titration); $M_W = 178{,}000$ g mol^{-1} and dispersity $Đ = 1.29$ (as determined by asymmetric flow field-flow fractionation).

Asymmetric flow field-flow fractionation (AF4). The measurements were performed on an AF2000 MT System from Postnova Analytics GmbH (Landsberg, Germany), equipped with a tip and focus pump (PN1130), an autosampler (PN5300), and a channel oven unit (PN4020) with the channel coupled to a multi angle laser light scattering (MALLS) detector (PN3621) equipped with a 532 nm laser. Depending on sensitivity, the highest and lowest angles have typically not been employed due to their low signal-to-noise ratio. The channel had a trapezoidal geometry with an overall footprint of 31.6 cm^2. The nominal height of the spacer was 350 µm and a regenerated cellulose (RC) membrane from Postnova Analytics GmbH (10 kDa RC membrane) with a molar mass cutoff of 10 kDa was used as accumulation wall. All experiments were carried out at a channel oven temperature of 25 °C and a fluid phase of 0.9 % (w/w) aqueous sodium chloride solution was used. For the measurements 20 µL of sample (14 mg mL^{-1}) were injected with an injection flow rate of 0.2 mL min^{-1}, a focus flow rate of 1.3 mL min^{-1} and a cross-flow rate of 1.2 mL min^{-1}, resulting in a detector flow rate of 0.3 mL min^{-1}. The focusing time was 7 min before switching to elution at a constant cross-flow of 1.2 mL min^{-1} for 1.5 min, followed by an exponential decay (with an exponent of 0.1) to 0.5 mL min^{-1} within 20 min. After a linear decrease to 0 mL min^{-1} within 1 min the elution was monitored for a further 40 min to identify potentially larger eluting species. A weight-average molar mass of 178,000 g mol^{-1} ($Đ = 1.29$) was found at a recovery of 84 %. Additionally, a later eluting species in a retention time range of 30 to 40 min was observed. The refractive index increment, dn/dc, was measured on an Optilab rEX system (Wyatt, Germany) by manual delivery of six known concentrations of the polymer in 0.9 % (w/w) aqueous sodium chloride solution, i.e., identical to that used as the liquid phase in AF4, via a plastic syringe. The temperature was set to 25 °C. The dn/dc was calculated by the slope of the plot from the refractive index against the concentration, which yielded a value of 0.1368 ± 0.0008 mL g^{-1}.

Membrane characterization

The both utilized types of dialysis membranes were characterized in terms of their thicknesses, electrical resistances, and by scanning electron microscopy.

Thicknesses. Membrane thicknesses of the dry and soaked membranes were measured using a digital caliper (Top Craft, Germany, tolerance: ±0.02 mm). Due to the expected magnitude of the membrane thicknesses in the lower to medium micrometer range, varying numbers of membranes (5, 6, 10 and 12 for hollow fiber type; 6, 8, 12, 16, 24 and 40 for flat type) were piled in order to decrease the relative measurement error by increasing the measured overall thickness. The membrane thicknesses were then obtained by dividing the overall thickness through the number of membranes (flat type) or the number of membranes multiplied by two (hollow fiber type, due to the two walls one fiber has). Thickness measurements of wet membranes were conducted with membranes stored in aqueous electrolyte solutions for at least 72 h prior to the measurement. The mean values and their corresponding standard errors (95 % confidence interval) were calculated from all related measurements and were taken as the measured membrane thicknesses.

Electrical resistances. Electrical resistances of the membranes were measured *via* electrochemical impedance spectroscopy in a frequency range from 0.2 MHz to 1 kHz at a voltage amplitude of 5 mV and 10 mV, respectively, using a VMP3-based 16-channel-potentiostat from BioLogics Scientific Instruments, France. Four-wire sensing was applied to the measurement of flat membranes and two-wire sensing for hollow fiber membranes. Membranes of each type were pre-treated by storage in the corresponding aqueous electrolyte for at least 12 hours to ensure that membranes were soaked with electrolyte completely prior to the measurement. They were then inserted into an electrochemical cell. The cell was divided into two half-cells by the membrane, which consequently allowed exchange of fluid and ions between the half-cells only *via* penetration of the membrane. Both half-cells were flooded with the same electrolyte and the electrical resistance values were obtained by measuring the setups total ohmic resistance (as high frequency abscissa intercept of the Nyquist plot) without membrane first and with membrane afterwards. The difference of both values was taken as the membrane resistance. For the flat membrane type, standard flow battery test cells (JenaBatteries GmbH, Germany)[7] with graphite current collectors, which reduced the effective cell thickness to 5 mm, were utilized as experimental setup. The hollow fiber membranes (inner diameter: 1 mm) were characterized in an experimental setup utilizing a T-piece LuerLock adapter (Pieper Filter GmbH, Germany), the stainless-steel part of a wire ferrule (PROTECT.-class, Germany; inner diameter: 3.50 ± 0.02 mm, length: 14.8 ± 0.5 mm) as the working electrode and a zinc wire as the counter electrode (Figure S2). Each measurement was performed 16 times for four different membranes of each membrane type, resulting in 64 resistance values per cell state (with/without membrane) and per electrolyte type. Membrane resistances stated in this study are mean values of these 64 measurements and their corresponding standard error of the mean (95 % confidence interval). Specific resistances of free aqueous solutions were measured four times each with a conductivity meter (Cond 3110, Xylem Analytics Germany Sales GmbH & Co. KG, Germany) at electrolyte temperatures of 294.9 ± 0.3 K.

Scanning electron microscopy. For the SEM investigations, flat membranes were cut into pieces with a scissor. Using the same approach for the hollow fiber membranes caused severe deformations of the membrane. Hence, another approach was taken: The micro-tubular membranes were cooled in liquid nitrogen for $>$2 min and broken afterwards to obtain a smooth edge. The prepared membrane samples were subsequently coated with a thin layer of gold *via* sputter coating for successive investigation in a Sigma VP Field Emission Scanning Electron Microscope (Carl Zeiss AG, Germany).

Cell assemblies

Conventional filter-press flow cell. Laboratory test cells in filter-press design (JenaBatteries GmbH, Germany) were used as reference cells according to previous studies.[8] These cells have a (geometric) electrode area and a membrane area of 5 cm^2, respectively, and a half-cell thickness of 4.5 mm. In the positive half-cell, a graphite current collector (MERSEN GmbH, Germany) is utilized along with a graphite felt (GFA6, area: 5 cm^2, thickness: 0.6 cm, SGL Group, Germany) as porous electrode (compression: 25 %). A flat membrane (ZelluTrans dialysis membrane T1, regenerated cellulose, MWCO: 3.5 kDa, Carl Roth GmbH & Co. KG, Germany) separated the positive half-cell from the negative half-cell. In the latter, no porous electrode was utilized. Instead, a zinc foil (99.98 %, thickness: 0.25 mm, Alfa Aesar GmbH & Co. KG, Germany) was applied as electrode as well as current collector and was roughened with a flat file, but only in the region of the foil where contact with the electrolyte within the cell was possible. Due to the missing porous electrode in the negative half-cell, the membrane was slightly vaulted into this half-cell. Consequently, the total inner volume of the cell was 4.5 mL with about 2.5 mL for the positive half-cell and 2 mL for the negative one.

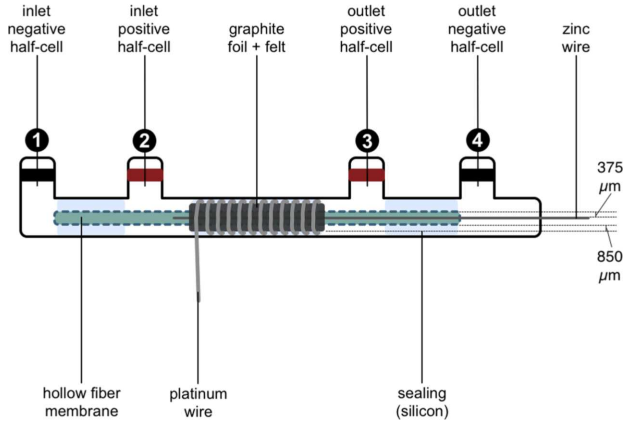

Figure 7. Experimental setup of the μTFC single-cell unit prototype with one micro-tubular membrane, a positive (outer) half-cell with a thickness of 850 μm and a negative (inner) half-cell with a thickness of 350 μm. The positive half-cell contains a graphite felt as porous electrode, while the negative half-cell contains a zinc wire only.

Micro-tubular flow cell. The μTFC was assembled from common laboratory materials. The setup is schematically illustrated in Figure 7. A piece (width: 2 cm, height: 1 cm) of graphite foil (99.8 % (metals basis), thickness: 0.254 mm, Alfa Aesar GmbH & Co. KG, Germany) was wrapped around a rod (3 mm diameter). Afterwards, platinum wire (diameter: 0.4 mm, BEDRA GmbH, Germany) was coiled around this unit as current collector and in order to fixate the foil in this tubular geometry of 2 cm length. A shrinking hose was placed around this assembly and was heated using a heat gun for less than 1 min. Subsequently, the rod was removed and a piece of graphite felt (GFA6, area: 5 cm^2, thickness: 0.6 cm, consisting of three 0.2 cm thick layers, SGL Group, Germany) was inserted into the obtained hollow cylinder using a tweezer. Prior to insertion of the graphite felt, one of the three layers of the felt was removed, resulting in a piece of 0.2 cm in width, 0.4 cm in height, and 2 cm in length; subsequently, the piece was ripped into smaller pieces for insertion. The compression of the porous electrode in the cell was approximately 28 %. The micro-tubular dialysis membrane (modified polyether sulfone (mPES), inner diameter: 1 mm, MWCO: 3 kDa, Spectrum Laboratories, Inc.) was drawn through the felt using a common sewing needle (diameter: 1 mm) and, subsequently, a piece of zinc wire (99.99+ %, diameter: 0.25 mm, length: 10 cm) was inserted into the membrane. The membrane itself was extracted from a hollow fiber dialysis module (D06-E003-10-N, Spectrum Laboratories, Inc.). A piece of polyurethane hose (length: 3.6 cm, inner diameter: 5 mm, outer diameter: 8 mm, Festo Vertrieb GmbH & Co. KG, Germany) was utilized as a case into which the previously built assembly was inserted for protection and fluid connection. A small cut in the hose allowed the end of the platinum wire to be let to the outside for external connection to the potentiostat; the cut was sealed with silicon (Scrintec 600, Carl Roth GmbH & Co. KG, Germany) after the cell was fully assembled. Afterwards, the hose was placed onto the end of two male LuerLock T-piece adapters (2) and (3) (inner diameter: 4 mm, outer diameter: 8 mm, Pieper Filter GmbH, Germany). The hollow fiber membranes were glued into opposite end of the T-pieces with silicon as well. This construction enabled to utilize the remaining third ends of each T-piece as fluid inlet and outlet, respectively, for the outer half-cell. A L-piece (1) and an additional T-piece adapter (4) were connected to the previously mounted T-pieces (2) and (3) using hose, Parafilm®, and silicon. The end of the zinc-wire was glued into the end of one T-piece, which provided both external connection to the potentiostat and a sealing point for the inner half-cell. While the L-piece (1) was the fluid inlet for the inner half-cell, the remaining third end of the T-piece (4) represented its fluid outlet. The total inner volume of the cell was 141.4 μL (including inner current collector and membrane) with 114.5 μL for the positive half-cell and 14.7 μL for the negative half-cell (half-cell volumes are given without current collector and membrane contribution). Three cells were assembled according to the described procedure in order to test its reproducibility.

Electrochemical measurements

All electrochemical measurements on the flow cells were conducted using a VMP3-based 16-channel-potentiostat from BioLogics Scientific Instruments, France, with the reference lead connected to the counter electrode. Four-wire sensing was applied to mitigate the wire resistances of the external circuit and the contact resistances between the current collectors and the external circuit. Furthermore, all experiments were conducted at room temperature (294±2 K) without active temperature control of the flow cells or electrolytes. The PC software EC-Labs v11.02 was used to control the potentiostat. Volumetric current densities are based on the total inner volume of the cells (without current collectors, membrane, feed pipes, etc.), i.e., 4.5 cm^3 (cFFC) and 0.1414 cm^3 (μTFC).

Electrolyte preparation. The same electrolyte configurations were utilized for all battery tests. For the positive half-cell, the synthesized poly(TMA-*co*-PEGMA) polymer was dissolved in pure water together with zinc chloride (≥98 %, Sigma-Aldrich Chemie GmbH, Germany) and ammonium chloride (99.5 %, Grüssing GmbH, Germany) as supporting electrolyte. The amount of polymer was chosen to yield a volumetric capacity of 2.4 $mAh\,mL^{-1}$ in the final solution and the supporting electrolytes yielded a concentration of 1.00±0.02 $mol\,L^{-1}$ each. Correspondingly, the same concentrations of zinc chloride and ammonium chloride in pure water were used for the negative half-cell without additional additives.

Ohmic resistances. Ohmic resistances of the flow cells were measured as the high-frequency abscissa intercept of electrochemical impedance spectra, which were recorded in a frequency range from 1 MHz to 100 Hz at a voltage amplitude of 5 mV. EIS was measured at 0 V *vs.* open-circuit voltage (OCV) before (≈1.2±0.1 V cell voltage) and after (≈1.5±0.1 V cell voltage) cycle stability experiments. The obtained resistances for initial cell states of both cell types were averaged and are stated as mean values and corresponding standard deviations.

OCV-SOC curves. Investigation of the relationship between the OCV and the SOC of the cells was performed by incremental galvanostatic charging and discharging; applied currents were 1 $mA\,cm^{-3}$ and 2 $mA\,cm^{-3}$, respectively. Galvanostatic periods lasted 10 s and were directly followed by open circuit periods with durations of 0.5 min, 2.5 min, or 5 min. The obtained data was averaged and voltages of 1.56 V and 1.74 V were taken as 0 % and 100 % SOC.

Polarization curves. The polarization behavior was investigated for static non-pumped and pumped cells (applied flow rates as normalized to the total inner cell volume: 5 min^{-1}, 10 min^{-1}, 35 min^{-1}). Prior to polarization curve measurements, 10 mL of each electrolyte were charged and discharged galvanostatically at a volumetric current density of 1 $mA\,cm^{-3}$ in a cFFC in a pumped operation mode. Afterwards, the electrolytes were charged galvanostatically at the same current to a voltage of 1.7 V, at which the cell was held potentiostatically for another 3 h. During an open circuit period of 4.5 h the cell reached a stable ($\dot{E}=$ 1.5 $mV\,h^{-1}$) open circuit voltage of 1.64±0.01 V. The stated open circuit voltage is the mean value and its standard deviation as obtained from the different OCV measurements before each polarization experiment. According to the OCV-SOC diagram (Figure S3) an OCV value of 1.64 V corresponds to a state of charge of 50±10 %. Following the approach of Chen *et al.*,[5a] polarization curve measurements were performed by applying linear voltage sweeps at a scan rate of 100 $mV\,s^{-1}$ to either 1.3 V (cathodic direction) or 1.9 V (anodic direction). Current responses were averaged over the last 50 % of step duration of 10 voltage steps.

Current rating. Current rating of the cells was investigated by galvanostatic charging of each cell at 1 $mA\,cm^{-3}$ until a voltage of 1.9 V was reached. Subsequent to each charging cycle, the cell was galvanostatically discharged at a particular volumetric discharging current density down to a voltage of 1.3 V. Such a charging-discharging cycle at a specific discharging current density was conducted three times. Afterwards, the remaining capacity of the battery was discharged at 1 $mA\,cm^{-3}$ to return to initial conditions of an empty battery. An open circuit period (10 min) followed before the procedure was repeated for the next value of discharging current. The latter was varied starting from 100 $mA\,cm^{-3}$ and going down to 1 $mA\,cm^{-3}$. For evaluation of the data the capacity of the second cycle of each current value was used. The experiment was repeated three times for each cell type with identically assembled cells and fresh electrolyte; mean values and their corresponding standard deviations are stated throughout this study.

Cycle stability. Both cells were investigated with regard to their cycle stability by successive galvanostatic charging and discharging in a voltage range from 1.3 to 1.9 V at a volumetric current density of 5 $mA\,cm^{-3}$. Prior to cycling and afterwards impedance spectroscopy measurements were performed. The experiment was repeated three times for each cell type with fresh electrolyte; mean values and their corresponding standard deviations are stated throughout this study.

Symbols & Abbreviations

Symbols

A	area
d	thickness
D	width/height of flow cell

L	length of flow cell
r	radius
R	ohmic resistance
ρ	specific ohmic resistance
V	volume

Subscripts

cell	flow cell
E	electrode/electrolyte mixed phase
M	membrane

Superscripts

neg	negative half-cell
pos	positive half-cell

Abbreviations

cFFC/cFFB	conventional filter-press flow cell/battery
µTFC/µTFB	micro-tubular flow cell/battery
MWCO	molecular weight-cutoff
OCV	open-circuit voltage
SOC	state of charge

Supporting Information

Electronic supporting information is available online: NMR, Photographs of laboratory prototypes, box plots of membrane area resistance data, SEM images of membranes, OCV-SOC diagram, coulombic efficiency data, exemplary potential-time diagrams for galvanostatic cycling, and Welch's t-Test data for current rating.

Acknowledgements

The financial support by the European Regional Development Fund (EFRE), the Thuringian Ministry for Economic Affairs, Science and Digital Society (TMWWdG), and the Thüringer Aufbaubank (TAB) are gratefully acknowledged. The authors also thank Steffi Stumpf for performing the SEM measurements of the membranes. The SEM/TEM facilities of the Jena Center for Soft Matter (JCSM) were established with a grant from the German Research Council (DFG) and the EFRE. For the AF4 measurements, Mandy Grube and PD Dr. Ivo Nischang as well as the corresponding funding from the Carl-Zeiss Foundation (JCSM Strukturantrag) and the TMWWdG (ProExzellenz II, NanoPolar) are gratefully acknowledged.

Conflict of interest

The authors declare no conflict of interest.

Keywords: Aqueous Flow Battery · Tubular · Micro-tubular · Flow Cell · Cell Design

[1] W. Kangro, Germany, **1949**, DE914264.

[2] a) P. Leung, A. A. Shah, L. Sanz, C. Flox, J. R. Morante, Q. Xu, M. R. Mohamed, C. Ponce de León, F. C. Walsh, *J. Power Sources* **2017**, *360*, 243–283; b) J. Noack, N. Roznyatovskaya, T. Herr, P. Fischer, *Angew. Chem. Int. Ed.* **2015**, *54*, 9776–9809; c) M. Park, J. Ryu, W. Wang, J. Cho, *Nat. Rev. Mater.* **2016**, *2*, 16080; d) Z. Qi, G. M. Koenig, *J. Vac. Sci. Technol. B* **2017**, *35*, 040801; e) M. Skyllas-Kazacos, M. H. Chakrabarti, S. A. Hajimolana, F. S. Mjalli, M. Saleemd, *J. Electrochem. Soc.* **2011**, *158*, R55-R79; f) J. Winsberg, T. Hagemann, T. Janoschka, M. D. Hager, U. S. Schubert, *Angew. Chem. Int. Ed.* **2017**, *56*, 686–711.

[3] a) D. S. Aaron, Q. Liu, Z. Tang, G. M. Grim, A. B. Papandrew, A. Turhan, T. A. Zawodzinski, M. M. Mench, *J. Power Sources* **2012**, *206*, 450–453; b) B. R. Chalamala, T. Soundappan, G. R. Fisher, M. R. Anstey, V. V. Viswanathan, M. L. Perry, *Proc. IEEE* **2014**, *102*, 976–999.

[4] a) B. Fang, Y. Wei, T. Arai, S. Iwasa, M. Kumagai, *J. Appl. Electrochem.* **2003**, *33*, 197–203; b) M. Park, D. S. Shin, J. Ryu, M. Choi, N. Park, S. Y. Hong, J. Cho, *Adv. Mater.* **2015**, *27*, 5141–5146; c) S. Ressel, A. Laube, S. Fischer, A. Chica, T. Flower, T. Struckmann, *J. Power Sources* **2017**, *355*, 199–205; d) C. Stolze, C. Schmerbauch, C. Friebe, U. S. Schubert, *Energy Technol.* **2017**, *5*, 225–227.

[5] a) Q. Chen, M. R. Gerhardt, M. J. Aziz, *J. Electrochem. Soc.* **2017**, *164*, A1126-A1132; b) M. Wu, T. Zhao, R. Zhang, H. Jiang, L. Wei, *Energy Technol.* **2018**, *6*, 333–339; c) X. L. Zhou, Y. K. Zeng, X. B. Zhu, L. Wei, T. S. Zhao, *J. Power Sources* **2016**, *325*, 329–336.

[6] a) V. Lawlor, S. Griesser, G. Buchinger, A. G. Olabi, S. Cordiner, D. Meissner, *J. Power Sources* **2009**, *193*, 387–399; b) F. Calise, G. Restucccia, N. Sammes, *J. Power Sources* **2010**, *195*, 1163–1170; c) K. S. Howe, G. J. Thompson, K. Kendall, *J. Power Sources* **2011**, *196*, 1677–1686; d) V. Lawlor, *J. Power Sources* **2013**, *240*, 421–441; e) S. M. Jamil, M. H. D. Othman, M. A. Rahman, J. Jaafar, A. F. Ismail, K. Li, *J. Eur. Ceram. Soc.* **2015**, *35*, 1–22.

[7] T. Janoschka, N. Martin, U. Martin, C. Friebe, S. Morgenstern, H. Hiller, M. D. Hager, U. S. Schubert, *Nature* **2015**, *527*, 78–81.

[8] J. Winsberg, T. Janoschka, S. Morgenstern, T. Hagemann, S. Muench, G. Hauffman, J. F. Gohy, M. D. Hager, U. S. Schubert, *Adv. Mater.* **2016**, *28*, 2238–2243.

[9] D. Aaron, Z. Tang, A. B. Papandrew, T. A. Zawodzinski, *J. Appl. Electrochem.* **2011**, *41*, 1175–1182.

[10] Q. Chen, M. R. Gerhardt, L. Hartle, M. J. Aziz, *J. Electrochem. Soc.* **2015**, *163*, A5010-A5013.

[11] Q. H. Liu, G. M. Grim, A. B. Papandrew, A. Turhan, T. A. Zawodzinski, M. M. Mench, *J. Electrochem. Soc.* **2012**, *159*, A1246-A1252.

[12] M. C. Wu, T. S. Zhao, H. R. Jiang, Y. K. Zeng, Y. X. Ren, *J. Power Sources* **2017**, *355*, 62–68.

Manuscript received: March 5, 2018
Revised manuscript received: June 12, 2018
Accepted manuscript online: June 12, 2018
Version of record online: September 13, 2018

Energy Technology

Supporting Information

Micro-Tubular Flow Cell Design Utilizing Commercial Hollow Fiber Dialysis Membranes for Size-Exclusion Based Flow Batteries

C. Stolze, T. Janoschka, J. Winsberg, M. Strumpf, M. D. Hager, and U. S. Schubert*

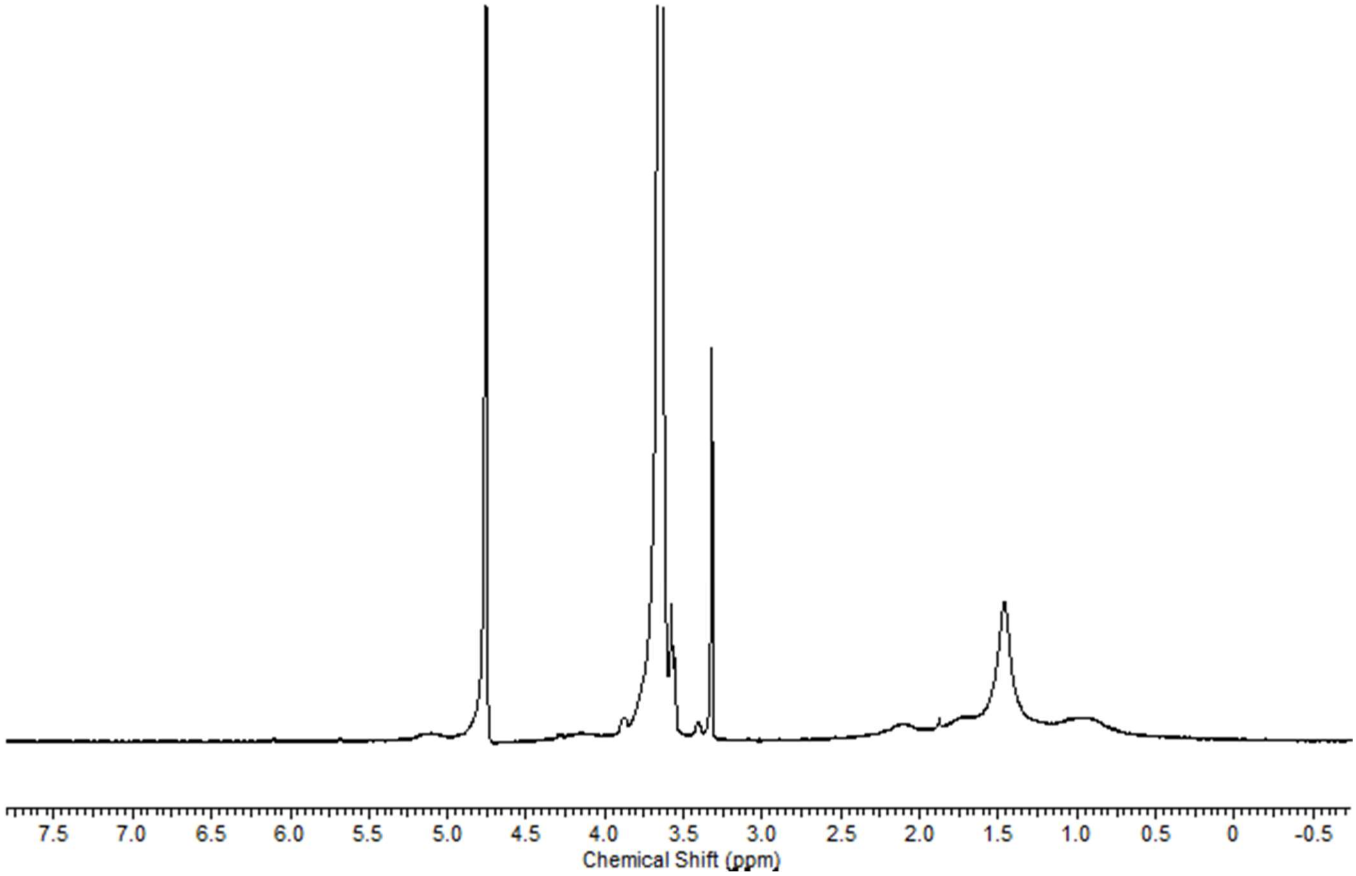

Figure S1. ^{1}H NMR of the non-oxidized poly(TMA-*co*-PEGMA) polymer used as redox species for electrochemical tests in the positive half-cells of both conventional filter-press flow cell and micro-tubular flow cell.

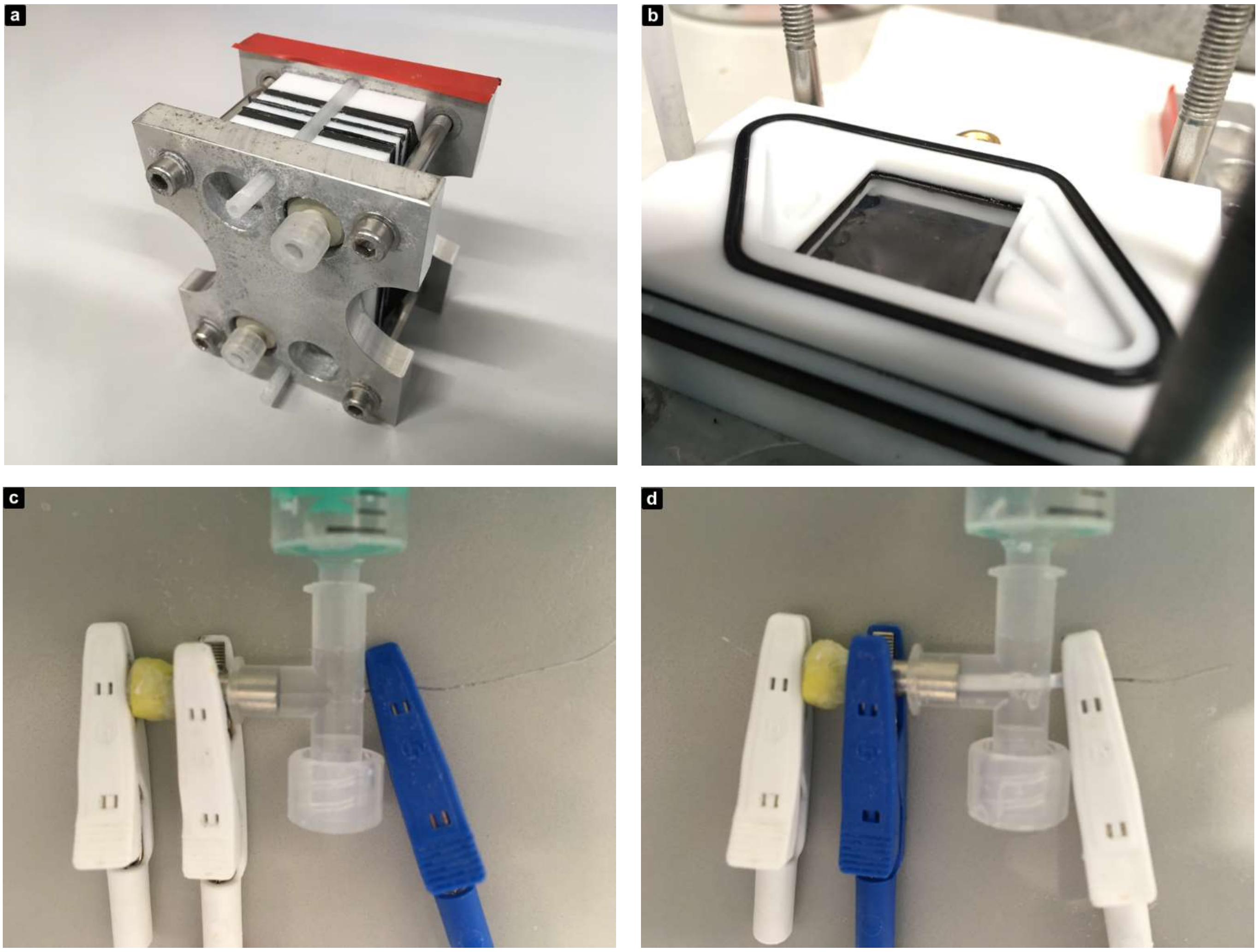

Figure S2. Photographs of the setups used for the measurement of membrane resistances: (a) Conventional filter-press flow cell in the assembled state; (b) conventional filter-press flow cell during assembly with a flat membrane; (c) setup for the micro-tubular membrane without membrane and (d) with membrane.

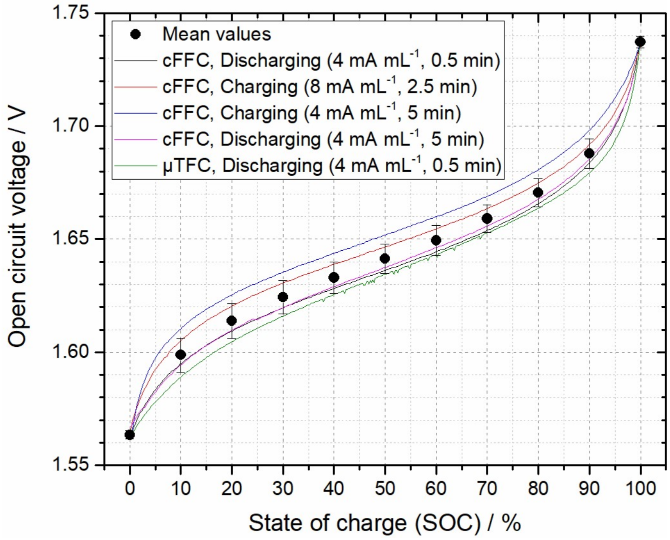

Figure S3. Relationship between open circuit voltage and state of charge of the utilized electrolyte system as obtained from incremental galvanostatic charging and discharging, respectively, for both cell types. Open circuit periods of 0.5 or 2.5 min were utilized and open circuit voltages of 1.56 and 1.74 V were taken as 0% and 100% SOC. Mean values and their standard error (95% confidence interval) were calculated from the different curves and are depicted as full circles.

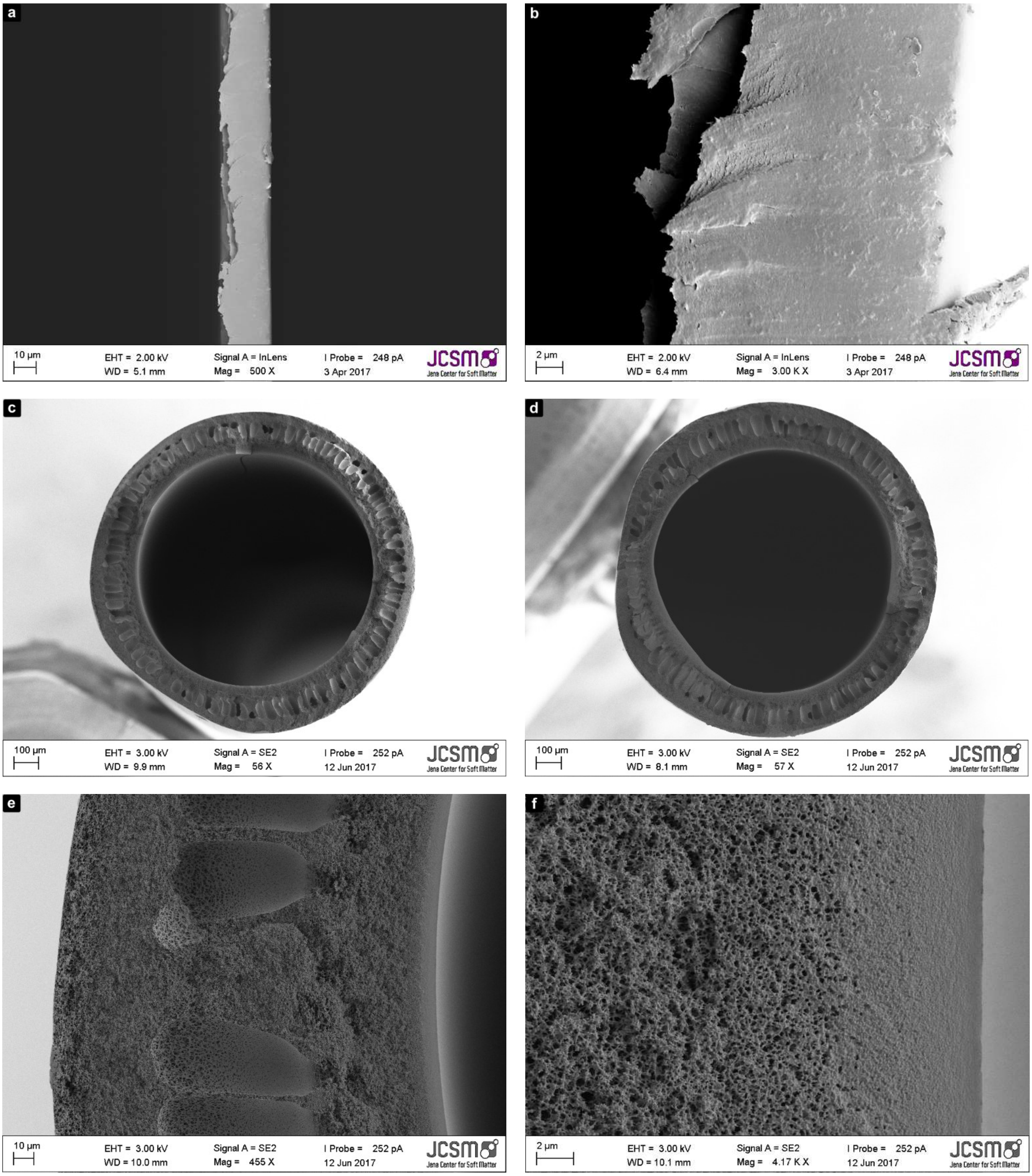

Figure S4. Scanning electron micrographs of the utilized (a-b) flat membrane type and (c-f) micro-tubular membrane type in different magnifications. The different manufacturing types are clearly visible with the flat membranes consisting completely of a very dense pore structure, while the micro-tubular membranes consist of a macro-porous supporting layer with a thin meso- to micro-porous separation layer on its inner side; (f) shows the dense separation layer and allows the estimation of its thickness in the dry state (≈ 10 to 20 µm).

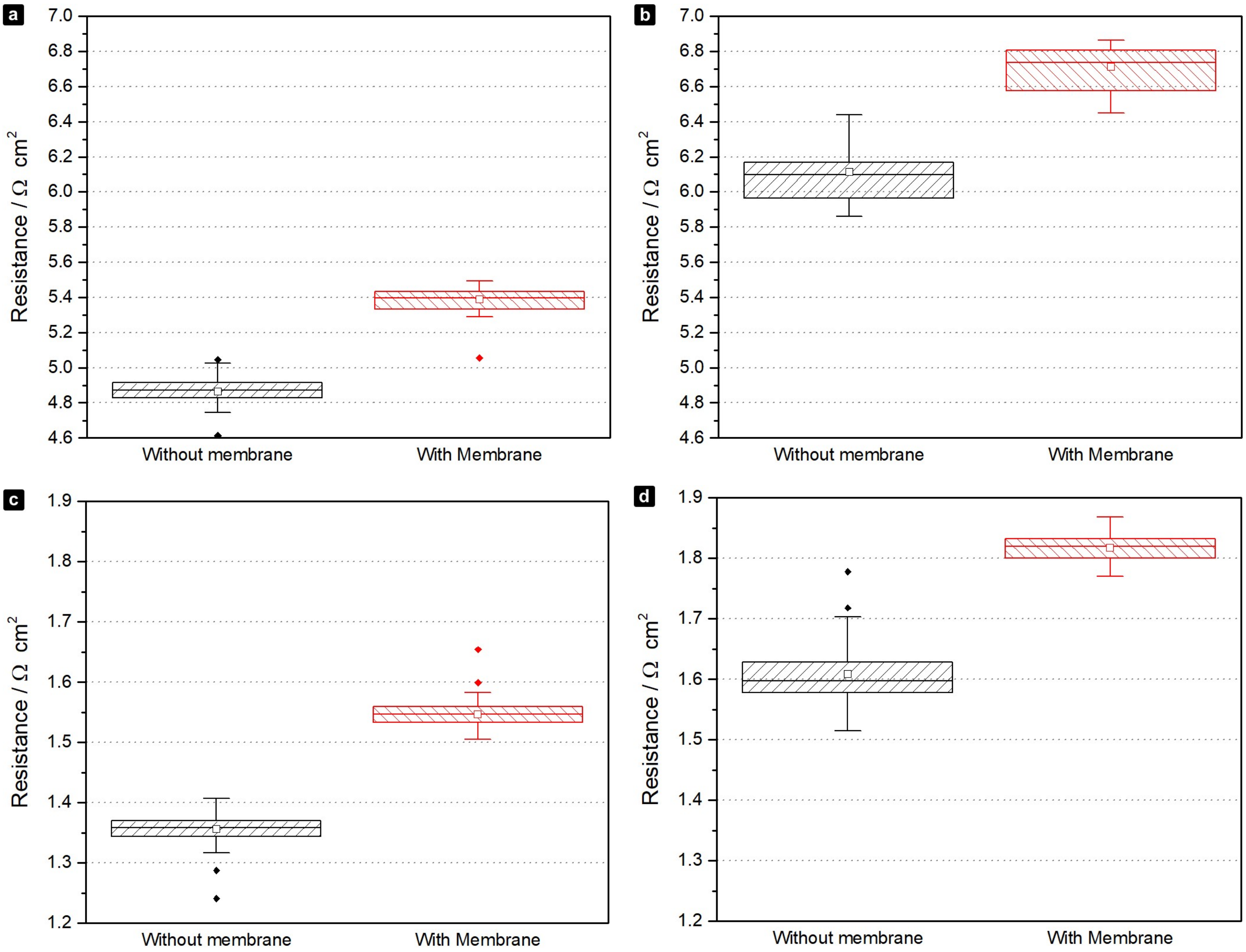

Figure S5. Box plots of the measured membrane area resistances as obtained from 64 measurements per box, showing the statistical variation of the measurement as well as the median (horizontal line within each box) and mean value (square within the box) for (a) the flat membranes in 1.00 ± 0.02 mol L^{-1} NH_4Cl, (b) the flat membranes in 1.00 ± 0.02 mol L^{-1} $ZnCl_2$, (c) the micro-tubular membranes in 1.00 ± 0.02 mol L^{-1} NH_4Cl, and (d) the micro-tubular membranes in 1.00 ± 0.02 mol L^{-1} $ZnCl_2$.

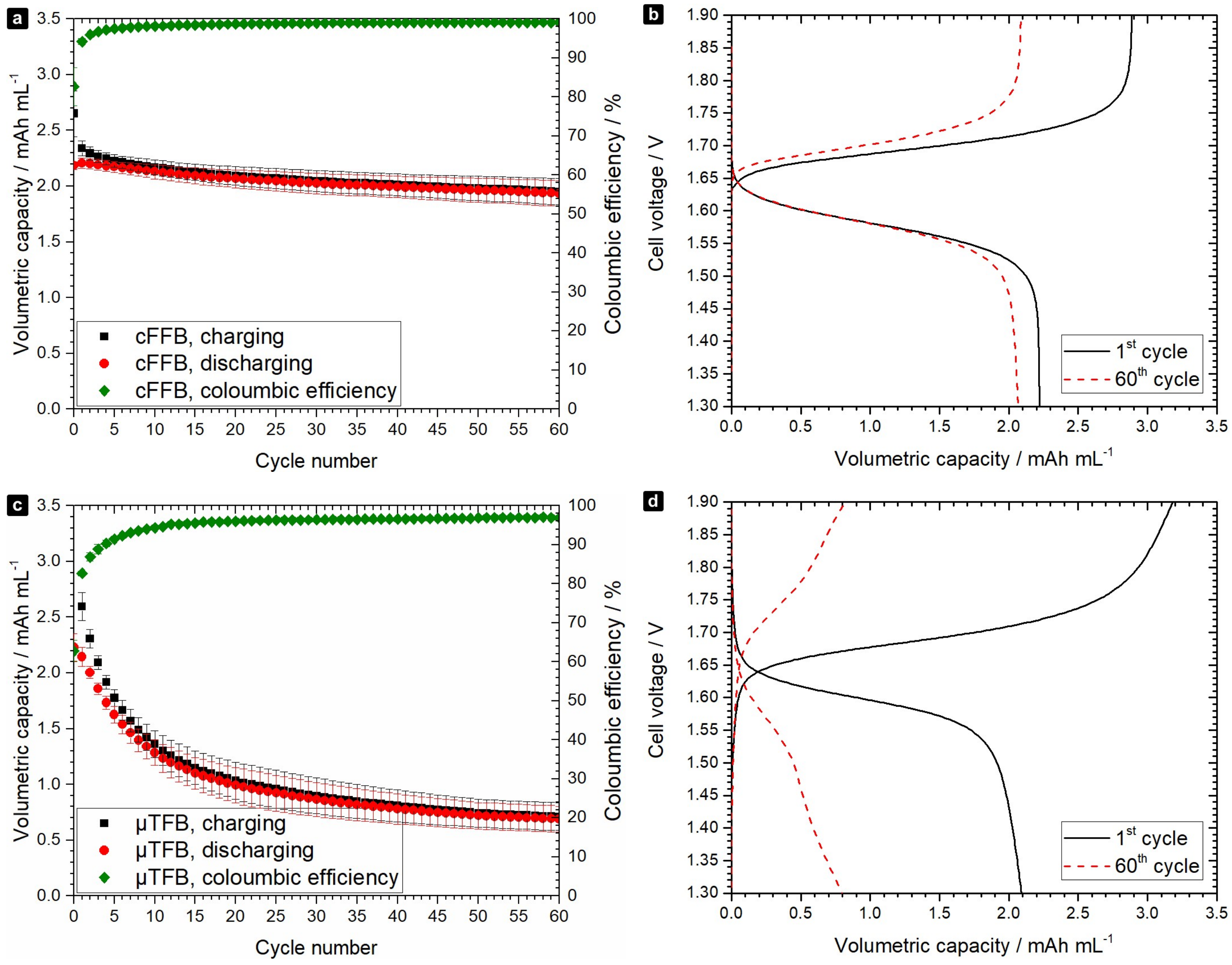

Figure S6. Cycle stability experiments shown in Figure 6 including additionally the coulombic efficiencies for (a) the conventional filter-press flow cell and (c) the micro-tubular flow cell. Potential-time diagrams during galvanostatic charging and discharging at 5 mA mL^{-1} of the cycle stability experiments for (b) the conventional filter-press flow cell and (d) the micro-tubular flow cell.

Table S1. The table shows the results of Welch's *t*-Test in order to verify the statistical significance of the observed performance differences between both cell types with respect to the observed standard deviations of three repetitions of the experiment. Discharge capacity retention values were obtained from the current rating experiments performed with three independently assembled cells of each cell type and are normalized to the discharge capacity value obtained at 1 mA cm^{-3} directly before the current rating experiment was started. The listed mean values of the capacity retention and their corresponding standard deviations are also plotted in Figure 6a of the publication.

Current density / mA cm^{-3}	**Normalized capacity (cFFB)* / %**					**Current density / mA cm^{-3}**	**Normalized capacity (µTFB)** / %**					**Welch's *t*-Test values**	
cFFB	First cell	Second cell	Third cell	Mean	Std.-dev.	µTFB	First cell	Second cell	Third cell	Mean	Std.-dev.	t-value	p-value
88.9	0.015	0.004	0.004	0.008	0.007	99.9	7.925	7.318	4.519	6.587	1.817	6.273	0.024
66.7	0.059	0.007	0.003	0.023	0.031	74.9	12.391	11.859	8.645	10.965	2.027	9.349	0.011
44.4	2.934	0.007	0.057	0.999	1.676	49.9	21.096	21.341	18.386	20.274	1.640	14.239	0.001
35.6	13.308	0.020	1.881	5.070	7.195	40.0	30.096	26.978	24.679	27.251	2.719	4.995	0.038
26.7	31.520	1.842	23.867	19.076	15.408	30.0	37.704	34.841	34.268	35.605	1.841	1.845	0.206
22.2	40.504	14.989	36.087	30.527	13.636	25.0	42.681	39.416	39.448	40.515	1.876	1.257	0.336
17.8	51.659	35.772	48.278	45.236	8.369	20.0	50.513	45.281	46.509	47.435	2.736	0.432	0.708
13.3	61.793	51.513	58.891	57.399	5.300	15.0	56.339	51.769	53.348	53.818	2.321	1.072	0.396
8.9	72.384	74.402	77.276	74.688	2.458	10.0	62.907	59.990	63.000	61.966	1.712	7.356	0.005
4.4	82.696	75.393	65.593	74.561	8.582	5.0	71.856	71.581	75.292	72.910	2.068	2.215	0.114
2.7	86.183	79.286	-[§]	82.734	4.877	3.0	75.876	76.047	78.914	76.946	1.706	1.940	0.192
1.8	87.457	79.395	-[§]	83.426	5.701	2.0	77.652	76.558	83.017	79.076	3.457	1.130	0.341
0.9	88.836	79.387	-[§]	84.112	6.681	1.0	76.546	73.462	83.383	77.797	5.077	1.303	0.283

* Normalized capacities of 100% of the cFFBs correspond to 5.931 mAh (first cell), 5.555 mAh (second cell), and 5.655 mAh (third cell); ** normalized capacities of 100% for the µTFBs correspond to 0.291 mAh (first cell), 0.271 mAh (second cell), and 0.319 mAh (third cell); [§] no meaningful values available due to cell failure (leakage of electrolyte due to damaged sealing).

Publication P5

State-of-charge Monitoring for Redox Flow Batteries: A Symmetric Open-circuit Cell Approach

C. Stolze, M. D. Hager, U. S. Schubert,

J. Power Sources **2019**, *423*, 60-67.

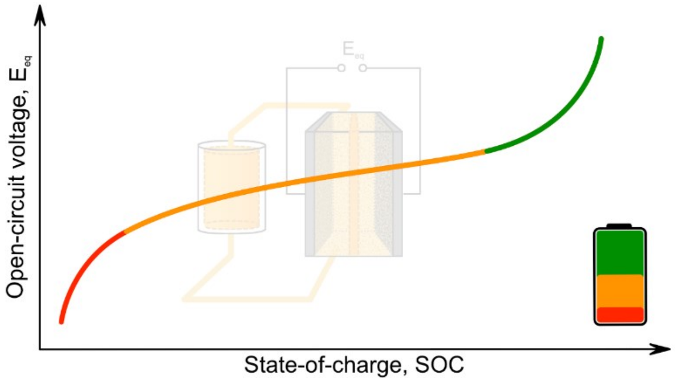

Journal of Power Sources 423 (2019) 60–67

Contents lists available at ScienceDirect

Journal of Power Sources

journal homepage: www.elsevier.com/locate/jpowsour

State-of-charge monitoring for redox flow batteries: A symmetric open-circuit cell approach

C. Stolze[a,b], M.D. Hager[a,b], U.S. Schubert[a,b,*]

[a] Laboratory of Organic and Macromolecular Chemistry (IOMC), Friedrich Schiller University Jena, Humboldtstraße 10, 07743, Jena, Germany
[b] Center for Energy and Environmental Chemistry Jena (CEEC Jena), Friedrich Schiller University Jena, Philosophenweg 7a, 07743, Jena, Germany

HIGHLIGHTS

- State-of-charge is accurately monitored on half-cell level using a symmetric open-circuit cell.
- A stable reference potential is provided by the flow battery electrolyte itself.
- Symmetric open-circuit cell shows a significantly lower reference potential drift.
- Conventional re-calibration can be replaced by a 100 to 10,000 times faster method.
- Reference electrolyte can be prepared in-situ during battery operation.

ARTICLE INFO

Keywords:
Flow battery
Flow cell
State-of-Charge
Open-circuit
Symmetric

ABSTRACT

A method for the real-time monitoring of the state-of-charge of redox flow batteries is presented, which provides half-cell resolution. The well-known standard procedure for the state-of-charge monitoring, which utilizes the equilibrium potential of the monitored electrolyte *versus* a standard reference electrode in an open-circuit cell, is modified. It is demonstrated that the flow battery electrolyte itself provides a stable reference potential if used in the reference compartment of a symmetric open-circuit cell. This reference potential can be used to monitor the state-of-charge of a flow battery electrolyte during battery operation. The proposed method is validated with *N,N,N*-2,2,6,6-heptamethylpiperidinyloxy-4-ammonium chloride (TEMPTMA) catholytes and *N,N′*-dimethyl-4,4-bipyridinium dichloride (MV) anolytes in aqueous flow batteries using both a symmetric open-circuit cell and a standard open-circuit cell with a Ag/AgCl reference electrode. Reference potential drift rates are determined and drift mechanisms are investigated, demonstrating that the utilization of a symmetric open-circuit cell reduces the reference potential drift. It is validated that the exchange of the *in-situ* producible reference electrolyte can replace time-consuming re-calibration procedures.

1. Introduction

Flow batteries represent a promising and fast evolving technology for the stationary storage of volatile wind and solar power. Their unique system design enables for the separate scaling of its power capability and capacity, which sets them apart from other battery types [1–5]. As for any battery technology, however, an efficient operation can only be achieved, if the battery properties are accurately known at any point in time. Therefore, battery management systems are required which allow the real-time estimation of important properties such as the temperature, the electrolyte flow rate, the terminal voltage, the battery's state-of-charge (SOC), and the electrolytes' state-of-health (SOH).

A variety of methods have been investigated in particular for the monitoring of the last two properties during flow battery operation. Those utilize, *e.g.*, the spectral properties of the electrolytes [6,7], the electrolytes' conductivities [6,8,9], the electrolytes' densities [10], the electrolytes' viscosities [11], the transferred charge (coulomb counting), the terminal voltage of the battery in combination with electrochemical models (ECM) and online fitting procedures [12–15], and the open-circuit potential of the electrolytes *versus* standard reference electrodes [8,16]. Table 1 provides an overview of the most important characteristics of these methods. Except for the coulomb counting methods and ECM models, all methods have in common, that they require additional measurement hardware. Despite its simple implementation, coulomb counting suffers from SOC estimation errors due to accumulating errors originating from current measurements, species

---

[*] Corresponding author. Laboratory of Organic and Macromolecular Chemistry, Friedrich Schiller University Jena, Humboldtstraße 10, 07743, Jena, Germany.
E-mail address: ulrich.schubert@uni-jena.de (U.S. Schubert).

https://doi.org/10.1016/j.jpowsour.2019.03.002
Received 21 January 2019; Received in revised form 22 February 2019; Accepted 1 March 2019

Table 1

Important characteristics of the various methods used for the SOC and SOH monitoring of flow batteries.

	UV-VIS	Electrolyte conductivity	Electrolyte density	Electrolyte viscosity	Coulomb counting	ECM & online fitting	Open-circuit voltages
No additional hardware required					x	x	
SOC estimation	x	x	x	x	x	x	x
SOH estimation						x	(x)
Half-cell resolution	x	x	x	x			x
Online monitoring	x	x	x	x	x	x	x

cross-over, and undesired side-reactions. In contrast, ECM models have been shown to be online adaptable and to estimate SOC and capacity loss accurately from the terminal voltage of redox flow cells [14,15]. However, they can only predict the SOC of the whole battery and can give no information on the SOCs of the individual electrolytes. Furthermore, the reported algorithms have only been tested on the single cell level. Due to slight overvoltage variations, SOC differences, and shunt currents between the single cells of a complete cell stack, it is not yet known whether the reported ECM models can be directly applied to practical flow battery systems. Open-circuit cells, which measure the equilibrium half-cell potentials of each electrolyte against a standard reference electrode (*e.g.*, Ag/AgCl), have been proven to predict the individual SOCs of both anolyte and catholyte accurately. While methods based on the open-circuit potentials provide half-cell resolution, they are sometimes criticized for their additional hardware requirements. However, hardware in form of open-circuit cells is technologically rather simple and its cost is small compared to the overall system costs. Nevertheless, a significant problem of this method is the instability of the reference potential caused by unpredictable species cross-over between reference electrode and half-cell electrolyte. Due to this, frequent re-calibration is required to prevent SOC estimation errors. Even the most recent calibration methods necessitate the measurement of at least a major portion of the potential-charge curve and, thus, demand a measurement time of a few to several hours for large-scale redox flow batteries [10].

In this study, an alternative to the utilization of standard reference electrodes in open-circuit cells is investigated. A symmetric open-circuit cell without standard reference electrode is used. Instead, the reference potential is provided by the equilibrium potential of a portion of the monitored flow battery electrolyte itself. Because of the chemically nearly identical composition of the monitored electrolyte and the reference electrolyte, cross-over and osmotic pressure can be minimized leading to a significantly lower reference potential drift rate. The approach is investigated experimentally by monitoring the SOC of the catholyte in TEMPTMA/MV and symmetric TEMPTMA/TEMPTMA aqueous redox flow batteries [17]. An open-circuit cell with a standard Ag/AgCl reference electrode is operated to validate the symmetric open-circuit cell data against a well-known and accurate reference system.

2. Experimental details

2.1. Materials & experimental setups

Electrolyte Preparation. 1 M TEMPTMA 1.5 M NaCl aqueous catholytes were prepared by dissolving 4.374 g of NaCl in 15 mL distilled water and, subsequently, using this NaCl solution to dilute 25 g of a 2 M TEMPTMA stock solution (provided by JenaBatteries GmbH, Germany) to a total electrolyte volume of 50 mL. 1 M MV 1.5 M NaCl aqueous anolytes were prepared by dissolving 4.032 g NaCl in 15 mL distilled water and, subsequently, using this solution to dilute 25 g of a 2.1 M MV stock solution (provided by JenaBatteries GmbH, Germany) to a total volume of 46 mL. The chemical structures of TEMPTMA and MV as well as their corresponding redox reactions are schematically illustrated in Fig. S1 (supporting information).

Potentiostat. Measurements were conducted utilizing a 16-channel-potentiostat (VMP3, BioLogics Scientific Instruments, France) which was controlled with the EC-Labs v11.16 software package. Four-terminal sensing was applied for the redox flow battery and two-wire sensing to the open-circuit cells with only the voltage sensing reference wires attached and the counter electrodes' current lead connected to ground. No temperature control was directly applied to the flow cells or electrolytes; however, all experiments were performed in an air-conditioned room at 294 ± 1 K.

Open-circuit Cells. Standard open-circuit cells were built from tubes (inner diameter: 4 mm), glass frits (diameter: 3.2 mm, length: 4.0 mm, Ion Permeability Porous Glass (IPPG), ALS Co. Ltd, Japan), and LuerLock adapters (Pieper Filter GmbH, Germany). A graphite rod (MERSEN GmbH, Germany) with a diameter of 2 mm in contact with the flow battery electrolyte was utilized as working electrode and silver wire (coated with AgCl, diameter: 0.4 mm) immersed in 0.1–0.15 mL saturated aqueous KCl-AgCl solution as the reference electrode. The glass frit was surrounded by a piece of shrinking hose and placed in a T-piece LuerLock adapter to separate the working and reference electrode compartments. The symmetric open-circuit cells were constructed in the same way except that a second graphite rod immersed in approximately 0.05 mL reference electrolyte was used instead of the silver wire and the KCl-AgCl solution. The setups are illustrated in Fig. S2 (supporting information).

Flow Battery. A literature-known redox flow battery setup was used as published elsewhere [18]. The flow cells have a geometric area of 5 cm^2 (electrode and membrane area). Porous graphite electrodes (GFA6, thickness: 6 mm, SGL Group, Germany) are compressed by 25% between graphite current collectors (MERSEN GmbH, Germany). A FAA-3-50 anion-exchange membrane (Fumatech GmbH, Germany) was used to separate the half-cells. The redox flow batteries utilized within the experiments of the present study were operated using the prepared TEMPTMA and MV electrolytes. Each half-cell was fed using a metering pump (SIMDOS 10, KNF Neuberger GmbH, Germany) at a volumetric flow rate of 100 mL min^{-1}. A standard open-circuit cell was connected to the inlet of the flow battery's positive half-cell, while a symmetric open-circuit cell was connected to the outlet of the catholyte tank.

2.2. Calibration method

The calibration was performed for both the standard and the symmetric open-circuit cell *via* the fitting method reported by Ressel *et al.* recently [10]. This method combines coulomb counting for the transferred charge, Q, and the measured equilibrium potential, E_{eq}, during a sufficiently large portion of a galvanostatic charging or discharging cycle of the battery to obtain a E_{eq}-Q-relationship for the monitored electrolyte. For the study at hand, a complete half-cycle was used for each calibration. The Nernst equation,

$$E_{eq}(Q) = E^{0\prime} \pm \frac{RT}{nF} \ln\left(\frac{\frac{Q}{Q_{max}} + SOC_0}{1 - \frac{Q}{Q_{max}} - SOC_0}\right), \quad (1)$$

is fitted to the obtained data by a least-squares approach. The formal potential of the redox reaction, $E^{0\prime}$, the total capacity of the electrolyte, Q_{max}, and the initial state-of-charge, SOC_0, are the fitting parameters, while R represents the universal gas constant, T the temperature, n the number of transferred electrons, and F the Faraday constant. The plus and minus signs correspond to catholytes and anolytes, respectively. The method can also be used for re-calibration during battery runtime but is time-consuming due to the time required to measure a sufficiently large portion of the E_{eq}-Q-diagram (especially for large-scale flow batteries). It should also be noted that equation (1) contains the formal potential and not the standard potential. Any activity coefficients for the redox active species in the battery electrolytes are not neglected, but instead are included in the formal potential term. Furthermore, the total capacity, Q_{max}, must not be confused with the battery capacity yielded during a specific charge and discharge experiment. Q_{max} corresponds to the absolute number of redox-active molecules present in the electrolyte, while the charge/discharge capacity of the battery corresponds to the number of charges transferred during an experiment and is dependent on the specific experimental parameters (current, cell resistance, voltage limits etc.).

2.3. Reference potential stability investigations

For investigation of the reference potential stability, a redox flow battery was galvanostatically cycled for at least 50 h at current densities of ± 50 mA cm^{-2} with both a Ag/AgCl open-circuit cell and a symmetric open-circuit cell with a 50% SOC reference electrolyte. The reference potential drift was quantified by applying Ressel's (re-)calibration procedure (see section 2.2) to every 5th charging cycle. The corresponding fit parameter for the formal potential, $E^{0\prime}$, of the redox reaction *versus* a Ag/AgCl reference electrode and the reference potential, E_{ref}, of the reference electrolyte in the symmetric open-circuit cell were plotted over time. Subsequently, linear regressions were performed on the obtained data and the slope was taken as a measure for the reference potential drift in both cell types. This experiment was repeated four times with flow batteries that operated 65 cycles, 35 cycles, 30 cycles, and 25 cycles, respectively. The mean value and its standard deviation were calculated for the drift rates of these experiments.

2.4. Cross-over and self-discharge investigations

After preparation of a TEMPTMA reference electrolyte at a SOC of 50%, about 1.5 mL of that electrolyte were extracted and stored in a separate glass vial over 26 days at room temperature. Several aliquots of this electrolyte were used as reference electrolytes in a symmetric open-circuit cell connected to the catholyte of a TEMPTMA/TEMPTMA redox flow battery. The latter was operated over the same time period in a galvanostatic cycling mode at 50 mA cm^{-2} utilizing the unbalanced symmetric redox flow battery approach suggested by Goulet *et al.* [19]. A standard open-circuit cell with Ag/AgCl reference electrode was operated at the same redox flow battery as a reference system. Both open-circuit cells were calibrated according to the previously described procedure (see section 2.2). The reference potential drift was measured as described in section 2.3.

3. Results & discussion

3.1. Reference potential in symmetric open-circuit cells

The voltage measured by a symmetric open-circuit cell can simply be expressed by the difference in equilibrium potentials of the monitored electrolyte and the reference electrolyte, *i.e.*,

$$E_{eq}(SOC) = \pm\frac{RT}{nF}\ln\left(\frac{SOC}{1-SOC}\right) - \left[\pm\frac{RT}{nF}\ln\left(\frac{SOC_{ref}}{1-SOC_{ref}}\right)\right]. \tag{2}$$

In this equation, SOC and SOC_{ref} are the state-of-charge of the monitored electrolyte and the reference electrolyte. Plus and minus signs correspond to catholytes and anolytes, respectively. The second term corresponds to the formal potential of the redox reaction measured *versus* the reference electrolyte. It will be termed reference potential, E_{ref}, throughout this study. Hence, the equilibrium voltage of the symmetric open-circuit cell can be expressed as

$$E_{eq}(SOC) = E_{ref}(SOC_{ref}) \pm \frac{RT}{nF}\ln\left(\frac{SOC}{1-SOC}\right). \tag{3}$$

The reference potential, E_{ref}, and the formal potential, $E^{0\prime}$, which is used to describe redox potentials *versus* a standard reference electrode, basically have the same meaning and just reflect the difference in the chosen reference system. Hence, the cell voltage can be expressed mathematically in the same way for standard open-circuit cells and symmetric open-circuit cells and, consequently, Ressel's calibration method can be used for both cell types.

Reference potential stability can be estimated from analyzing the time-derivative of the equilibrium potential. Assuming constant SOC for the monitored flow battery electrolyte, the time-derivative of the symmetric open-circuit cell voltage with a time-dependent, *i.e.* drifting, reference potential can be derived from equations (2) and (3) and its absolute value is

$$\left|\frac{dE_{eq}}{dt}\right| = \left|\frac{dE_{ref}}{dt}\right| = \frac{RT}{nF}\frac{1}{SOC_{ref}(1-\ SOC_{ref})}\left|\frac{dSOC_{ref}}{dt}\right| \tag{4}$$

It is evident, that the pre-factor on the right-hand side and, thus, the time-derivative of the reference potential has a minimum at SOC_{ref}= 0.5. Hence, a reference state-of-charge of 50% is expected to be the optimum for symmetric open-circuit cells in terms of reference potential stability.

3.2. Calibration and SOC estimation accuracy

In a first series of experiments, TEMPTMA/MV redox flow batteries were galvanostatically cycled, while the TEMPTMA electrolyte was monitored with both types of open-circuit cells. This electrolyte system was chosen due to its synthetically easy accessibility, its suitable electrochemical properties, and due to the underrepresentation of SOC monitoring methods that were validated using organic molecules in literature. However, the herein presented method is not limited to organic redox species. It is equally suited for metal containing electrolytes like, *e.g.*, vanadium-, iron-, and chromium-based systems.

The evolution of the cell voltages over time is shown in Fig. 1a for five cycles of an exemplary experiment. Calibration data was obtained for both the standard open-circuit cell and the symmetric open-circuit cell from the first charging cycle (Fig. 1b). The coefficient of determination, R^2, was over 0.999 in both cases indicating a well-defined fit. The resulting fit parameters for both calibrations are given in Table 2. The obtained initial state-of-charge, SOC_0, and total capacity, Q_{max}, of both cell types do not show any considerable deviations. A graphically beneficial property of the calibration curve of the symmetric open-circuit cell is that the SOC of the reference electrolyte, SOC_{ref}, can be directly read out at the abscissa intercept of the calibration curve. Once the SOC_{ref} is known, the flow battery electrolyte's state-of-charge, SOC, can be monitored by continuously measuring the open-circuit voltage, E_{eq}, of the symmetric open-circuit cell and utilizing equation (5):

$$SOC(E_{eq}) = \frac{SOC_{ref}\exp\left(\frac{nF}{RT}E_{eq}\right)}{1 - SOC_{ref} +\ SOC_{ref}\exp\left(\frac{nF}{RT}E_{eq}\right)}. \tag{5}$$

This equation was derived from equation (2) by applying the exponential function and rearranging the resulting equation for SOC. Another calculation option for both types of open-circuit cell represents the inverse of the Nernst equation,

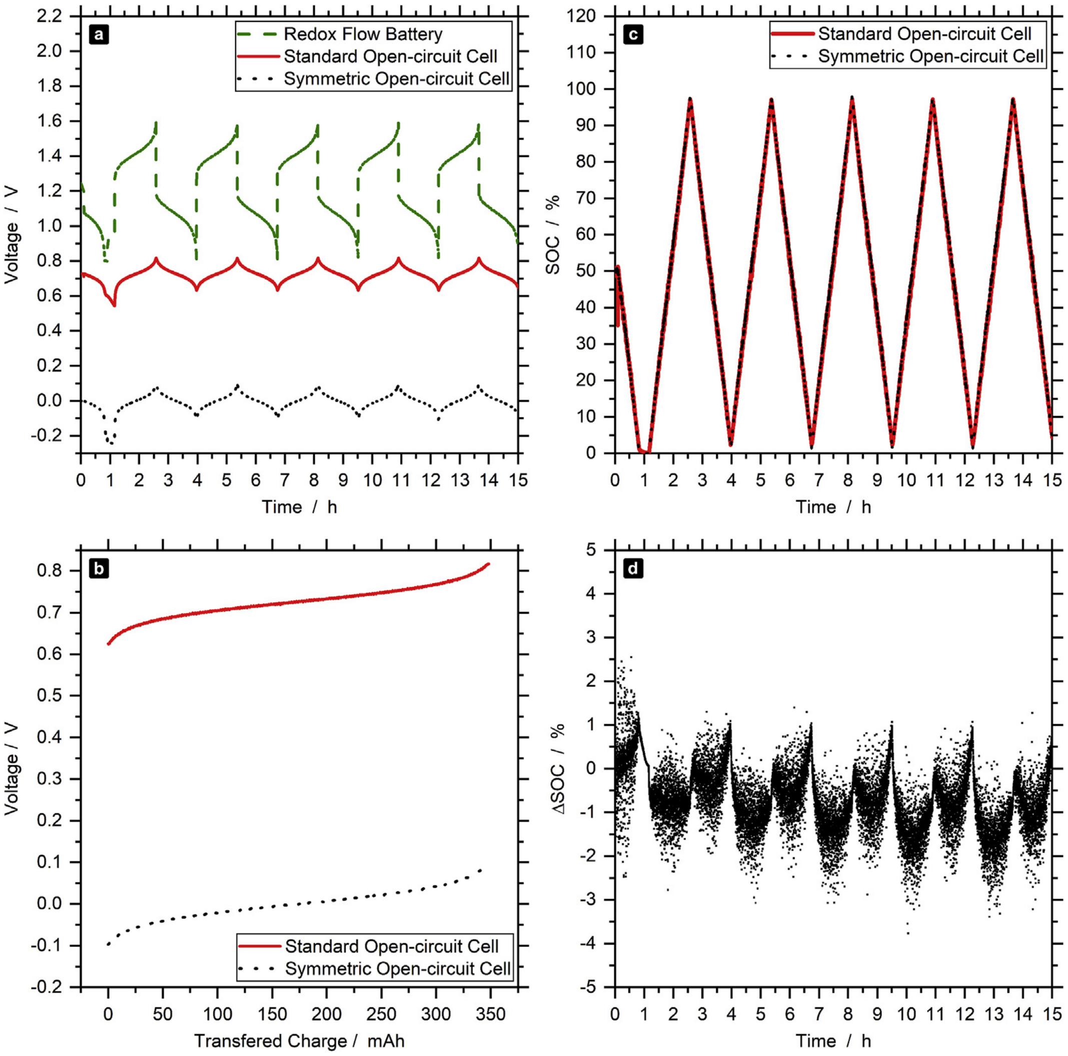

Fig. 1. After *in-situ* production of the reference electrolyte at 50% SOC, cell voltages of the TEMPTMA/MV redox flow battery and the corresponding open-circuit cells were monitored over five consecutive galvanostatic cycles at 50 mA cm^{-2} (a). The open-circuit voltages of the first charging cycle (b) were used for the calibration of the OCV-SOC relationship. The obtained calibration was used to monitor the SOC (c) of the catholyte over five successive cycles. The absolute difference in the SOC estimation between the both open-circuit cells is depicted in (d).

Table 2

Fit parameters from an exemplary calibration of both Ag/AgCl open-circuit cell and the symmetric open-circuit cell. Data was obtained during the first charging cycle after reference electrolyte preparation. Given uncertainties correspond to the standard deviation of the fitting procedure.

	Ag/AgCl open-circuit cell	Symmetric open-circuit cell
R^2	0.9993	0.9994
$E^{0\prime}/E_{ref}$	726.92 ± 0.05 mV	−0.02 ± 0.05 mV
SOC_0	1.78 ± 0.02%	2.40 ± 0.02%
$Q_{\max}$	364.9 ± 0.1 mAh	364.2 ± 0.1 mAh

$$SOC\,(E_{eq}) = \frac{\exp\left(\frac{nF}{RT}(E_{eq} - E_{ref})\right)}{1 + \exp\left(\frac{nF}{RT}(E_{eq} - E_{ref})\right)}. \tag{6}$$

For the standard open-circuit cell, the term $(E_{eq} - E_{ref})$ needs to be replaced by $(E_{eq} - E^{0\prime})$. Equations (5) and (6) are derived for catholytes (plus signs in equation (2)). For anolytes the exponents need to have a negative sign. The obtained calibration curves were used to calculate the SOC-time diagrams from the measured open-circuit cell voltages. Exemplary SOC-time diagrams are illustrated in Fig. 1c for four cycles after the calibration and their absolute difference is displayed in Fig. 1d. The variance within the measured SOC differences in this figure is mainly caused by measurement noise from the voltage measurement. In four repetitions of this calibration procedure for separate experiments, the absolute SOC estimation differences for the calibration cycles of both cell types revealed a mean difference of −0.03% with a standard deviation of 0.29%. In other words, the both open-circuit cells perform equally accurate with a negligible difference in their SOC estimates.

It should be noted that Ressel's calibration method is based on the Nernst equation and, thus, is only strictly applicable to redox species whose redox reaction does not involve any side reactions or additional reaction partners (*e.g.,* hydrogen, oxygen *etc.*). Although this particular method was used for calibration in this study, any other validated calibration procedures can be applied. A procedure that, *e.g.,* does not pose any requirements on the redox reaction was frequently used by Wei *et al.* recently [13–15]. These authors utilized a combination of constant-current constant-voltage charging, coulomb counting, and a polynomial fitting of fifth order to obtain OCV-SOC-relationships.

3.3. Reference potential stability

Investigation of the reference potential stability for both open-

Table 3
Fit parameters obtained from the linear regressions, which were performed on the reference potential plots (Fig. S3). Stated uncertainties correspond to the standard deviation of the fitting procedure.

No.	1		2		3		4	
	Standard	Symmetric	Standard	Symmetric	Standard	Symmetric	Standard	Symmetric
Duration	160 h / 65 cycles		73 h / 35 cycles		80 h / 30 cycles		52 h / 25 cycles	
R^2	0.95963	0.70526	0.87241	0.9462	0.90069	0.82676	0.99838	0.51939
$\frac{dE_{ref}}{dt}$	$-78 \pm 4\,\mu V\,h^{-1}$	$18 \pm 3\,\mu V\,h^{-1}$	$-108 \pm 15\,\mu V\,h^{-1}$	$55 \pm 5\,\mu V\,h^{-1}$	$-66 \pm 9\,\mu V\,h^{-1}$	$48 \pm 9\,\mu V\,h^{-1}$	$-98 \pm 2\,\mu V\,h^{-1}$	$25 \pm 10\,\mu V\,h^{-1}$

circuit cell types was performed during galvanostatic operation of TEMPTMA/MV redox flow batteries, respectively. For the measurements, the symmetric open-circuit cell utilized a reference electrolyte with a reference state-of-charge, SOC_{ref}, of about 50%. This value was chosen due to the expected reference potential stability at this state-of-charge according to equation (4). The reference potentials are plotted over time in Fig. S3 (supporting information) for all four repetitions of the experiment. In each case, the potential drift is faster in the first 5 to 10 cycles after reference electrolyte exchange and slows down afterwards. The drift rates were obtained by linear regressions performed on each full data set. The results of these linear regressions are summarized in Table 3. In the average, the potential drift of the Ag/AgCl reference electrode was $-87 \pm 20\,\mu V\,h^{-1}$ and the potential drift for the symmetric open-circuit cell was $37 \pm 18\,\mu V\,h^{-1}$. The potential drift rate of the symmetric open-circuit cell was, thus, by a factor of two lower. In order to exclude an influence of the specific construction of the open-circuit cell (*e.g.*, the exact position of the glass frit), the setups have been interchanged between the experiments; *i.e.,* the setup used for the symmetric open-circuit cell was used for the standard cell and *vice versa*. No significant difference was observed. However, two other important points deserve a thorough discussion to enable a proper judgement of the presented drift-rates:

(1) While the symmetric open-circuit cells were filled with 0.05 mL of reference electrolyte (in order to be economical with the amount of available electrolyte), standard open-circuit cells contained 0.1–0.15 mL of saturated KCl-AgCl reference electrolyte.
(2) The low amount of reference electrolyte of both cell types is prone to volume errors and causes slight variations in the filling state of the reference compartment between the experiments.

In general, if a certain amount of substance enters or leaves the reference compartment over time (diffusion/cross-contamination) the composition of a large electrolyte volume is less affected than a small electrolyte volume. Hence, the rather high standard deviation of the measured drift rates can be explained by both point (1) and point (2). Based on the same reasoning, it has to be concluded from point (1) that the true relative difference in drift rates is rather under-estimated by the presented measurements. Consequently, it can be stated that the average drift rate of the symmetric open-circuit cell is *at least* two-fold lower. The origin of the observed reference potential drift within the symmetric open-circuit cell was further investigated.

3.4. Cross-over and self-discharge investigations

The most prominent causes for reference potential drift in standard open-circuit cells are temperature changes and species cross-over. In symmetric open-circuit cells, an additional source of reference drift can be self-discharge of the reference electrolyte, *e.g.*, by chemical decomposition of the oxidized/reduced redox species. While drift which is due to temperature changes is predictable if the temperature is monitored or kept constant, this is not the case for species cross-over and self-discharge. Both mechanisms cannot be precluded as the source of reference potential drift in the previously described experiment. To investigate the cause, another experiment was performed: A defined amount of TEMPTMA reference electrolyte was prepared with a SOC_{ref} of 50% and was stored in a separate and closed glass vial over 26 days. During this time period, a symmetric open-circuit cell with a fraction of this previously prepared reference electrolyte was utilized to monitor the SOC of one half-cell of a TEMPTMA/TEMPTMA redox flow battery during long-term galvanostatic cycling. In the first cycle after reference electrolyte insertion, the symmetric open-circuit cell was calibrated revealing an initial reference potential, E_{ref}, of -1.25 ± 0.06 mV corresponding to a reference state-of-charge of 51%. The evolution of the reference potential over time was subsequently investigated using re-calibration procedures applying the same methodology as presented before. Additionally, the reference electrolytes of both open-circuit cells were replaced three times. For the symmetric open-circuit cell a fraction of the separately stored reference electrolyte was used as replacement. The exchange procedure was performed after 12 days, after 18 days, and after 26 days of battery operation, respectively.

Fig. 2 depicts the reference potential evolution over time measured in this experiment. It can be seen that the reference potential dropped by several millivolts after each reference electrolyte exchange and it differed from its initial calibration value by not more than 1.5 mV in each case. According to equations (3) and (4) the state-of-charge of the reference electrolyte was, thus, constant within an absolute range of approximately ± 1.5% during storage in a separate glass vial over 26

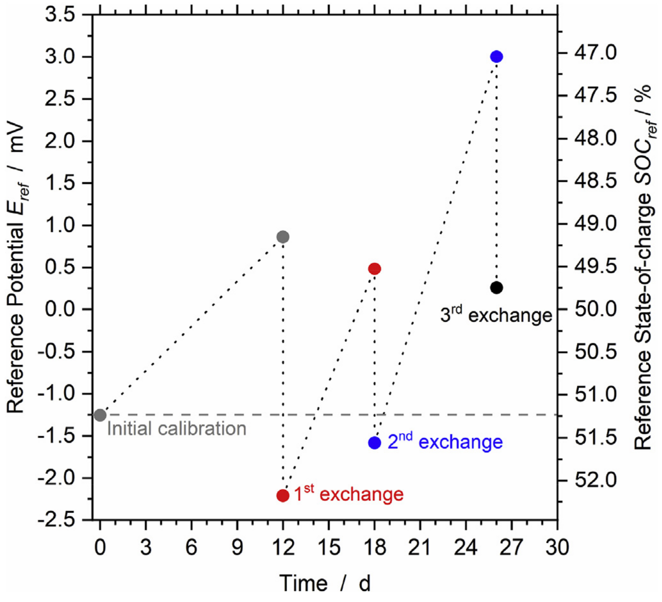

Fig. 2. Temporal evolution of the reference potential of the symmetric open-circuit cell used to monitor the SOC of one half-cell of a TEMPTMA/TEMPTMA redox flow battery. The reference potentials obtained during initial calibration as well as during re-calibration directly before and after the reference electrolyte replacement from the separately stored reference electrolyte reservoir are shown. The ordinate on the right displays the associated reference electrolyte's state-of-charge, SOC_{ref}.

days. The variations are most-likely caused by small electrolyte contaminations during the manual exchange-procedure, some electrolyte self-discharge, the varying membrane potentials, and/or the uncertainty of the re-calibration procedure. Further distinction between these possible causes demands additional intensive investigations in the future. Despite that, this experiment proved that the reference electrolyte stored in the glass vial had not changed to a large extend within approximately one month. Consequently, self-discharge mechanisms are not the main cause for the previously observed reference potential drift rate. The latter has to be attributed mainly to cross-over effects instead. A further significant reduction of the reference potential drift can, therefore, be achieved by further inhibition of cross-over mechanisms. For example, the application of ion-selective membranes instead of glass frits as separators within the symmetric open-circuit cells could be beneficial in this context.

3.5. Reference electrolyte exchange

The observed stability for a separately stored reference electrolyte offers a novel opportunity to keep SOC estimation errors of open-circuit cells small. Time-consuming re-calibration procedures are usually performed to correct reference potential drifts. These procedures necessitate the measurement of a sufficiently large portion of the E_{eq}-t-curve of the battery electrolyte. For large-scale batteries it takes hours to charge/discharge and, therefore, it also takes hours to re-calibrate an open-circuit cell. An alternative is to replace the reference electrolyte within the open-circuit cell to mitigate cross-over effects and, thus, to recover the initial reference potential. The data obtained from the previous experiment enabled an analysis of the accuracy of such a replacement procedure in comparison to the conventional re-calibration procedure.

During the experiment described above, an additional standard open-circuit cell with Ag/AgCl reference electrode was operated on the flow battery electrolyte. This standard open-circuit cell was frequently re-calibrated, which allowed to calculate a reliable reference SOC for each cycle. The initial reference potential value of -1.25 ± 0.06 mV obtained during initial calibration of the symmetric open-circuit cell was used to calculate the SOC from the voltage of the symmetric open-circuit cell instead of re-calibrating it. The absolute difference between the SOC measured by the re-calibrated standard open-circuit cell and the SOC obtained from the not re-calibrated symmetric open-circuit cell is shown in Fig. S4 (supporting information) for the complete cycles. A concise form of the same data is presented as box plots in Fig. 3a. Each box represents the data of the full charging cycle which directly succeeded the reference electrolyte exchange procedure. It is evident that after the exchange the estimated SOC values do not differ from the reference SOC by more than ± 6% SOC at any point during the cycle. Indeed, the mean values of each of the four data sets and their corresponding two-fold standard deviations indicate that 95% of the measured data points within each cycle show a deviation of less than ± 3% from the “true” SOC value. The average estimation error and its standard deviation calculated from the mean values of the four cycles is 0.07 ± 0.77%.

In another analysis approach, the SOC estimation error was evaluated by re-calibrating the symmetric open-circuit cell and comparing it to the not re-calibrated data. This was done for the charging cycles before and after each reference electrolyte exchange in order to verify that the reference electrolyte exchange had a significant effect on the SOC estimation at all. The result is shown in Fig. 3b. While the SOC estimation error is in general small on the investigated time scale due to the low reference potential drift rate of the symmetric open-circuit cell, a significant reduction of the estimation error by approximately 1 to 2% is observed after each reference electrolyte exchange.

In conclusion, the difference between re-calibration and reference electrolyte exchange procedure is insignificant and both methods can be used interchangeably. However, while the re-calibration requires hours to achieve accurate results, the reference electrolyte exchange was performed manually within 5–10 min by the experimenter. Automated procedures integrated into a flow battery monitoring system will be able to exchange the reference electrolyte within seconds at any point during battery operation. Therefore, the presented electrolyte exchange procedure is 100 to 10,000 times faster than conventional re-calibration procedures. Judging from the observed SOC estimation error increase over time and considering a 5% error as the highest acceptable estimation error, a reference electrolyte exchange once or twice a month would suffice to maintain sufficiently accurate monitoring of the flow batteries' state-of-charge *via* symmetric open-circuit cells.

It is worth noting that – in principle – the demonstrated electrolyte exchange procedure is applicable to standard open-circuit cells as well. Nevertheless, the application of this procedure to these cells would require an external supply of, *e.g.*, saturated KCl-AgCl reference electrolyte once the reservoir is emptied. Furthermore, the electrolyte replacement procedure would be required to be performed more often due to the faster reference potential drift observed for standard open-circuit cells (see section 3.3). In contrast to that, the symmetric open-circuit cell approach allows an *in-situ* production of reference electrolyte from the flow battery electrolyte itself without interrupting the

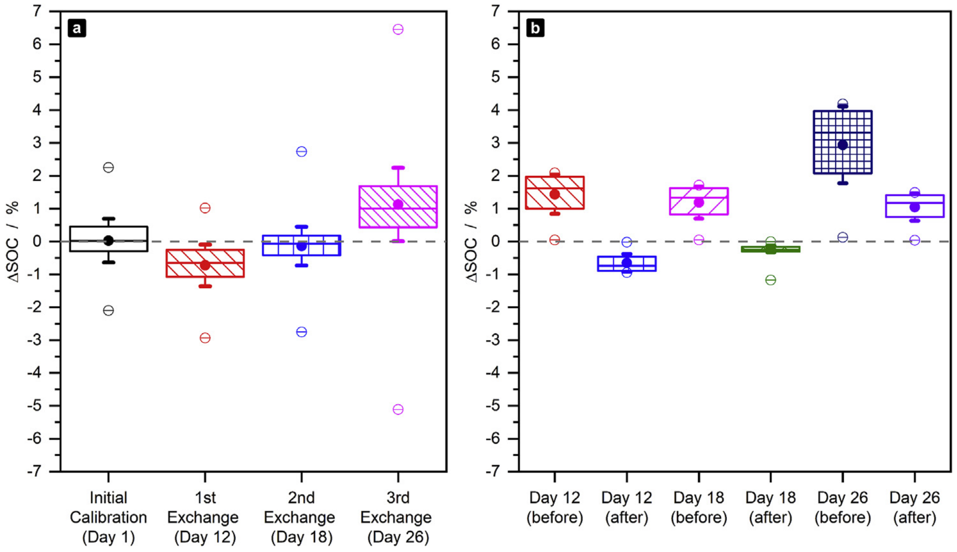

Fig. 3. Box plots of the SOC estimation differences between (a) the data of the re-calibrated standard open-circuit cell with Ag/AgCl reference electrode and the data of the not re-calibrated symmetric open-circuit cell after the reference electrolyte exchange and (b) between the re-calibrated symmetric open-circuit cell data and the not re-calibrated symmetric open-circuit cell data before and after the reference electrolyte exchange. Each box plot represents the data for the full charging cycle. The boxes mark the 25th and 75th percentile, the whiskers represent one standard deviation, the circles within the box show the mean value, the horizontal lines represent the medians, and the outer circles show the minimum and maximum values within the data set. Observed variances originate mainly from the measurement noise of the cell voltage measurement.

battery's operation. That is, as soon as the reference electrolyte reservoir is getting empty, it can be refilled from the flow battery electrolyte tanks. A defined SOC of the battery electrolyte can be guaranteed during this step, if a reference electrolyte exchange is carried out on the symmetric open-circuit cell prior to the reservoir refill.

4. Conclusions

A modification to the standard approach for state-of-charge monitoring by open-circuit cells was investigated. Instead of using standard reference electrodes, a symmetric open-circuit cell is presented which utilizes a fraction of the monitored flow battery electrolyte itself as stable reference electrolyte. The method was validated against a standard open-circuit cell with a Ag/AgCl reference electrode for the catholyte of an aqueous TEMPTMA/MV flow battery.

With a mean absolute difference of $-0.03 \pm 0.29\%$ between the SOC estimates obtained from both types of open-circuit cells for four separate calibration cycles, both cell types revealed no significant accuracy difference. It was demonstrated that reference potential drift naturally occurs in both systems and drift values were quantified to be $-87 \pm 20\,\mu\text{V}\,\text{h}^{-1}$ for the standard open-circuit cell with Ag/AgCl reference electrode and $37 \pm 18\,\mu\text{V}\,\text{h}^{-1}$ for the symmetric open-circuit cell. The comparably high drift rate values observed for both cell types are attributed to the low reference electrolyte volumes and the steep concentration gradients between highly concentrated flow battery electrolyte and the Ag/AgCl reference electrolyte. Furthermore, the presented investigations allow the conclusion that the observed potential drift within the reference electrolyte of the symmetric open-circuit cell is not predominantly caused by self-discharge/chemical decomposition of the electrolyte but most-likely by cross-over effects. This observation enabled the development of a simple reference electrolyte exchange procedure, which has been demonstrated to be equally accurate to conventional re-calibration procedures. The results are promising and encourage to invest further research efforts on the presented approach. The latter should concentrate on the investigation of the impact of temperature variations on the accuracy of the SOC estimation. This impact is expected to be small and mathematically predictable. Nevertheless, detailed temperature-dependent experiments are required to verify this expectation. Furthermore, the application of ion-selective membranes instead of glass frits as separators in the symmetric open-circuit cells is likely to improve the reference potential stability and should also be investigated experimentally.

In conclusion, the presented approach for the monitoring of a redox flow battery's state-of-charge provides a variety of inherent advantages, *i.e.*:

(1) Symmetric open-circuit cells can be applied to any type of organic and inorganic (*i.e.*, also vanadium-based) redox flow chemistries and provide half-cell resolution.
(2) Symmetric open-circuit cells show significantly lower reference potential drift rates compared to standard open-circuit cells with Ag/AgCl reference electrodes.
(3) Time-consuming and frequent re-calibration usually required for open-circuit cells can be replaced by 100 to 10,000 times faster reference electrolyte exchange procedures.
(4) Reference electrolytes can be prepared *in-situ* during battery operation enabling a self-sustaining SOC monitoring system.

As for almost all SOC monitoring techniques, additional hardware is required to realize the presented approach; however, this hardware is robust, comparably simple, and its additional cost is negligible compared to the overall system costs.

Finally, it is worth noting that the main prerequisites for an accurate and reliable SOC estimation by symmetric open-circuit cells correspond to the requirements that are mandatory for an applicable and efficient redox flow battery in general: Stable electrolytes with low self-discharge and efficient membranes that reduce cross-over effects. The proposed symmetric open-circuit cells for the state-of-charge monitoring of redox flow battery electrolytes will, therefore, naturally benefit from the progress in flow battery development and research in the future. Significant progress within these areas might eventually render reference electrolyte exchange and re-calibration procedures unnecessary at all.

Acknowledgements

We gratefully acknowledge the financial support by the European Regional Development Fund (EFRE), Thüringer Aufbaubank(TAB), and the Thuringian Ministry for Economic Affairs, Science and Digital Society (TMWWdG). Furthermore, the authors kindly thank the JenaBatteries GmbH for providing the electrolyte stock solutions for the experiments.

Glossary

Symbols

E_{eq}	Equilibrium / open-circuit voltage
$E^{0\prime}$	Reference potential of the standard open-circuit cell
E_{ref}	Reference potential of the symmetric open-circuit cell
F	Faraday's constant
n	Number of electrons participating in a redox reaction
Q	Charge transferred during battery (dis)charging
Q_{max}	Total electrolyte capacity
R	Universal gas constant
SOC_0	Initial state-of-charge of the monitored battery electrolyte
SOC	State-of-charge of the monitored battery electrolyte
SOC_{ref}	State-of-charge of the reference electrolyte in the symmetric open-circuit cell
T	Temperature

Abbreviations

MV	*N,N′*-Dimethyl-4,4-bipyridinium dichloride (methyl viologen)
OCV	Open-circuit voltage
SOC	State-of-charge
TEMPTMA	*N,N,N*-2,2,6,6-Heptamethylpiperidinyloxy-4-ammonium chloride

Appendix A. Supplementary data

Supplementary data to this article can be found online at https://doi.org/10.1016/j.jpowsour.2019.03.002.

Competing interests

The authors do not have any competing interests to declare.

References

[1] J. Noack, N. Roznyatovskaya, T. Herr, P. Fischer, The chemistry of redox-flow batteries, Angew. Chem. Int. Ed. 54 (2015) 9776–9809.
[2] M. Park, J. Ryu, W. Wang, J. Cho, Material design and engineering of next-generation flow-battery technologies, Nat. Rev. Mater. 2 (2016) 16081–16099.
[3] L.F. Arenas, C. Ponce de León, F.C. Walsh, Engineering aspects of the design, construction and performance of modular redox flow batteries for energy storage, J. Energy Storage 11 (2017) 119–153.
[4] P. Leung, A.A. Shah, L. Sanz, C. Flox, J.R. Morante, Q. Xu, et al., Recent developments in organic redox flow batteries: a critical review, J. Power Sources 360 (2017) 243–283.
[5] J. Winsberg, T. Hagemann, T. Janoschka, M.D. Hager, U.S. Schubert, Redox-flow batteries: from metals to organic redox-active materials, Angew. Chem. Int. Ed. 56 (2017) 686–711.
[6] M. Skyllas-Kazacos, M. Kazacos, State of charge monitoring methods for vanadium redox flow battery control, J. Power Sources 196 (2011) 8822–8827.

[7] S. Rudolph, U. Schröder, I.M. Bayanov, K. Blenke, D. Hage, High resolution state of charge monitoring of vanadium electrolytes with IR optical sensor, J. Electroanal. Chem. 694 (2013) 17–22.
[8] S. Corcuera, M. Skyllas-Kazacos, State-of-charge monitoring and electrolyte rebalancing methods for the vanadium redox flow battery, Eur. Chem. Bull. 1 (2012) 511–519.
[9] K. Ngamsai, A. Arpornwichanop, Measuring the state of charge of the electrolyte solution in a vanadium redox flow battery using a four-pole cell device, J. Power Sources 298 (2015) 150–157.
[10] S. Ressel, F. Bill, L. Holtz, N. Janshen, A. Chica, T. Flower, et al., State of charge monitoring of vanadium redox flow batteries using half cell potentials and electrolyte density, J. Power Sources 378 (2018) 776–783.
[11] X. Li, J. Xiong, A. Tang, Y. Qin, J. Liu, C. Yan, Investigation of the use of electrolyte viscosity for online state-of-charge monitoring design in vanadium redox flow battery, Appl. Energy 211 (2018) 1050–1059.
[12] J. Kalawoun, K. Biletska, F. Suard, M. Montaru, From a novel classification of the battery state of charge estimators toward a conception of an ideal one, J. Power Sources 279 (2015) 694–706.
[13] Z. Wei, T.M. Lim, M. Skyllas-Kazacos, N. Wai, K.J. Tseng, Online state of charge and model parameter co-estimation based on a novel multi-timescale estimator for vanadium redox flow battery, Appl. Energy 172 (2016) 169–179.
[14] Z. Wei, A. Bhattarai, C. Zou, S. Meng, T.M. Lim, M. Skyllas-Kazacos, Real-time monitoring of capacity loss for vanadium redox flow battery, J. Power Sources 390 (2018) 261–269.
[15] Z. Wei, R. Xiong, T.M. Lim, S. Meng, M. Skyllas-Kazacos, Online monitoring of state of charge and capacity loss for vanadium redox flow battery based on autoregressive exogenous modeling, J. Power Sources 402 (2018) 252–262.
[16] M.R. Mohamed, H. Ahmad, M.N. Abu Seman, Estimating the state-of-charge of all-vanadium redox flow battery using a divided, open-circuit potentiometric cell, Elektron Elektrotech 19 (2013) 37–42.
[17] T. Janoschka, N. Martin, M.D. Hager, U.S. Schubert, An aqueous redox-flow battery with high capacity and power: the TEMPTMA/MV system, Angew. Chem. Int. Ed. 55 (2016) 14427–14430.
[18] T. Janoschka, N. Martin, U. Martin, C. Friebe, S. Morgenstern, H. Hiller, et al., An aqueous, polymer-based redox-flow battery using non-corrosive, safe, and low-cost materials, Nature 527 (2015) 78–81.
[19] M.-A. Goulet, M.J. Aziz, Flow battery molecular reactant stability determined by symmetric cell cycling methods, J. Electrochem. Soc. 165 (2018) A1466–A1477.

Journal of Power Sources

- Supplementary Data -

State-of-Charge Monitoring for Redox Flow Batteries: A Symmetric Open-circuit Cell Approach

C. Stolze,[a,b] M. D. Hager,[a,b] and U. S. Schubert*,[a,b]

[a] *Laboratory of Organic and Macromolecular Chemistry (IOMC), Friedrich Schiller University Jena, Humboldtstraße 10, 07743 Jena, Germany.*

[b] *Center for Energy and Environmental Chemistry Jena (CEEC Jena), Friedrich Schiller University Jena, Philosophenweg 7a, 07743 Jena, Germany.*

---

* *Corresponding author: Laboratory of Organic and Macromolecular Chemistry, Friedrich Schiller University Jena, Humboldtstraße 10, 07743 Jena, Germany.*
E-Mail: ulrich.schubert@uni-jena.de

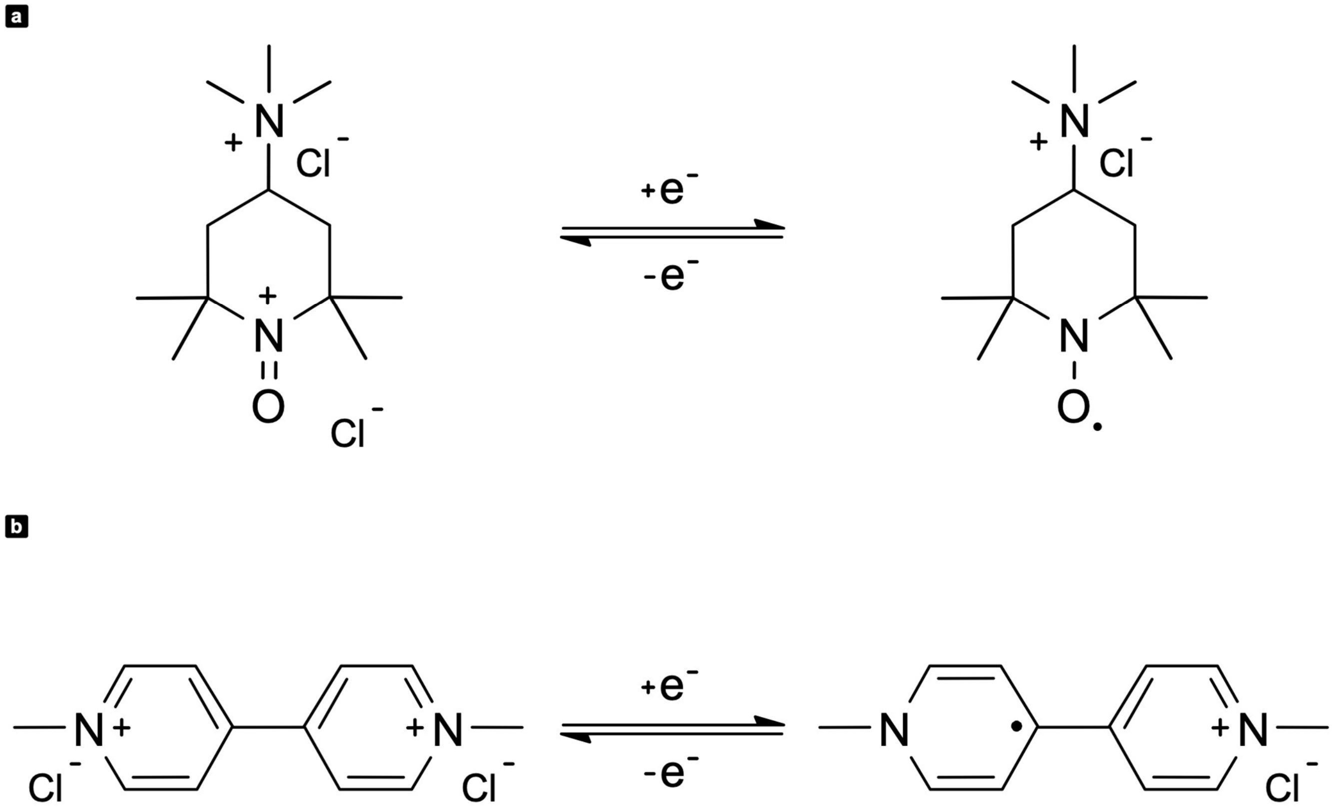

Figure S1. Schematical representation of (a) *N,N,N*-2,2,6,6-heptamethylpiperidinyloxy-4-ammonium chloride (a TEMPO molecule with a trimethyl ammonium substituent, abbreviation: TEMPTMA, catholyte) and (b) *N,N'*-dimethyl-4,4-bipyridinium dichloride (methyl viologen, abbreviation: MV, anolyte) both with their corresponding redox reactions.

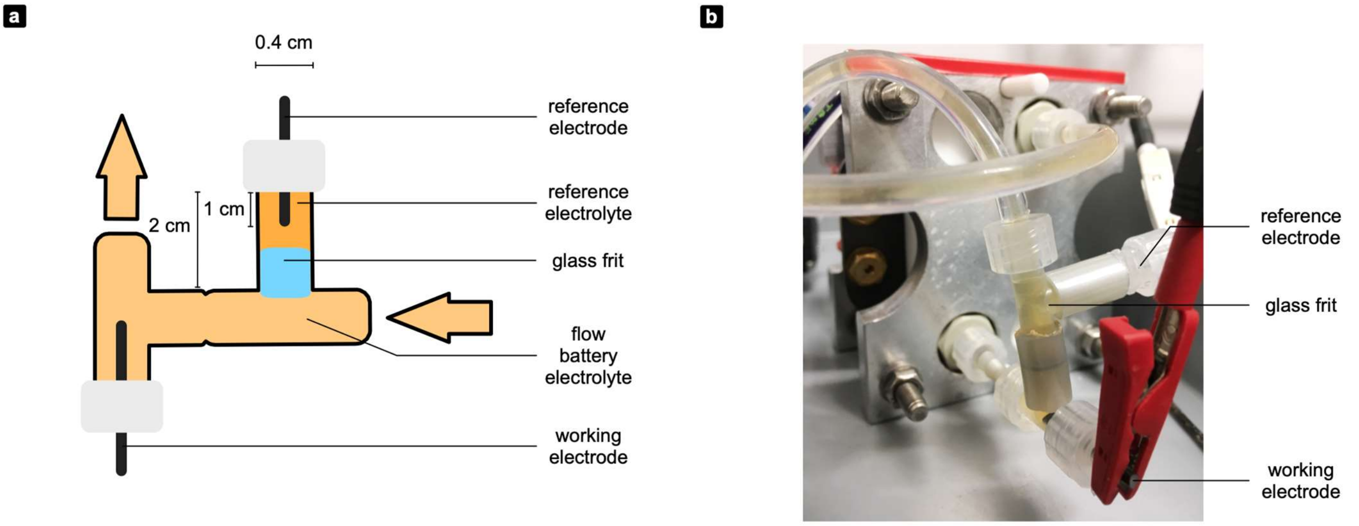

Figure S2. Schematical representation (a) and photograph (b) of the experimental setup of the standard and symmetric open-circuit cells. The silver wire used for the standard open-circuit cells had a diameter of 0.4 mm, the graphite rod used for the symmetric open-circuit cell had a diameter of 2 mm, and both had a length of approximately 1 cm (inside the reference compartment). The glass frits (blue in (a)) had a diameter of 3.2 mm, a height of 4 mm, and consisted of ion permeability porous glass (IPPG) according to the manufacturer (ALS Co, Ltd., Japan).

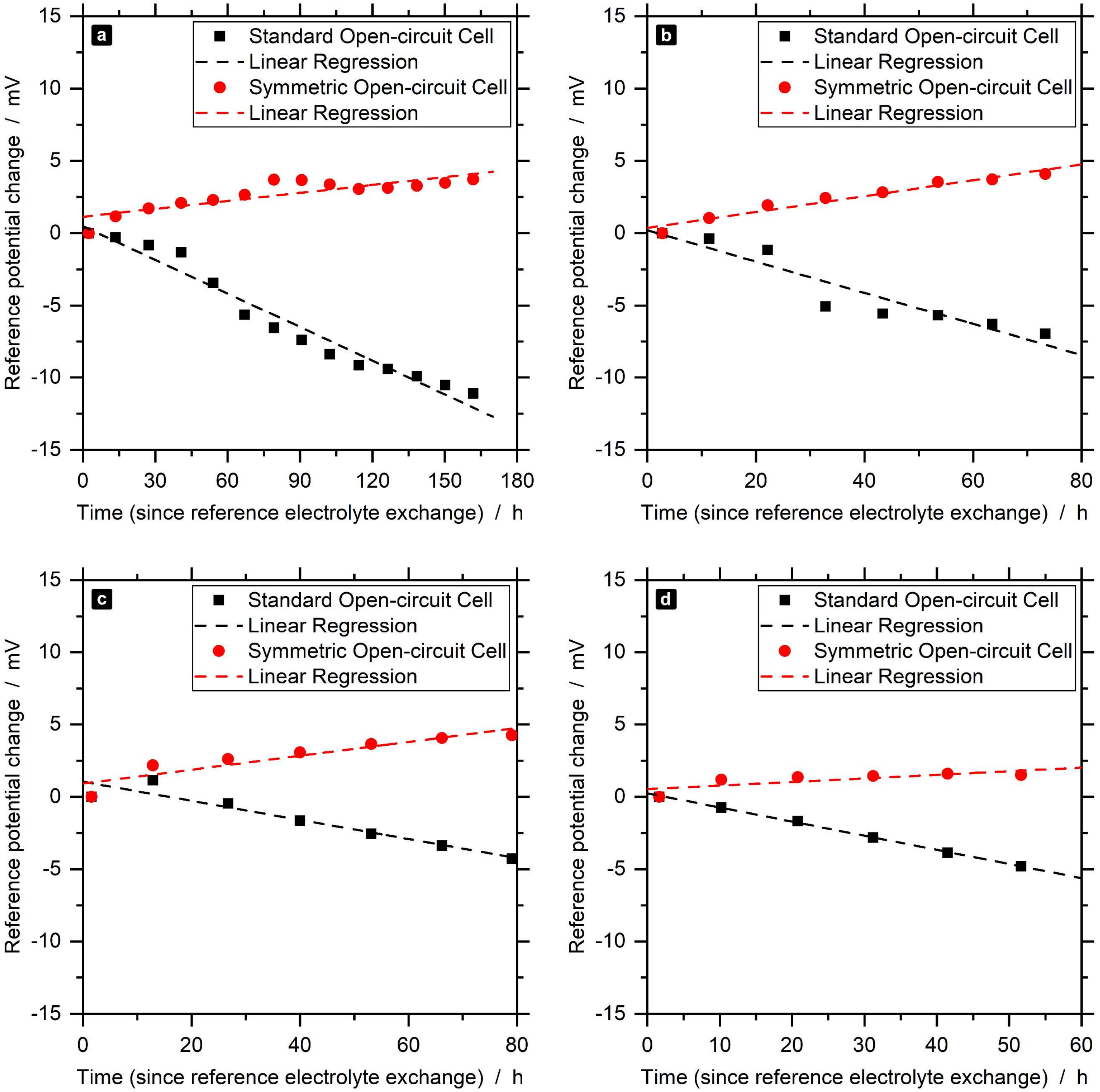

Figure S3. Reference potential drift of both standard and symmetric open-circuit cells obtained from four repetitions of the experiment. The measurements were performed on the catholyte of TEMPTMA / MV redox flow batteries during galvanostatic cycling at 50 mA cm^{-2} over at least three days. Reference potential values were obtained by fitting the Nernst equation to the obtained potential-time diagrams of each fifth charging cycle and drift rates were obtained from linear regressions of the temporal evolution of these reference potentials. The Figure represents experiments performed over (a) 65 cycles, (b) 35 cycles, (c) 30 cycles, and (d) 25 cycles.

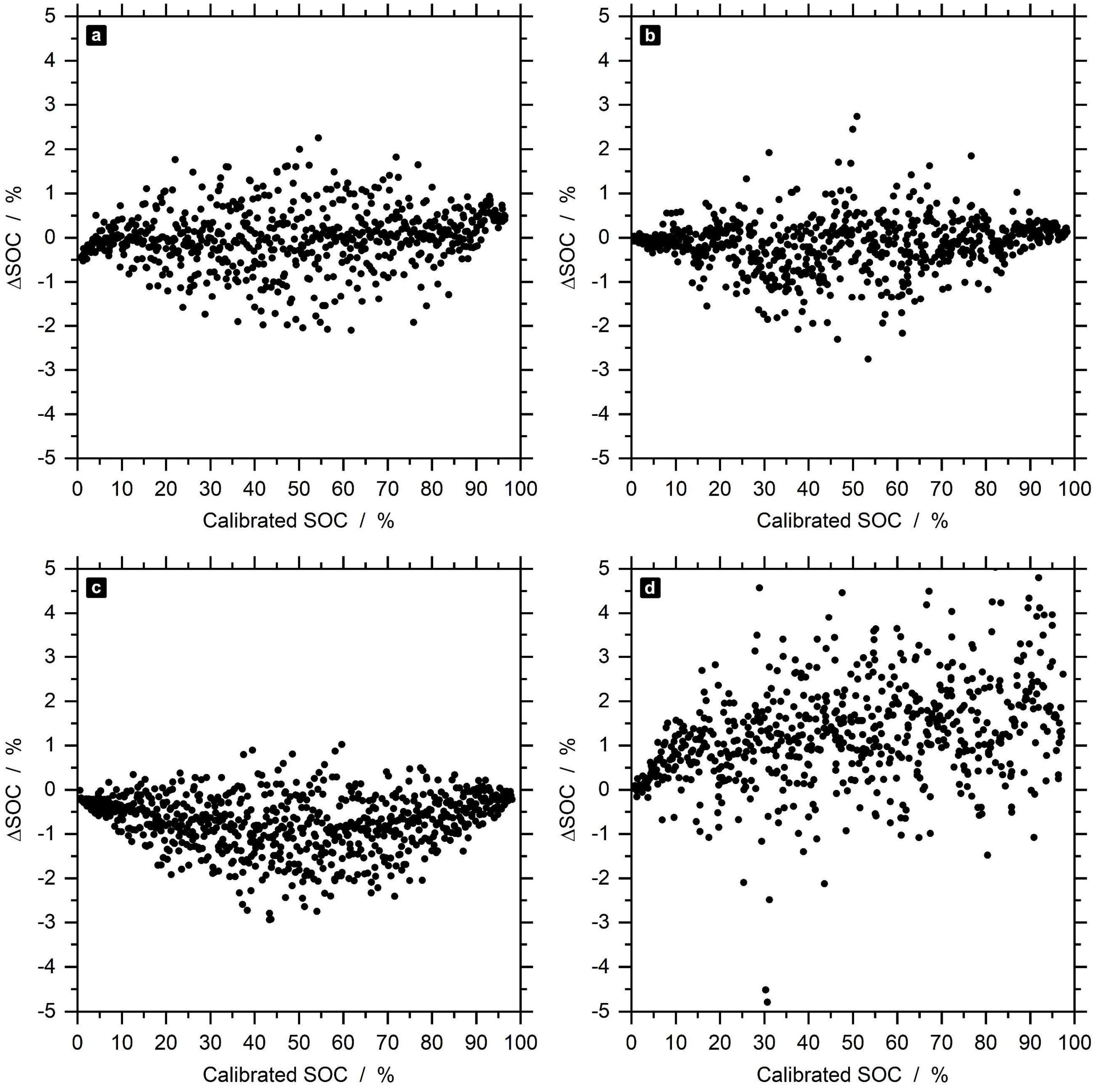

Figure S4. The absolute differences between the state-of-charge estimations obtained from a calibrated standard open-circuit cell and the not re-calibrated symmetric open-circuit cell after reference electrolyte exchanges. The plots show the charging cycles for (a) the initial calibration, (b) the reference electrolyte exchange after 12 days, (c) the reference electrolyte exchange after 18 days, and (d) the reference electrolyte exchange after 26 days of battery operation. A concise form of the data is presented in Figure 3a of the publication. For (b) and (c) the reference electrolyte exchange was performed during battery operation, when the symmetric open-circuit cell had reached a voltage of 0 V (*i.e.*, battery electrolyte at 50% SOC). In contrast, for (d) the exchange was done at a symmetric open-circuit cell voltage of 0.096 V. The observed variances between the data points (especially in (d)) originate mainly from measurement noise of the open-circuit voltage measurement.

Publication P6

An Amperometric, Temperature-Independent, and Calibration-Free Method for the Real-Time State-of-Charge Monitoring of Redox Flow Battery Electrolytes

C. Stolze, J. P. Meurer, M. D. Hager, U. S. Schubert,

Chem. Mater. **2019**, *31*, 5363-5369.

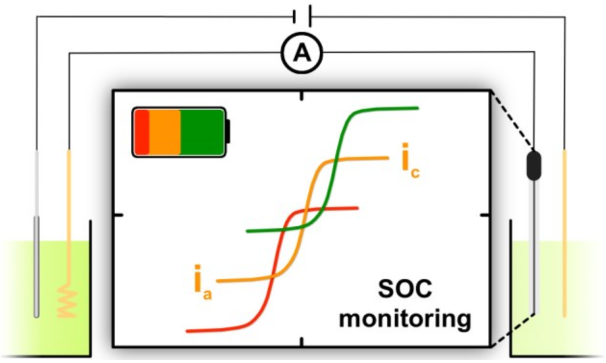

CHEMISTRY OF MATERIALS
Cite This: Chem. Mater. 2019, 31, 5363−5369
Methods/Protocols
pubs.acs.org/cm

An Amperometric, Temperature-Independent, and Calibration-Free Method for the Real-Time State-of-Charge Monitoring of Redox Flow Battery Electrolytes

Christian Stolze,[†,‡] Jan P. Meurer,[†,‡] Martin D. Hager,[†,‡] and Ulrich S. Schubert*[,†,‡]

[†]Laboratory of Organic and Macromolecular Chemistry (IOMC), Friedrich Schiller University Jena, Humboldtstraße 10, 07743 Jena, Germany

[‡]Center for Energy and Environmental Chemistry Jena (CEEC Jena), Friedrich Schiller University Jena, Philosophenweg 7a, 07743 Jena, Germany

Supporting Information

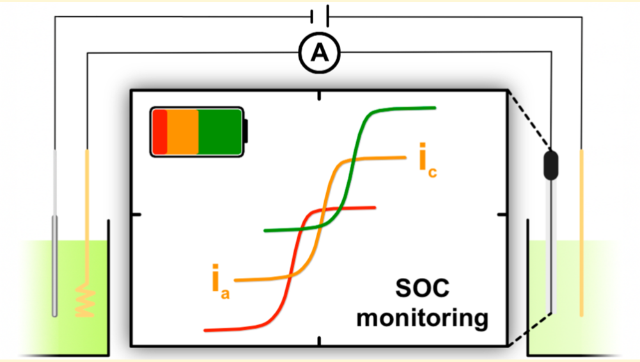

ABSTRACT: A simple mathematical framework for a calibration-free real-time state-of-charge (SOC) monitoring of redox flow battery (RFB) electrolytes, which is based on mass-transfer limited amperometry, is theoretically derived. The equations are initially validated with literature data for a vanadium-based RFB electrolyte, revealing absolute root-mean-square deviations (RMSD) of 4−6% for the obtained SOC estimates. Subsequently, our own experimental results based on a microelectrode as an amperometric sensor are presented. Absolute RMSDs of 2−7% are obtained for ferri-/ferrocyanide-based RFB electrolytes at two different concentrations in an offline measurement. Furthermore, the real-time SOC monitoring capability is demonstrated for the capacity limiting half-cell of a symmetric aqueous RFB utilizing *N*,*N*,*N*-2,2,6,6-heptamethylpiperidinyloxy-4-ammonium chloride (TEMPTMA) as an active organic molecule, yielding an absolute RMSD of below 3%. The theoretical considerations and the experimental results imply a complete independence of the presented approach from, e.g., the type of mass-transfer limiting process, the temperature, the RFB type (organic/inorganic, aqueous/nonaqueous), and the electrolyte composition.

Redox flow batteries (RFBs) represent a rapidly evolving and promising technological response to the growing demand for stationary energy storage solutions. Remarkable progress has been achieved in terms of their power density, efficiency, and energy density within the past two decades.[1−7] While an increasing number of RFB chemistries is gradually approaching practical applicability, the need for technologically simple and cost-efficient battery management systems (BMS) is increasing as well. One of the most important tasks of a BMS is the state-of-charge (SOC) and the state-of-health (SOH) monitoring, which are essential for a performance optimized and safe operation of any RFB. A notable variety of methods utilizing different physicochemical properties of the RFB electrolytes already exists. While the specific details of each method have been discussed elsewhere,[8−21] we would like to stress that each of the reported approaches struggles with one and often several of the following issues:

- error accumulation over time;
- calibration and frequent, time-consuming recalibration;
- dependencies on changing system parameters (e.g., temperature, salt concentration, electrolyte capacity, etc.);
- no individual electrolyte SOC prediction (i.e., no half-cell resolution);
- no real-time monitoring capability;
- mathematical complexity;
- complex and costly instrumentation;
- limitation to certain types of electrolytes.

The study at hand demonstrates that the sole measurement of theoretically any kind of mass-transfer limited current provides a pathway to effectively overcome most, if not all, of these issues. A simple mathematical relationship between the SOC and the ratio of cathodic to anodic mass-transfer limited current is derived, which requires neither calibration nor the knowledge about the temperature, concentration, or any other system parameter.

In theory, the anodic and the cathodic limiting currents, $i_{l,a}$ and $i_{l,c}$, which are obtained at different types of electrodes, can be described in a general mathematical form by[22]

$$i_{l,a} = -nFAm_{\mathrm{R}}c_{\mathrm{R}} \text{ and } i_{l,c} = nFAm_{\mathrm{O}}c_{\mathrm{O}} \qquad (1)$$

Herein, F represents the Faraday's constant, n the number of transferred electrons, A the electrochemically active area of the electrode, $m_{\mathrm{O/R}}$ the mass-transfer coefficients, and $c_{\mathrm{O/R}}$ the bulk

Received: June 18, 2019
Revised: July 11, 2019
Published: July 12, 2019

DOI: 10.1021/acs.chemmater.9b02376
Chem. Mater. 2019, 31, 5363−5369

concentrations of the oxidized and the reduced form of the redox molecule under investigation, respectively. Furthermore, the state-of-charge of a catholyte is defined as $\mathrm{SOC} \equiv c_{\mathrm{O}}c^{-1}$ and that of an anolyte as $\overline{\mathrm{SOC}} \equiv \overline{c}_{\mathrm{R}}\overline{c}^{-1}$, where $c \equiv c_{\mathrm{O}} + c_{\mathrm{R}}$ and $\overline{c} \equiv \overline{c}_{\mathrm{O}} + \overline{c}_{\mathrm{R}}$ are the total molar concentrations of each redox couple within the catholyte and the anolyte, respectively. The relationships between the limiting currents and the SOC of an RFB catholyte and an RFB anolyte, consequently, are

$$i_{l,a} = -\mathrm{n}FAm_{\mathrm{R}}c(1 - \mathrm{SOC}) \text{ and } i_{l,c} = nFAm_{\mathrm{O}}c\mathrm{SOC} \tag{2a}$$

$$\overline{i}_{l,a} = -nFA\overline{m}_{\mathrm{R}}\overline{c}\,\overline{\mathrm{SOC}} \text{ and } \overline{i}_{l,c} = nFA\overline{m}_{\mathrm{O}}\overline{c}(1 - \overline{\mathrm{SOC}}) \tag{2b}$$

By calculating the ratios of the limiting currents, $i_{l,\,c}\, i_{l,a}^{-1}$ or $\overline{i}_{l,a}\, \overline{i}_{l,c}^{-1}$, and rearranging for SOC and $\overline{\mathrm{SOC}}$, respectively, we arrive at:

$$\mathrm{SOC} = \frac{1}{1 - \frac{i_{l,a}}{i_{l,c}}\frac{m_{\mathrm{O}}}{m_{\mathrm{R}}}} \tag{3a}$$

$$\overline{\mathrm{SOC}} = \frac{1}{1 - \frac{\overline{i}_{l,c}}{\overline{i}_{l,a}}\frac{\overline{m}_{\mathrm{R}}}{\overline{m}_{\mathrm{O}}}} \tag{3b}$$

These equations enable the determination of the SOC of an RFB catholyte (eq 3a) and an RFB anolyte (eq 3b) from the mass-transfer limited currents at theoretically any electrode, if the ratio of the mass-transfer coefficients is known. However, if the total concentration and the mass-transfer coefficients of the electrolyte do not change between two distinct times, t_2 and t_1, a simple relationship can be derived from eq 2a for a catholyte (and analogously for a anolyte from eq 2b):

$$\frac{\Delta i_{l,c}}{\Delta i_{l,a}} \equiv \frac{i_{l,c}(\mathrm{SOC}(t_2)) - i_{l,c}(\mathrm{SOC}(t_1))}{i_{l,a}(\mathrm{SOC}(t_2)) - i_{l,a}(\mathrm{SOC}(t_1))} = \frac{nFAm_{\mathrm{O}}c\Delta\mathrm{SOC}}{nFAm_{\mathrm{R}}c\Delta\mathrm{SOC}} = \frac{m_{\mathrm{O}}}{m_{\mathrm{R}}} \tag{4}$$

Hence, the ratios of the mass-transfer coefficients can be evaluated from the limiting currents measured at two different SOCs of the electrolyte. Finally, combination of eqs 3a, 3b, and 4 results in a general relationship between the limiting currents and the electrolytes' SOC:

$$\mathrm{SOC} = \frac{1}{1 - \frac{i_{l,a}}{i_{l,c}}\frac{\Delta i_{l,c}}{\Delta i_{l,a}}} \tag{5a}$$

$$\overline{\mathrm{SOC}} = \frac{1}{1 - \frac{\overline{i}_{l,c}}{\overline{i}_{l,a}}\frac{\Delta \overline{i}_{l,a}}{\Delta \overline{i}_{l,c}}} \tag{5b}$$

Thus, it is theoretically possible to calculate an electrolyte's SOC without prior knowledge of any specific system parameter by measuring the mass-transfer limited currents at any electrode. The derived relationships enable a simple, cost-efficient, and calibration-free state-of-charge monitoring with half-cell resolution. In particular, eqs 5a and 5b are independent from system properties like, e.g., temperature and concentration. Furthermore, these equations were derived without assumptions regarding the electrolyte properties; consequently, they are theoretically applicable to a large variety of organic/inorganic aqueous/nonaqueous electrolytes. A minor limitation of eqs 5a and 5b is that they cannot be used during open-circuit periods of the battery.

A first example of a mass-transfer limited amperometric system for SOC monitoring was published by Kroner et al., recently.[23] The authors constructed an electrode with a ceramic gas diffusion layer (GDL) to realize a mass-transfer limited current response in vanadium-based electrolytes. While the authors' SOC monitoring method relies on a calibration approach, their sensor data also obeys eqs 1 with $m_{\mathrm{O/R}} = D_{\mathrm{O/R}}\ \delta^{-1}$, where δ is the GDL thickness. Their reported amperometric data, therefore, represents an excellent candidate for a first verification of our proposed method for a vanadium-based catholyte. Setting $m_{\mathrm{O/R}} = D_{\mathrm{O/R}}\ \delta^{-1}$, it is theoretically expected from eq 3a that for catholytes:

$$\mathrm{SOC} = \frac{1}{1 - \frac{i_{l,a}}{i_{l,c}}\frac{D_{\mathrm{O}}}{D_{\mathrm{R}}}} \tag{6}$$

The SOCs were estimated using two different approaches: The first assumes that $D_{\mathrm{O}}D_{\mathrm{R}}^{-1} = 1$ in eq 6, which is a good and frequently used assumption for redox couples. The second approach calculates the SOC directly from eq 5a using the differences in mass-transfer limited currents according to eq 4 (details: Table S1 to S4, Supporting Information). A significant offset current of about 0.1 and 0.2 mA was evident at zero concentration for both oxidized and reduced species. To obtain correct SOC estimates by eqs 5a and 6, the offset currents were subtracted from all measured current values. With absolute root-mean-square deviations (RMSD) of approximately 4% (eq 6) and 6% (eq 5a) SOC, our novel evaluation method provides an accurate SOC estimate for a vanadium-based RFB electrolyte. Despite the promising results, the mentioned offset currents still necessitate a calibration and, thus, represent a remaining issue of the amperometric sensor reported by Kroner and coworkers. For the experiments in the study at hand, an amperometric SOC monitoring approach utilizing the mass-transfer limited currents at a microelectrode was combined with a closed bipolar electrode (CPE) setup. In general, CPEs combine two separate half-cells with a bipolar electrode instead of a liquid junction (e.g., a membrane or salt bridge).

For a better understanding of the fundamental processes and the opportunities of bipolar electrochemical concepts, we refer to the literature.[24−26] The specific setup used for the present study is illustrated in Figure 1. Its bipolar electrode consists of

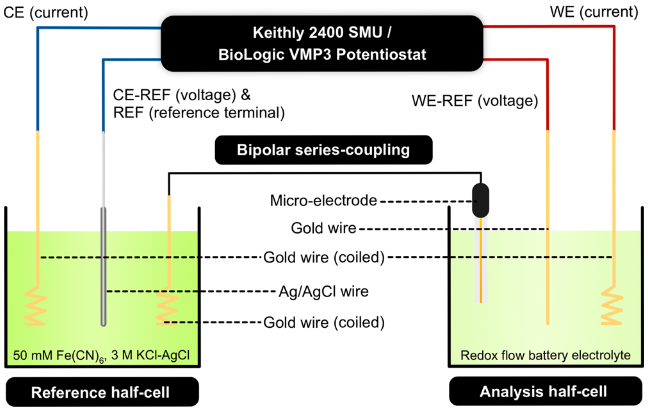

Figure 1. Schematic representation of the closed bipolar microelectrode setup used for SOC monitoring. Left: Reference half-cell providing the reference potential value. Right: Analysis half-cell with the electrolyte, whose SOC is to be measured.

DOI: 10.1021/acs.chemmater.9b02376
Chem. Mater. 2019, 31, 5363−5369

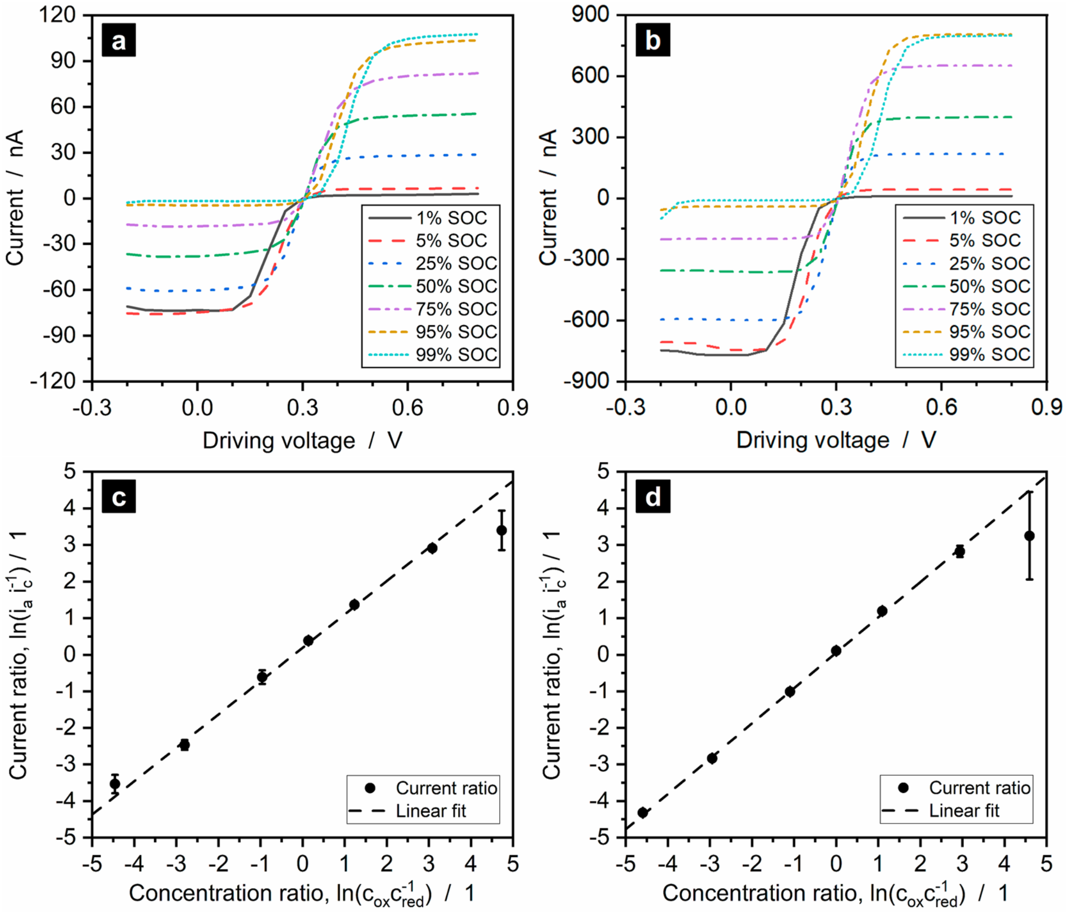

Figure 2. Exemplary steady-state voltammograms obtained at the gold microelectrode (diameter: 25 μm) for different SOCs of ferri-/ferrocyanide aqueous electrolytes with total concentrations of (a) 50 and (b) 500 mM. Current ratios of the limiting cathodic (at 0.8 V) and anodic (at −0.2 V) currents were obtained from panels a and b. Their natural logarithmic values were plotted over the concentration ratio of ferricyanide and ferrocyanide for (c) the 50 mM electrolyte and (d) the 500 mM electrolyte (data points: average values of three repetitions; error bars: corresponding standard deviations).

a macroelectrode within the left half-cell (reference half-cell), which is series-coupled to a microelectrode in the right half-cell (analysis half-cell). The fundamental principles of closed bipolar microelectrodes were investigated by Guerrette et al., Cox et al., Zhong et al., and Fakhruddin et al. since 2012.[27−30] Such setups benefit from the missing liquid junction because neither interference from liquid-junction potentials nor cross-contamination between the half-cells is possible, which results in a long-term stable reference potential (Supporting Information). Furthermore, the surface of the series-coupled macroelectrode is by several orders of magnitude larger than that of the microelectrode. As a consequence, the setup's current response is solely governed by the electrochemical processes at the microelectrode. The limiting currents at a microelectrode can be calculated in accordance with eq 1 as $Am_{O/R} = 4D_{O/R}r$ for this electrode type and, hence,

$$i_{l,a} = -4nFrD_R c_R \text{ and } i_{l,c} = 4nFrD_O c_O \quad (7)$$

where r is the radius of the microelectrode.[22] Obviously, eq 6 holds for microelectrodes as well.

The SOC measuring principle was investigated for offline samples of RFB catholytes-containing the ferri-/ferrocyanide redox couple prior to the verification of the method's online SOC monitoring capability at a symmetric TEMPTMA/TEMPTMA RFB. The exact details of each experiment and additional data are provided in the Supporting Information. In short: An electrolyte containing approximately 25 mM ferricyanide and 22 mM ferrocyanide was prepared in an aqueous 3 M KCl solution saturated with AgCl and was used as reference electrolyte of the bipolar setup in all experiments. Furthermore, electrolytes containing two different total concentrations (50 and 500 mM) and different concentration ratios (i.e., different SOCs) of ferricyanide and ferrocyanide were prepared in aqueous solutions of 0.5 and 1 M KCl, respectively. Driving voltages were applied between a AgCl coated silver wire in the reference half-cell and a gold wire in the analysis half-cell using a four-terminal configuration. The current terminals were connected to coiled gold wires as macroelectrodes, while another coiled gold wire and a gold microelectrode (r = 12.5 μm) were combined to a bipolar electrode (Figure 1). A voltage range between −0.2 and 0.8 V was scanned in discrete 50 mV steps.

Exemplary steady-state voltammograms as obtained by the experiments for different SOCs and for the two total concentrations are displayed in Figures 2a and 2b. The ratio of the limiting currents obtained at −0.2 and 0.8 V of each voltammogram was plotted versus the ratio of the concentrations of oxidized and reduced species in Figures 2c and 2d, respectively. The ratios are plotted as natural logarithmic values, and no significant differences were observed between

Table 1. SOC Estimates Obtained from the Derived Amperometric Equations for Offline Samples of the Ferri-/Ferrocyanide Redox Couple in Aqueous 0.5 and 1 M $KCl_{(aq)}$ Solutions, Respectively[a]

	50 mM[b]		50 mM[c]			500 mM[b]		500 mM[c]	
SOC_{ref} (%)	SOC (%)	ΔSOC (%)	SOC (%)	ΔSOC (%)	SOC_{ref} (%)	SOC (%)	ΔSOC (%)	SOC (%)	ΔSOC (%)
1.1	3.3	2.2			1.0	1.3	0.3		
5.7	8.3	2.6	−2.3	−7.9	5.0	5.6	0.6	−5.4	−10.4
27.7	34.6	6.9	21.5	−6.2	25.0	26.7	1.7	14.3	−10.7
53.5	60.5	7.1	52.5	−1.0	50.0	52.7	2.7	47.4	−2.6
77.5	81.3	3.8	75.3	−2.2	75.0	76.7	1.7	72.3	−2.7
95.6	95.3	−0.3	93.5	−2.1	95.0	94.2	−0.8	93.0	−2.0
99.1	97.0	−2.2	95.7	−3.4	99.0	94.5	−4.5	95.1	−3.9
RMSD	4.3		4.5			2.2		6.5	

[a] Total concentrations of 50 and 500 mM were prepared, and reference SOCs, SOC_{ref}, were determined from the weighed substance masses and the calculated concentrations. $\Delta SOC \equiv SOC - SOC_{ref}$ represents the deviation from the reference SOC. [b] Calculated from eq 6 using the assumption $D_O D_R^{-1} = 1$. [c] Calculated from eq 5a using the current difference to the first current value.

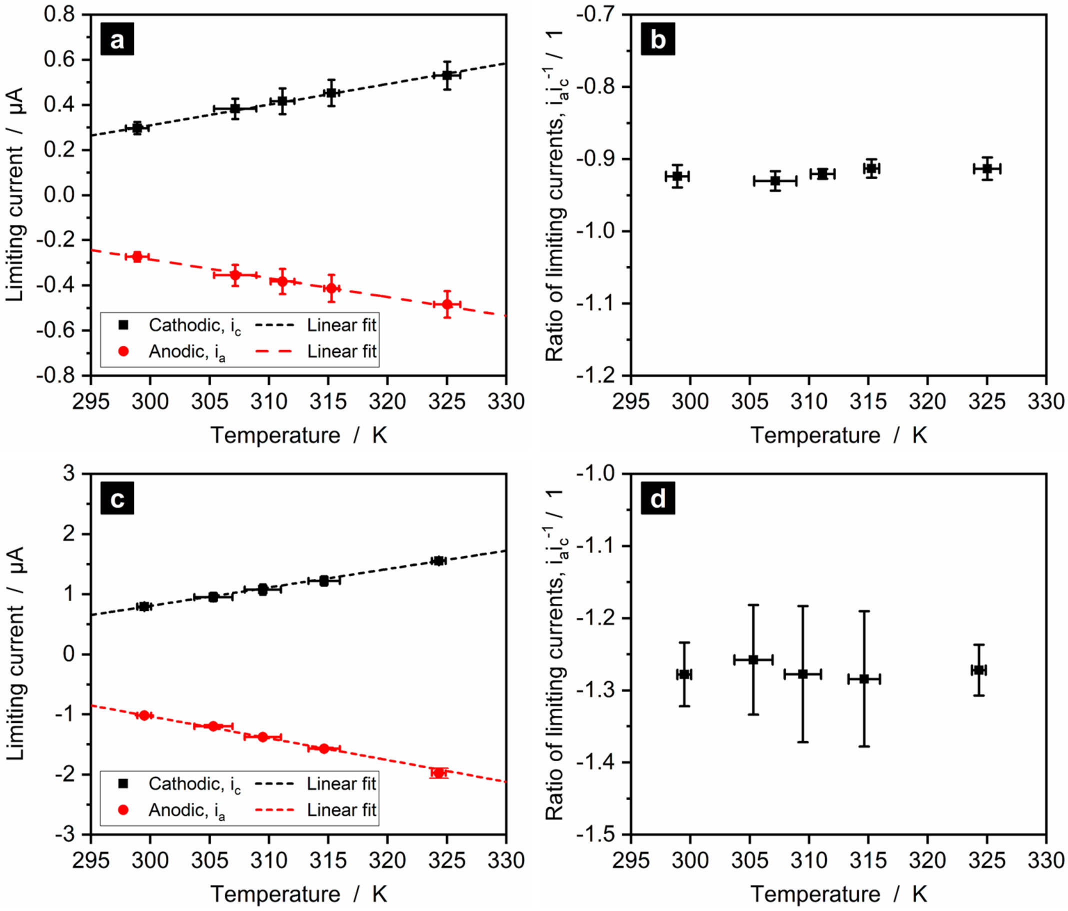

Figure 3. Cathodic and anodic limiting currents obtained in an electrolyte temperature range from 25 to 50 °C for (a, b) 500 mM ferri-/ferrocyanide in 0.5 M $KCl_{(aq)}$ at ~50% SOC and (c, d) 1.3 M aqueous TEMPTMA at ~50% SOC: (a, c) absolute current values are shown as average values of four (a) and three (c) repetitions, respectively; (b, d) ratios of cathodic to anodic limiting current. All error bars represent the corresponding standard deviations.

both concentrations. In contrast to the amperometric sensor data reported by Kroner et al.,[23] negligible offset currents were evident due to the inherent properties of the microelectrode. The SOCs were estimated from eqs 5a and 6 using the limiting currents with the two approaches described already for the data of Kroner et al. above. The SOC estimates were compared to the "true" or reference state-of-charge, SOC_{ref}, which was calculated from the known concentrations of ferri- and ferrocyanide according to the concentration-based definition $SOC \equiv c_{ox}(c_{ox} + c_{red})^{-1}$. Data for each offline sample are included in the Supporting Information (Figure S6 and S7), while the averages of the calculated SOC estimates are listed in Table 1. With absolute RMSDs of not more than 6.5%, the SOC estimates exhibited accuracies that are comparable to state-of-the-art methods.[15,16,20] However, in some of the repetitions of the experiment, deviations significantly higher than 6.5% were observed for some SOC values (Supporting Information).

DOI: 10.1021/acs.chemmater.9b02376
Chem. Mater. 2019, 31, 5363−5369

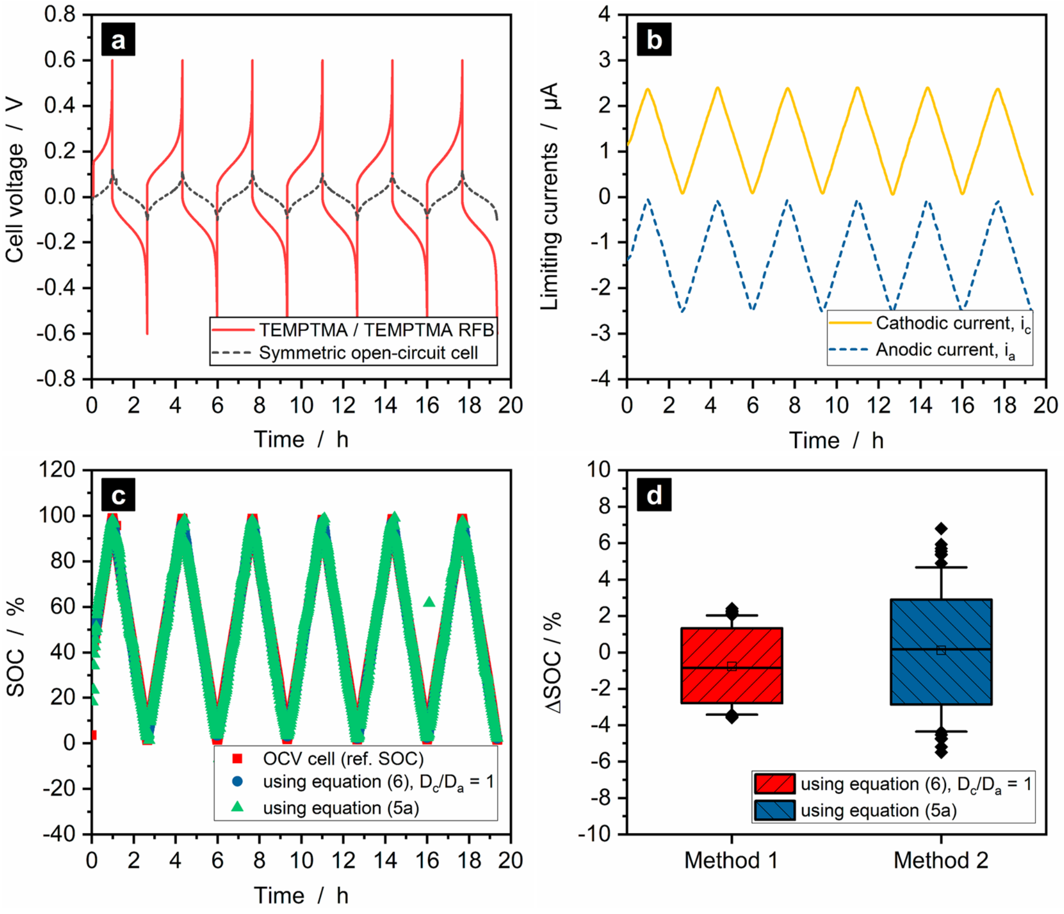

Figure 4. Real-time SOC monitoring experiment for a symmetric TEMPTMA/TEMPTMA RFB (1.3 M $\text{TEMPTMA}_{(aq)}$; galvanostatic cycling: ± 200 mA): (a) cell voltages of the RFB and an open-circuit cell connected to the capacity-limiting half-cell; (b) limiting currents measured by a closed bipolar carbon-fiber disk microelectrode (diameter: 33 µm; driving voltages: −0.2 and 0.8 V); (c) SOC as determined from the open-circuit cell and the limiting currents; (d) box plots for the SOC estimation differences of open-circuit cell and amperometric approach, $\Delta\text{SOC} \equiv \text{SOC} - \text{SOC}_{\text{ref}}$ (box: 10−90% percentile; whiskers: 1−99% percentile; squares (□): mean; line (—): median; diamonds (♦): outliers).

These uncertainties are most likely due to the rather low concentrations, the inaccuracies in the low-current measurement, and the small number of offline samples used to cover the full range from 0 to 100% SOC. The latter causes higher estimation errors for $\Delta i_{l,c}$ and $\Delta i_{l,a}$. The higher accuracy obtained during the real-time SOC monitoring presented later in this study supports these considerations.

Despite the differences in the amperometric setups, the nature of the mass-transfer limiting processes, the total concentrations, the supporting electrolytes, and the redox couples, the proposed approach works equally accurate for the offline sample data published by Kroner et al. (Table S4) and the data obtained in our laboratory. Furthermore, it is particularly notable that the assumption of $D_O D_R^{-1} = 1$ for eq 6 yielded accurate results for both vanadium- and ferrocyanide-based electrolytes. The influence of temperature on the measured current response was investigated in a temperature range from 25 to 50 °C for a ferricyanide/ferrocyanide and a TEMPTMA electrolyte at ~50% SOC, respectively. The obtained voltammograms of each repetition of the experiment are provided in Figure S8 of the Supporting Information, while the mean values of the limiting currents evaluated from these voltammograms are plotted versus the mean values of the applied temperatures in Figure 3. A nearly linear relationship was observed in this temperature range, and the current ratios, $i_{l,a} i_{l,c}^{-1}$, revealed no significant dependency on temperature. The latter implies a temperature independence of $D_O D_R^{-1}$. A theoretical explanation for this independence is discussed on page S27 of the Supporting Information. If this observation can be confirmed for a broader temperature range and other RFB electrolytes in future studies, eq 6 might be the simplest option for the SOC estimation with diffusion-limited amperometric sensors. Otherwise, eqs 5a and 5b can be used, which estimate $D_O D_R^{-1}$ (or $m_O m_R^{-1}$) from $\Delta i_{l,c} \Delta i_{l,a}^{-1}$ and, therefore, represent a real-time correction for any possible parameter dependence (including temperature and concentration).

The real-time SOC monitoring capability of the presented amperometric method was verified using a TEMPTMA/TEMPTMA RFB following the considerations about unbalanced symmetric RFBs published by Goulet et al., recently.[31] The SOC of the capacity limiting half-cell of the RFB was monitored using both the microelectrode setup and a symmetric open-circuit cell.[21] A carbon fiber microelectrode (r = 16.5 µm) was utilized for the measurement and the electrolyte tank was directly applied as analysis half-cell of the CPE setup (Figure S1, Supporting Information). Care was taken that the electrolyte inlet as well as the outlet were placed far away from the microelectrode surface to minimize distortions by electrolyte convection. The voltage evolution of the RFB during galvanostatic cycling and the corresponding open-circuit voltage of the open-circuit cell are displayed in Figure 4 for five full cycles. The mass-transfer limited currents were measured in 1 min intervals. To increase the SOC estimation accuracy, a weighted moving average method was applied to smoothen both current signals. The obtained currents are displayed in Figure 4. Subsequently, eq 5a and eq 6 (with $D_O D_R^{-1} = 1$) were used to estimate the SOC from the current signals. The evolution of the electrolyte's SOC over time as obtained from both the symmetric open-circuit cell and the steady-state currents are presented in Figure 4. For the open-circuit cell, each half-cycle was calibrated separately for accuracy maximization (Figure S10, Supporting Information). The calibration was performed according to previous reports.[20,21] A quantitative accuracy evaluation was performed by using the SOC estimates of the open-circuit cell as a reference state-of-charge, SOC_{ref}, and calculating the deviations, $\Delta SOC \equiv SOC - SOC_{ref}$, of the SOC estimates obtained by eqs 5a and 6. The statistical evaluation of ΔSOC over all the cycles is presented in the form of box plots in Figure 4. Despite a low number of outliers, the whiskers of the box plots (1−99% percentiles) imply that the vast majority of estimated SOC values deviated by not more than ±5% from the reference SOC. On average, an absolute deviation from the OCV method of 0.1−1% was observed over all cycles, and the corresponding absolute RMSDs were 1.7−2.9%. Consequently, the method's overall accuracy is on par with most of the state-of-the-art real-time SOC monitoring methods reported in the literature.[15,16,19−21] Some additional thoughts on the reference SOC, options for further accuracy improvement, and an alternative operation mode of the microelectrode are discussed within the Supporting Information.

In conclusion, simple equations for the SOC monitoring based on the sole measurement of mass-transfer limited currents were theoretically derived and experimentally verified for RFB electrolytes based on vanadium, ferro-/ferricyanide, and TEMPTMA. While the real-time estimation accuracy is on par with the state-of-the-art methods (i.e., absolute RMSDs below 3%), it most likely can be increased by focusing further research on, e.g., microelectrodes of different sizes, microelectrode arrays, more sophisticated current smoothing procedures, and other types of amperometric sensors. The approach is independent from virtually any system parameter as has been empirically demonstrated for temperature, electrolyte composition, and concentration. As an absolute method for the real-time SOC estimation, it does not require any form of calibration. The underlying mathematical framework is simple and theoretically applicable to a broad range of aqueous/nonaqueous organic/inorganic electrolytes. While the experiments presented herein were performed with a potentiostat, such complicated hardware is, theoretically, not required. Consequently, ongoing work focuses on the further simplification of the experimental setup by utilization of simple constant voltage sources and ampere meters. Furthermore, the use of pseudoreference electrodes instead of a closed bipolar setup might enable a further cost reduction; however, their stability and applicability for this purpose needs to be investigated in detail.

■ ASSOCIATED CONTENT

Ⓢ Supporting Information

The Supporting Information is available free of charge on the ACS Publications website at DOI: 10.1021/acs.chemmater.9b02376.

> Materials and experimental setups; experimental methods; details on the verification of the derived equations using literature data; investigations on the reference potential of the closed bipolar setup; detailed data on concentration investigations; detailed data on temperature investigations; detailed data on real-time SOC monitoring investigations (PDF)

■ AUTHOR INFORMATION

Corresponding Author

*E-mail: ulrich.schubert@uni-jena.de.

ORCID

Martin D. Hager: 0000-0002-6373-6600
Ulrich S. Schubert: 0000-0003-4978-4670

Notes

The authors declare no competing financial interest.

■ ACKNOWLEDGMENTS

We gratefully acknowledge the financial support by the European Regional Development Fund (EFRE), the Thuringian Ministry for Economic Affairs, Science and Digital Society (TMWWdG), and the Thüringer Aufbaubank (TAB). Furthermore, the authors kindly thank the JenaBatteries GmbH for providing the TEMPTMA-based electrolyte stock solutions for the experiments.

■ REFERENCES

(1) Arenas, L. F.; Ponce de León, C.; Walsh, F. C. Engineering aspects of the design, construction and performance of modular redox flow batteries for energy storage. *J. Energy Storage* **2017**, *11*, 119−153.

(2) Wei, X.; Pan, W.; Duan, W.; Hollas, A.; Yang, Z.; Li, B.; Nie, Z.; Liu, J.; Reed, D.; Wang, W.; Sprenkle, V. Materials and Systems for Organic Redox Flow Batteries: Status and Challenges. *ACS Energy Lett.* **2017**, *2* (9), 2187−2204.

(3) Arenas, L. F.; Loh, A.; Trudgeon, D. P.; Li, X.; Ponce de León, C.; Walsh, F. C. The characteristics and performance of hybrid redox flow batteries with zinc negative electrodes for energy storage. *Renewable Sustainable Energy Rev.* **2018**, *90*, 992−1016.

(4) Armstrong, C. G.; Toghill, K. E. Stability of molecular radicals in organic non-aqueous redox flow batteries: A mini review. *Electrochem. Commun.* **2018**, *91*, 19−24.

(5) Chen, H.; Cong, G.; Lu, Y.-C. Recent progress in organic redox flow batteries: Active materials, electrolytes and membranes. *J. Energy Chem.* **2018**, *27* (5), 1304−1325.

(6) Dinesh, A.; Olivera, S.; Venkatesh, K.; Santosh, M. S.; Priya, M. G.; Inamuddin; Asiri, A. M.; Muralidhara, H. B. Iron-based flow batteries to store renewable energies. *Environ. Chem. Lett.* **2018**, *16* (3), 683−694.

(7) Singh, V.; Kim, S.; Kang, J.; Byon, H. R. Aqueous organic redox flow batteries. *Nano Res.* **2019**, 1−14.

(8) Skyllas-Kazacos, M.; Cao, L.; Kazacos, M.; Kausar, N.; Mousa, A. Vanadium Electrolyte Studies for the Vanadium Redox Battery-A Review. *ChemSusChem* **2016**, *9* (13), 1521−43.

(9) Skyllas-Kazacos, M.; Kazacos, M. State of charge monitoring methods for vanadium redox flow battery control. *J. Power Sources* **2011**, *196* (20), 8822−8827.

(10) Corcuera, S.; Skyllas-Kazacos, M. State-of-Charge Monitoring and Electrolyte Rebalancing Methods for the Vanadium Redox Flow Battery. *Eur. Chem. Bull.* **2012**, *1* (12), 511−519.

(11) Mohamed, M. R.; Ahmad, H.; Abu Seman, M. N. Estimating the State-of-Charge of all-Vanadium Redox Flow Battery using a Divided, Open-circuit Potentiometric Cell. *Elektron. Elektrotech.* **2013**, *19* (3), 37−42.

(12) Rudolph, S.; Schröder, U.; Bayanov, I. M.; Blenke, K.; Hage, D. High resolution state of charge monitoring of vanadium electrolytes with IR optical sensor. *J. Electroanal. Chem.* **2013**, *694*, 17−22.

(13) Buckley, D. N.; Gao, X.; Lynch, R. P.; Quill, N.; Leahy, M. J. Towards Optical Monitoring of Vanadium Redox Flow Batteries (VRFBs): An Investigation of the Underlying Spectroscopy. *J. Electrochem. Soc.* **2014**, *161* (4), A524−A534.

(14) Ngamsai, K.; Arpornwichanop, A. Measuring the state of charge of the electrolyte solution in a vanadium redox flow battery using a four-pole cell device. *J. Power Sources* **2015**, *298*, 150−157.

(15) Chou, Y.-S.; Hsu, N.-Y.; Jeng, K.-T.; Chen, K.-H.; Yen, S.-C. A novel ultrasonic velocity sensing approach to monitoring state of charge of vanadium redox flow battery. *Appl. Energy* **2016**, *182*, 253−259.

(16) Li, X.; Xiong, J.; Tang, A.; Qin, Y.; Liu, J.; Yan, C. Investigation of the use of electrolyte viscosity for online state-of-charge monitoring design in vanadium redox flow battery. *Appl. Energy* **2018**, *211*, 1050−1059.

(17) Wei, Z.; Lim, T. M.; Skyllas-Kazacos, M.; Wai, N.; Tseng, K. J. Online state of charge and model parameter co-estimation based on a novel multi-timescale estimator for vanadium redox flow battery. *Appl. Energy* **2016**, *172*, 169−179.

(18) Wei, Z.; Bhattarai, A.; Zou, C.; Meng, S.; Lim, T. M.; Skyllas-Kazacos, M. Real-time monitoring of capacity loss for vanadium redox flow battery. *J. Power Sources* **2018**, *390*, 261−269.

(19) Wei, Z.; Xiong, R.; Lim, T. M.; Meng, S.; Skyllas-Kazacos, M. Online monitoring of state of charge and capacity loss for vanadium redox flow battery based on autoregressive exogenous modeling. *J. Power Sources* **2018**, *402*, 252−262.

(20) Ressel, S.; Bill, F.; Holtz, L.; Janshen, N.; Chica, A.; Flower, T.; Weidlich, C.; Struckmann, T. State of charge monitoring of vanadium redox flow batteries using half cell potentials and electrolyte density. *J. Power Sources* **2018**, *378*, 776−783.

(21) Stolze, C.; Hager, M. D.; Schubert, U. S. State-of-charge monitoring for redox flow batteries: A symmetric open-circuit cell approach. *J. Power Sources* **2019**, *423*, 60−67.

(22) Bard, A. J.; Faulkner, L. R. *Electrochemical Methods: Fundamentals and Applications*, 2nd ed.; John Wiley & Sons, Inc.: 2001.

(23) Kroner, I.; Becker, M.; Turek, T. Monitoring the State of Charge of the Positive Electrolyte in a Vanadium Redox-Flow Battery with a Novel Amperometric Sensor. *Batteries* **2019**, *5* (1), 5.

(24) Mavre, F.; Anand, R. K.; Laws, D. R.; Chow, K. F.; Chang, B. Y.; Crooks, J. A.; Crooks, R. M. Bipolar electrodes: a useful tool for concentration, separation, and detection of analytes in microelectrochemical systems. *Anal. Chem.* **2010**, *82* (21), 8766−74.

(25) Fosdick, S. E.; Knust, K. N.; Scida, K.; Crooks, R. M. Bipolar electrochemistry. *Angew. Chem., Int. Ed.* **2013**, *52* (40), 10438−56.

(26) Sequeira, C. A. C.; Cardoso, D. S. P.; Gameiro, M. L. F. Bipolar Electrochemistry, a Focal Point of Future Research. *Chem. Eng. Commun.* **2016**, *203* (8), 1001−1008.

(27) Cox, J. T.; Guerrette, J. P.; Zhang, B. Steady-state voltammetry of a microelectrode in a closed bipolar cell. *Anal. Chem.* **2012**, *84* (20), 8797−804.

(28) Guerrette, J. P.; Oja, S. M.; Zhang, B. Coupled electrochemical reactions at bipolar microelectrodes and nanoelectrodes. *Anal. Chem.* **2012**, *84* (3), 1609−16.

(29) Zhong, P.; Yu, P.; Wang, K.; Hao, J.; Fei, J.; Mao, L. Ferricyanide-backfilled cylindrical carbon fiber microelectrodes for in vivo analysis with high stability and low polarized potential. *Analyst* **2015**, *140* (21), 7154−9.

(30) Fakhruddin, S. M. b.; Inoue, K. Y.; Tsuga, R.; Matsue, T. Closed bipolar electrode system for a liquid-junction-free reference electrode integrated in an amperometric probe sensor. *Electrochem. Commun.* **2018**, *93*, 62−65.

(31) Goulet, M.-A.; Aziz, M. J. Flow Battery Molecular Reactant Stability Determined by Symmetric Cell Cycling Methods. *J. Electrochem. Soc.* **2018**, *165* (7), A1466−A1477.

DOI: 10.1021/acs.chemmater.9b02376
Chem. Mater. 2019, 31, 5363−5369

- Supporting Information -

An Amperometric, Temperature-Independent, and Calibration-Free Method for the Real-Time State-of-Charge Monitoring of Redox Flow Battery Electrolytes

Christian Stolze[1,2], *Jan Meurer*[1,2], *Martin D. Hager*[1,2], *Ulrich S. Schubert*[1,2]*

[1] Laboratory of Organic and Macromolecular Chemistry (IOMC), Friedrich Schiller University Jena, Humboldtstraße 10, 07743 Jena, Germany.

[2] Center for Energy and Environmental Chemistry Jena (CEEC Jena), Friedrich Schiller University Jena, Philosophenweg 7a, 07743 Jena, Germany.

AUTHOR INFORMATION

Corresponding Author

* Corresponding author: Laboratory of Organic and Macromolecular Chemistry (IOMC), Friedrich Schiller University Jena, Humboldtstraße 10, 07743 Jena, Germany. E-Mail: ulrich.schubert@uni-jena.de

TABLE OF CONTENTS

Materials and experimental setups

Materials. Potassium ferricyanide (VEB Laborchemie Apolda, Germany), potassium ferrocyanide trihydrate (AppliChem GmbH, Germany), sodium chloride (Sigma-Aldrich Chemie GmbH, Germany), and potassium chloride (Merck KGaA, Germany) were used as received without further purification for the electrolyte preparation. A 2 M aqueous *N,N,N*-2,2,6,6-heptamethylpiperidinyloxy-4-ammonium chloride (TEMPTMA, JenaBatteries GmbH, Germany) stock solution was also used as provided except for dilution with distilled water. The chemical structure of TEMPTMA is schematically illustrated in **Figure S1**. An aqueous 3 M KCl solution saturated with AgCl (Sigma-Aldrich Chemie GmbH, Germany) was used as basis for the reference electrolytes in the closed bipolar setup. Silver wire (99.99% purity, diameter: 500 μm, Goodfellow GmbH, Germany) was partially coated with AgCl by applying a current density of ~ 1 mA cm^{-2} for 5 min in an 1.5 M aqueous NaCl solution (an identical piece of silver wire was used as counter electrode) and used as reference electrode. Gold wire (99.99% purity, diameter: 200 μm) was also purchased from Goodfellow GmbH, Germany and utilized for the macroelectrodes in a coiled form. Two different commercial microelectrodes were utilized within the experiments: A gold microelectrode (diameter: 25 μm, GAMEC Analysentechnik, Germany) was used for measurements performed on ferri- and ferrocyanide, while a carbon fiber microelectrode (diameter: 33 μm, C3 Prozess- und Analysentechnik GmbH) was used for the TEMPTMA-based electrolytes.

Electrolyte preparation. The ferri- and ferrocyanide containing solutions were prepared from distilled water and solid potassium ferricyanide and potassium ferrocyanide trihydrate weighed with a Discovery DV114CM scale from Ohaus Corporation, USA. The 1.3 M TEMPTMA electrolytes were prepared from the 2 M stock solutions without further additives by dilution with distilled water. For the symmetric redox flow battery, 100 mL of the 1.3 M TEMPTMA solution were charged to 100% SOC using a galvanostatic charging procedure at 300 mA with a limiting voltage of 1.45 V. A potentiostatic hold time followed as soon as the limiting voltage was reached and the current was continuously monitored until it decreased to approximately 4 mA. An equal amount of methyl viologen electrolyte was used as anolyte in this procedure. The 100 mL of virtually fully charged TEMPTMA electrolyte was mixed with an equal amount of pristine (uncharged) 1.3 M TEMPTMA solution to obtain an electrolyte at approximately 50% SOC.

Closed bipolar setup. The construction of the closed bipolar microelectrode setup followed the basic principle demonstrated by Guerrette *et al.* with minor modifications.[1] Briefly, two separate beaker glasses were filled with a reference electrolyte and a flow battery electrolyte, respectively. The reference electrolyte contained 25 mM of potassium ferricyanide and 22 mM of potassium ferrocyanide trihydrate dissolved in an aqueous 3 M KCl solution saturated with AgCl (~ 0.16 M). Three electrodes per half-cell were immersed into the corresponding electrolyte. For the reference half-cell these electrodes were: A AgCl-coated Ag wire connected to the reference terminal of the potentiostat and the voltage sensing terminal of the counter electrode, a coiled gold wire connected to the current-carrying terminal of the counter electrode, and another coiled gold wire as the macroelectrode of the bipolar electrode. Correspondingly, for the analysis half-cell the electrodes were: a microelectrode connected to the macroelectrode of the reference half-cell *via* a standard copper cable as second part of the bipolar electrode, a gold wire connected to the working electrode's voltage sensing terminal, and another coiled gold wire connected to the current-carrying terminal of the working electrode. The described setup is illustrated in **Figure 1** of our manuscript as a scheme. The AgCl-coated silver wire in the reference half-cell and the straight gold wire in the analysis half-cell represent the driving electrodes of the bipolar setup. Voltages are always applied between these two electrodes. The same setup was used for the real-time state-of-charge monitoring of an operating redox flow battery; however, in this case the electrolyte tank of the capacity limiting half-cell of the flow battery was directly used as analysis half-cell of the closed bipolar setup. Hence, the three electrodes (microelectrode, gold wire, coiled gold wire) were directly inserted into the electrolyte tank. Care was taken that the tubes of the electrolyte inlet and outlet were positioned as far away from the microelectrode as possible. In particular, the outlet tube feeding back the electrolyte into the tank was placed directly at the wall, which caused the electrolyte to funnel along the tank wall reducing electrolyte convection within the tank. A scheme of the utilized setup is depicted in **Figure S1**.

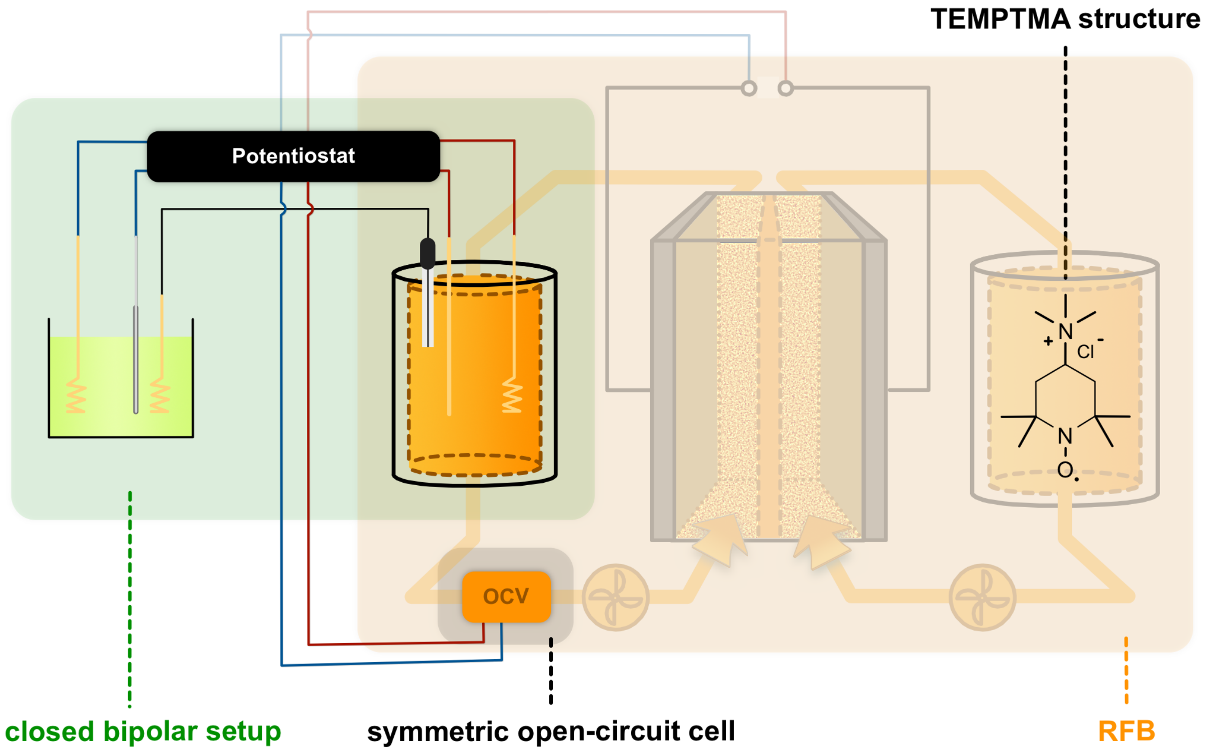

Figure S1. Schematical representation of the setup utilized for the real-time state-of-charge monitoring experiment of a symmetric TEMPTMA/TEMPTMA RFB (orange box). The electrolyte tank of the capacity-limiting half-cell is used as the analysis half-cell of the closed bipolar setup (green box). A symmetric open-circuit cell (gray box) is built into the electrolyte channel of the capacity-limiting half-cell as a reference SOC monitoring system.[2]

Symmetric open-circuit cell. The symmetric open-circuit cell setup for the state-of-charge monitoring of the operating RFB was identical to the one described in our recent publication.[2] The reference solution of this open-circuit cell was a small fraction of the same 1.3 M TEMPTMA electrolyte in its initial state (~50% SOC), which was also used as flow battery electrolyte for the symmetric RFB.

Redox flow cell. The specific details of the redox flow cell setup that was used for the experiments were published in a previous study of our group.[3] In short, the cell is characterized by: A geometric electrode/membrane area of 5 cm^2, a half-cell thickness of 4.5 mm, a FAA-3-50 anion-exchange membrane (Fumatech GmbH, Germany), two graphite composite current collectors (MERSEN GmbH, Germany), and two graphite felts as porous electrodes (GFA6, area: 5 cm^2, thickness: 6 mm compressed to 4.5 mm, SGL Group, Germany). Flow rates of approximately 16 mL min^{-1} were applied with a Pumpdrive 5001 peristaltic pump (Heidolph Instruments GmbH & CO. KG, Germany).

Potentiostats. The electrochemical experiments which were performed on offline samples were controlled using a 2400 SourceMeter Unit (SMU) from Keithley. This instrument was operated in four-terminal mode and measurements were recorded manually, *i.e.*, without the use of a computer. With respect to the real-time monitoring of an operating flow battery, a computer-controlled 16-channel VMP3 potentiostat from BioLogics Scientific Instruments was employed. The PC software EC-Lab v11.26 provided by the manufacturer was used for instrument control and data acquisition.

Experimental methods

Steady-state voltammetry. The steady-state voltammograms at the bipolar microelectrode were recorded using the Keithley 2400 SMU. Driving voltages were applied between the driving electrodes of the bipolar setup and currents were measured with a delay of 30 s. It should be noticed that for this kind of setup the anodic currents are measured at negative driving voltages and cathodic currents are measured at positive driving voltages, which is inverse to the measurements at usual three-electrode setups. That is also the reason why the historic current convention (*i.e.*, anodic currents are negative) is used during the derivation of all equations within the manuscript. A voltage range from –0.2 to 0.8 V was scanned in 50 mV steps in both forward (negative to positive) and backward (positive to negative) direction. If not explicitly stated otherwise, the voltammograms were recorded at room temperature in an air-conditioned laboratory (~ 294 K) but without active temperature control of the setup. Voltammograms recorded at higher temperatures were obtained using a stirred oil bath tempered by a heating plate, whose temperature sensor was immersed into the oil and not into the sample. The oil was constantly stirred by a magnetic stirrer to facilitate uniform heat distribution. Both the reference half-cell and the analysis half-cell of the closed bipolar setup were immersed into the oil. Due to the location of the temperature sensor, the temperatures stated within the study are – strictly spoken – those of the oil bath and not exactly those of the samples. To reduce the difference between oil bath and sample temperature, however, the amperometric measurement was started approximately 20 min after the oil had reached the specified temperature.

Real-time SOC monitoring. The VMP3 was operated with three synchronized channels which were used to simultaneously fulfil the following measurement tasks: (1) Galvanostatically charge and discharge the redox flow battery at 200 mA, (2) monitor the open-circuit voltage of the symmetric open-circuit cell, and (3) perform an amperometric measurement with the closed bipolar setup. The amperometric measurement was performed by switching the driving voltage applied to the setup between the two values –0.2 V and 0.8 V. The voltages were applied for 10 s, after which the steady-state current was measured. Subsequently to each of the 0.8 V intervals, a 1 min resting period at 0.3 V (*i.e.*, the approximate equilibrium voltage of the closed bipolar setup) followed. The latter was merely introduced to reduce the number of data points recorded during the monitoring. The measured steady-state currents were smoothed using a weighted moving average method with a window size, N, of 8 data points and parabolic weights of the form $w_j = 1 - [2(j-i)(N+1)^{-1}]^2$, where j = 0, 1, ... (N - 1) and i is the center of the window. Subsequently, the smoothed curves were used for the SOC estimation. The voltage of the symmetric open-circuit cell was used to estimate the SOC of the redox flow battery electrolyte according to Ressel's calibration method,[4] which has already been applied for the symmetric open-circuit cell type recently.[2] In order to maximize the SOC estimation accuracy, the calibration was performed on each half-cycle separately.

Verification of the derived equations using literature data

Data extraction. Values of the diffusion-limited current responses of the amperometric sensor reported by Kroner *et al*., recently, were extracted from Figure 6 of their publication.[5] The software ImageJ was utilized to measure the distance between the axes and each data point to obtain accurate values. The extracted data points are listed in **Table S1** below.

Table S1. Data extracted from reference (5), which were obtained on a positive vanadium electrolyte using an amperometric sensor for the measurement of diffusion-limited currents. Given concentrations of the vanadium species were obtained with redox titration in the original publication. The "true" SOCs are calculated from the concentrations.

c_V / mol L^{-1} [*]	i_c / mA [*]	c_{IV} / mol L^{-1} [#]	i_a / mA [#]	SOC_{true} / %
0.068	–0.119	1.565	1.558	4.2
0.21	–0.192	1.413	1.372	12.9
0.381	–0.322	1.263	1.225	23.2
0.506	–0.435	1.015	1.053	33.3
0.724	–0.547	0.956	0.895	43.1
0.89	–0.666	0.773	0.751	53.5
1.064	–0.765	0.618	0.627	63.3
1.236	–0.880	0.466	0.539	72.6
1.394	–1.033	0.313	0.491	81.7
1.625	–1.163	0.093	0.336	94.6

[*] Data extracted from Figure 6b of reference (5).

[#] Data extracted from Figure 6d of reference (5).

The true SOC of each vanadium sample, SOC_{true}, was calculated from the reported concentrations of the oxidized and reduced vanadium species in accordance to the definition of a catholyte's SOC, $SOC \equiv c_V(c_V + c_{IV})^{-1}$.

Offset current correction. A linear regression was performed on the cathodic and anodic currents, i_c and i_a, listed in **Table S1** above. The offset currents at zero concentration of both vanadium species were obtained as ordinate intercepts and yielded values of –0.066 mA for the cathodic currents and 0.1785 mA for the anodic currents.

Table S2. Offset corrected current values and the calculated ratio of anodic to cathodic current, which is used to calculate the SOC estimate (see **Table S4**).

c_V / mol L^{-1} [*]	i_c / mA [*]	c_{IV} / mol L^{-1} [#]	i_a / mA [#]	SOC_{true} / %	$i_a i_c^{-1}$ / 1
0.068	–0.053	1.565	1.3795	4.2	–26.028
0.21	–0.126	1.413	1.1935	12.9	–9.472
0.381	–0.256	1.263	1.0465	23.2	–4.088
0.506	–0.369	1.015	0.8745	33.3	–2.370
0.724	–0.481	0.956	0.7165	43.1	–1.490
0.89	–0.600	0.773	0.5725	53.5	–0.954
1.064	–0.699	0.618	0.4485	63.3	–0.642
1.236	–0.814	0.466	0.3605	72.6	–0.443
1.394	–0.967	0.313	0.3125	81.7	–0.323
1.625	–1.097	0.093	0.1575	94.6	–0.144

[*] Data extracted from Figure 6b of reference (5).

[#] Data extracted from Figure 6d of reference (5).

In order to obtain a reasonable accuracy in our SOC estimates, the offset currents were subtracted from all measured current values. The offset-corrected currents and the ratio of anodic to cathodic current, $i_a i_c^{-1}$, required for SOC estimation are provided in **Table S2**.

Table S3. The current differences calculated from the currents listed in **Table S2**. Each value represents the difference to the first current value, which is also the reason for the missing value for Δi_c and Δi_c in the first line. The ratio $\Delta i_c \Delta i_a^{-1}$ is used to calculate the SOC estimate in accordance with equation (5a) of our manuscript.

$\boldsymbol{i_c}$ **/ mA**	$\boldsymbol{\Delta i_c}$ **/ mA** [*]	$\boldsymbol{i_a}$ **/ mA**	$\boldsymbol{\Delta i_a}$ **/ mA** [*]	$\boldsymbol{\Delta i_c \Delta i_a^{-1}}$ **/ 1** [#]
–0.053	-	1.3795	-	-
–0.126	–0.073	1.1935	–0.186	0.392
–0.256	–0.203	1.0465	–0.333	0.610
–0.369	–0.316	0.8745	–0.505	0.626
–0.481	–0.428	0.7165	–0.663	0.646
–0.600	–0.547	0.5725	–0.807	0.678
–0.699	–0.646	0.4485	–0.931	0.694
–0.814	–0.761	0.3605	–1.019	0.747
–0.967	–0.914	0.3125	–1.067	0.857
–1.097	–1.044	0.1575	–1.222	0.854

[*] Difference of the current value in the same row to the current value in the first row.

[#] This ratio is equivalent to $D_O D_R^{-1}$ as was derived with equation (4) of the manuscript.

Verification of the derived equations. The SOCs were estimated using two different approaches:

(1) It was assumed that $D_O D_R^{-1} \approx 1$ in equation (6) of the manuscript, which is a good assumption for most redox species and, hence, frequently used in the electrochemical literature;

(2) the SOC was calculated directly from equation (5a) using the differences in mass-transfer limited currents to the first value and the ratio of these differences for anodic and cathodic currents, $\Delta i_c \Delta i_a^{-1}$.

The data basis for the SOC estimation, *i.e.*, the offset corrected currents, the calculated current differences Δi_c and Δi_a, and the ratio $\Delta i_c\ \Delta i_a^{-1}$ are presented in **Table S3**. Finally, the obtained SOC estimates, SOC_{est}, and the differences between the true state-of-charge and the estimated states-of-charge, ΔSOC_{est}, are listed in **Table S4** for both approaches. The first value for approach (2) could not be calculated since the first current difference cannot be calculated due to the naturally missing preceding current value for the first data point. However, this is a particular issue of the offline sample measurement and not a problem for the real-time SOC monitoring. Root-mean-square deviations (RMSD) were calculated from ΔSOC according to $\sqrt{\Delta SOC^2\ N^{-1}}$, where N is the number of values. The main source of error originates from the inaccuracy in current measurement for the reduced vanadium species as discussed by Kroner *et al.* in their publication. However, the authors have not presented repetitions of the measurement or any statistical information for neither of the vanadium species. Therefore, no statistical evaluation is possible and it is likely that repeated measurement of currents during a real-time SOC monitoring alongside with sophisticated smoothing procedures will provide a significantly higher accuracy. This assumption is also supported by our own experiments for the real-time SOC monitoring of a symmetric TEMPTMA / TEMPTMA redox flow battery (see manuscript and pages S29ff. below).

Table S4. The SOC estimates for the data of Kroner *et al*. calculated with equation (6) ($SOC_{est,1}$) and equation (5a) ($SOC_{est,2}$) of our manuscript. The deviations from the "true" SOC are listed as $\Delta SOC_{est,1}$ and $\Delta SOC_{est,2}$. Root-mean-square deviations (RMSD) for each approach are given in the last line.

SOC_{true} / %	$SOC_{est,1}$ / %[*]	$\Delta SOC_{est,1}$ / %	$SOC_{est,2}$ / %[#]	$\Delta SOC_{est,2}$ / %
4.2	3.7	–0.5	-	-
12.9	9.5	–3.4	21.2	8.3
23.2	19.7	–3.5	28.6	5.5
33.3	29.7	–3.6	40.3	7.0
43.1	40.2	–2.9	51.0	7.9
53.5	51.2	–2.3	60.7	7.2
63.3	60.9	–2.3	69.2	5.9
72.6	69.3	–3.3	75.1	2.5
81.7	75.6	–6.1	78.3	–3.3
94.6	87.4	–7.1	89.1	–5.5
	RMSD$_1$:	3.9	RMSD$_2$:	6.2

[*] Estimated from $SOC = (1-(i_a i_c^{-1})(D_O D_R^{-1}))^{-1}$ assuming $D_O D_R^{-1} = 1$.

[#] Estimated from $SOC = (1-(i_a i_c^{-1})(D_O D_R^{-1}))^{-1}$ using the equivalence derived from equations (4) and (7) of the manuscript, *i.e.*, $D_O D_R^{-1} = \Delta i_c \Delta i_a^{-1}$.

Investigations on the reference potential of the closed bipolar setup

Reproducibility. For evaluation of the reproducibility of the reference electrolyte and the reference potential, three identical reference electrolytes were prepared independently from each other. The reference electrolytes contained approximately 25 mM potassium ferricyanide and 22 mM potassium ferrocyanide trihydrate (*i.e.*, 53% SOC) and were prepared in aqueous 3 M KCl solutions saturated with AgCl (~0.16 M). Following the preparation, each of the three reference solutions was used to measure the steady-state voltammogram of the same 53% SOC ferri-/ferrocyanide solution at a total concentration of 50 mM in forward and backward scan. The voltammograms are displayed in **Figure S2**.

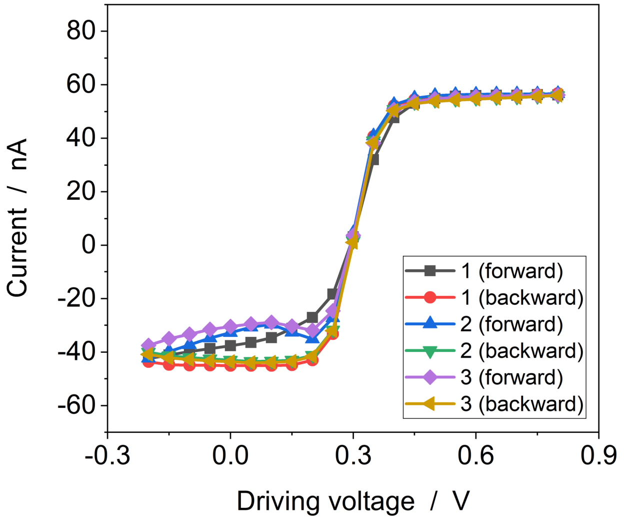

Figure S2. Steady-state voltammograms obtained at a closed bipolar gold microelectrode (diameter: 25 μm) for a 50 mM ferri-/ferrocyanide electrolyte in 0.5 M KCl in forward and backward scan mode. Three different batches of 25 mM potassium ferricyanide and 22 mM potassium ferrocyanide trihydrate were prepared in aqueous 3 M KCl solutions and used as reference electrolyte in the closed bipolar setup.

The mean value and the standard deviation of the reference potentials of all six measurements was 295 ± 3 mV. The six values were obtained at the abscissa intercept of the voltammograms and, hence, in the systems equilibrium state. The low standard deviation of the observed reference potential of about 1% indicates an excellent reproducibility.

Long-term stability. In order to obtain a first indicator for the long-term stability of the reference half-cell, the first reference electrolyte that was prepared and used within measurements with the closed bipolar setup was kept over longer time periods in a closed glass vial at room temperature. After 27 days and after 41 days of its first use, respectively, it was refilled into the reference half-cell of the closed bipolar setup. Steady-state voltammograms of the same three ~ 50% SOC samples of 50 mM ferri-/ferrocyanide in aqueous 0.5 M KCl which had been used for the reproducibility measurements displayed in **Figure S2** were recorded in forward and backward scans. Subsequently, the equilibrium potential was evaluated from these six curves at the abscissa intercept (*i.e.*, zero current) and the obtained mean values are plotted over time in **Figure S3**. The error bars represent the corresponding standard deviations. It is evident that the reference potential did not change significantly over the course of 41 days. While these results are promising, clearly other long-term experiments have to be performed to evaluate the long-term stability of the full closed bipolar setup and its electrodes. Apart from that, the results reported by Kroner *et al.* suggest that the utilization of a pure pseudo-reference electrode might suffice for amperometric sensors.[5] However, detailed studies on the long-term stability and the long-term accuracy of an amperometric sensor with pseudo-reference electrode need to be performed as well.

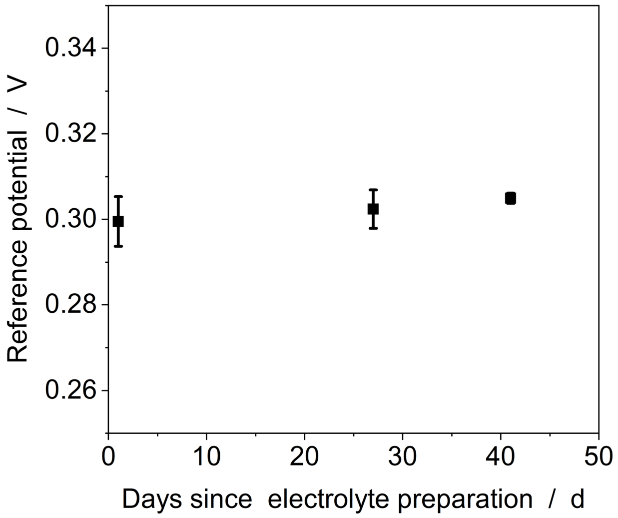

Figure S3. The first reference electrolyte prepared was stored in a closed glass vial for several weeks and measured *versus* the same solution within the analysis half-cell (50 mM ferri-/ferrocyanide at 53% SOC) several times. Displayed are the reference potentials extracted at equilibrium (*i.e.*, zero current) as mean values of the three samples (six voltammograms) and error bars are the corresponding standard deviations.

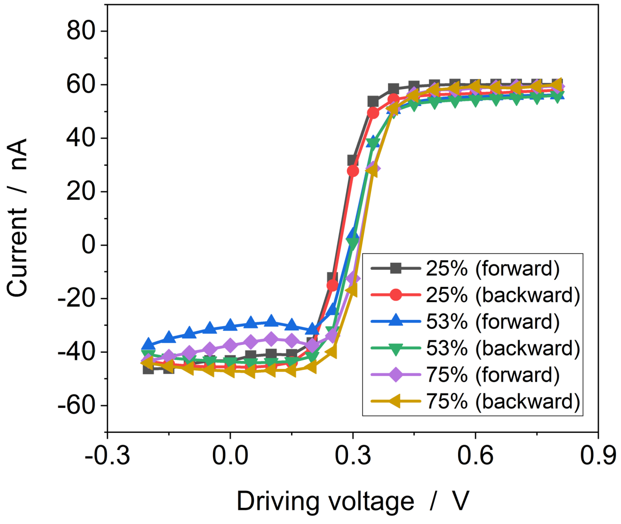

Figure S4. Steady-state voltammograms obtained for three reference electrolytes at equal total concentrations but different concentration ratios and, therefore, different SOCs.

Concentration ratio. A short experiment was also conducted on the influence of the concentration ratios of ferricyanide and ferrocyanide within the reference solution. Three solutions were prepared at concentrations ratios of 13 mM ferricyanide / 38 mM ferrocyanide (*i.e.*, 25% SOC), 25 mM ferricyanide / 22 mM ferrocyanide (*i.e.*, 53% SOC), and 37 mM ferricyanide / 13 mM ferrocyanide (*i.e.*, 75% SOC), respectively. Again, the reference solutions were used to measure the steady-state voltammograms of the 50% SOC ferri-/ferrocyanide solution at a total concentration of 50 mM. The results are depicted in **Figure S4**. It can be clearly seen that the steady-state voltammogram shifts with changing concentration ratio of ferri- and ferrocyanide within the reference electrolyte. **Table S5** lists the reference potentials obtained at zero current for each of the six voltammograms and the corresponding mean value of the forward and backward scan of each sample.

Table S5. The reference potentials measured at different SOCs of the reference electrolyte for the forward, $E_{eq,f}$, and backward, $E_{eq,b}$, scan. The mean values, $\bar{E}_{eq}$, are compared to the theoretical values, E_{Nernst}, which are calculated from the Nernst equation.

SOC / %	$E_{eq,f}$ / V [*]	$E_{eq,b}$ / V [#]	$\bar{E}_{eq}$ / V [+]	E_{Nernst} / V [-]
25	0.2638	0.2676	0.266	0.264
53.4	0.2934	0.2984	0.296	0.295
75	0.3151	0.3188	0.317	0.319

[*] Equilibrium voltages / reference potentials as obtained from the forward scans.

[#] Equilibrium voltages / reference potentials as obtained from the backward scans.

[+] Average of the values of forward and backward scan.

[-] Values according to the Nernst equation with $E^{0'} = 291.5$ mV.

A quantitative analysis reveals that the reference potential and the concentration ratios of the ferri- and ferrocyanide couple within the reference electrolyte obey the Nernst equation:

$$E_{eq} = 291.5\ \mathrm{mV} + \frac{RT}{F}\ln\left(\frac{c_{ox}}{c_{red}}\right) = 291.5\ \mathrm{mV} + \frac{RT}{F}\ln\left(\frac{SOC}{1 - SOC}\right). \tag{S1}$$

This is an expected behavior and originates from the properties of closed bipolar setups as investigated and discussed by Guerrette and Cox *et al.*.[1, 6] In contrast to their work, the equilibrium voltage / reference potential of our setup is determined by the composition of the reference electrolyte. Further investigations are, however, required to obtain an in-depth understanding of the closed bipolar setup utilized in this study.

Temperature dependence. In **Figure S8** and **Figure S9**, data on the temperature dependence of the steady-state voltammograms of 50% SOC electrolytes is depicted. The temperature dependence of the reference potential of the closed bipolar setup could be evaluated as well from the data and the results are plotted in **Figure S5**. A linear relationship is evident. Due to the low slope of approximately 1.1 mV K^{-1}, it can be concluded that the observed dependence of reference potential on temperature has no significant impact on the measured steady-state currents in the mass-transfer limiting potential region. That is, if sufficiently large overpotentials are applied the minor variances originating from temperature changes are negligible.

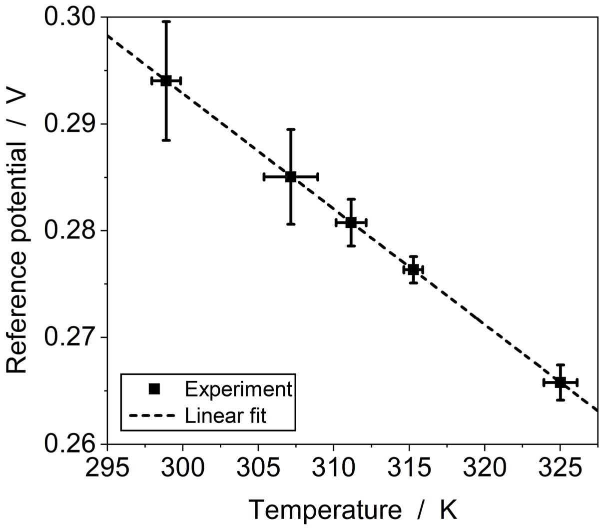

Figure S5. Temperature dependence of the reference potential in the temperature range from approximately 25 to 50 °C.

Limiting currents & SOC data for ferri-/ferrocyanide samples at various concentrations

Offline sample data. Offline samples of several 50 mM and 500 mM ferri-/ferrocyanide electrolytes with different SOCs (*i.e.*, 1%, 5%, 25%, 50%, 75%, 95%, 99%) were prepared and steady-state voltammograms were recorded at the microelectrode. The limiting currents obtained at –0.2 V and 0.8 V were used to estimate the SOCs of all offline samples. Each offline sample of defined SOC and total concentration was prepared three times separately yielding 42 samples. Each sample was measured one time in forward and backward scan mode. The microelectrode was polished and its tip was kept in a sonic bath for 10 min during each sample exchange. Although maximum care was taken in the cleaning procedure, the measured absolute current values exhibited larger standard deviations. This effect was primarily observed for larger concentrations of ferri-/ferrocyanide indicating a species-related interaction with the gold microelectrode. While the absolute values changed, the ratios of cathodic to anodic limiting currents stayed reproducible. Consequently, the observed difference can be attributed to a change in electrode surface area and it was concluded that the standard cleaning procedure did not suffice. However, since our SOC monitoring approach relies on the current ratios rather than their absolute values, the variation itself was not further investigated. Nevertheless, this observation highlights both the importance of the choice of microelectrode material for specific redox couples and the robustness of our approach regarding unknown surface changes at the microelectrode.

SOC estimates. While the average results have been presented within the manuscript, the SOC estimates as well as the cathodic and anodic limiting currents obtained for each sample in the forward and backward scans are provided in **Figure S6** and **Figure S7** below. The "true" SOCs of the samples, SOC_{true}, were calculated from the known concentrations determined by the weighed substances. $SOC_{est,1}$ was determined from equation (6) of the manuscript and by assuming $D_O D_R^{-1} = 1$, wheras

$SOC_{est,2}$ was determined from equation (5a) of the manuscript with $\Delta i_{l,c}$ and $\Delta i_{l,a}$ representing the difference of each current to the limiting currents obtained at 1% SOC.

Figure S6. Limiting currents obtained from the steady-state voltammograms measured with a closed bipolar gold microelectrode (diameter: 25 μm) for offline samples of a 50 mM ferri-/ferrocyanide electrolyte in 0.5 M KCl$_{(aq)}$ at different SOCs: (a) First sample, forward scan; (b) first sample, backward scan; (c) second sample, forward scan; (d) second sample, backward scan; (e) third sample, forward scan; (f) third sample, backward scan. SOC estimates, $SOC_{est,1}$, were calculated by equation (6) with the assumption $D_O D_R^{-1} = 1$ and $SOC_{est,2}$ values were calculated by equation (5a).

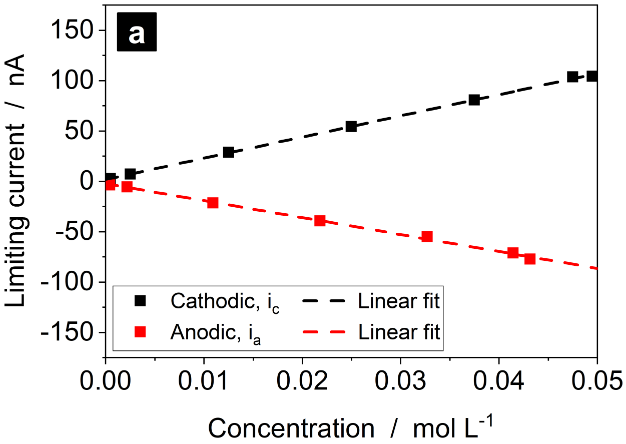

SOC_{true} / %	$SOC_{est,1}$ / %	$SOC_{est,2}$ / %
1.1	3.4	-
5.7	9.0	12.3
27.6	34.5	22.7
53.4	58.0	50.4
77.5	78.9	72.7
95.6	95.0	93.1
99.1	96.6	95.4

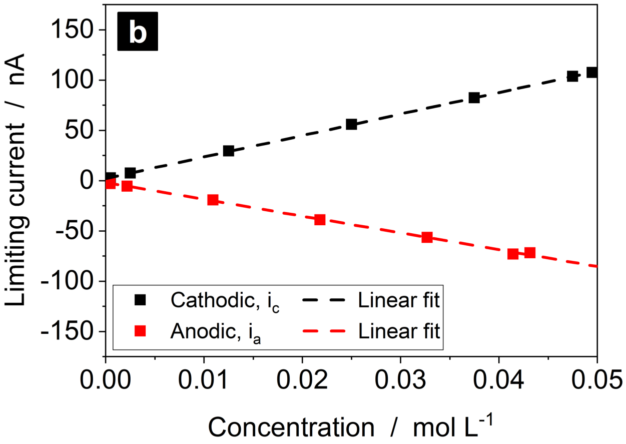

SOC_{true} / %	$SOC_{est,1}$ / %	$SOC_{est,2}$ / %
1.1	3.5	-
5.7	9.3	–2.7
27.6	34.3	16.5
53.4	58.9	46.9
77.5	80.9	73.6
95.6	95.0	92.6
99.1	97.3	96.0

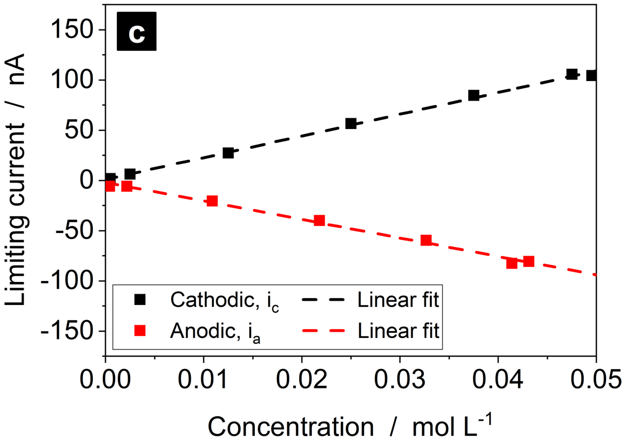

SOC_{true} / %	$SOC_{est,1}$ / %	$SOC_{est,2}$ / %
1.1	2.1	-
5.7	7.0	–3.8
27.7	31.4	20.5
53.5	58.5	51.1
77.5	80.3	74.8
95.6	94.8	92.9
99.1	94.7	92.8

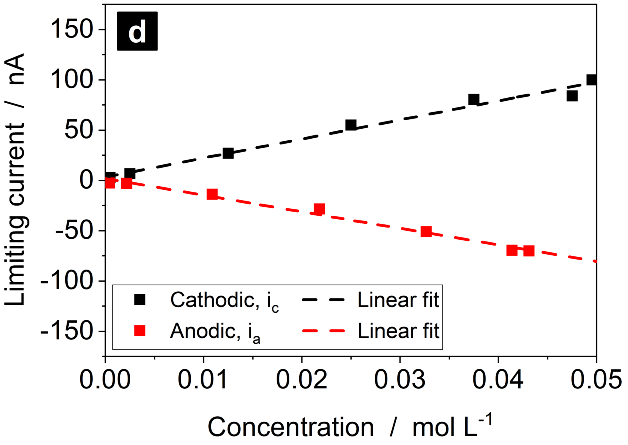

SOC_{true} / %	$SOC_{est,1}$ / %	$SOC_{est,2}$ / %
1.1	3.7	-
5.7	8.6	1.3
27.7	34.5	21.4
53.5	65.8	60.5
77.5	85.2	80.6
95.6	96.5	95.9
99.1	97.5	96.5

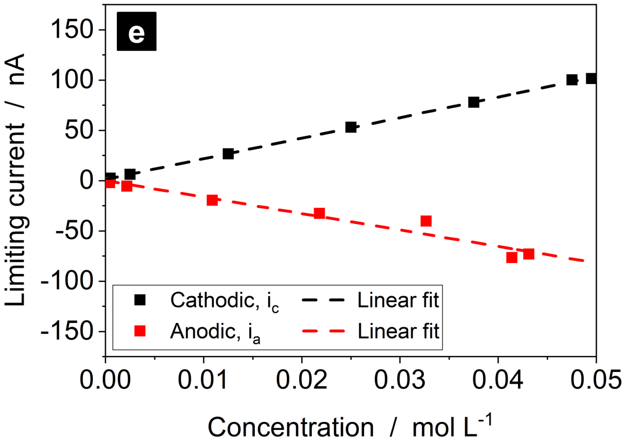

SOC_{true} / %	$SOC_{est,1}$ / %	$SOC_{est,2}$ / %
1.1	3.1	-
5.7	7.6	–8.5
27.7	39.8	34.7
53.5	61.8	56.2
77.5	79.9	73.8
95.6	94.7	92.5
99.1	98.1	97.4

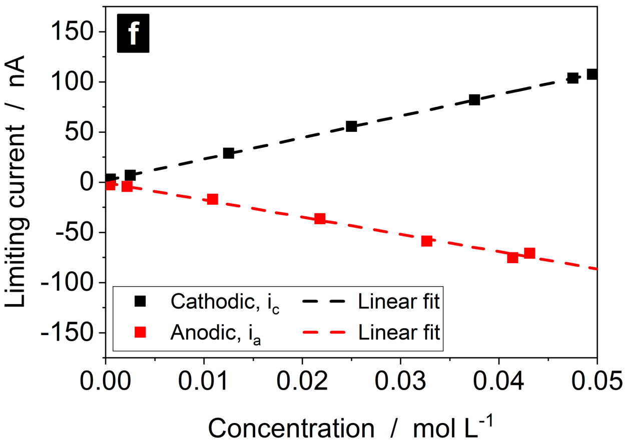

SOC_{true} / %	$SOC_{est,1}$ / %	$SOC_{est,2}$ / %
1.1	4.0	-
5.7	8.2	–12.2
27.7	32.8	13.2
53.5	60.3	49.7
77.5	82.8	76.5
95.6	95.9	93.9
99.1	97.5	96.2

Figure S7. Limiting currents obtained from the steady-state voltammograms measured with a closed bipolar gold microelectrode (diameter: 25 μm) within offline samples of a 500 mM ferri-/ferrocyanide electrolyte in 1 M $KCl_{(aq)}$ at different SOCs: (a) First sample, forward scan; (b) first sample, backward scan; (c) second sample, forward scan; (d) second sample, backward scan; (e) third sample, forward scan; (f) third sample, backward scan. SOC estimates, $SOC_{est,1}$, were calculated by equation (6) using the assumption, $D_O D_R^{-1} = 1$ and SOC estimates, $SOC_{est,2}$, were calculated by equation (5a).

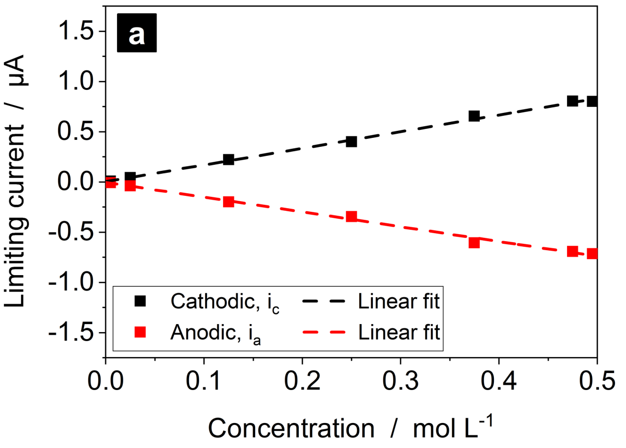

SOC_{true} / %	$SOC_{est,1}$ / %	$SOC_{est,2}$ / %
1.0	1.3	-
5.0	6.0	4.1
25.0	26.6	12.1
50.0	53.6	52.3
75.0	76.6	72.4
95.0	95.2	94.4
99.0	99.0	98.9

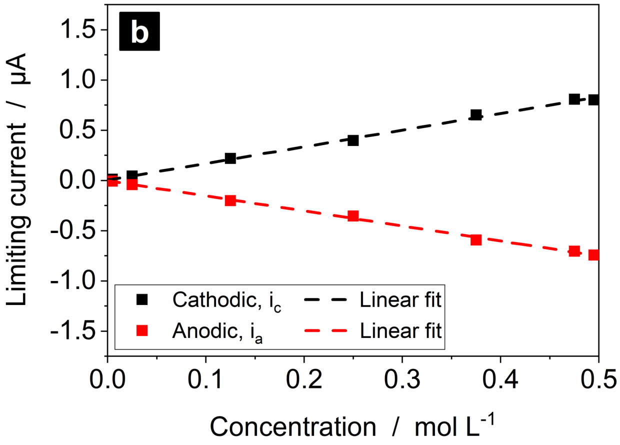

SOC_{true} / %	$SOC_{est,1}$ / %	$SOC_{est,2}$ / %
1.0	1.5	-
5.0	5.8	8.0
25.0	26.9	24.8
50.0	52.8	53.5
75.0	76.4	76.2
95.0	95.0	94.3
99.0	98.8	94.7

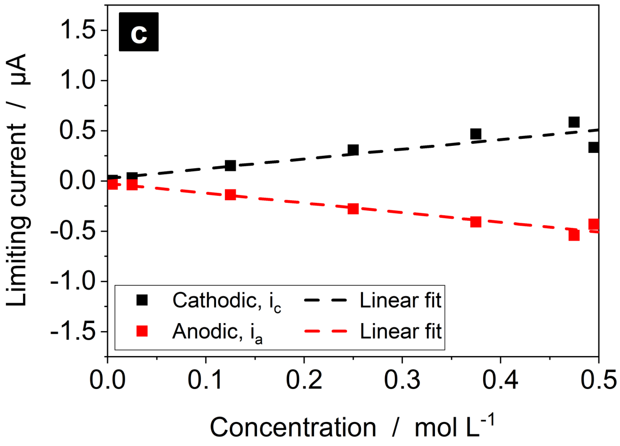

SOC_{true} / %	$SOC_{est,1}$ / %	$SOC_{est,2}$ / %
1.0	1.3	-
5.0	5.3	–33.1
25.0	26.8	4.2
50.0	52.3	35.8
75.0	77.0	68.1
95.0	93.7	90.9
99.0	90.9	92.5

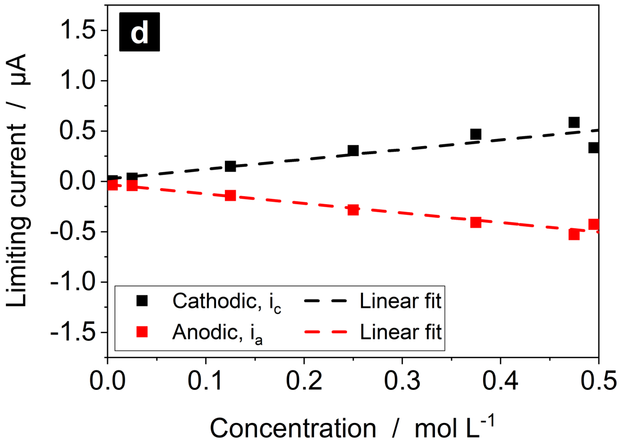

SOC_{true} / %	$SOC_{est,1}$ / %	$SOC_{est,2}$ / %
1.0	1.2	-
5.0	5.3	–30.0
25.0	26.7	3.7
50.0	51.6	33.8
75.0	76.5	67.0
95.0	93.2	90.1
99.0	90.4	91.8

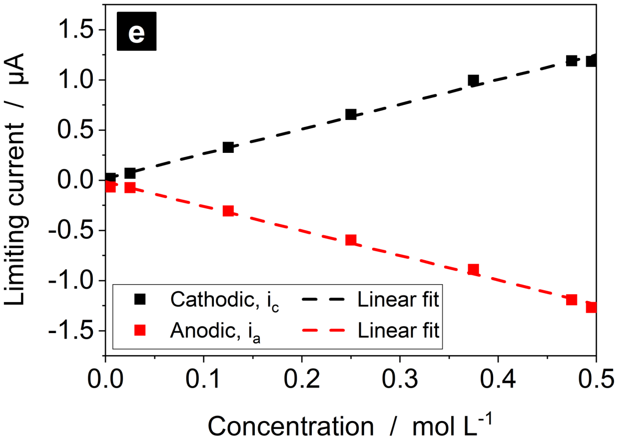

SOC_{true} / %	$SOC_{est,1}$ / %	$SOC_{est,2}$ / %
1.0	1.4	-
5.0	5.4	8.0
25.0	26.8	24.8
50.0	52.3	53.5
75.0	76.5	76.2
95.0	94.2	94.3
99.0	94.5	94.7

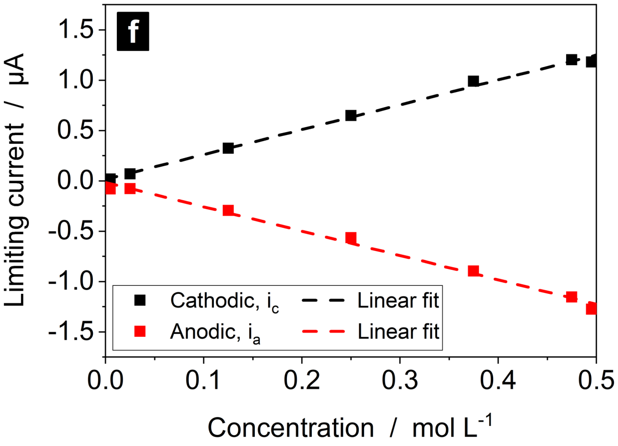

SOC_{true} / %	$SOC_{est,1}$ / %	$SOC_{est,2}$ / %
1.0	1.3	-
5.0	5.5	12.0
25.0	26.5	24.6
50.0	53.5	56.3
75.0	77.0	77.1
95.0	94.0	94.0
99.0	93.5	93.7

Voltammograms for ferri-/ferrocyanide and TEMPTMA samples at various temperatures

Steady-state voltammograms. The voltammograms obtained for different temperatures during backward scans between 0.8 V and –0.2 V are depicted in **Figure S8** for 500 mM ferri-/ferrocyanide in 1 M $KCl_{(aq)}$ and in **Figure S9** for 1.3 M $TEMPTMA_{(aq)}$. Both electrolytes were at ~50% SOC.

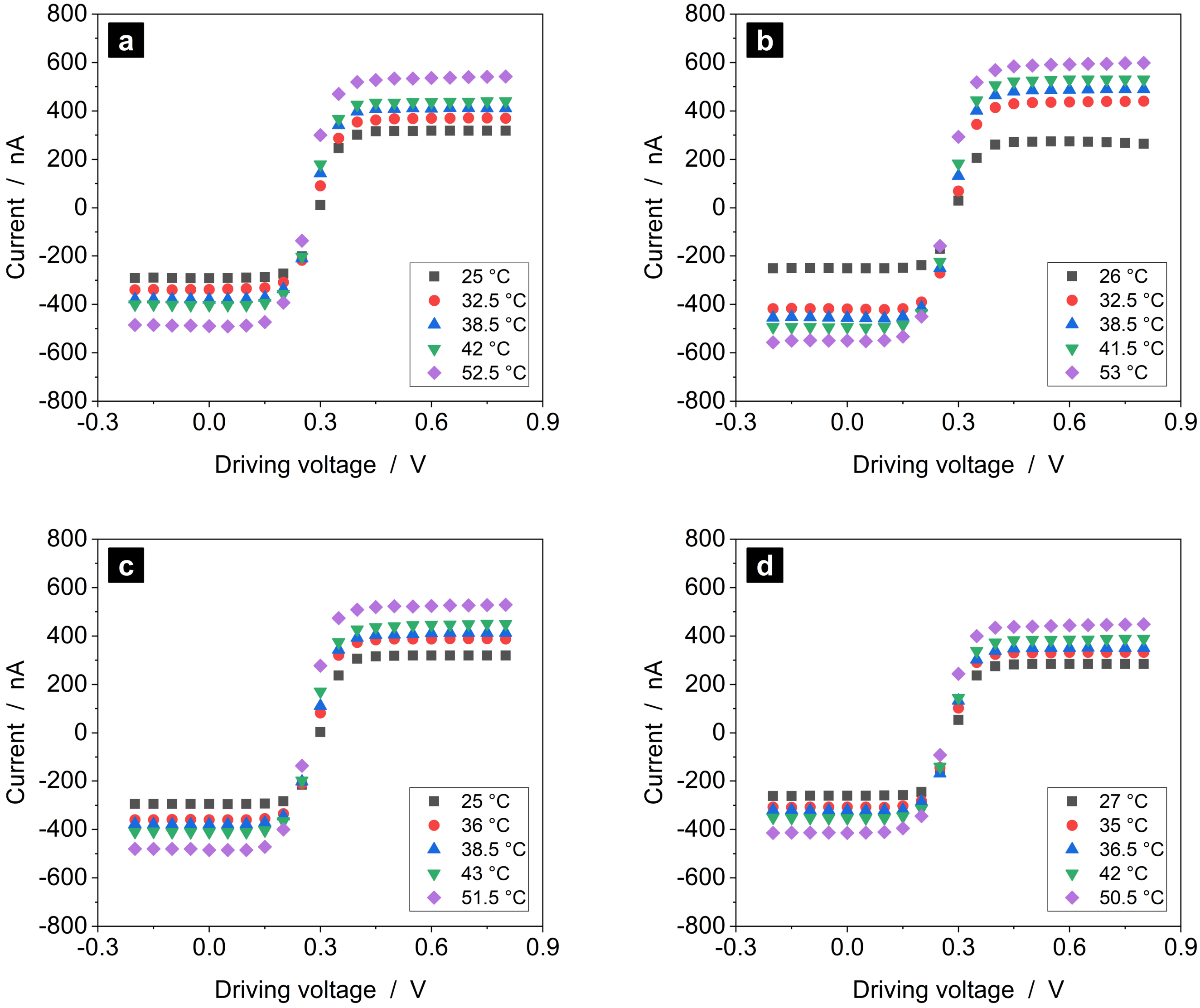

Figure S8. Steady-state voltammograms for a 500 mM ferri-/ferrocyanide electrolyte in 1 M $KCl_{(aq)}$ obtained at a closed bipolar gold microelectrode (diameter: 25 μm). Four repetitions are displayed.

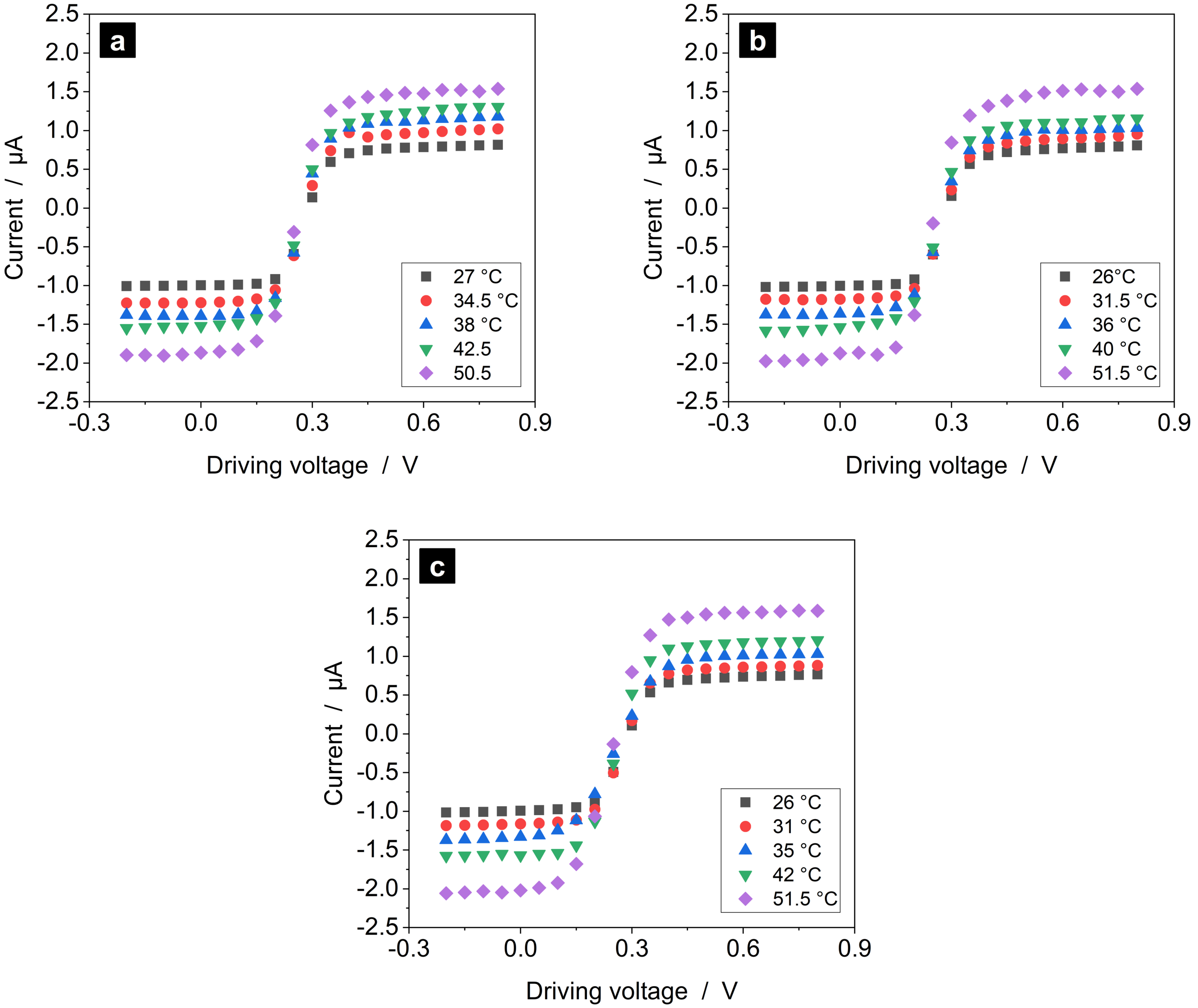

Figure S9. Steady-state voltammograms for a 1.3 M TEMPTMA$_{(aq)}$ electrolyte obtained at a closed bipolar carbon-fiber microelectrode (diameter: 33 μm). Three repetitions are displayed.

Temperature dependence of diffusion coefficients. As can be easily derived from the theoretical description of the limiting currents at a microelectrode, equations (7) of our manuscript, the ratio of the limiting currents equals the (negative) ratio of the diffusion coefficients, $D_O D_R^{-1}$, under the assumption that the voltammogram of a 50% SOC solution ($i.e.$, $c_O = c_R$) is recorded.

$$\frac{i_{l,c}}{i_{l,a}} = \frac{4nFrD_O c_O}{-4nFrD_R c_R} = -\frac{D_O c_O}{D_R c_R} = -\frac{D_O}{D_R}. \tag{S2}$$

The voltammograms of 50% SOC solutions of ferri-/ferrocyanide were recorded at different temperatures as depicted in **Figure S8** above. As discussed within our manuscript, quantitative evaluation reveals that the ratio $i_{l,c} i_{l,a}^{-1}$ does not change within its error margins with increasing temperature. As a consequence, $D_O D_R^{-1}$ was also observed to be temperature independent as was already mentioned in the manuscript. This is an interesting result, considering that it is well-known that diffusion coefficients in liquids usually exhibit a complicated non-linear temperature dependence. Our approach to explain the temperature independence observed for $D_O D_R^{-1}$ theoretically stems from the Stokes-Einstein equation which predicts that

$$\frac{D\eta}{T} = \text{const.}, \tag{S3}$$

where η represents the (temperature dependent) viscosity of the electrolyte. It follows directly from the equation above for an oxidized and a reduced species within the same electrolyte that

$$\text{const.} = \frac{D_O \eta}{T} \left(\frac{D_R \eta}{T}\right)^{-1} = \frac{D_O}{D_R}. \tag{S4}$$

Although this argumentation is reasonable and in agreement with the observations, care should be taken with it. If treated with theoretical rigor, the Stokes-Einstein equation is only applicable to dilute solutions; however, while aqueous solutions of a molecule at 1 to 2 M concentrations can still be regarded as dilute, this is not necessarily the case for all flow battery electrolytes. As a consequence, further investigations (also for broader temperature ranges) are necessary to reveal and to understand the experimental limits of the observed temperature-independence of $D_O D_R^{-1}$.

Real-time SOC monitoring: Calibration curves for symmetric open-circuit cell

Calibration of open-circuit cell. In order to obtain SOC estimates from the equilibrium voltages measured by the symmetric open-circuit cell, a calibration was necessary. Ressel's calibration method,[4] which essentially is a non-linear regression of the Nernst equation to the measured equilibrium voltage over time, was performed on each half-cycle. Each calibration curve is shown in **Figure S10** and the fits exhibited R^2 values of nearly 0.999 in each case, which indicated good agreement between the obtained data and the Nernst equation.

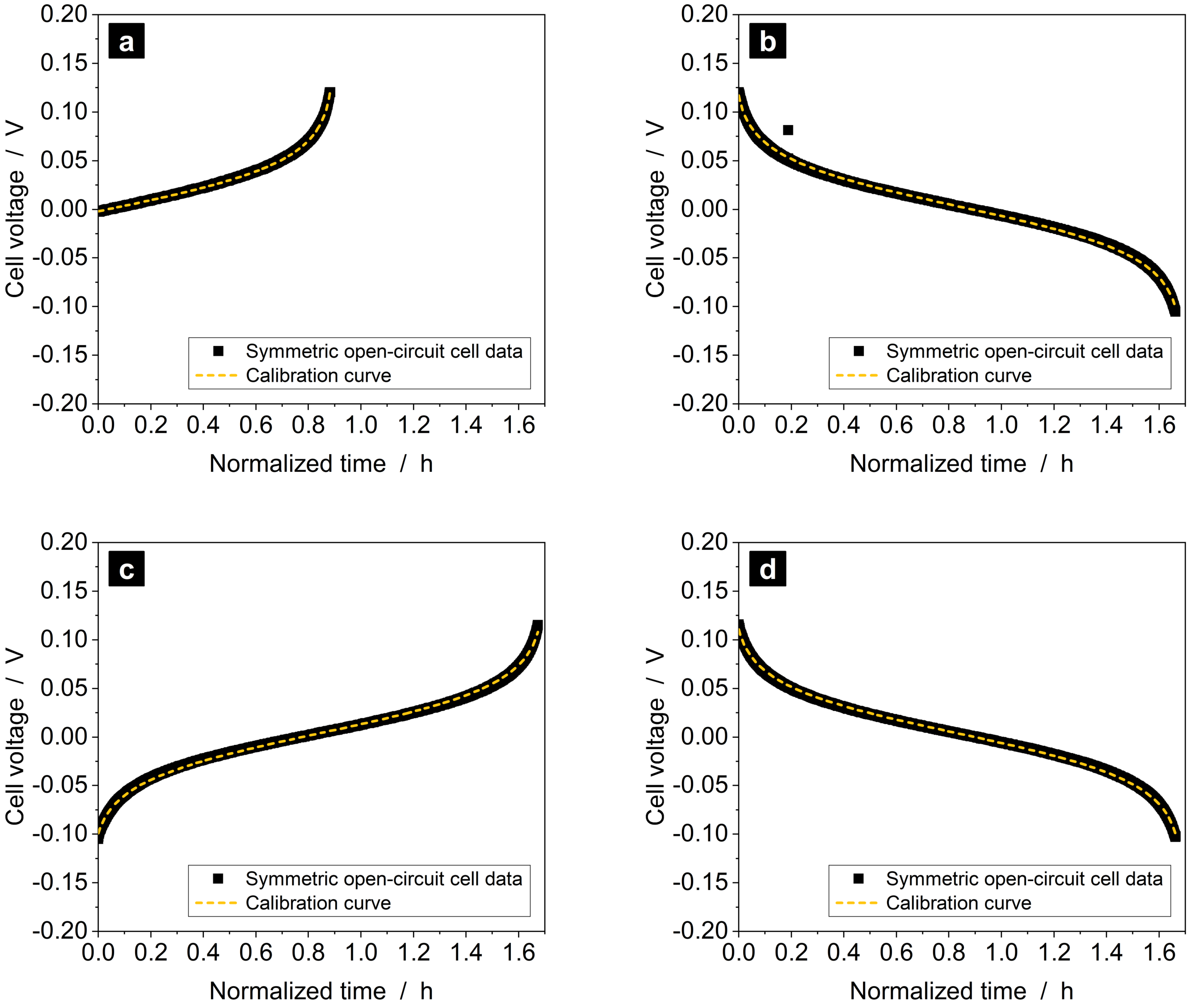

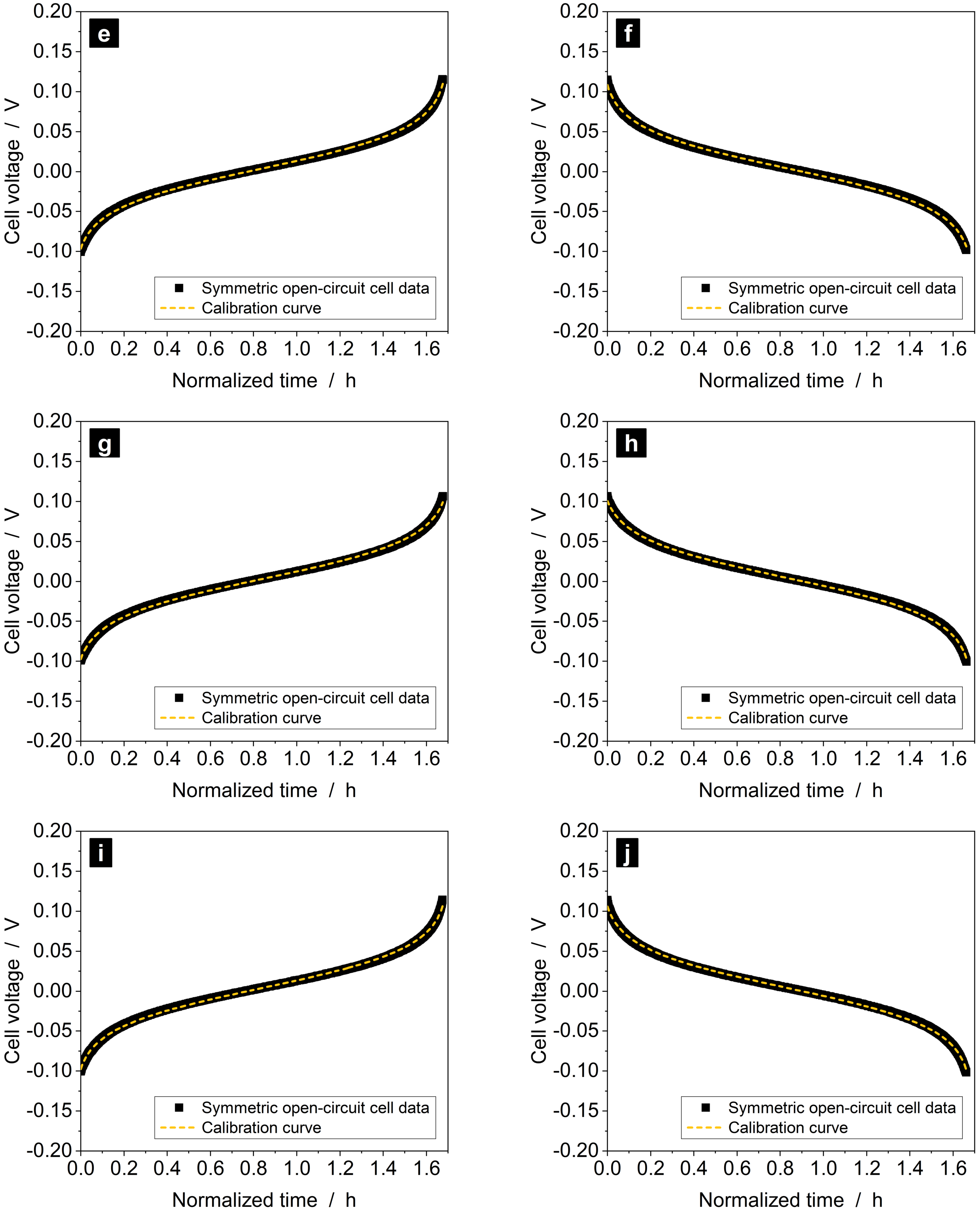
e
f
g
h
i
j
Cell voltage / V
0.20
0.15
0.10
0.05
0.00
-0.05
-0.10
-0.15
-0.20
Normalized time / h
0.0
0.2
0.4
0.6
0.8
1.0
1.2
1.4
1.6
Symmetric open-circuit cell data
Calibration curve

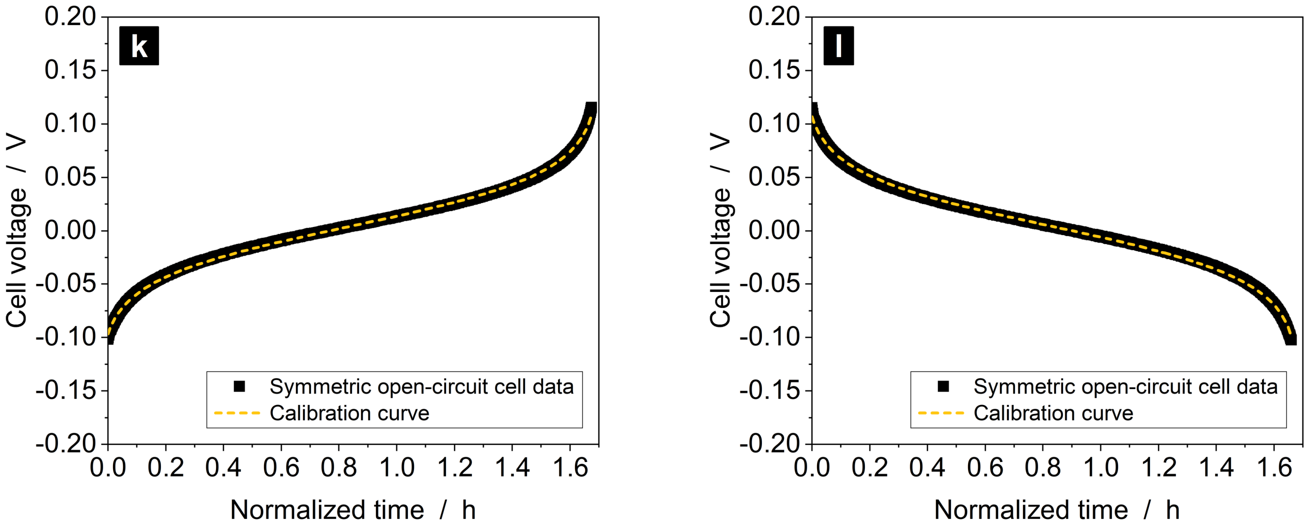

Figure S10. Experimental data and corresponding calibration curves as obtained from the symmetric open-circuit cell voltages for each half-cycle of the real-time SOC monitoring experiment.

Reference SOC. The SOC values derived from the symmetric open-circuit cell using the calibration curves above were used as reference. The amperometric method proposed in our study was evaluated against this reference SOC. However, it should be noted that despite the high acceptance of the open-circuit cell method, the SOC values provided by open-circuit cells rely on a calibration. Consequently, it’s accuracy strongly depends on the calibration data that, in turn, always relies on assumptions about the unknown SOC and mostly on coulomb counting. For example, it is often assumed that the battery or a battery electrolyte has 0% SOC or 100% SOC at a certain point. Another type of methods obtains the complete OCV-SOC relationship or the electrolytes formal potential by fitting. The latter is the case for Ressel’s method used above. Therefore, it should be emphasized that both open-circuit cell methods and coulomb counting are containing unknown systematic calibration errors themselves. As for any real-time SOC monitoring method reported in literature so far, the deviations and RMSDs reported in our study, consequently, do not reflect the real errors of the presented amperometric method with regard to the true value. They merely reflect the difference between the SOC estimates of the open-circuit cell method and the presented method. Due to the fact that our method does not rely on error-prone calibration procedures but instead is an absolute measurement method, it might well be that it is more accurate than the open-circuit cell. Further investigations on this circumstance are necessary in future studies. However, an analytical error propagation was already performed to obtain some first impressions.

Error propagation & accuracy. A theoretical error propagation for equations (5) of our manuscript delivers some insight into the error-proneness of the approach. We define $i_{l,a}i_{l,c}^{-1} \equiv A$ and $\Delta i_{l,c}\Delta i_{l,a}^{-1} \equiv B$ so that subsequent Gaussian error analysis leads to:

$$\Delta SOC = \frac{B}{(1+AB)^2}\Delta A + \frac{A}{(1+AB)^2}\Delta B. \tag{S5}$$

And after a final rearrangement one arrives at:

$$\Delta SOC = \frac{AB}{(1+AB)^2}\left(\frac{\Delta A}{A} + \frac{\Delta B}{B}\right) \tag{S6}$$

For constant relative errors of A and B, this function has a global maximum at $A = B^{-1}$:

$$\max(\Delta SOC) = \frac{1}{4}\left(\frac{\Delta A}{A} + \frac{\Delta B}{B}\right) \tag{S7}$$

In words, the maximum absolute error for the SOC estimate calculated from equations (5) of our manuscript is directly connected to the sum of the relative errors of the experimentally measured current ratios $i_{l,a}i_{l,c}^{-1}$ and $\Delta i_{l,c}\Delta i_{l,a}^{-1}$. Indeed, ΔAA^{-1} and ΔBB^{-1} are directly related to the measurement error for the anodic and cathodic current, $i_{l,a}$ and $i_{l,c}$. If one aims at absolute SOC estimation errors of not more than 5%, then the sum of relative measurement errors for $i_{l,a}i_{l,c}^{-1}$ and $\Delta i_{l,c}\Delta i_{l,a}^{-1}$ must not exceed 20%. In general, current measurement can easily be achieved with relative measurement errors lower than 1%. However, for currents in the nanoampere range, which is the order of magnitude usually recorded at microelectrodes, the necessary hardware becomes costly. Consequently, this error analysis clearly suggests two options for an improvement in both cost-efficiency and accuracy of the presented SOC monitoring approach:

(1) Increasing absolute currents to the moderate to low microampere range by utilization of microelectrodes with larger diameters (*e.g.*, 100 μm), multiple microelectrodes in electrical parallel connection (*e.g.*, microelectrode arrays), or macroelectrodes.

(2) Investigating cost-efficient hardware for low current measurements.

Real-time SOC monitoring: SOC estimates of the different methods

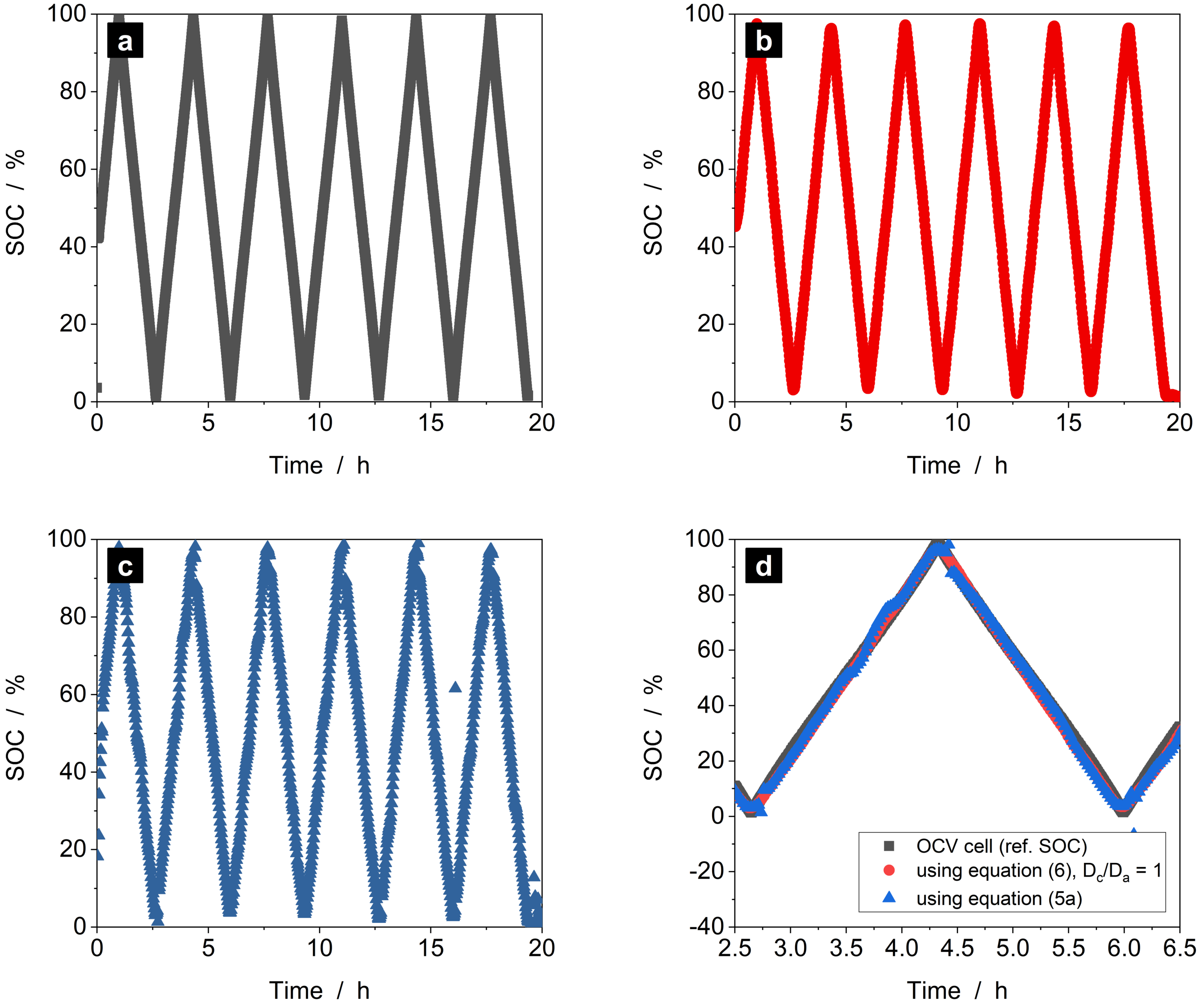

Figure S11. SOC estimates from (a) the symmetric open-circuit cell, (b) the amperometric approach using equation (6) of the manuscript with the assumption that $D_O D_R^{-1} = 1$, and (c) the amperometric approach using equation (5a) of the manuscript. (d) A superposition of (a) to (c) for the second cycle.

Alternating measurement mode. The steady-state currents at the mass-transfer limiting driving voltages of the closed bipolar setup were measured in an alternating measurement mode, *i.e.*, by alternating the driving voltage between –0.2 V and 0.8 V at a single microelectrode. The current value was then obtained after 10 s after the voltage was applied. After each 0.8 V interval a 1 min interval at 0.3 V (*i.e.*, approximately zero current) followed to reduce the number of measurement points. While the resulting currents and the SOC estimates have been depicted in a superposition within the manuscript already, we provide the SOC estimates of the different approaches in single graphs as well as a close-up of the second cycle in **Figure S11**.

Real-times SOC monitoring: An alternative operation mode of the closed bipolar setup

Continuous measurement mode. The experimental approach used for the real-time SOC monitoring presented within the manuscript relied on alternating the driving voltage of the bipolar microelectrode setup between positive and negative voltages. Another approach would be the simultaneous and continuous measurement of the anodic and cathodic steady-state currents with two identical microelectrodes. Unfortunately, this approach could not be investigated empirically due to hardware limitations of our laboratory. However, in order to demonstrate the basic opportunity of a continuous measurement, the bipolar microelectrode was operated at a constant voltage of –0.2 V for five cycles and, subsequently, at 0.8 V for another five cycles of the same redox flow battery. The obtained limiting currents (not smoothed) at the microelectrode and their evolution over time is depicted in **Figure S12**.

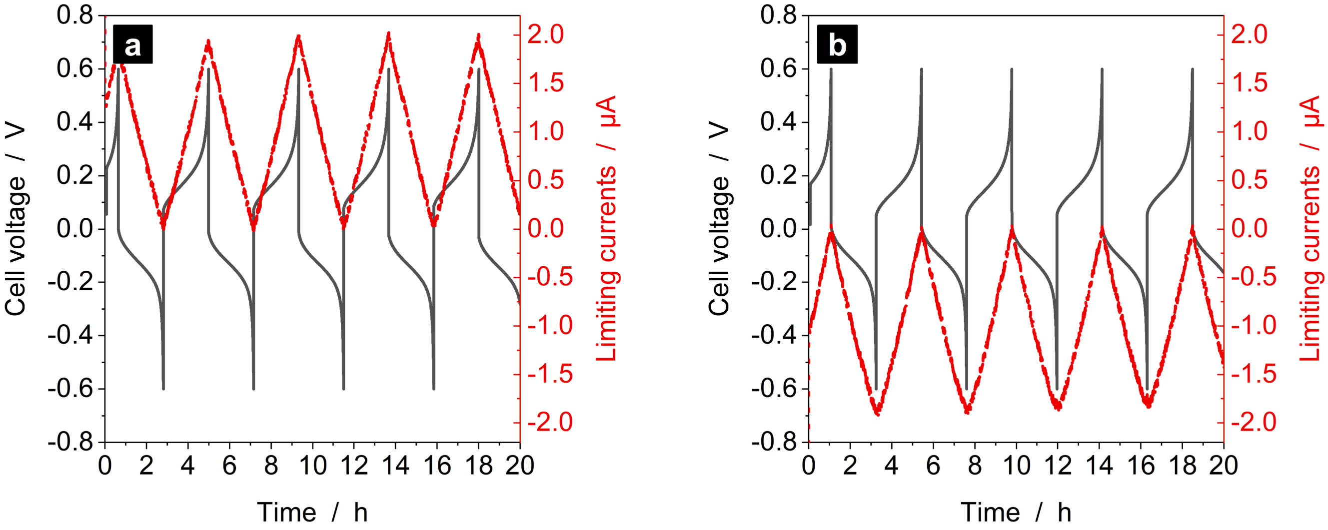

Figure S12. Continuous current measurement at the carbon fiber microelectrode (diameter: 33 μm) as an alternative operation mode of the amperometric sensor: (a) Cathodic current with the driving voltage at 0.8 V and (b) anodic current with the driving voltage at –0.2 V.

Again, a linear behavior was observed for both currents. Therefore, it is anticipated that the simultaneous and continuous measurement of limiting currents at two identical microelectrodes would deliver the same SOC estimation capability as the alternating mode. Indeed, from a theoretically point of view the restrictive wording “identical microelectrode” is not really necessary. Because even if the microelectrodes are not identical, the approach should theoretically work. If, for example, two microelectrodes with different surface areas are assumed, equations (3) and (4) of our manuscript only change in that they both would additionally contain the ratio of the microelectrode radii, $r_O r_R^{-1}$; that is, for a catholyte:

$$SOC = \frac{1}{1 - \frac{i_{l,a}}{i_{l,c}} \frac{r_O}{r_R} \frac{D_O}{D_R}}, \tag{S8}$$

$$\frac{\Delta i_{l,c}}{\Delta i_{l,a}} = \frac{4nFr_O D_O c(SOC_2 - SOC_1)}{-4nFr_R D_R c\big((1 - SOC_2) - (1 - SOC_1)\big)} = \frac{r_O}{r_R} \frac{D_O}{D_R}. \tag{S9}$$

Consequently, the combination of these equations still results in equation (5a). The same is true for the anolyte analogues of the equations above and equation (5b). However, further empirical studies are necessary to validate this alternative approach.

REFERENCES

(1) Guerrette, J. P.; Oja, S. M.; Zhang, B., Coupled Electrochemical Reactions at Bipolar Microelectrodes and Nanoelectrodes. *Anal. Chem.* **2012**, *84*, 1609-16.

(2) Stolze, C.; Hager, M. D.; Schubert, U. S., State-of-Charge Monitoring for Redox Flow Batteries: A Symmetric Open-Circuit Cell Approach. *J. Power Sources* **2019**, *423*, 60-67.

(3) Janoschka, T.; Martin, N.; Martin, U.; Friebe, C.; Morgenstern, S.; Hiller, H.; Hager, M. D.; Schubert, U. S., An Aqueous, Polymer-Based Redox-Flow Battery Using Non-Corrosive, Safe, and Low-Cost Materials. *Nature* **2015**, *527*, 78-81.

(4) Ressel, S.; Bill, F.; Holtz, L.; Janshen, N.; Chica, A.; Flower, T.; Weidlich, C.; Struckmann, T., State of Charge Monitoring of Vanadium Redox Flow Batteries Using Half Cell Potentials and Electrolyte Density. *J. Power Sources* **2018**, *378*, 776-783.

(5) Kroner, I.; Becker, M.; Turek, T., Monitoring the State of Charge of the Positive Electrolyte in a Vanadium Redox-Flow Battery with a Novel Amperometric Sensor. *Batteries* **2019**, *5*, 5.

(6) Cox, J. T.; Guerrette, J. P.; Zhang, B., Steady-State Voltammetry of a Microelectrode in a Closed Bipolar Cell. *Anal. Chem.* **2012**, *84*, 8797-804.